Ice nucleation ability of secondary aerosol particles at cirrus cloud conditions

Zur Erlangung des akademischen Grades eines

DOKTORS DER NATURWISSENSCHAFTEN

von der KIT-Fakultät für Physik des

Karlsruher Instituts für Technologie (KIT)

genehmigte

DISSERTATION

von

Barbara Bertozzi

ABSTRACT

Clouds are an important component of the atmosphere as they regulate the hydrological cycle and contribute to the Earth's radiative budget by scattering and absorbing short and longwave radiation. Clouds in the atmosphere can only form with the contribution of aerosol particles. Their availability together with the dynamic forcings (e.g. updraft velocity) define the microphysical and radiative properties of the clouds. Cirrus are high-level clouds composed uniquely of ice crystals and account for about 17 % of the clouds on a global average. The net radiative effect of cirrus clouds is highly sensitive to their microphysical properties, such as the number concentration and size of the ice crystals, which in turn depend on the formation mechanism. In the cirrus formation temperature range (T $< -38\,°$C), ice crystals can form via homogeneous freezing of ubiquitous aqueous solution droplets or via heterogeneous freezing with the contribution of solid or partially solid/liquid particles called ice nucleating particles (INPs). Currently, it is still poorly understood which of the two mechanisms dominates in different geographical locations and thermodynamic conditions. The abundance of aerosol particles and their ability to catalyze ice nucleation are key parameters to correctly interpret and describe cirrus cloud formation in the atmosphere. However, the role of secondary particles in ice cloud formation is still unsettled due to the complexity of their composition, the variety of processes affecting their chemical and physical properties, and the number of different ice formation pathways they can be subjected to.

In this thesis, the ice nucleation ability of secondary particles with compositions commonly found in the upper troposphere was investigated with ad-hoc measurement campaigns. The experiments were performed at the AIDA chamber at the Karlsruhe Institute of Technology and at the CLOUD experiment at the European Organization for Nuclear Research (CERN). The ice nucleation measurements were performed with expansion cooling experiments in the AIDA chamber and with continuous flow diffusion chambers at temperatures between $-38\,°$C and $-65\,°$C. The first part of the thesis describes the study of the ice nucleation ability of secondary inorganic and organic aerosol particles as a function of their chemical composition and phase state. The second part of the thesis explores the effect of aging processes and cloud cycling on the ice nucleation ability of internally mixed particles.

Two inorganic systems were chosen due to their strong relation with anthropogenic emissions, namely inorganic salts composed of sulfuric acid and ammonia, and ammonium nitrate. Ammoniated sulfate particles are among the most abundant in the atmosphere. Particles with different degrees of neutralization can form depending on the relative concentration of gas-phase sulfuric acid and ammonia. The ice nucleation ability of partially neutralized particles is investigated in this thesis for the first time. The measurements indicate that partially neutralized particles with an ammonium-to-sulfate ratio higher than 1.1 can initiate heterogeneous ice nucleation at temperatures below about $-50\,°$C. In particular, it was found that the ice nucleation ability of the ammonium-sulfate particles increases with their degree of neutralization.

Although ammonium nitrate is expected to remain in an aqueous phase state even at very low relative humidity, crystalline ammonium nitrate particles have been recently detected in the upper troposphere during the Asian summer monsoon. A new heterogeneous crystallization pathway for pure ammonium nitrate particles is here investigated by adding small amounts of sulfate by co-condensation of small amounts of sulfuric acid and ammonia. The results indicate that a sulfate content of about $0.4\,\mathrm{mol}\%$ is sufficient to initiate the heterogeneous crystallization of the ammonium nitrate particles. In agreement with previous studies, the crystalline ammonium nitrate particles showed a high ice nucleation ability, thus highlighting their importance as a potential seeds for heterogeneous cirrus cloud formation.

Secondary organic aerosol (SOA) particles originate from the oxidation and gas-to-particle conversion of volatile organic compounds (VOCs) and represent a large fraction of the organic aerosol burden. The ice nucleation ability of SOA particles was studied for three different systems: α-pinene, mixtures of α-pinene and isoprene, and naphthalene. Experiments with α-pinene SOA were performed at different temperatures and relative humidities to investigate how the thermody-

namic conditions at which SOA particles form (e.g., in the boundary layer or the upper troposphere) may influence their chemical composition and thus their ice nucleation ability. As SOA particles in the atmosphere are likely to be mixtures of several compounds, the effect of isoprene oxidation products on the ice nucleation ability of α-pinene SOA particles was also investigated. Finally, naphthalene SOA particles were studied as a representative system for anthropogenic SOA. All the investigated SOA particles were found to initiate ice formation only at or above the ice saturation ratio threshold for homogeneous freezing of aqueous solution droplets. These results suggest that the SOA particles investigated here likely do not contribute significantly to heterogeneous cirrus formation.

Mineral dust particles, sulfates, and organics have often been found internally mixed in upper tropospheric aerosol samples and also in cirrus ice crystal residuals. Experiments were performed with internally mixed particles composed of ammonium sulfate (AS) and secondary organic material (SOM) from the oxidation of α-pinene to investigate the effect of different atmospheric processes on their ice nucleation ability. The measurements show that small organic mass fractions of $5-8\,wt\%$ condensed on the surface of AS crystals are sufficient to completely suppress their heterogeneous ice nucleation ability. However, ice or liquid cloud processing of such SOM-coated AS crystals significantly improved their ice nucleation ability. Most probably the particles adopt a partially engulfed structure, where some ice nucleating sites of the AS component remain uncovered by the organic material. The morphology of the internally mixed particles is found to be a key aspect to describe their ice nucleation ability.

The effect of atmospheric aging has also been investigated for feldspar mineral dust particles. Mineral dust particles are among the most ice-active INPs present in the atmosphere. However, during their uplift or transport in the upper troposphere, they can acquire coatings of different substances. In the experiments presented in this thesis, thin coatings of sulfuric acid and SOM from the oxidation of α-pinene were condensed on the surface of the mineral dust particles to simulate atmospheric aging. The high ice nucleation ability of the bare mineral dust particles was strongly suppressed by the thin coatings. Both the low ice nucleation onset of the bare particles and the strong suppression of their ice nucleation ability by small amounts of condensed material suggest that pores and cracks are responsible for the high ice nucleation ability of the uncoated feldspar particles. These results indicate that aging processes can strongly alter the ice nucleation ability of mineral particles, at least those including feldspar components, and should be considered when calculating or predicting cirrus cloud formation.

The results presented in this thesis show that the chemical composition of the particles can critically define the ice nucleation ability of some secondary aerosol particles, such as for particles in the ammonium-sulfate and ammonium-nitrate systems. Instead, the secondary organic aerosol particles investigated here did not show such a dependency on their chemical composition. Atmospheric processes, such as coating and cloud cycling were shown to modify the ice nucleation ability of internally mixed particles by changing their surface properties and morphology. This thesis provides a comprehensive and coherent investigation of the ice nucleation ability in the cirrus cloud temperature range for relevant atmospheric secondary aerosol particles also considering the effects of the most common atmospheric aging processes.

CONTENTS

1 | INTRODUCTION

1.1 ATMOSPHERIC AEROSOLS

Aerosol particles are solid or liquid particles suspended in a carrier gas. Atmospheric aerosol particles, or just aerosols, range in size from a few nanometers to tens of micrometers in diameter, and vary widely in concentration and composition within the atmosphere (Seinfeld and Pandis, 2012). The complexity of the aerosol temporal and spatial distribution depends on the geographical non-uniformity of their sources and on the atmospheric processes they are subjected to (such as chemical processing, transport, and removal mechanisms), which is why a quantitative description of their properties and interactions in the Earth system is still challenging (Sorensen et al., 2019).

Atmospheric aerosols influence several aspects of our lives, from air quality and human health (e.g., Schwartz et al., 1996; Silva et al., 2013; Shiraiwa et al., 2017) to weather and climate, also by means of their interactions with clouds (e.g., Boucher et al., 2013; Charlson et al., 1992; Pöschl, 2005; Fan et al., 2016). Clouds are important regulators of the hydrological cycle through precipitation (Ramanathan, 2001), and of the Earth's temperature through their radiative effect (Lohmann and Feichter, 2005). It is thus crucial to study their formation mechanism and properties. In particular, cloud formation in the atmosphere is underpinned by aerosol particles that act as seeds for droplets, called cloud condensation nuclei (CCN), or ice crystals, called ice-nucleating particles (INPs) (Pruppacher and Klett, 1997).

Atmospheric aerosols are usually classified according to their (i) physical characteristics, (ii) sources, or (iii) chemical composition (Seinfeld and Pandis, 2012). *Aerosol size distributions* are usually described with four characteristic modes: nucleation mode (1-10 nm in diameter), Aitken mode (10-100 nm), accumulation mode (0.1-1 µm), and coarse mode (1-10 µm). Particles with diameters larger than 2.5 µm and 10 µm are identified as coarse and giant particles, respectively, while those with diameters smaller than 2.5 µm and 0.1 µm are called fine and ultrafine particles. Schematics of these classes of particle number, surface, and mass size distributions are shown in Figure 1.1. The nucleation and Aitken modes usually dominate the number size distribution, while the accumulation mode contribute, together with the coarse mode, to the majority of the aerosol surface. Finally, despite their low number concentration, particles in the coarse mode are responsible for a large fraction of the aerosol mass.

Aerosol particles are also classified according to their *origin*. Aerosols are defined as primary if directly emitted into the atmosphere, or secondary if originated by chemical reactions resulting in gas-to-particle conversion (Seinfeld and Pandis, 2012). Examples of natural *primary* aerosols are mineral dust, sea spray, volcanic ash, and biological particles such as bacteria and pollen (Pandis et al., 1995). Primary particles can also originate from human-related activities like fuel combustion and industrial processes, and are thus labeled as anthropogenic primary particles (Tomasi and Lupi, 2017). Primary particles are emitted into the atmosphere via mechanical processes such as wind resuspension (Mahowald et al., 2005), wave crashing (Lewis and Schwartz, 2004), combustion (Lighty et al., 2000), and spore discharging (Elbert et al., 2007). *Secondary* particles of natural origin derive from the oxidation of gas precursors such as sulfur gases, emitted for example by oceans, wetlands and volcanoes (Bates et al., 1992), and organic compounds, mainly emitted from vegetation (Guenther et al., 1995). Sulfate (e.g., from biomass burning and fossil fuel combustion), nitrates (e.g., from fuel combustion, agriculture and biomass burning), and ammonium (e.g. from live-stocks) are the major components of anthropogenic secondary inorganic aerosol particles (Smith et al., 2011). Additionally, organic compounds (e.g., from cooking and transportation related emissions) are also often found in anthropogenic secondary aerosols (e.g., Parrish et al., 2009; McDonald et al., 2018). A description of the formation mechanism and thermodynamic properties of secondary aerosols are presented in Sections 2.3 and 2.4.
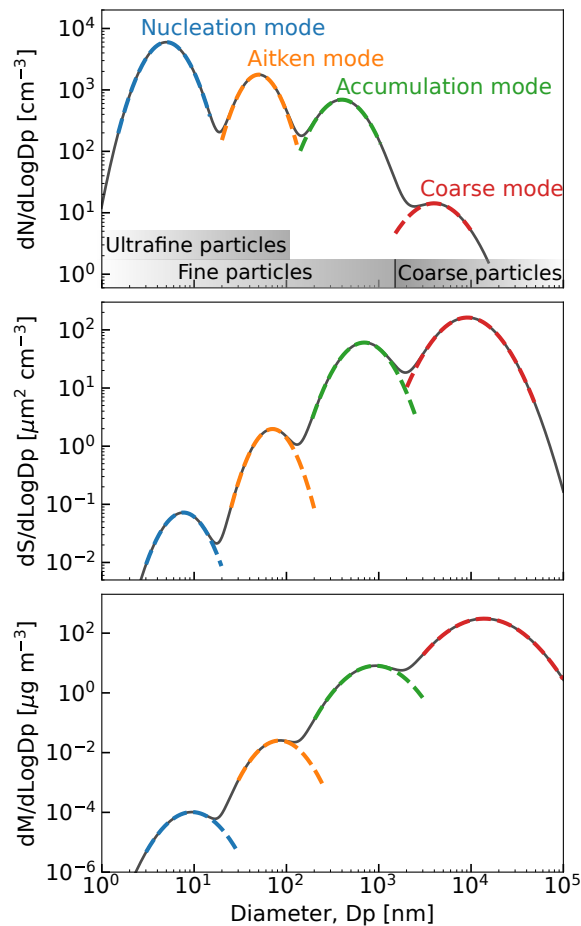
Figure 1.1: Schematic particle number (upper), surface (middle), and mass (lower) size distributions. Figure adapted from Seinfeld and Pandis (2012).

Finally, aerosols can be classified according to their *elemental composition* and *mixing state*. A primary distinction can be made between inorganic and carbonaceous aerosol particles, the first include sulfate and nitrate-containing compounds, while the second comprises carbon-containing compounds (Seinfeld and Pandis, 2012). Carbonaceous aerosol particles, in turn, can be divided in two major categories: organic carbon, which itself includes different classes such as terpenes and aromatics, and elemental (or black) carbon (Contini et al., 2018). The large variety of aerosol components results in a complex mixture of aerosol types that reside in the atmosphere. If each aerosol component can be assumed to be physically separated from the others the particles form a so-called external mixture, if instead each particle is a mixtures of the different components the aerosol population is defined as internally mixed (Seinfeld and Pandis, 2012).

While suspended in the atmosphere, aerosols continuously transform due to several atmospheric processes that can modify their chemical and physical characteristics. *Chemical aging*, for example, can occur due to the condensation and evaporation of gaseous compounds (Donahue et al., 2006; Jimenez et al., 2009) and to heterogeneous reactions on the surface of the particles (Zhang et al., 2008; Shiraiwa et al., 2011; Gaston, 2020). Aerosol *physical processing* results from temperature and humidity cycles the particles are exposed to during their lifetime in the atmosphere. In particular, cloud processing and subsequent evaporation or sublimation of the hydrometeors is estimated to be an important mechanism that involves a large fraction of the atmospheric aerosol particles (Pruppacher and Jaenicke, 1995; Hoose et al., 2008). Following a cloud process the particle number concentration and size distribution (Hoppel et al., 1986), their chemical composition (Herrmann et al., 2015), and morphology (Adler et al., 2013) can be affected.

Since this thesis focuses on secondary aerosol particles and their ability to catalyze ice crystals formation in the upper troposphere at temperatures below $-38\,°C$, a brief review of sources and composition of the upper tropospheric particles is presented in the following section. An overview of atmospheric ice nucleation and ice nucleating particles follows (Section 1.1.2), together with a summary of the radiative effects of clouds, with particular attention to clouds composed only of ice crystals (Section 1.1.3).

1.1.1 Aerosol particles in the upper troposphere

All aerosol sources are close to the Earth's surface, but several mixing and transport mechanisms contribute to their spread at different latitudes and altitudes. As the residence time of aerosol particles increases with altitude, particles in the upper troposphere have long lifetimes, ranging from days to months, and can spread over large geographical areas, making their influence on the Earth's climate of great importance (Seinfeld and Pandis, 2012). Sources and processes taking place in the lower troposphere have been extensively investigated, while studies on the concentration, distribution, and properties of upper tropospheric aerosols are still technically challenging and scarce. Our knowledge of the chemical-physical properties of upper tropospheric constituents essentially derives from aircraft measurements that are limited in space and time and can thus provide only snapshots of the atmospheric composition.

Aerosol particles and gas precursors are uplifted from the boundary layer to the upper troposphere (UT) and lower stratosphere (LS) mainly by deep convective systems (e.g., Twohy et al., 2002; Vernier et al., 2011). However, particles and gases originated from volcanic eruptions and biomass burning can directly reach high altitudes (e.g., Robock, 2000; Fromm et al., 2000). Aircraft measurements have shown large areas of the upper troposphere, especially in tropical and subtropical regions, with high number concentrations of aerosol particles in the fine and ultrafine modes, thus presumably originated in situ (Clarke, 1998; Andreae et al., 2018; Williamson et al., 2019).

The elemental composition of UTLS aerosol particles measured over a 10-year period revealed a high variability related to geographical location, season, and altitude (Martinsson et al., 2019). In fact, depending on where convection takes place, different types of primary particles and precursor molecules can be loft and lead to the formation of particles with different chemical compositions. *Sulfate* and *organics* have been suggested to dominate the formation and growth of the fine particles over pristine regions, such as the Amazon basin or the oceans (Clarke, 1998; Andreae et al., 2018). Chemical composition measurements performed in the remote troposphere over the Atlantic and Pacific oceans during the ATom (Atmospheric Tomography Mission) missions revealed that organic matter is one of the three dominant components of the submicron aerosol, together with sulfate and *sea salt* (Murphy et al., 2019; Hodzic et al., 2020).

Anthropogenic emissions, e.g. of sulfate and *nitrate*, can dominate over highly polluted regions, such as tropical and subtropical Asia. During the summer monsoon period, for example, pollutants produced close to the surface are uplifted to high altitudes and form the so-called Asian Tropopause Aerosol Layer (ATAL, Vernier et al., 2011). A weaker and of smaller extent aerosol layer associated with the North American monsoon was also observed over the Southwestern United States and Mexico (Vernier et al., 2011; Thomason and Vernier, 2013). Several aircraft measurement campaigns performed in the UT over central and north America have shown that most of the particles in the accumulation mode consist of sulfate and carbon compounds (both organic and black carbon), often found as *internal mixtures* (Murphy et al., 2006; Froyd et al., 2009).

Desert regions are significant sources of atmospheric *dust particles*. The most active dust sources are located in arid regions such as North Africa, which contributes to 55 % of the global emissions, Middle East, and central Asia (Ginoux et al., 2012). Atmospheric mixing and circulation can transport plums of dust particles far away from their strong sources. Saharan dust plumes, for example, can reach Northern Europe (Ansmann et al., 2003), Iceland (Varga et al., 2021), the United States (Prospero, 1999), and eventually the Southern Ocean (Li et al., 2008).

Changes in the emission rates of primary particles and gas precursors reflect in changes in the concentration and composition of tropospheric aerosols. Lidar and satellite measurements, for ex-

ample, have shown an increasing trend in the concentration of sulfur-containing gases and particles in the upper troposphere over Asia since the late 1990s (Kulkarni et al., 2008; Vernier et al., 2015). Bossolasco et al. (2021) modeled the composition and decadal trends of the ATAL and obtained a positive trend in the concentration of all the anthropogenic and biomass burning aerosols.

Biogenic sources are also affected by human activities and climate warming. The concentration of soil dust in the atmosphere, for example, is increasing due to processes such as deforestation (Satheesh and Krishnamoorthy, 2005). Emissions of volatile organic compounds from biogenic sources is expected to rise with increasing global temperature, thus leading to an increment of secondary organic material present in the atmosphere (Guenther et al., 1993).

As aerosol particles strongly affect the climate, it is important to understand how their concentration and properties (such as their ability to catalyze cloud formation) change with time, and to assess the contribution of anthropogenic activities.

1.1.2 Ice nucleation in the atmosphere

Atmospheric ice nucleation has been an emerging field of study since the 1950s (e.g., Smith and Heffernan, 1954; Mason and Maybank, 1958), and still drives the interest of several scientists at different processing scales, from molecular simulations (e.g., Fitzner et al., 2015) to laboratory and field studies (Hoose and Möhler, 2012; Kanji et al., 2017), to climate models (e.g., Atkinson et al., 2013). Ice in the atmosphere can be found either in mixed-phase clouds, where ice crystals coexist with supercooled water droplets, or in cirrus clouds, where only ice crystals are present. Ice formation in the atmosphere can occur by homogeneous nucleation from the liquid phase at temperatures below $-38\,°C$ or by heterogeneous nucleation from the vapor and liquid phases with the contribution of an external solid surface (Pruppacher and Klett, 1997). A detailed description of the homogeneous and heterogeneous nucleation mechanisms is presented in Sections 2.1 and 2.2.

Heterogeneous freezing strongly depends on the composition and surface features of the particle that catalyzes ice nucleation, called *ice nucleating particle* (INP). Only a limited subset of the atmospheric particles can promote ice nucleation at a higher temperature and/or lower relative humidity than required for homogeneous freezing. However, the criteria for an aerosol particle to act as INP are not fully understood yet. INP number concentration is typically a few per standard liter at temperatures down to $-20\,°C$, and their occurrence is highly variable in space and time (Pruppacher and Klett, 1997; DeMott et al., 2010). Despite their rarity, their impact on cloud properties and climate is significant (see Section 1.1.3 for more details).

Different *heterogeneous ice nucleation modes* are distinguished in the literature (Vali et al., 2015; Lohmann et al., 2016): (i) immersion freezing, when freezing is initiated from within a cloud or solution droplet; (ii) condensation freezing, when water vapor condenses and originates a supercooled liquid droplet which subsequently freezes; (iii) contact freezing, when freezing is induced by the collision of an aerosol particle with a droplet surface; (iv) deposition nucleation, when water vapor directly deposits as ice on the aerosol particle surface; (v) pore condensation and freezing when liquid water first condenses in pores and then freezes homogeneously or heterogeneously (David et al., 2019). The individual ice nucleation mechanisms are summarized in Figure 1.2 (Kanji et al., 2017).

Although a complete theoretical understanding of ice nucleation is not yet accomplished, several laboratory and field studies have investigated empirically the ice nucleation ability of different aerosol particles at different temperatures and relative humidity. Classes of known atmospheric relevant INPs are mineral dust, soot, bio-aerosols, crystalline salts, organic acids, and humic-like substances. As summarized by Hoose and Möhler (2012), and by Kanji et al. (2017), the ice nucleating ability of atmospheric particles covers a wide range of temperatures and relative humidity.

Different aging mechanisms can alter the ability of the aerosol particles to drive ice nucleation, by modifying their composition, surface properties, and morphology. For example, the ability of dust particles to initiate heterogeneous ice nucleation at cirrus cloud conditions (i.e., at $T < -38\,°C$) can be suppressed by coatings of secondary organic material or sulfuric acid (Möhler et al., 2008; Cziczo et al., 2009). However, in the immersion freezing mode, the ice nucleation ability of desert dust particles is not influenced by organic coatings. Additionally, Mahrt et al. (2020a) investigated the ice nucleation ability at cirrus cloud conditions of two different types of soot particles aged in
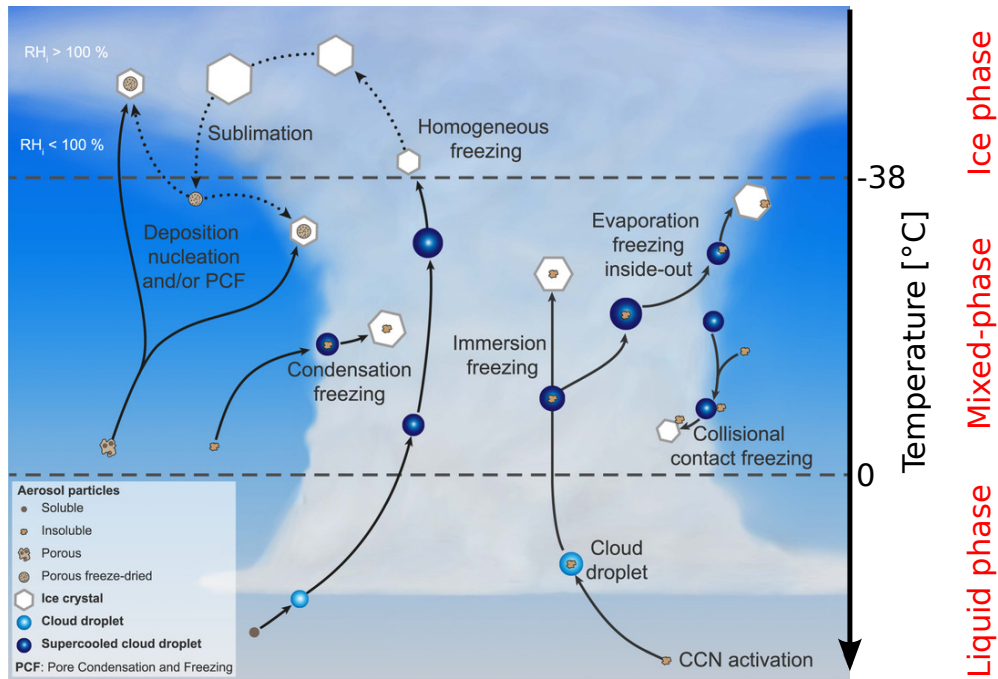
Figure 1.2: Schematic of the atmospheric ice nucleation modes. From Kanji et al. (2017). ©American Meteorological Society. Used with permission.

water and aqueous acidic solutions. Their experiments show an enhanced water uptake and ice nucleation activity of the aged soot particles compared to the fresh samples.

Aerosol particles are often subjected to temperature and relative humidity cycles and *cloud processing* during their lifetime in the atmosphere. These processes can alter the ice nucleation ability of the particles via to the so-called pre-activation phenomenon (Roberts and Hallett, 1968) or by changing their morphology (Adler et al., 2013). Highly viscous organic particles, for example, have shown an enhanced ice nucleation ability after being pre-cooled (Ladino et al., 2014) or processed in a cloud cycle (e.g., Wagner et al., 2012; Wagner et al., 2017; Kilchhofer et al., 2021). More recently, the effect of different cloud processing (i.e., liquid or ice cloud processing) on the ice nucleation ability of soot particles has also been investigated (Mahrt et al., 2020b; Kilchhofer et al., 2021).

1.1.3 The aerosol indirect effect on climate

Aerosol particles affect the climate both directly, by scattering and absorbing radiation (aerosol-radiation interaction), and indirectly, by defining the radiative properties of clouds (*aerosol-cloud interaction*). As 70% of the Earth's surface is covered by clouds (annual mean average, Stubenrauch et al., 2013), their contribution to the radiation budget is significant. In particular, cirrus clouds represent 17 % of the clouds on a global average and have a maximum occurrence frequency of 70 % near the tropics (Sassen et al., 2008).

Clouds have both an *albedo effect*, by scattering back to space a fraction of the incoming solar radiation, and a *greenhouse effect*, by absorbing and re-emitting the longwave radiation emitted by the Earth (Lohmann et al., 2016). Which of the two effects dominate, determining the cooling or warming effect of the clouds, depends on the microphysical properties, thickness, altitude, and geographical location of the formed cloud. Warm low-level clouds, composed only of liquid droplets, generally have a cooling effect by being optically opaque to solar radiation (i.e. having an high albedo) and by having a low greenhouse effect. By contrast, high-level clouds composed only of ice crystals are semitransparent to the solar radiation and trap the outgoing thermal radiation, with a resulting warming effect.

Globally, clouds have a net cooling effect (Loeb et al., 2009) but changes in their properties due to anthropogenic warming and modification of the atmospheric aerosol composition can amplify

(positive feedback) or reduce (negative feedback) the initial forcing. The *Cloud feedback* is commonly associated with changes in cloud occurrence, altitude, and opacity (Zelinka et al., 2016). The last includes changes in cloud water content and microphysical properties such as phase, size, and number concentration of the hydrometeors. The cloud feedback to a warmer planet is assumed to be positive (Zelinka et al., 2017).

Since cloud formation relays on the presence of seed particles and on their ability to catalyze droplets and ice crystals formation, number concentration and properties of the atmospheric aerosol particles play a crucial role in assessing the microphysical properties of the clouds and their radiative effect (Storelvmo, 2017; Murray et al., 2021). In particular, the effect of a change in concentration and ability of ice nucleating particles (INPs) induced by climate changes or directly due to anthropogenic activities has been defined as the *ice indirect effect* (DeMott et al., 2010), whose magnitude and sign are still very uncertain (Boucher et al., 2013).

Cirrus clouds form below the homogeneous freezing temperature ($-38\,°C$), and can thus originate either via homogeneous freezing of diluted solution droplets at a high relative humidity, or via heterogeneous freezing at a lower relative humidity if INPs are present (Pruppacher and Klett, 1997). Solution droplets are ubiquitous in the upper troposphere and are present in much higher number concentrations than INPs, that are typically on the order of $0.01\,\mathrm{cm}^{-3}$ or less (DeMott et al., 2003). Cirrus clouds formed via homogeneous freezing are thus characterized by a higher concentration of smaller ice crystals compared to cirrus clouds formed via heterogeneous freezing. The abundance and ice nucleation ability of the aerosol particles significantly determines the formation mechanism and the microphysical and radiative properties of the clouds (Krämer et al., 2016). Perturbations in their number concentration and ice nucleation ability can modify the formation mechanism of clouds and thus their radiative properties (Storelvmo, 2017). On the one hand, an increase of INPs in cirrus clouds formed via homogeneous freezing may induce the formation of ice crystals at lower relative humidity, and by depleting the ambient water vapor, suppress the homogeneous freezing of aqueous solution droplets. On the other hand, if particles able to nucleate ice heterogeneously are subjected to aging mechanisms that reduce or suppress their ice nucleation ability, the cirrus cloud will then only form at higher relative humidity via homogeneous freezing.

1.2 RESEARCH QUESTIONS AND THESIS OUTLINE

To understand and protect our climate, we need to understand the processes involved, and how natural and anthropogenic perturbations may modify them. Laboratory studies have a central role in addressing the incomplete fundamental knowledge of atmospheric science, thus linking field measurements and models. Cloud chamber studies, especially, allow to simulate the atmosphere with different complexity levels and to address the processes individually.

The role of secondary particles in ice cloud formation is still highly uncertain due to the complexity of their composition, the variety of processes affecting their chemical and physical properties, and the number of different ice nucleation pathways they can be subjected to. Secondary inorganic and organic particles with compositions commonly found in the upper troposphere, as well as their internal mixtures, have been investigated with ad-hoc measurement campaigns.

In this thesis, experimental results from laboratory measurement campaigns performed at the **A**erosol **I**nteraction and **D**ynanimcs in the **A**tmospshere (AIDA) facility at the Karlsruhe Institute of Technology and at the **C**osmic **L**eaving **Ou**tdoor **D**roplets (CLOUD) experiment at the European Organization for Nuclear Research (CERN) are presented.

The scientific basis necessary to interpret the results presented is summarized in Chapter 2. First homogeneous and heterogeneous nucleations are introduced. Follows a brief explanation of the formation mechanism and properties of secondary organic aerosols, and the description of the thermodynamic behavior of atmospheric inorganic salts.

The experimental facilities and instrumentation used are introduced in Chapter 3. A detailed characterization of the two continuous flow diffusion chambers developed and employed to perform the experiments is also provided.

Ammoniated sulfate particles are presented as first system. Those particles are among the most abundant in the upper troposphere, however their neutralization state (i.e., acidity) is highly unknown and strongly related to surface emissions (Park, 2004; Erisman et al., 2008). The ice nucleation ability of acidic (i.e., sulfuric acid, H_2SO_4) and fully neutralized (i.e., ammonium sulfate, $(NH_4)_2SO_4$) sulfate particles at cirrus condition has already been extensively investigated in the past. The role of partially neutralized particles (such as ammonium bisulfate, NH_4HSO_4, and letovicite, $(NH_4)_3H(SO_4)_2$) in cirrus cloud formation, instead, is still unclear. In Chapter 4, the ice nucleation ability of particles composed of sulfate and ammonium is investigated in regard to their chemical composition (i.e., degree of neutralization) and phase state.

Although ammonium nitrate is expected to remain in an aqueous phase state even at very low relative humidity, crystalline ammonium nitrate particles have been recently detected in the upper troposphere during the Asian summer monsoon (Höpfner et al., 2019). The low temperature crystallization behavior and ice nucleation ability of ammonium nitrate particles mixed with small amounts of sulfate have been recently investigated by Wagner et al. (2020). In Chapter 5, the work of Wagner et al. (2020) is extended to study a new heterogeneous crystallization pathway for the aqueous ammonium nitrate particles. In these new experiments, the uptake of sulfuric acid and ammonia from the gas phase onto pure, initially liquid ammonium nitrate particles was simulated for the first time. The ice nucleation ability of the aqueous and crystalline ammonium nitrate particles was also measured.

As a third system, a study on secondary organic aerosols will be presented. The complex chemical and physical properties of those aerosols have stimulated several experimental and modeling works aiming to understand their effect on cloud formation and climate (Shiraiwa et al., 2017). Their ice nucleation ability is still under debate, with controversial experimental results obtained in the last years (e.g., Ignatius et al., 2016; Wagner et al., 2017; Wolf et al., 2020). Chapter 6 reports the results from a suit of experiments performed at the CLOUD chamber to investigate the effect of different gas precursors and thermodynamic conditions during the nucleation and growth of the aerosol particles on their ice nucleation ability.

Aerosol particles in the upper troposphere likely undergo aging processes that can modify their chemical and physical properties. Mixed particles composed of sulfate and organics represent a major type of aerosol particles in the upper troposphere, but their ice nucleation ability was not yet investigated in laboratory studies. The study of internally mixed particles composed of ammonium sulfate and secondary organic material is presented in Chapter 7. The effect of liquid and ice cloud processes on the morphology and ice nucleation ability of the particles is also investigated.

Aging mechanisms do not only concern particles originated from the gas phase, but also primary particles. Dust particles are among the most active ice nucleating particles, but during their transport in the atmosphere condensable species can modify their surface properties. In chapter 8 the effect of thin coatings of secondary organic material and sulfuric acid on the ice nucleation ability of mineral dust particles is studied.

The findings presented in this thesis are summarized in Chapter 9.

2 | SCIENTIFIC BACKGROUND

The physical basis underlying the experiments shown in this thesis are presented in this chapter. The concepts of homogeneous and heterogeneous nucleation are presented in Sections 2.1 and 2.2, respectively. A brief description of the formation mechanism and properties of secondary organic aerosols is given in Section 2.3. Finally, the thermodynamic behavior of secondary inorganic particles is explained in Section 2.4.

2.1 HOMOGENEOUS NUCLEATION

The term nucleation denotes a phase transition which involves the overcoming of an energy barrier (Seinfeld and Pandis, 2012). Nucleation events are associated with first-order phase transitions, which frequently take place in the atmosphere. Transitions from the gas to the condensed phase occur, for example, when new aerosol particles form from gaseous precursors, or when ice crystals nucleate via deposition mode. Nucleation is said to be homogeneous when it happens in the absence of foreign materials, and heterogeneous when an external surface catalyzes the nucleation process.

Homogeneous nucleation is typically described by the so-called *classical nucleation theory* (CNT). CNT aims to describe the nucleation process thermodynamically and kinetically (e.g., Pruppacher and Klett, 1997; Ickes et al., 2015). Let's consider for simplicity the case of vapor as the initial (parent) phase and the nucleation of its condensed phase (liquid or solid). The energy of the system can be expressed through the Gibbs free energy G (Blundell and Blundell, 2010):

$$G = \sum_i \mu_i N_i \tag{2.1}$$

with i representing the different phases present in the system, μ their chemical potential, and N the number of molecules of the specific phase i. During a phase transition the number of molecules in the different phases change and so does the free energy of the system. The difference between the free energy of the system initially composed only of the vapor phase μ_v and its energy after the nucleation of a condensed cluster μ_c composed of n molecules is:

$$\begin{aligned} \Delta G(n) &= n(\mu_v - \mu_c) + \sigma A(n) \\ &= n\Delta\mu + \sigma A(n) \end{aligned} \tag{2.2}$$

where σ is the surface tension, and $A(n)$ the surface area of the newly formed cluster. The first term corresponds to the variation in the Gibbs free energy due to the change in the chemical potential of the system. The second term represents an increase in the energy of the system due to the new formed surface. For an ideal gas, the difference in chemical potential $\Delta\mu$ can be written as:

$$\Delta\mu = -k_B T \ln S \tag{2.3}$$

with k_B being the Boltzmann constant, T the temperature, and S the saturation ratio defined as:

$$S = \frac{p(T)}{p_s(T)} \tag{2.4}$$

where $p(T)$ is the actual vapor pressure, and $p_s(T)$ is the saturation vapor pressure of the gaseous compound. For the specific case of water vapor, the actual vapor pressure and its saturation value are usually indicated with the symbols e and e_s, respectively.

Assuming that the newly formed cluster has a spherical shape of diamter d, the variation in the Gibbs free energy can thus be written as:

$$\Delta G(d) = -\frac{\pi d^3}{6 V_m} k_B T \ln S + \pi d^2 \sigma \tag{2.5}$$

with V_m being the volume of a monomer of the nucleating substance. For the homogeneous nucleation of a water droplet or ice crystal, for example, V_m corresponds to the volume of a molecule of liquid water or ice, respectively. The first term in Equation 2.5 represents a volume contribution ($\Delta G_{volume} \sim d^3$), while the second term scales with the surface of the formed cluster ($\Delta G_{surface} \sim d^2$). Two $\Delta G(d)$ curves for the nucleation of liquid water from its vapor phase are represented in Figure 2.1 for two different saturation ratios ($S_w = 1.01$ and $S_w = 1.02$). The maximum in the variation of the free energy ΔG corresponds to the energy barrier ΔG^* the system has to overcome to form a critical stable cluster:

$$\Delta G^* = \frac{16\pi}{3} \frac{V_m^2 \sigma^3}{(k_B T \ln S)^2} \tag{2.6}$$

At sub-saturated conditions ($S < 1$) the surface term dominates and the formation of a new cluster is not energetically favored (red line). At super-saturated conditions ($S > 1$) two different regimes are possible depending on the diameter of the formed cluster. If the cluster is smaller than a critical value d^*, it will tend to evaporate to reduce its energy. If the cluster exceeds the critical size d^*, instead, the energy barrier ΔG^* is overcome and the cluster will spontaneously grow.
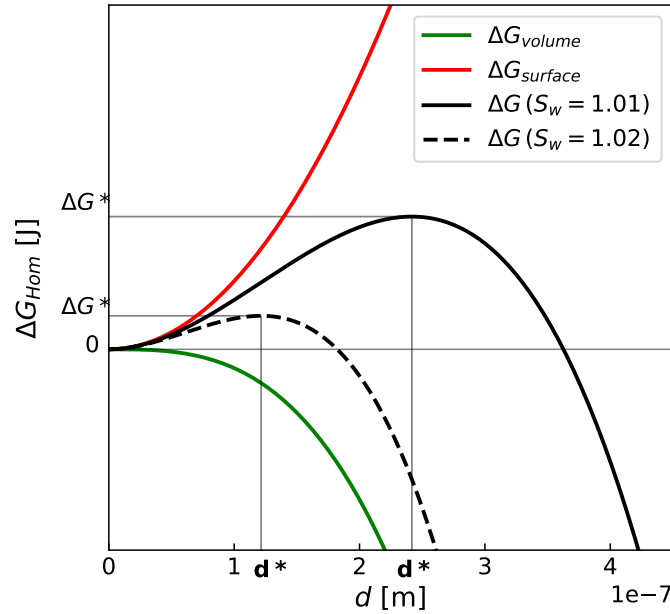

Figure 2.1: Variation in the Gibbs free energy for the homogeneous nucleation of a water droplet of diameter d from the vapor phase at $0\,^\circ C$ for two different water vapor saturation values S_w (black lines). Red and green curves represent the contribution from the surface and volume terms for the case with $S_w = 1.01$.

At equilibrium, and for $S > 1$, the number of stable clusters that form described by a Boltzmann distribution:

$$N_{clusters} = N_0 \exp\left(-\frac{\Delta G^*}{k_B T}\right) \tag{2.7}$$

where N_0 is the number of molecules in the parent phase.

By including the kinetic component K, the net number of clusters per unit time and unit volume that grow larger than the critical size, i.e. the *homogeneous nucleation rate coefficient* J_{hom}, can be estimated as (Pruppacher and Klett, 1997):

$$J_{hom} = K \cdot N_0 \exp\left(-\frac{\Delta G^*}{k_B T}\right) \tag{2.8}$$

The exponential part is the thermodynamic term, and K is the kinetic factor related to the number of molecules in the parent phase which can potentially be incorporated into the cluster (Ickes et al., 2015).

Finally, the nucleation rate ω inside a spherical volume V can be calculated as:

$$\omega = J_{hom} \cdot V = J_{hom} \cdot \frac{\pi}{6} \, d^3 \tag{2.9}$$

with d being the diameter of the aqueous droplet.

Nucleation of liquid water or ice from the vapor phase requires nucleation rates, and thus saturation ratios, too high for these phenomena to occur at atmospheric conditions (Lohmann et al., 2016). However, the nucleation of ice from the liquid phase (e.g., in a cloud droplet) at $-38\,°C$ is characterized by sufficiently high nucleation rates (i.e. above $1\,cm^{-3}s^{-1}$), to make this process possible in the atmosphere. The number of particles that freeze in a time interval Δt from a population of N water droplets of volume V is given by (Pruppacher and Klett, 1997):

$$N_{hom} = N \cdot P = N \cdot [1 - \exp{(-J_{hom} \, V \, \Delta t)}] \tag{2.10}$$

where P is the freezing probability of a single droplet.

Pure water droplets, or highly diluted solution droplets, exist in equilibrium only at or above liquid water saturation (Köhler, 1936). However, at low temperature in the atmosphere ice crystal formation from the liquid phase is observed also for $S_w < 1$, even in the absence of an external solid surface (i.e. without heterogeneous nucleation to occur). In fact, the liquid parent phase in this case is not a cloud droplet (e.g., a highly diluted solution) but a solution droplet, which achieve equilibrium at lower saturation ratios because of its reduced vapor pressure. For diluted solutions, this reduction in vapor pressure can be described with Raoult's law (Raoult, 1889):

$$p^* = \frac{n_A}{n_A + n_B} p_s^B \tag{2.11}$$

with p^* being the equilibrium vapor pressure of the solution, n_A the number of molecules of solute A, n_B the number of molecules of solvent B (i.e., water), and p_s^B the equilibrium vapor pressure of the pure solvent. As a consequence, solutions have lower freezing temperature than pure water, and can induce homogeneous freezing at subsaturated conditions with respect to liquid water.

To describe the *homogeneous freezing of aqueous solution droplets* in the atmosphere, different parameterizations have been suggested. Among the others, the parameterization introduced by Koop et al. (2000) is of easy application and often used as a reference. Koop et al. (2000) suggested that the homogeneous freezing rate of supercooled aqueous solutions is independent of the nature of the solute, and only depends on the water activity of the solution. The activity, a, of a solution is defined as:

$$a = \frac{p^*}{p_s^B} = \frac{n_A}{n_A + n_B} \, . \tag{2.12}$$

When water is the solvent (B), the water activity of the solution is indicated as a_w. In thermal equilibrium, the water activity of a solution corresponds to the ambient water saturation ratio ($e/e_{s,wat}$). A solution with higher activity has a larger fraction of solute (n_A) and thus a lower equilibrium vapor pressure (p^*). Koop et al. (2000) combined the experimental homogeneous nucleation rates coefficients J_{hom} of different type of solutions with their water activities, and obtained the following parameterization:

$$\log(J_{hom}) = -906.7 + 8502 \cdot \Delta a_w - 26924 \cdot (\Delta a_w)^2 + 29180 \cdot (\Delta a_w)^3 \tag{2.13}$$

where $\Delta a_w = a_w(T) - a_w^i(T)$. $a_w^i(T)$ is the water activity of a solution in equilibrium with ice at temperature T. Homogeneous freezing rate coefficients J_{hom} as a function of the temperature are shown in Figure 2.2a. The blue line represents the case of pure water ($a_w = 1$), the orange and red lines refer to solutions with $a_w = 0.98$ and $a_w = 0.96$, respectively. The three horizontal lines correspond to an atmospheric relevant homogeneous freezing rate ω of $1\,cm^{-3}\,s^{-1}$ (see equation 2.9) for aqueous droplets of different diameters ($d_1 = 0.1\,\mu m$, $d_2 = 1\,\mu m$, and $d_3 = 10\,\mu m$). The same three green lines are reported in Figure 2.2b as a function of the saturation ratio with respect to ice S_{ice}. These curves are often reported as a reference for the homogeneous freezing threshold of aqueous solution droplets in ice nucleation studies. A pure water droplet of $10\,\mu m$ in diameter, for example, reaches an atmospheric relevant freezing rate of $1\,cm^{-3}\,s^{-1}$ only at $-38\,°C$. If a solute is added (i.e. $a_w < 1$) to the same water droplet, a lower temperature is required to obtain the same nucleation rate.

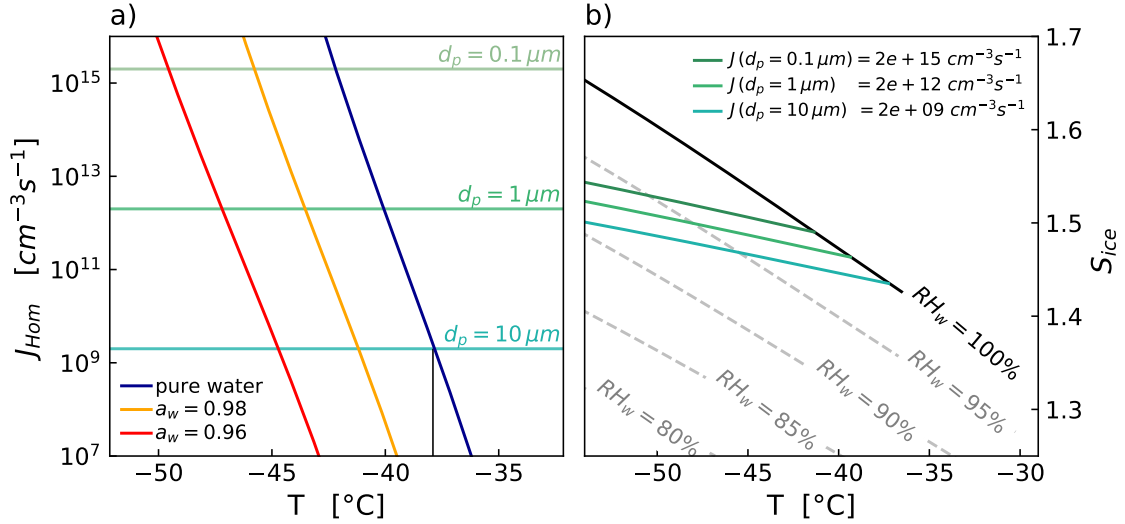**Figure 2.2: a)** Nucleation rate coefficients J_{hom} for the homogeneous freezing of pure water and aqueous solution droplets with two different water activities a_w (Koop et al., 2000). Green lines correspond to the homogeneous nucleation rate of $\omega = 1\,cm^{-3}\,s^{-1}$ for particles with different diameters. **b)** Same homogeneous freezing rate coefficients as in panel a as a function of the saturation ratio with respect to ice S_{ice}. Isolines of relative humidity are also reported.

2.2 HETEROGENEOUS NUCLEATION

Heterogeneous nucleation occurs when an external surface reduces the nucleation energy barrier and thus catalyzes the formation of a critical cluster.

Several approaches, from molecular dynamics simulations (e.g., Lupi et al., 2014) to laboratory studies (e.g., Kiselev et al., 2017), are improving our representation of heterogeneous ice nucleation, but a coherent unified theory is not yet available. Currently, two different hypotheses drive its interpretation. On the one hand, heterogeneous nucleation is described by using the classical nucleation theory, assuming that it is a stochastic, and thus time-dependent, process (e.g., Fletcher, 1958). On the other hand, the singular hypothesis assumes that particles have special features on their surface (i.e., active sites) that trigger ice nucleation at deterministic temperature and saturation values characteristic of the particle (e.g., Connolly et al., 2009). Combined approaches, that merge the stochastic and singular descriptions, have also been proposed (e.g., Vali, 1994; Marcolli et al., 2007; Herbert et al., 2014; Niedermeier et al., 2011).

In the *stochastic approach*, heterogeneous nucleation can be formulated analogously to homogeneous nucleation. The decrease in the nucleation energy barrier due to the presence of an external surface is introduced with a compatibility function f that describes the nucleation efficiency of the specific surface (Fletcher, 1958). The energy barrier for heterogeneous nucleation becomes:

$$\Delta G^*_{het} = \frac{16\pi}{3} \frac{V_m^2 \sigma^3}{(k_B T \ln S)^2} \cdot f(\cos\theta) \tag{2.14}$$

where θ is the contact angle between the cluster and the substrate, assuming that the critical cluster has a spherical cap shape. Small contact angles between the cluster and the surface indicate that the surface facilitates heterogeneous nucleation. For water droplet formation the contact angle represents the wettability of the solid surface, while for ice nucleation it represents the affinity of the ice cluster with the surface. Figure 2.3 shows the variation in the Gibbs free energy for homogeneous nucleation ($\theta = 180°$) and heterogeneous nucleation on two substrates characterized by two different contact angles ($\theta = 120°$ and $\theta = 60°$).

To describe the energy barrier ΔG^*_{het} for heterogeneous ice nucleation occurring in the immersion freezing mode, σ and S in equation 2.14 refer to the surface tension at the interface between liquid water and ice and to the ratio between the saturation pressures over water and ice, respectively
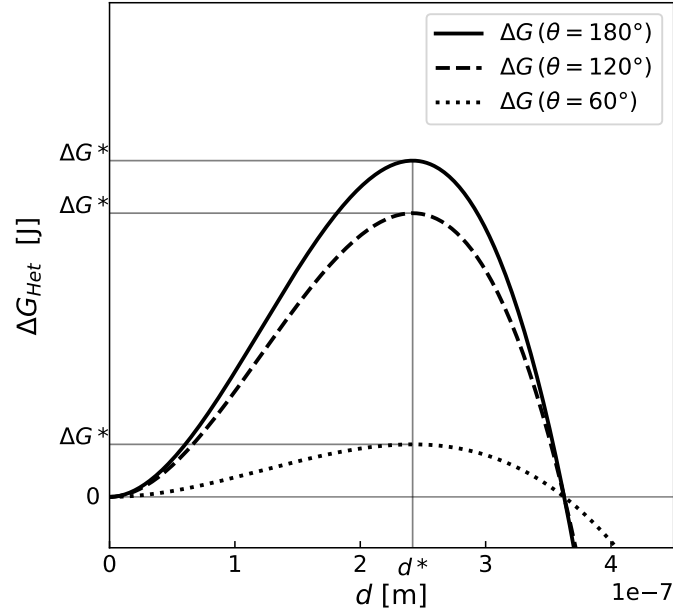
Figure 2.3: Comparison of the variation in the free Gibbs energy for homogeneous ($\theta = 180°$) and heterogeneous nucleation of liquid water at $0\,°C$ and $S_w = 1.01$.

(Chen et al., 2008). In case of deposition nucleation, σ is the surface tension at the water vapor/ice interface, and S is the saturation ratio with respect to ice (Chen et al., 2008).

The heterogeneous freezing rate coefficient is calculated analogously to the homogeneous case:

$$J_{het} = K_{het} \cdot N_0 \exp\left(-\frac{\Delta G^*_{het}}{k_B T}\right) \tag{2.15}$$

where the kinetic factor K_{het} is specific to each ice nucleation mode (Chen et al., 2008).

The number of freezing particles N_{het}, in the time interval Δt is given by:

$$N_{het} = N \cdot [1 - \exp(-J_{het} A \Delta t)] \tag{2.16}$$

where N is the total number of particles, and A is the surface area of each particle.

The *singular hypothesis* assumes that heterogeneous nucleation is time-independent and that the nucleation events occur at specific sites of the external surface and at deterministic temperature and saturation values (e.g., Levine, 1950; Connolly et al., 2009). The number of nucleation events dN_i in a temperature interval dT can be written as:

$$dN_i(T) = N_{na}(T) A k(T) dT \tag{2.17}$$

where $N_{na}(T) = N_{tot} - N_i(T)$ is the number of non-activated particles, N_{tot} is the initial number of particles, A is the surface area of a single particle, and $k(T)$ corresponds to the number of activated particles per unit surface and per unit temperature interval. The cumulative number of ice nucleation active surface sites (INAS, n_S) per unit surface is obtained by integrating $k(T)$:

$$n_S(T) = -\int_0^T k(T')dT' \tag{2.18}$$

Without any particle size dependency in $k(T)$ and $n_S(T)$, this approach assumes that the ice nucleation sites are uniformly distributed on the surface of the particles.

The number concentration of nucleated ice crystals can thus be calculated as:

$$\int_0^{N_{ice}} \frac{dN_i(T)}{N_{tot} - N_i(T)} = A \int_0^T k(T')dT' \tag{2.19}$$

Resulting in:

$$N_i(T) = N_{tot}\left[1 - \exp\left(-An_s(T)\right)\right] \tag{2.20}$$

In the case of heterogeneous deposition nucleation, the INAS density $n_S(T)$ and the number of ice nucleating particles $N_i(T)$ depend on both temperature and saturation S.

2.3   SECONDARY ORGANIC AEROSOL: FORMATION AND PROPERTIES

Organic aerosols (OA) make up from 20 to 90 % of the fine aerosol particles mass (Kanakidou et al., 2005), and in various atmospheric environments the predominant fraction of OA is associated with secondary formation (Zhang et al., 2007; Crippa et al., 2014). Secondary organic aerosols (SOA) form in the atmosphere by oxidation and gas-to-particle conversion of compounds characterized by high saturation vapor pressures, namely *volatile organic compounds* (VOCs). VOCs are directly emitted into the atmosphere from several biogenic and anthropogenic sources (Williams and Koppmann, 2007). Vegetation and fossil-fuel combustion are the major sources of biogenic and anthropogenic VOCs, respectively (Reimann and Lewis, 2007; Steiner and Goldstein, 2007). Globally, biogenic emissions dominate (Guenther et al., 1995), with isoprene (C_5H_8) being the most abundant compound (Steiner and Goldstein, 2007). Although the emission rate of α-pinene ($C_{10}H_{16}$) is ten times lower compared to isoprene (60 vs 600 $Tg\,yr^{-1}$) the mass yield of compounds derived from terpenes, especially αP, is higher (Guenther et al., 2006).

In the atmosphere, the volatility (i.e., the saturation vapor pressure) of organic molecules is reduced via different *oxidation pathways* by atmospheric oxidants as the hydroxil radicals ($\cdot$OH), ozone (O_3), and nitrate radicals ($\cdot NO_3$) (Seinfeld and Pandis, 2012). Compounds with sufficiently low volatility can form new particles or condense into pre-existing ones. Different processes, namely functionalization, fragmentation, and oligomerization, can modify the properties of volatile species, including their oxidation state and volatility (Kroll et al., 2009; Seinfeld and Pandis, 2012; Donahue et al., 2011).

The *partitioning* of the oxidation products between the gas and particle phase is determined by their volatility and is a key factor in the formation and aging of SOA particles. The fraction X_i of a specific compound i present in the particle phase depends on its effective saturation mass concentration C_i^* and total organic mass concentration C_{OA} (Donahue et al., 2006):

$$X_i = \left(1 + \frac{C_i^*}{C_{OA}}\right)^{-1} \tag{2.21}$$

$$C_i^* = \gamma_i C_i^0 \tag{2.22}$$

being C_i^0 the saturation mass concentration of the pure compound i, and γ_i its activity coefficient. For $\gamma_i < 1$ the compound i tends to stay in the particle phase.

The partitioning of each compound i present in the gas and particle phase needs to be represented to explicitly describe SOA formation. However, atmospheric SOA comprise a large number of different molecules many of which have not been chemically identified yet (Kroll and Seinfeld, 2008; Hallquist et al., 2009), thus limiting this approach to the description of well controlled laboratory systems. To simplify and describe atmospheric aerosol partitioning, empirical methods based on parameterizations of experimental data have been developed. In the *volatility basis set* (VBS) approach (Donahue et al., 2006), for example, organic oxidation products are classified in different logarithmically spaced volatility bins according to their effective saturation mass concentration C^*:

- ELVOCs: extremely low-volatility organic compounds, $C^* \leqslant 10^{-4}\,\mu g\,m^{-3}$. These compounds immediately condense into the particle phase and usually contribute to the nucleation of new particles;

- LVOCs: low-volatility organic compounds, $10^{-3} \leqslant C^* \leqslant 10^{-1}\,\mu g\,m^{-3}$. At typical atmospheric concentrations these compounds exist in the particle phase;

- SVOCs: semivolatile organic compounds, $1 \leqslant C^* \leqslant 10^2\,\mu g\,m^{-3}$. These compounds are present in the particle and gas phase in the atmosphere.

- IVOCs: intermediate-volatility organic compounds, $10^3 \leqslant C^* \leqslant 10^6\,\mu g\,m^{-3}$. These compounds are usually in the gas phase, but can readily oxidize and convert to condensable compounds.

- VOCs: volatile organic compounds, $C^* > 10^6\,\mu g\,m^{-3}$. These compounds are directly emitted in the atmosphere in the gas phase.

The chemical composition, and thus the volatility, of the compounds present in SOA particles determines their chemical-physical properties, among which their phase state. Several studies (e.g., Grieshop et al., 2007; Vaden et al., 2011; Virtanen et al., 2010) have shown that SOA can exhibit properties of *amorphous highly viscous particles* depending on their composition, temperature, and relative humidity. The phase state of organic particles is an important property that strongly affect climate, air quality, and health (Pöschl and Shiraiwa, 2015). Some of the mechanisms influenced by the phase state of SOA particles are illustrated in Figure 2.4 (Reid et al., 2018). A semi-solid or solid phase state can, for example, limit the diffusion of molecules from the surface into the particle bulk, thus influencing the gas-particle partitioning and modifying the heterogeneous reaction rates (e.g., Shiraiwa et al., 2011). Additionally, the phase state of the particles can affect their homogeneous and heterogeneous freezing ability (e.g., Murray et al., 2010; Berkemeier et al., 2014).
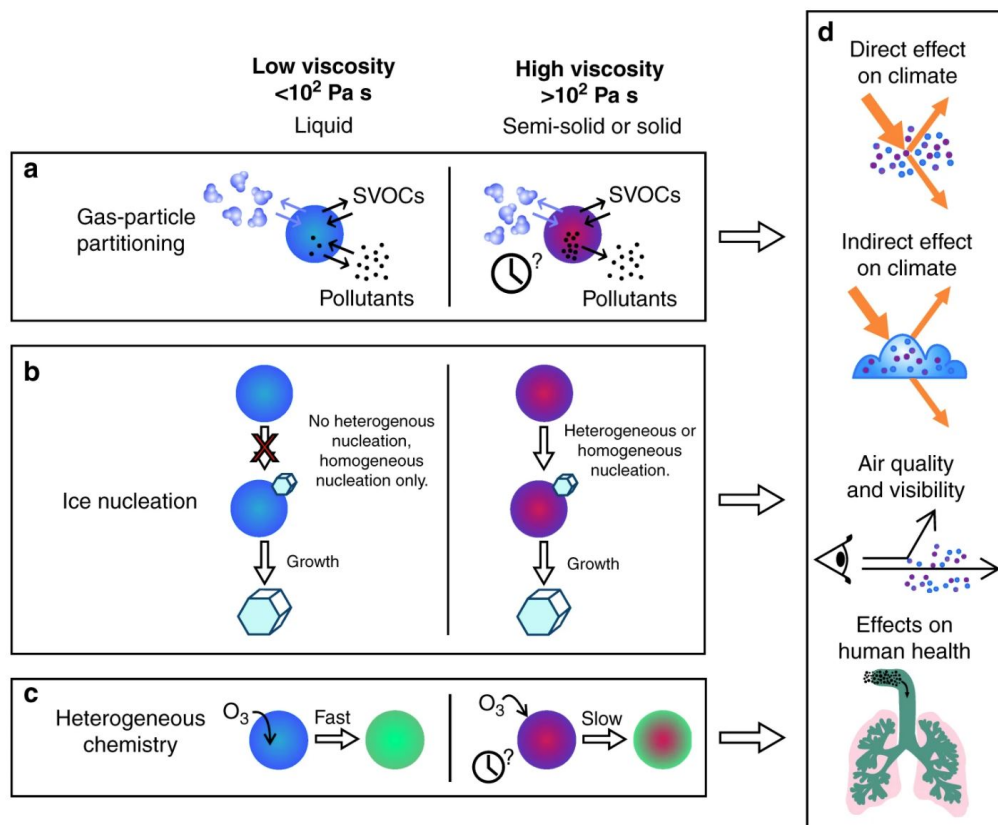
Figure 2.4: Impacts of ambient particle viscosity and phase on climate and health. **a** Although low-viscosity aerosol particles equilibrate in composition rapidly, highly viscous particles may require time to achieve an equilibrium composition through the gas-particle partitioning of water, semi-volatile organic compounds (SVOCs) and other pollutants. **b** Unlike liquid droplets, glassy particles can act as heterogeneous nuclei for ice nucleation. **c** Heterogeneous chemistry can occur rapidly in low-viscosity particles throughout the particle bulk. In viscous particles, heterogeneous chemistry may occur only very slowly and be confined to the particle surface. **d** In combination, differences in the mechanisms and rates of microphysical processing in viscous aerosol particles when compared to low-viscosity solution droplets can have important consequences for the impacts of aerosols on climate, visibility, air quality and health. Figure and caption from Reid et al., 2018.

Glass transition temperature, T_g, and viscosity, η, are two fundamental parameters used to quantify and describe the phase state of substances. The *glass transition* is a non-equilibrium transition

from the liquid to an amorphous solid phase[1] that occurs over a temperature interval defined as glass transition temperature (Koop et al., 2011). The glass transition is a dynamic phenomenon investigated in diverse fields such as food quality and safety (Slade et al., 1991), in several technological applications as engineering of plastics and metallic glasses (Greer, 1995), and in the stabilization of dry biomaterial (Crowe et al., 1998). However, despite its importance, the present knowledge about glass transition is essentially phenomenological (Champion et al., 2000). Direct measurements of T_g for bulk materials are usually performed with differential scanning calorimetry thermograms (Angell, 2002). Due to the difficulty to directly measure the glass transition temperature of complex organic molecules, empirical structure activity relationships have been suggested. The Boyer–Beaman rule, for example, associates the glass transition temperature of a substance to its melting temperature (Beaman, 1952), and the Fox-Flory relation describes T_g as a function of the inverse molar mass of the polymer (Fox and Flory, 1950). Those relations, introduced for large polymers, can not be easily generalized to atmospheric secondary organic compounds due to their complex composition. However, Koop et al. (2011) showed that T_g of a wide range of organic compounds, used as surrogates for SOA particles, strongly correlates with their inverse molar mass, while it has a minor dependence on their degree of oxygenation.

The glass transition temperature of a compound is directly related to its *viscosity*. Liquids are characterized by $\eta < 10^2\,Pa\,s$, semi-solids have viscosity in the range $10^2 - 10^{12}\,Pa\,s$, and solids have $\eta > 10^{12}\,Pa\,s$ (Shiraiwa et al., 2011). Depending on their viscosity, particles have different molecular diffusion coefficients D defined by the Stokes-Einstein equation (Blundell and Blundell, 2010):

$$D = \frac{k\,T}{6\,\pi\,\eta\,r} \tag{2.23}$$

being k the Boltzmann constant, T the temperature, and r the apparent radius of the diffusing molecule. However, equation 2.23 does not correctly estimate the diffusion coefficients for atmospheric photo-oxidants and small molecules (e.g., O_3, $\cdot OH$, H_2O) in an organic matrix (Tong et al., 2011), and it breaks down in the vicinity of the glass transition (Champion et al., 2000). Table 2.1 reports diffusion coefficients of organic and small molecules, such as water, for different viscosity ranges (Shiraiwa et al., 2011).

Table 2.1: Viscosity and molecular diffusion values (magnitudes) for different particle phase states for organic molecules, D_{org}, and water, D_{H_2O}. Adapted from Shiraiwa et al. (2011)

| Phase state	η [Pa s]	D_{org} [$cm^2 s^{-1}$]	D_{H_2O} [$cm^2 s^{-1}$]
Liquid	$\approx 10^{-3}$	$\approx 10^{-5}$	$\approx 10^{-5}$
Semi-solid	$\approx 10^2 - 10^{12}$	$\approx 10^{-10} - 10^{-20}$	$\approx 10^{-7} - 10^{-9}$
Solid	$\geqslant 10^{12}$	$\leqslant 10^{-20}$	$\approx 10^{-10}$

The characteristic time of mass-transport and mixing by molecular diffusion can be computed as (Seinfeld and Pandis, 2012):

$$\tau = \frac{d_p^2}{4\pi^2 D} \tag{2.24}$$

where d_p is the particle diameter, and D the diffusion coefficient from equation 2.23. Figure 2.5 shows the equilibration times for various particle diameters as function of their diffusion coefficient and viscosity (Shiraiwa et al., 2011). The light green arrow indicate the wide range of equilibration times (from seconds to years) for a 100 nm semi-solid organic particle.

In the atmosphere, secondary organic aerosols are composed of thousands of compounds, of which we still don't know the exact molecular structure, making the prediction of their viscosity and glass transition temperature challenging. Recently, semi-empirical parameterizations have been developed to predict the phase state of complex atmospheric particles as a function of their chemical properties. Particles made of compounds with a low saturation mass concentration (C_i^0), thus particles with a high fraction of ELVOCs and LVOCs, have been associated with a higher viscosity (e.g., Shiraiwa et al., 2017; Champion et al., 2019; Zhang et al., 2019; Li et al., 2020). Furthermore, Rothfuss

---

1 Amorphous solids do not have a long-range molecular order, in contrast to crystalline solids, and are usually termed glasses (Debenedetti and Stillinger, 2001)
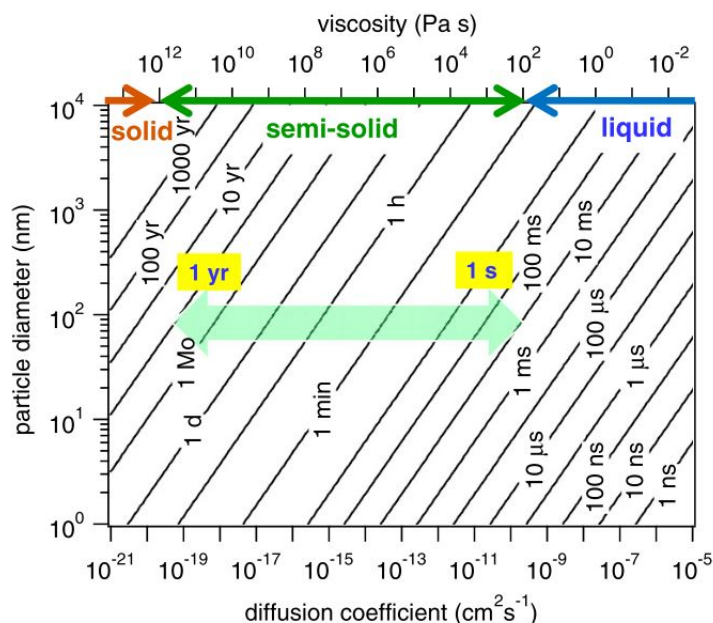
Figure 2.5: Characteristic time of bulk diffusion (τ) in liquid, semisolid, and solid particles as a function of the diffusion coefficient and particle diameter. In the size range of the atmospheric aerosol accumulation mode ($d_p \approx 100\,nm$), τ in semisolid particles varies from seconds to years (light green arrow). Figure and caption from Shiraiwa et al. (2011).

and Petters (2017) found that both vapor pressure and viscosity correlate with type and number of functional groups added to the compounds. Based on these parameterizations, modeling studies have suggested that in the cold, dry regions of the upper troposphere, aerosols are most likely to exist in a glassy state (Shiraiwa et al., 2017). It is thus important to understand how particles viscosity affect their hygroscopic behavior and their ice nucleation ability. Additionally, particles in the atmosphere are usually internal mixtures of organic compounds and inorganic species characterized by a very low glass transition temperature, such as water, sulfate, and nitrate, that can substantially reduce their viscosity by acting as plasticizers (Gordon and Taylor, 1952; Zobrist et al., 2008a; Dette and Koop, 2015).

The hygroscopic behavior of organic particles strongly depends on their viscosity (Mikhailov et al., 2009). A liquid particle exposed to increasing relative humidity takes up water molecules that almost instantaneously diffuse into the particle, making this process independent of the humidification (or drying) rate. Figure 2.6a shows the growth factor (ratio of the humid and dry particle diameter) of a liquid particle as a function of the ambient relative humidity. Water uptake in highly-viscous/glassy particles, instead, can be kinetically limited due to the slow diffusion of water molecules to the bulk of the particles, as shown in Figure 2.6b. Therefore, during humidification, water uptake initially occurs only in the outer shell of the particles, that becoming less viscous due to the plasticizing effect of water, facilitates the water uptake in a self-accelerating process called humidity-induced glass transition or *amorphous deliquescence* (Burnett et al., 2004). A symmetrical effect can occur during the drying of the particle. A glassy outer shell can form around a liquid core, thus retarding water evaporation from the particle with an hysteresis effect.

Since water uptake and release in viscous particles strongly depend on the diffusion kinetics of water, the diameter of the particle and the rate of humidification/drying are critical parameters to determine the non equilibrium phase state of these particles. However, the significance of the kinetically limited water uptake for the ability of these particles to act as ice nuclei at low temperature is still poorly quantified.

The ice nucleation ability of glassy particles in the cirrus cloud temperature regime ($T < -38\,°C$) results from two competing mechanisms, namely heterogeneous nucleation on the solid surface of the particle (e.g., Murray et al., 2010; Wang et al., 2012; Ignatius et al., 2016) or homogeneous
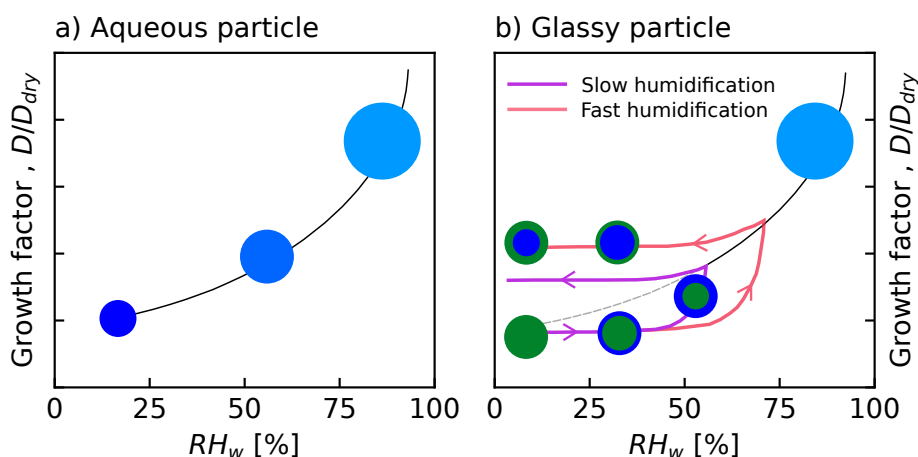
Figure 2.6: Water uptake behavior for (a) a liquid particle, and (b) an amorphous solid with an humidity-induced glass transition. Adapted from Koop et al., 2011.

freezing after its amorphous deliquescence (e.g., Zobrist et al., 2008a). Heterogeneous ice nucleation on glassy particles was mainly observed in experiments with single organic compounds (e.g., Wilson et al., 2012), whereas the majority of the studies performed with secondary organic aerosol particles showed ice formation only at or above the homogeneous freezing threshold (e.g., Möhler et al., 2008). Recently, a few studies have investigate the relation between water uptake and prevailing ice nucleation mechanism in glassy organic particles by means of kinetic simulations leading to conflicting results (e.g., Berkemeier et al., 2014; Lienhard et al., 2015; Price et al., 2015; Fowler et al., 2020).

A more detailed overview of the ice nucleation studies on secondary aerosol particles is provided in Chapter 6.

2.4 THERMODYNAMICS OF ATMOSPHERIC INORGANIC SALTS

Inorganic salts can comprise $25 - 65\%$ of the total dry aerosol mass (Heintzenberg, 1989). The major inorganic ions present in atmospheric aerosol particles are sulfate (SO_4^{2-}), nitrate (NO_3^-), and ammonium (NH_4^+). Among them, sulfate is the most abundant and studied component. The production of *sulfate and nitrate aerosols* strongly depends on the concentrations of their gaseous precursors (SO_2 and NO_x) and atmospheric oxidants (e.g., ozone, hydroxyl radical, and nitrate radical), as well as on the ambient thermodynamic conditions (Seinfeld and Pandis, 2012). Acidic aerosol particles are usually dominated by sulfuric acid (H_2SO_4) and nitric acid (HNO_3), which can be partly or fully neutralized by the most abundant base present in the atmosphere, ammonia (NH_3). The reaction of sulfuric acid with increasing molar ratios of ammonia leads to the formation of salts with different neutralization states (i.e., ratios of ammonium to sulfate ions): ammonium bisulfate (NH_4HSO_4), letovicite (($NH_4)_3H(SO_4)_2$), and ammonium sulfate (($NH_4)_2SO_4$). Nitric acid is also abundant in the atmosphere, but its higher volatility compared to sulfuric acid makes its partitioning to the particle phase less frequent in the lower atmosphere (Tang, 1980). The reaction of ammonia with nitric acid can lead to the formation of ammonium nitrate (NH_4NO_3). Since sulfuric acid has a stronger acidity than nitric acid, ammonium nitrate mainly forms when high ammonia and nitric acid, but low sulfuric acid concentrations are achieved (Seinfeld and Pandis, 2012).

Acidic particles show a smooth hygroscopic response to changes in the ambient relative humidity (Seinfeld and Pandis, 2012). The growth factor (the ratio of the wet to dry particle diameter) for a sulfuric acid particle as a function of the ambient relative humidity is shown in red in Figure 2.7. As the ambient relative humidity rises, a liquid particle takes up water to maintain the thermodynamic equilibrium, thus becoming larger and more diluted. A symmetric behavior occurs when the particle experiences a decreasing relative humidity. Partially or fully neutralized particles, instead,

are likely to undergo phase changes with cycles of relative humidity. At low relative humidity, inorganic salts can be found in a crystalline solid phase, and they remain solid until the relative humidity reaches a threshold value, called *deliquescence relative humidity* (DRH), at which particles spontaneously take up water. The solid orange line in Figure 2.7 shows the hydration curve for crystalline ammonium sulfate particles, which deliquesce at a relative humidity of about 80 %.

The Gibbs free energy of a solid particle does not depend on the ambient relative humidity but only on ambient pressure and temperature (green line in Figure 2.8). The chemical potential of its liquid solution, instead, is proportional to the mole fraction of the solute and thus decreases when the solution dilutes, i.e. when the relative humidity increases (blue line in Figure 2.8). The deliquescence of the salt occurs at the relative humidity for which the free energy of the liquid solution equals the free energy of the solid phase, thus when the solution is saturated (dashed orange line in Figure 2.8). During the dehydration process (dashed orange line in Figure 2.7), the aqueous solution will stay in a metastable state also for RH < DRH, although the solid phase would be the energetically most favorable state. The solid crystal will only form when the supersaturation over the aqueous solution will be high enough to overcome the energy barrier for the homogeneous nucleation of a critical solid germ (see section 2.1). This process, called efflorescence, occurs at the *efflorescence relative humidity* (ERH), which is determined by the kinetics of the nucleation process and not by thermodynamic principles (as for deliquescence). For ammonium sulfate particles the ERH is estimated at a relative humidity of about 30 − 40 % (see Figure 2.7). For a relative humidity between the ERH and the DRH, salt particles can exist in two different phase states depending on their thermodynamic history (hysteresis effect).
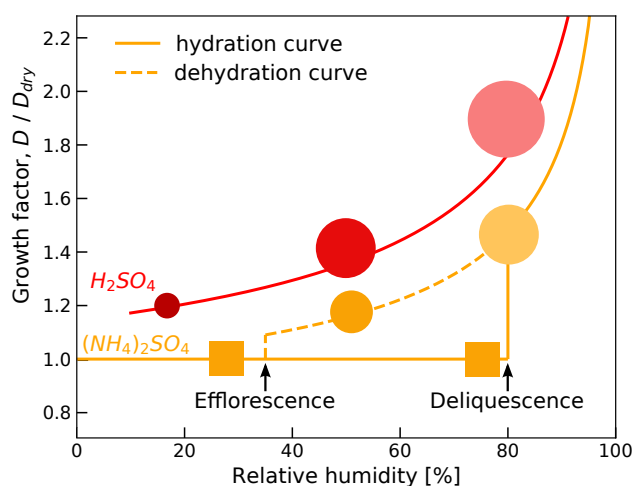
Figure 2.7: Growth factor (i.e., diameter change) of sulfuric acid (H_2SO_4) and ammonium sulfate ($(NH_4)_2SO_4$) particles as a function of relative humidity with respect to water. Adapted from Seinfeld and Pandis, 2012.

As the concentration of a saturated solution depends on the temperature, the DRH is temperature-dependent. Exemplary theoretical deliquescence curves as a function of THE temperature obtained from the Extended Aerosol Inorganic Model (E-AIM, Clegg et al., 1998), are reported in Figure 2.9. The DRH of the different salts shows different temperature-dependency due to their different temperature-dependent solubility (Tang and Munkelwitz, 1993). Ammonium sulfate (AS, Figure 2.9c) shows a weak temperature dependency with a variation of only about 5 % over a temperature range of 70 °C, DRH(20 °C) = 80.4 % and DRH(−50 °C) = 85.7 %. Ammonium nitrate (AN, Figure 2.9d) has a stronger temperature dependency with a variation of about 30 % over the same temperature range, DRH(20 °C) = 64.5 % and DRH(−50 °C) = 97.0 %.

For the ammonium bisulfate-water system (AHS, Figure 2.9a), the E-AIM predicts a more complex behavior. Upon deliquescence of the ammonium bisulfate (dashed blue line), the aqueous solution is supersaturated with respect to solid letovicite (LET), and LET is thus forced to precipitate leading to the formation of mixed liquid-solid particles. Only at a higher relative humidity, the particles are
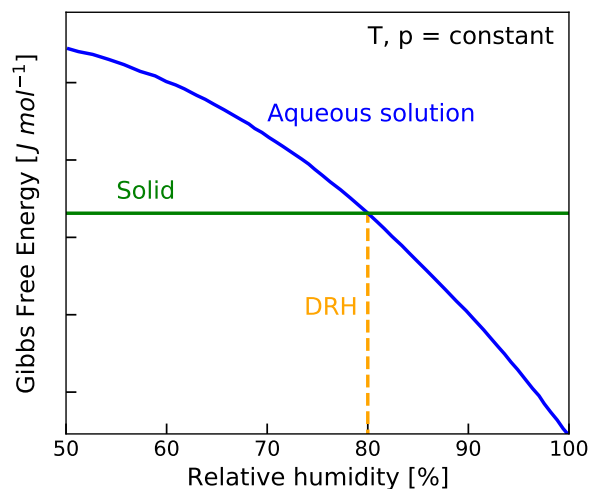
Figure 2.8: Gibbs free energy of a solid salt (green) and its aqueous solution (blue) as a function of relative humidity respect to water. Adapted from Seinfeld and Pandis, 2012.

expected to fully deliquesce (solid blue line). A similar behavior is predicted for letovicite particles for temperatures higher than $-20\,°C$ (Figure 2.9b), with the formation of solid ammonium sulfate after deliquescence of the LET particles (dashed orange line).

It is important to highlight that the E-AIM does not allow supersaturated conditions by default, but always forces the formation of the saturated phase. However, in atmospheric aerosol particles supersaturated conditions often occur over a wide range of thermodynamic conditions. As described above, for example, experimental data have shown that aqueous ammonium sulfate particles stay in a supersaturated state down to $RH_w \approx 30\,\%$ (efflorescence), suggesting that AS cannot precipitate when LET particles deliquesce at $\approx 70\,\%$, as predicted by the thermodynamic model.

Atmospheric aerosol particles are likely multicomponent mixtures composed of different ions and organic matter, with a more complex phase state compared to the pure systems. Particles with non-stoichiometric compositions, for example, can feature a manifold of different phase states, ranging from a homogeneous liquid phase to mixtures of multiple solid phases, or mixtures of a solid component in equilibrium with an aqueous solution. In the following, the phase diagram of the system $H_2SO_4/NH_3/H_2O$ with ammonium-to-sulfate ratios ($ASR = [NH_4^+]/[SO_4^{2-}]$) greater than 1 is described in more detail. The ice nucleation ability of such particles will be investigated in Chapter 4.

Within the $H_2SO_4/NH_3/H_2O$ system three different solid components can form, namely ammonium bisulfate (NH_4HSO_4, $ASR = 1.0$), letovicite ((NH_4)$_3H(SO_4)_2$, $ASR = 1.5$), and ammonium sulfate ((NH_4)$_2SO_4$, $ASR = 2.0$). The phase diagram at room temperature (i.e., the efflorescence and deliquescence relative humidity) of particles with $1.0 < ASR < 2.0$ was first investigated by Spann and Richardson (1985). The results from their study are shown as solid lines in Figure 2.10 together with more recent literature results (symbols). Efflorescence, initial/partial deliquescence, and full deliquescence data are reported in red, green, and blue, respectively. The reported values are also shown in Table 2.2, where the experimental temperature from the different studies is also indicated. The homogeneous crystallization of particles with $ASR = 1.0$ (ammonium bisulfate) was observed at low relative humidity only in the studies from Spann and Richardson (1985) and Tang and Munkelwitz (1994). However, as reported by the authors, ammonia contamination was difficult to prevent and quantify, and the ammonium bisulfate particles could have already modified their composition to a more neutralized state (i.e., with a higher ASR) before the start of the experiment. Colberg et al. (2003) reported of solid letovicite precipitation in ammonium bisulfate solution droplets at $RH_w \approx 15\,\%$ and at temperatures between $0\,°C$ and $-10\,°C$ (shown as left-pointing triangles with black edge in Figure 2.10). Cziczo and Abbatt (2000) and Schlenker et al. (2004), instead, did not observe AHS particles to homogeneously crystallize at $-35\,°C$ and $20\,°C$ (represented with red empty symbols in Figure 2.10). From the measurements of Spann and Richardson (1985), particles with
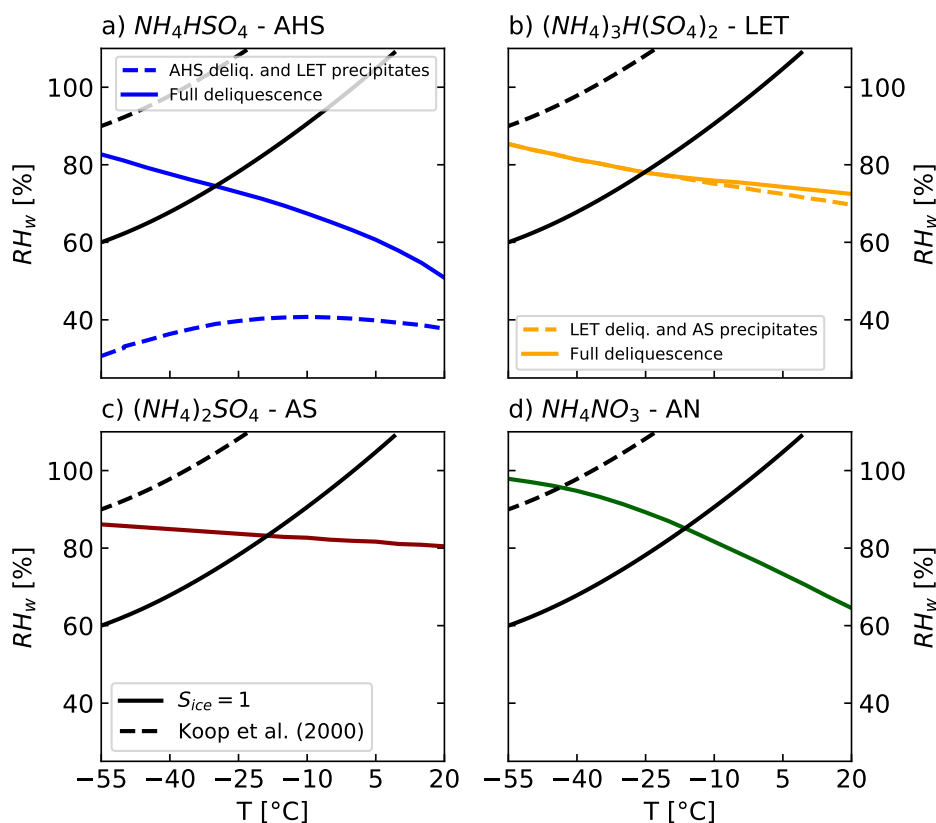
Figure 2.9: Deliquescence relative humidity as a function of temperature for **a)** NH_4HSO_4 (AHS, ammonium bisulfate), **b)** $(NH_4)_3H(SO_4)_2$ (LET, letovicite), **c)** $(NH_4)_2SO_4$ (AS, ammonium sulfate), and **d)** NH_4NO_3 (AN, ammonium nitrate). Solid and dashed black lines indicate ice saturation ($S_{ice} = 1$) and homogeneous freezing onset for aqueous solution droplets (for $\Delta a_w = 0.3$, Koop et al., 2000). Model results from Clegg et al. (1998).

composition $1.0 < ASR < 2.0$ (composed of AHS+LET or LET+AS) are expected to effloresce at increasing relative humidity with increasing ASR (red curve). The heterogeneous crystallization of AHS in initially homogeneous liquid solutions after the precipitation of letovicite was measured also by Schlenker et al. (2004) (red circles). As expected for particles composed of two different salts, the deliquescence occurs in two steps, with the initial water uptake occurring at a relative humidity close to the lower DRH of the two salts, so-called partial deliquescence relative humidity (PDRH, green lines). For particles with $1.0 < ASR < 1.5$ (composed of AHS+LET), the first component to deliquesce at $RH_w = 40\%$ is AHS, while for $1.5 < ASR < 2.0$ (composed of LET+AS) the letovicite component starts to deliquesce at $RH_w = 70\%$. At the PDRH the remaining solid (LET or AS) is in equilibrium with the aqueous solution, and if the relative humidity is further increased the solid will progressively dissolve until the full deliquescence value is reached (blue curve). For an $ASR = 1.5$, the particles are composed of pure letovicite, and are thus expected to show a one-step deliquescence, measured at $\approx 70\%$ at room temperature (Spann and Richardson, 1985; Tang and Munkelwitz, 1994). Similarly, pure ammonium sulfate particles ($ASR = 2$) deliquesce at $\approx 80\%$.

Knowing the phase state of inorganic salts, especially at low temperatures, is important to understand their reactivity, lifetime, and impacts on atmospheric chemistry and climate (Boucher et al., 2013). In particular, liquid solution droplets can lead to cirrus cloud formation only via homogeneous freezing, while solid crystalline particles could initiate ice nucleation at lower relative humidity via heterogeneous nucleation (e.g., Zobrist et al., 2011; Wise et al., 2012). Figure 2.11 shows the possible ice nucleation modes for a single and a multicomponent salt particle as a function of temperature and relative humidity, therefore as a function of the particle phase state. Ice supersaturated conditions ($S_{ice} \geqslant 1$) are highlighted with a green shaded area, and the parameterization for homogeneous freezing of aqueous solution droplets is indicated with a blue line (Koop et al., 2000).
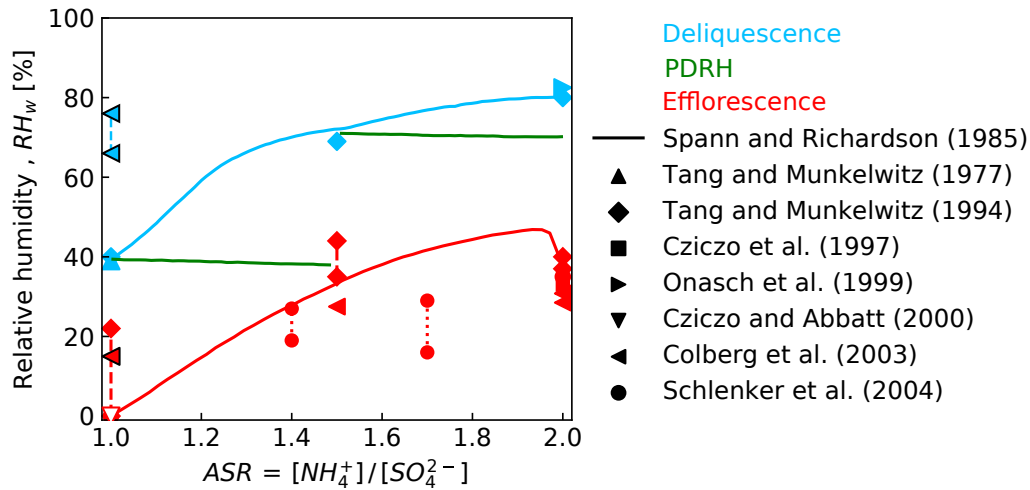
Figure 2.10: Phase diagram of the $H_2SO_4/NH_3/H_2O$ system for particles with an ammonium-to-sulfate ratio (ASR) between 1.0 and 2.0. Efflorescence, partial deliquescence, and full deliquescence data are reported in red, green, and blue, respectively. Solid lines show the results from Spann and Richardson (1985), symbols refer to the literature results reported in the legend. The empty red symbol at ASR = 1.0 from Cziczo and Abbatt (2000) and Schlenker et al. (2004) indicate that the particles did not crystallize. Data from Colberg et al. (2004) for an ASR = 1.0 (left-pointing triangles with black edge) refer to the efflorescence and deliquescence of letovicite in solution droplets with the composition of ammonium bisulfate.

Following a hypothetical atmospheric trajectory, different ice nucleation modes can be identified as a function of the particle phase state. For a single component salt (panel a), the particle will stay in its solid phase up to its DRH value, and could thus act as ice nucleating particle in the deposition or pore condensation and freezing (PCF) mode. When the relative humidity equals the DRH, the particle intermediately forms a crystalline core surrounded by its solution, and ice nucleation via the immersion freezing mode may occur. Once the particle is fully deliquesced, it can nucleate ice only homogeneously. For a multicomponent salt (panel b), the overall behavior is similar, but deposition nucleation and PCF can occur within a smaller range of conditions due to the lower partial deliquescence relative humidity. Immersion freezing, instead, can take place over a larger range of conditions.

Table 2.2: Measured effloresce and deliquescence relative humidity (ERH, DRH) values for particles with different ammonium to sulfate ratios (ASR). The temperature at which the measurements were performed is also indicated.

ASR	ERH [%]	DRH [%]	T [°C]	Ref
1		39	5 to 25	Tang and Munkelwitz (1977)
	$0.05 - 22$	40	25	Tang and Munkelwitz (1994)
	No		-35 to 0	Cziczo and Abbatt (2000)
	$15 - 16$ (as LET)	$66 - 76$	-13 to 0	Colberg et al. (2003)
	No		20	Schlenker et al. (2004)
1.4	$19 - 27$		20	Schlenker et al. (2004)
1.5	31	71	25	Spann and Richardson (1985)
	$35 - 44$	69	25	Tang and Munkelwitz (1994)
	27.5	72.8	-10	Colberg et al. (2003)
1.7	$16 - 29$		20	Schlenker et al. (2004)
2	35	80	25	Spann and Richardson (1985)
	$37 - 40$	80	25	Tang and Munkelwitz (1994)
	33		25	Cziczo et al. (1997)
	32	82.5	-10	Onasch et al. (1999)
	$28.5 - 30.8$	81	-10	Colberg et al. (2003)
	35		20	Schlenker et al. (2004)
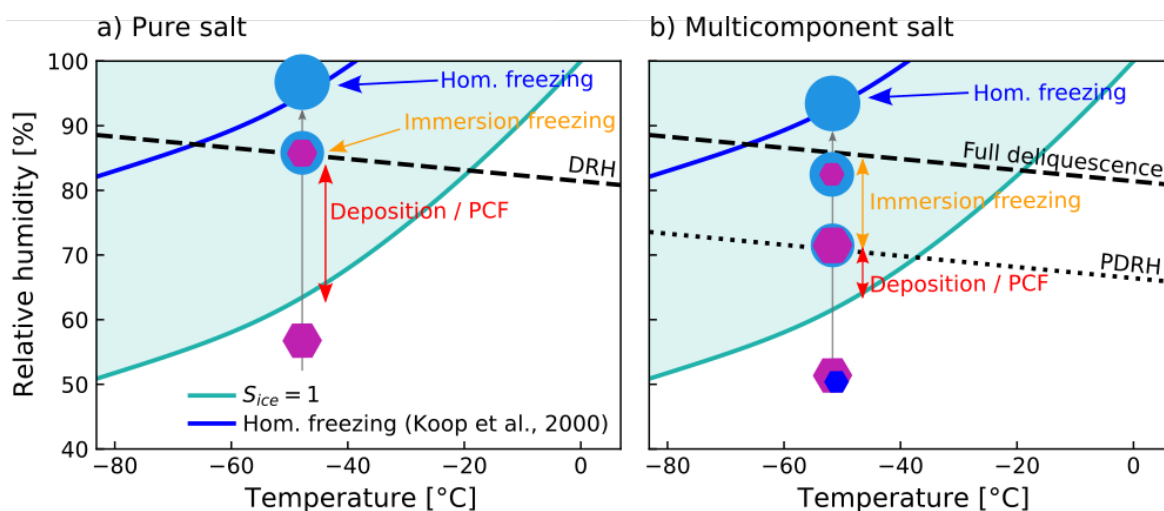
Figure 2.11: Hypothetical atmospheric trajectory of a crystalline single component salt (panel a) and a multicomponent system (panel b). Ice saturated conditions are highlighted with a green shaded area. The homogeneous freezing threshold for aqueous solution droplets is shown in blue. The possible ice nucleation mechanisms are indicated together with the phase state of the particles. Adapted with permission from Zuberi et al. (2001). Copyright 2021 American Chemical Society.

3 | METHODS

In this chapter, the working principle of the standard aerosol instrumentation used in this thesis is introduced first (section 3.1). The experiments presented here have been performed at the AIDA facility at the Karlsruhe Institute of Technology and at the CLOUD experiment at CERN. The experimental facilities are described in sections 3.2 and 3.3. Finally, the two Continuous Flow Diffusion Chambers of the Karlsruhe Institue of Technology (INKA and mINKA) are described and characterized in section 3.4.

3.1 AEROSOL INSTRUMENTATION

Particle number concentration

Aerosol particle number concentration is measured with *condensation particle counters* (CPC). The sample flow passes through a light beam and the number of detected scattering events corresponds to the number of aerosol particles (Cheng, 2011). As the scattering intensity scales with the diameter of the particles as D_p^6, the limit of detection using light in the visible range is at diameters of about $100\,\mathrm{nm}$ (Mishchenko et al., 2002). To enlarge small particles, and thus to lower the limit of detection down to the nm scale, the sample is drawn through a conditioner region which is saturated with vapor, and the sample is brought to thermal equilibrium. Next, the sample is pulled into a region where condensation occurs (saturator). In an alcohol based CPC, in which the vapor used is for example butanol, the conditioner region is at a warm temperature, and the condensation region is cooler.

Particle size distribution

To measure the number size distribution of the particles over a wide size range, such as from a few nm to tens of μm, measurements from different methods and instruments need to be combined. As each technique makes use of different particle properties to asses their sizes, it is necessary to define a unique parameter to combine measurements from different instruments. The *volume equivalent diameter*, d_{ve}, is defined as the diameter of a spherical particle with the same volume of the measured one (DeCarlo et al., 2004).

SMPS In scanning mobility particle counters, the mobility of charged particles in an electric field is used to measure the diameter of particles in the size range $10 - 800\,\mathrm{nm}$ (Flagan, 2011). Aerosol particles are initially charged to their equilibrium charge with a neutralizer, and then selected by their electrical mobility in a differential mobility analyzer (DMA). The selected particles are then counted with a CPC. To convert the measured electrical mobility diameter d_{em} to its volume equivalent diameter d_{ve} the following relation is used (Hinds, 1999):

$$d_{ve} = \frac{d_{em}}{\chi} \tag{3.1}$$

with χ being the dynamic shape factor that takes into account the non-sphericity of the particles. For spheres $\chi = 1$, and for aspherical particles $\chi > 1$.

APS The aerosol aerodynamic mobility is used to measure the diameter of particles in the size range $0.7 - 20\,\mu m$ with aerodynamic particle sizers. Particle velocity is measured by passing the

particle through two laser beams, and the velocity is then related to its aerodynamic diameter d_{ae} (Baron et al., 2011). The volume equivalent diameter is calculated as (Hinds, 1999):

$$d_{ve} = \sqrt{\frac{\chi}{\rho}} d_{ae} \tag{3.2}$$

where χ is the particle shape factor, and ρ the particle density in $g\,cm^{-3}$.

OPC The light scattering ability of the particles is used in optical particle counters (OPC) to measure the size distribution of larger particles ($0.5 - 200\,\mu m$) (Sorensen et al., 2011). Most OPCs operate with visible light ($\lambda \approx 0.5 - 1\,\mu m$) and treat the scattering with Mie theory ($d \approx \lambda$) (Mishchenko et al., 2002). By passing through the measuring volume, particles scatter the incident light, which is then collected by one or two detectors. The number of scattering events corresponds to the particle number concentration, and the intensity of the scattered light to their optical diameter. The optical diameter is a complex function of particle size, refractive index, and shape (Hinds, 1999). Calibration with materials of known shape and refractive index is often needed to retrieve the geometric diameter of the particles. The strong dependency of the scattering intensity to the shape of the particles is often used to distinguish spherical liquid water droplets to aspherical ice crystals, the latter detected with much larger optical diameters.

In this thesis, data from two different OPC models are presented, welas (Palas GmbH) and Climet. The welas OPC uses a 90° scattering angle in combination with a white light source, characterized by a broad continuous wavelength spectrum (Umhauer et al., 2000). The use of white light minimizes the oscillations in the Mie-calibration curve and provide a smooth unambiguous scattering response. A detailed description and characterization of the Climet OPC is provided in section 3.4.3.

3.2 AIDA FACILITY

3.2.1 AIDA chamber

The *AIDA chamber* is an aluminum vessel of $84.3\,m^3$ in volume located inside a thermostatic housing (e.g., Möhler et al., 2003; Möhler et al., 2006). Air ventilation through heat exchangers inside the housing allows to control the temperature of the cloud chamber from 60 to $-90\,°C$, with an accuracy of $\pm 0.3\,°C$. Inside the chamber, a fan located near the chamber bottom ensures homogeneous conditions during the experiments. Mechanical pumps allow to control and reduce the chamber pressure down to $0.01\,hPa$, with different pumping speeds. The chamber is cleaned by several flushing cycles with clean and dry synthetic air at pressures between 1 to $10\,hPa$. Before re-filling to ambient pressure with synthetic air, ultra-pure water is evaporated into the evacuated chamber to add the amount of water vapor required for the experiment. With this procedure, the walls can be partially covered with an ice layer to maintain ice-saturated conditions and to provide sufficient water vapor during the expansion cooling experiments (described in section 3.2.3).

A second vessel is located in proximity to the AIDA chamber. It is called aerosol preparation and characterization (*APC*) chamber, is made of stainless steel, has a volume of $3.7\,m^3$, is operated at ambient temperature, can also be evacuated down to $1\,hPa$ and flushed with synthetic air for cleaning purposes, and is re-filled with clean and dry synthetic air before the start of the experiments. A fan homogeneously mixes the volume. The APC chamber allows to prepare the aerosol particles in a reproducible way (i.e., under well-controlled and repeated experimental conditions) and to transfer them into the AIDA chamber.

Water vapor partial pressure, e, is measured in situ in the AIDA chamber with a tunable diode laser (TDL) absorption spectrometer (*APicT*) with an accuracy of $5\,\%$ (Fahey et al., 2014). The relative humidity with respect to water and the saturation ratio with respect to ice are calculated as:

$$RH_w = \frac{e(T)}{e_{s,wat}(T)} \cdot 100 \quad ; \quad S_{ice} = \frac{e(T)}{e_{s,ice}(T)} \tag{3.3}$$

where T is the chamber temperature. The saturation vapor pressure over liquid water and ice as function of the temperature are calculated with the parametrization from Murphy and Koop (2005):

$$e_{s,wat}(T) \approx \exp\Big\{ 54.842763 - \frac{6763.22}{T} - 4.21 \cdot \log(T) +$$
$$+ 0.000367 \cdot T + \tanh\big(0.0415 \cdot (T - 218.8)\big) \cdot$$
$$\cdot \Big[53.878 - \frac{1331.21}{T} - 9.44523 \cdot \log(T) + 0.014025 \cdot T \Big] \Big\} \quad (3.4)$$

$$e_{s,ice}(T) = \exp\Big\{ 9.550426 - \frac{5723.265}{T} + 3.53068 \cdot \log(T) - 0.00728332 \cdot T \Big\} \quad (3.5)$$

Standard *aerosol particle instrumentation* is present at the facility to measure the aerosol number concentration and number size distribution. Both the AIDA and the APC chambers are equipped with condensation particle counters (models 3010 and 3022, TSI), scanning mobility particle sizers (DMA models 3071 and 3071A, CPCs model 3772, all TSI), and aerodynamic particle sizers (model 3321, TSI). Two optical particle counters (model welas, Palas GmbH) are installed at the bottom of the AIDA chamber to measure the size distribution of large aerosol particles, cloud droplets, and ice crystals in two different size ranges ($0.7 - 46\,\mu m$ and $5 - 240\,\mu m$, Wagner and Möhler, 2013). The two OPCs are located inside the thermal housing to prevent the evaporation of cloud droplets and sublimation of ice crystals.

Laser light scattering by aerosol particles and hydrometeors is measured with the *SIMONE* instrument (Schnaiter et al., 2012). A polarized and collimated laser beam ($\lambda = 488\,nm$) crosses horizontally the diameter of the AIDA chamber ($\approx 4\,m$). Detectors probe the light scattered from the center of the chamber in the forward ($2°$, I_{for}) and backward ($178°$) directions. The back-scattered light is decomposed in its parallel ($I_{\parallel}$) and perpendicular ($I_{\perp}$) components with respect to the incident laser polarization. From these values the linear back-scattering depolarization ratio can be calculated as:

$$\delta = \frac{I_{\perp} - I_{\perp}^{bgr}}{I_{\parallel} - I_{\parallel}^{bgr}} \quad (3.6)$$

where $I_{\perp}^{bgr}$ and $I_{\parallel}^{bgr}$ are the background intensities of the particle free chamber.

To characterize the chemical and physical properties of the aerosol particles, a Fourier transform infrared spectrometer (*FTIR*, type IFS66v, Bruker) (Wagner et al., 2006; Wagner et al., 2009) was operated during the AIDA experimental campaigns presented in this thesis[1]. Additionally, a high-resolution time of flight aerosol mass spectrometer[2] (*HR-ToF-AMS*, Aerodyne) measured the chemical composition of the particles during the experiments presented in Chapter 7.

Figure 3.1 shows a schematic of the AIDA and APC chambers, together with the instrumentation used in the experiments presented in this thesis.

3.2.2 Aerosol preparation

Hereafter the aerosol generation methods used during the AIDA experiments are briefly described.

ULTRASONIC NEBULIZER   An ultrasonic nebulizer (GA 2400, SinapTec) is used to generate aqueous solution droplets. The generated droplets are then dried with a series of diffusion dryers to prevent their instantaneous freezing upon injection into the AIDA chamber at low temperatures and eventually to induce their crystallization (if RH<ERH). Dry and clean synthetic air, with a total flow of $5\,L\,min^{-1}$, is used as carrier gas for the thus prepared aerosol.

The solutions are prepared by dissolving the respective salts in deionized water ($18\,M\Omega$). The solutes used in the experiments presented in this thesis are ammonium sulfate (from Merck 99.5 % or Acro Organics 99.5 %), ammonium bisulfate (from Acro Organics 99 % or AppliChem 99.5 %), and ammonium nitrate (from VWR Chemicals 99 % or Acros Organics > 99 %). The concentration of the

---

1 The FTIR data are curtesy of Dr. Robert Wagner.
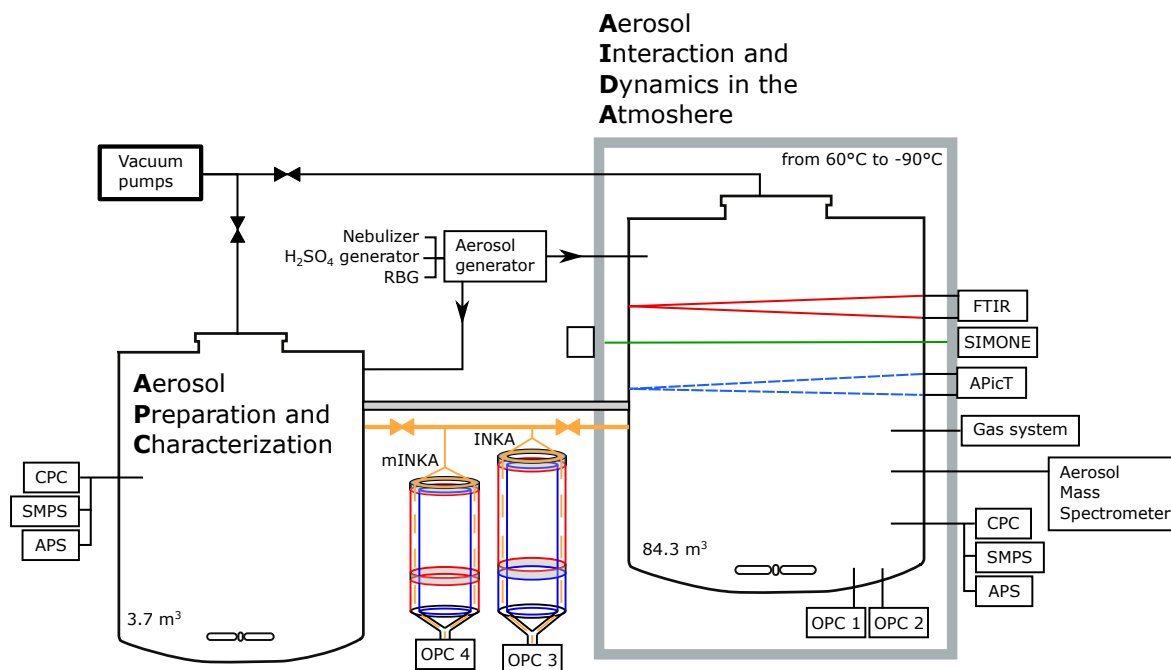2 The AMS data are curtesy of Junwei Song.

Figure 3.1: Schematic of the AIDA chamber and the instrumentation used.

solution determines the diameter of the generated particles. Figure 3.2 reports the volume equivalent median diameter of solid ammonium sulfate particles obtained from bulk solutions of different concentrations in the range $0.1 - 8$ wt%. The median diameter was estimated with a lognormal fit.
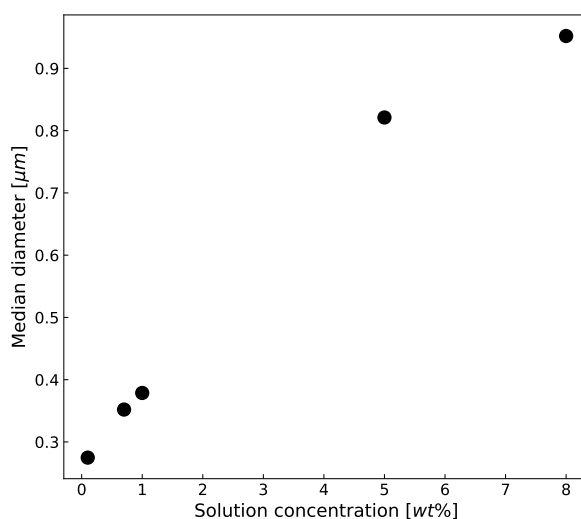

Figure 3.2: Median diameter of crystalline ammonium sulfate particles generated with the ultrasonic nebulizer as function of the solution concentration.

RBG   A rotating brush generator (RBG1000, Palas GmbH) is used to break-up agglomerates and disperse solid aerosol particles. A cyclone impactor is also operated to remove particles larger than $\approx 2\,\mu m$ in diameter. The aerosol particles are then transported from the generator to the chamber with dry and clean synthetic air.

SULFURIC ACID SOLUTION DROPLETS GENERATOR   Aqueous sulfuric acid particles are generated via homogeneous nucleation outside of the AIDA chamber in a home-built generator (Möhler et al., 2003). A sulfuric acid reservoir is heated at $140\,°C$, and dry, clean synthetic air flows over it ($1.17\,L\,min^{-1}$), becoming saturated with gas phase sulfuric acid. Homogeneous nucleation occurs

when the saturated flow cools to ambient temperature. The flow with sulfuric acid particles is diluted with synthetic air ($5.53 \, \text{L} \, \text{min}^{-1}$) before injection into the chamber. Finally, the solution droplets adjust to their equilibrium concentration depending on the conditions inside the AIDA chamber.

GAS PHASE REACTIONS   Solid particles, such as ammonium sulfate and mineral dust, were aged by condensing secondary materials on their surfaces. In the AIDA chamber, ozone (O_3), α-pinene ($C_{10}H_{16}$), sulfur dioxide (SO_2), and ammonia (NH_3) have been used as precursor gases. In particular, the reaction of α-pinene with ozone was used to produce low volatile oxygenated molecules which were able to condense on the solid seeds. To generate sulfuric acid (H_2SO_4) in the gas phase, SO_2 was reacted with ·OH radicals produced from the ozonolysis of tetramethylethylene (TME, C_6H_{12}). Different neutralization reactions and coating procedures have been used for the different experiments, as described in the respective chapters.

3.2.3   Expansion cooling experiments

The ice nucleation ability of aerosol particles can be investigated in the AIDA chamber with expansion cooling experiments (e.g., Möhler et al., 2003; Möhler et al., 2006). Hereafter a typical expansion cooling experiment performed with crystalline ammonium sulfate particles at cirrus cloud conditions (starting temperature of $-50\,^{\circ}\text{C}$) is described. The crystalline ammonium sulfate particles were generated with the ultrasonic nebulizer as described above. Figure 3.3 shows the time series of several AIDA records during the experiment.

Two vacuum pumps allow to evacuate the AIDA chamber with a controlled and variable evacuation rate. The related pressure reduction and expansion of the gas inside the chamber induces a temperature drop. Figure 3.3a depicts the drop in pressure and temperature. The temperature reduction, associated with an almost linear decrease of the water vapor partial pressure due to the pressure drop, results in an increase of the ice saturation ratio, that eventually leads to ice nucleation. The ice saturation ratio time series measured by APicT is reported in Figure 3.3b. The homogeneous freezing threshold for aqueous solution droplets with a variation of the water activity $\Delta a_w = 0.3$ is also shown in the same panel (Koop et al., 2000).

Ice crystals start to form as soon as the critical temperature and saturation for heterogeneous and/or homogeneous ice formation are reached, which depends on the aerosol particle type. The detection of the ice nucleation onset is associated with a steep increase in the laser depolarization ratio δ (Figure 3.3c, green trace) and with the detection of ice crystals in the OPCs. As already mentioned, two welas sensors, measuring in two different size ranges, sample from the AIDA chamber (indicated as OPC1 and OPC2 in Figure 3.3d). A fraction of the larger aerosol particles is detected by the OPC1 (light blue dots). The data before the start of the expansion ($t < 0$) from OPC1 relate to the aerosol particles at the corresponding optical diameter. The ice crystals, instead, appear at larger sizes only when the ice saturation ratio reaches ≈ 1.3. The ice crystal number concentration is evaluated by defining a size threshold to distinguish between the smaller inactivated aerosol particles and the larger ice crystals. The formed ice nuclei quickly grow to large ice crystals, which further deplete the water vapor present in the chamber. The fraction of aerosol particles that nucleate ice, called ice nucleating fraction (INF), is calculated as the ratio of the ice crystal number concentration to the total aerosol particle number concentration as measured by the CPC. The INF is reported on the right axis of Figure 3.3d, the black dotted vertical line indicates when the threshold of $0.1\,\%$ is reached. In the experiment shown, the ice crystals start to nucleate at a saturation ratio of $S_{\text{ice}} = 1.29$, below the homogeneous freezing threshold, indicating that heterogeneous ice nucleation occurred.
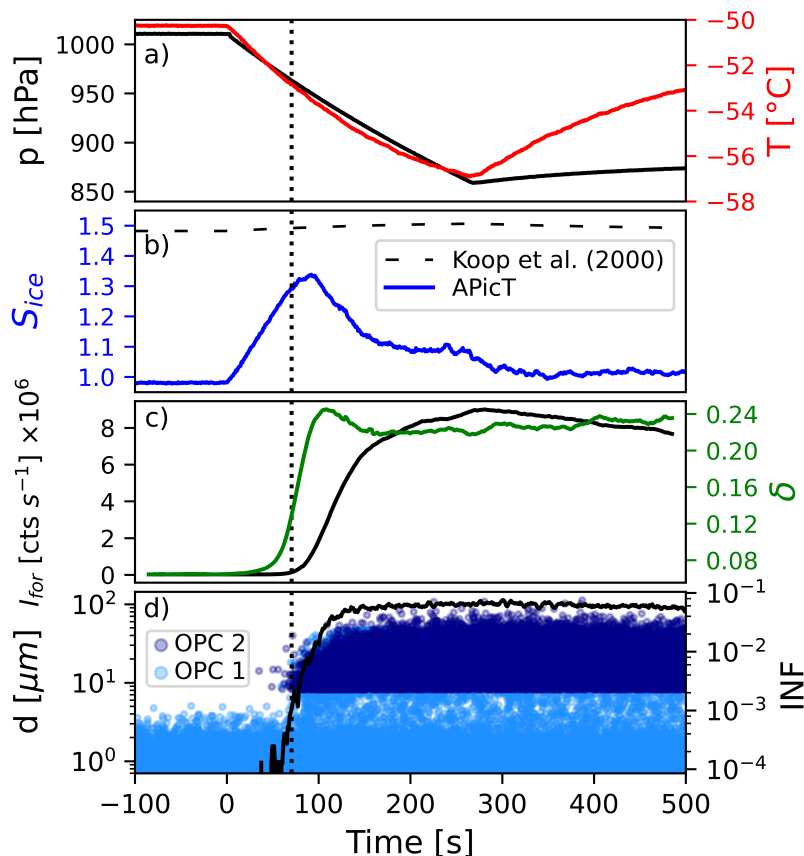
Figure 3.3: Time series of an AIDA expansion cooling experiment for crystalline ammonium sulfate particles. Panel **a)** shows pressure (black line, left axis) and temperature (red line, right axis), and panel **b)** shows the ice saturation ratio (blue line). The homogeneous freezing threshold computed for a Δa_w of 0.3 of the ice-melting curve (Koop et al., 2000) is indicated in panel b with an horizontal dashed line. Panel **c)** reports the SIMONE light scattering intensity in the forward direction (black line, left axis) and the linear depolarization ratio (green trace, right axis). Panel **d)** shows the OPCs single particle data (left axis) and the fraction of aerosol particles that induced ice formation (INF, right axis). The vertical dotted line indicates when 0.1 % of the aerosol particles acted as INPs.

3.3 CLOUD EXPERIMENT

The CERN cloud chamber is an electro-polished stainless steel tank with a volume of $26\,\mathrm{m}^3$ designed to achieve high standards of cleanliness and temperature stability (Kirkby et al., 2011; Voigtländer et al., 2012). The experiment was established to investigate the effects of cosmic rays and ions on aerosols, clouds, and climate under atmospheric conditions (Carslaw et al., 2002; Kirkby, 2007; Kulmala et al., 2010). A schematic of the chamber and the experimental setup is shown in Figure 3.4. The chamber is placed inside a thermostatic housing and its temperature can be controlled in the range from -60 to $100\,^\circ\mathrm{C}$ with a stability of $\pm 0.01\,^\circ\mathrm{C}$ (Almeida et al., 2013). To ensure homogeneous conditions inside the chamber two counter-rotating fans are mounted at the bottom and top of the chamber (Voigtländer et al., 2012). To simulate different ion concentrations, the chamber can be exposed to an adjustable pion beam, provided by the proton synchrotron particle accelerator, or to a high voltage field to simulate neutral conditions. Vapors of several precursor substances are generated in temperature stabilized evaporators, and carried to the chamber by a N_2 flow. More volatile compounds are directly injected into the chamber from gas cylinders. Ozone is generated by illuminating synthetic air with a UV light. Precise delivery of selected trace gases and ultra-pure humidified synthetic air ensures an accurate control of the gas precursors concentration and humidity conditions in the chamber. Photochemical reactions are enabled by four different light sources working at different wavelengths and adjustable intensities (Kupc et al., 2011). In particular,

for the experiments presented in this thesis a UV fibre-optic system has been used to trigger the production of ·OH radicals via ozone photolysis. The chamber is cleaned with different procedures depending on the need. This includes rinsing of the walls with pure water, heating to 100 °C, flushing with high ozone concentrations, and flushing with pure air.

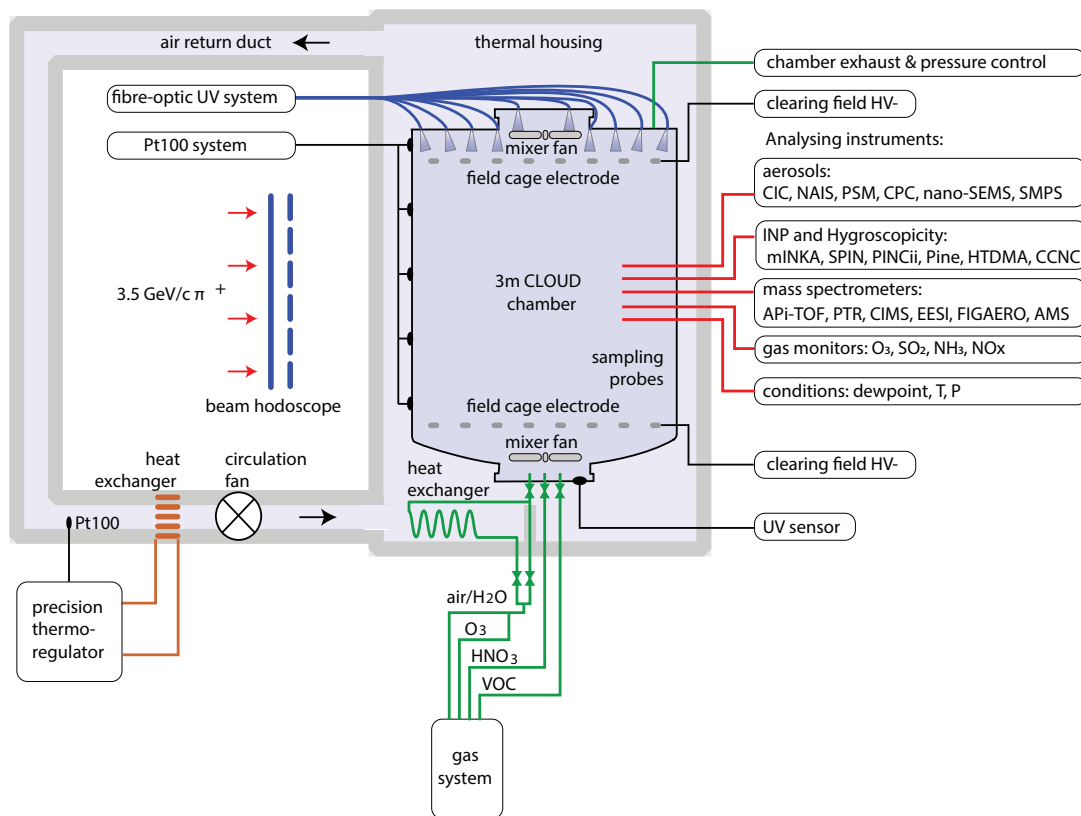**Figure 3.4:** Schematic diagram of the CLOUD experiment. Adapted from Kirkby et al. (2011). The list of instrument acronyms can be found in the caption of Table 3.1.

3.3.1 Instrumentation and set up

During the CLOUD14 campaign (autumn 2019) a wide variety of instruments was operated. The scientific aims of the campaign, in fact, ranged from studies on aerosol particle nucleation to hygroscopicity and ice nucleation ability of secondary aerosol particles. The list of instruments operated during the CLOUD14 campaign is given in Table 3.1. A brief description of the measured quantities is also provided. Data only from a small subset of instruments will be presented in this thesis (highlighted with bold font in Table 3.1). However, the full list of instrument is shown to acknowledge all the institutes and teams that participated in the campaign.

In particular, four ice nuclei counters measured during the campaign: three continuous flow diffusion chambers, namely mINKA, SPIN and PINCii, and one portable expansion chamber, PINE. A detailed description of the CFDC working principle is given in Section 3.4. The results presented in this thesis mainly focus on the measurements performed with the continuous flow diffusion chamber of the Karlsruhe Institue of Technology (mINKA), specifically developed for the CLOUD14 campaign. Some of the results from the SPIN and PINCii instruments will also be presented.

Table 3.1: Instruments operated at the CLOUD experiment during the CLOUD14 campaign. Abbreviations are tunable laser diode (TDL), atmospheric pressure interface time-of-flight mass spectrometer (APi-TOF), proton transfer reaction mass spectrometer (PTR), chemical ionization mass spectrometer (CIMS), cluster ion counter (CIC), neutral cluster and air ion spectrometer (NAIS), particle size magnifier (PSM), condensation particle counter (CPC), scanning electrical mobility spectrometer (SEMS), scanning mobility particle sizer (SMPS), extractive electrospray ionization time-of-flight mass spectrometer (EESI-TOF), thermal desorption differential mobility analyser (TD-DMA), filter inlet for gas and aerosol (FIGAERO), aerosol mass spectrometer (AMS), mobile Ice Nucleation Instrument of the KArlsruhe Institute of Technology (mINKA), SPectrometer for Ice Nuclei (SPIN), Portable Ice Nucleation Chamber II (PINCii), Portable Ice Nucleation Experiment (PINE), humidified tandem differential mobility analyzer (HTDMA), cloud condensation nuclei counter (CCN).

Observation type	Instrument name	Measured variables	Institute
Gas monitors	O_3 monitor (Thermo 49C)	O_3 mixing ratio	UFRA
	SO_2 monitor (Thermo 43i-TLE)	SO_2 mixing ratio	UFRA
	NH_3 monitor (Picarro G2103)	NH_3 mixing ratio	EMPA
	NO_x monitors (CAPS and CLD 780 TR)	NO_x mixing ratios	PSI
Water vapor	TDL	Water vapor mixing ratio	CERN/KIT
	Dew point mirror (MBW)	Dew or frost point temperature	KIT
Trace gases	APi-TOF (Tofwerk)	Chemical composition of positive and negative ions	Aerodyne/UHEL
	PTR3 (Ionikon)	Concentration of volatile organic compounds (e.g., α-pinene, isoprene), NH_3	UIBK
	PTRS (Ionikon)	Concentration of volatile organic compounds	UIBK
	Br^--CIMS (Tofwerk)	Gas phase concentration of gaseous iodine species, H_2SO_4, HNO_3 and VOCs	CMU
	NO_3^--CIMS (Tofwerk)	Gas phase concentration of highly oxigenated organic molecules, H_2SO_4, HIO_3, DMA and other compounds	UFRA
Particle microphysics	CIC (Airel)	Concentration of positive and negative ions $(0.9 - 2.84\,\mathrm{nm})$	CERN
	NAIS (Airel)	Particle number size distribution $(2 - 45\,\mathrm{nm})$, ion size distribution $(0.8 - 45\,\mathrm{nm})$	CERN
	PSM (Airmodus)	Particle number concentration with lower cutoff at $1\,\mathrm{nm}$	UHEL
	CPC (TSI)	Particle number concentration with lower cutoff at $2.5\,\mathrm{nm}$	PSI
	nano-SEMS	Particle number size distribution $(1.5 - 25\,\mathrm{nm})$	CalTech
	nano SMPS (TSI)	Particle number size distribution $(3 - 60\,\mathrm{nm})$	PSI
	long SMPS	Particle number size distribution $(50 - 300\,\mathrm{nm})$	PSI
	SMPS	Particle number size distribution $(10 - 800\,\mathrm{nm})$	TROPOS
Particle chemical composition	EESI-TOF (Tofwerk)	Extractive electrospray-based measurement of gas and particle phase composition	PSI
	TD-DMA	Size resolved thermal desorption-based measurement of particle phase composition	UFRA
	FIGAERO (Aerodyne)	Thermal desorption-based measurement of particle phase composition	CMU
	AMS (Aerodyne)	Thermal vaporisation-based measurement of particle phase composition	PSI/CMU
Ice nucleation	**mINKA**	INP concentration for $T > -65\,°C$	KIT
	SPIN (DMT)	INP concentration for $T > -60\,°C$	FMI
	PINCii	INP concentration for $T > -50\,°C$	UHEL
	PINE	INP concentration for $T > -40\,°C$	KIT
Hygroscopicity	HTDMA	Aerosol particle hygroscopicity $(50 - 300\,\mathrm{nm})$	UEF
	CCNC (DMT)	CCN number concentration	TROPOS

3.3.2 Experimental procedure

The scientific motivations, the experimental conditions, and the results of some of the ice nucleation experiments performed during the CLOUD14 campaign will be provided in Chapters 5 and 6. Hereafter a technical description of an exemplary experiment is provided.

The CLOUD chamber is usually operated in a continuous flow mode due to the large instrument sampling flow rate ($\approx 250\,\mathrm{L\,min^{-1}}$ during CLOUD14). Under these conditions after $\approx 1.5\,\mathrm{h}$, if any change is performed in the injection rates, steady state conditions are achieved (Levenspiel, 1999). Additionally, the continuous injection of clean synthetic air lead to the dilution of the chamber contents, with a dilution lifetime of $\approx 3\,\mathrm{h}$ for the specific total flow rate of the CLOUD14 campaign.

Each ice nucleation experiment (i.e., run) consisted of three different stages: (i) cleaning and conditioning of the CLOUD chamber, (ii) nucleation and growth of the aerosol particles, and (iii) ice nucleation and hygroscopicity measurements. For some experiments, after the ice nucleation measurements, a relative humidity scan was performed by constantly increasing, or decreasing, the relative humidity inside the CLOUD chamber, and by simultaneously measuring the ice nucleation ability of the particles.

A typical experiment is shown in Figure 3.5. In particular, the experiment shown was performed in the CLOUD chamber prepared at $\approx -53\,^{\circ}\mathrm{C}$ and $\mathrm{RH}_w = 15 - 20\,\%$, and aimed to investigate the $\mathrm{H_2SO_4/NH_3/H_2O}$ system.

In between of the experiments, the *cleaning* of the CLOUD chamber is usually performed by increasing the rotating speed of the mixing fans, thus facilitating the condensation of vapors on the walls, and by switching on and off the high voltage field to reduce the aerosol number concentration. When the electric field is off, the particles get charged by the atmospheric radiation, and when the electric filed is turned on they are drifted towards the electrodes. Additionally, because of to the dilution lifetime both vapors and particles get diluted with time. During the cleaning stage the chamber *conditioning* for the following experiment is also performed, meaning that the desired vapor concentrations are achieved by changing their injection flow rates accordingly.

Once the number concentration of particles falls below a desired threshold ($\approx 100\,\mathrm{cm^{-3}}$), and the preset concentration of gas precursors is achieved, the *nucleation* of a new batch of particles is started by increasing the concentration of one of the reactants or by turning on the illumination system. In the experiment shown in Figure 3.5, particles nucleate as soon as the lights are turned on (panel b, yellow shaded area) and gas phase sulfuric acid is formed (panel d, dark red line). The continuous production and condensation of sulfuric acid on the already nucleated particles leads to their growth. When the larger particles reach $\approx 300\,\mathrm{nm}$ in diameter (panel e) the production of sulfuric acid, and thus the growth of the particles, is stopped by turning off the lights.

Finally, for the following $6\,\mathrm{h}$ the ice nucleation ability of the particles is investigated in ice saturation ratio scans performed at different temperatures with the continuous flow diffusion chambers (CFDC, more details on their working principle and operation are provided in Section 3.4). Figure 3.5f shows the saturation scans performed with mINKA color-coded by the investigated temperature.

The sampling lines of the ice nuclei counters were insulated to preserve the phase state of the particles formed in the CLOUD chamber. Additionally, the sampling lines of mINKA, PINE, and SPIN were actively cooled with external chillers to the CLOUD chamber temperature or the minimum working temperature of the chillers ($-65\,^{\circ}\mathrm{C}$ for mINKA and PINE, $-35\,^{\circ}\mathrm{C}$ for SPIN).
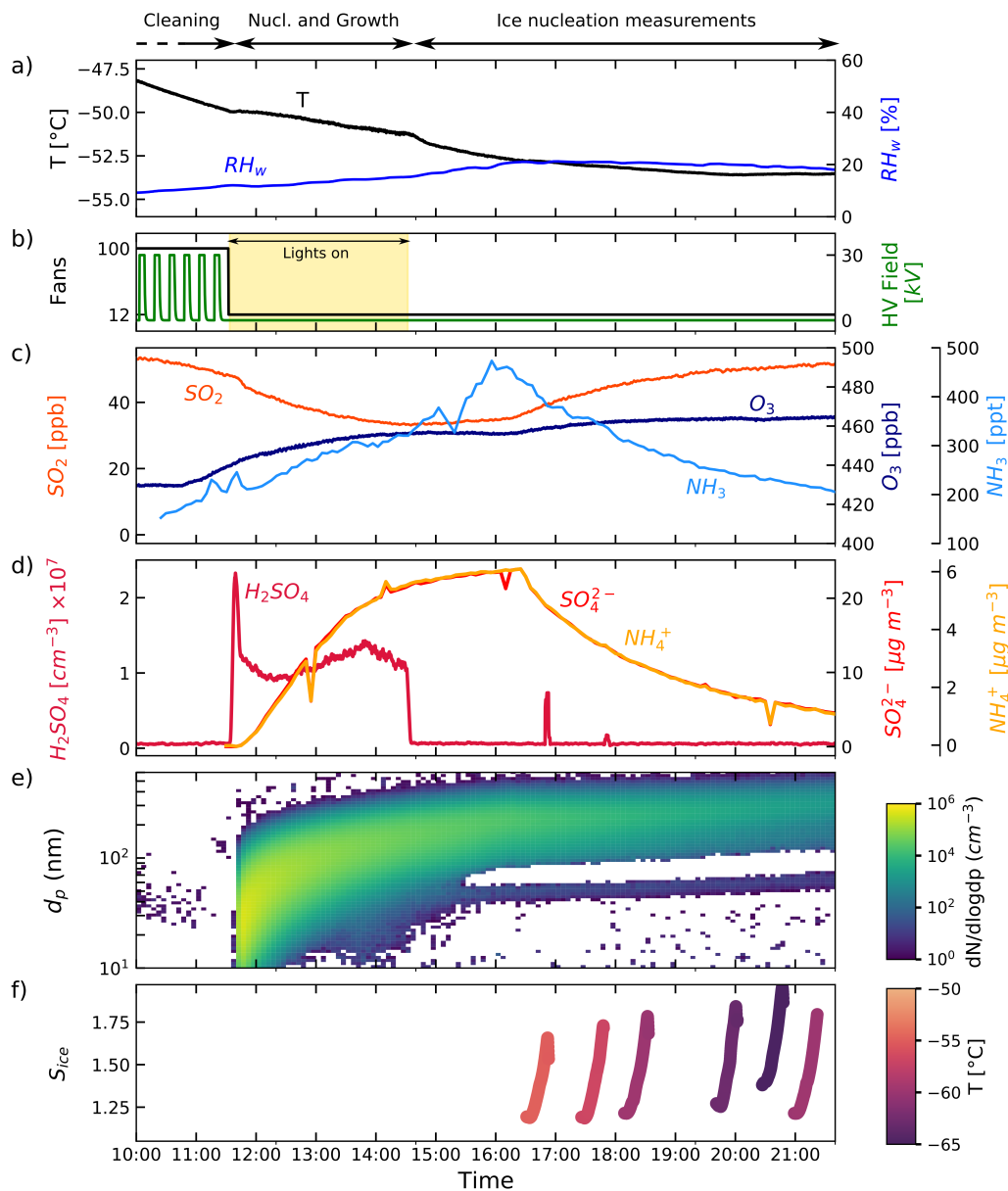
Figure 3.5: Time series of a typical experiment performed in the CLOUD chamber during the CLOUD14 campaign for ice nucleation studies. **a)** Thermodynamic conditions (temperature and relative humidity with respect to liquid water) inside the CLOUD chamber. **b)** Rotation speed of the mixing fans (in percentage) and intensity of the high voltage field used during the cleaning stage. The yellow shaded area indicates the time period with the UV lights on. **c)** Concentration of the gaseous precursors used during the experiment, namely sulfur dioxide (SO_2), ozone (O_3), and ammonia (NH_3). **d)** Gas phase concentration of sulfuric acid, and particle phase concentration of sulfate (SO_4^{2-}) and ammonium (NH_4^+). **e)** Particle number size distribution. **f)** Saturation scans performed with mINKA to measure the ice nucleation ability of the formed particles at the temperatures indicated.

3.4 CONTINUOUS FLOW DIFFUSION CHAMBERS

Continuous Flow Diffusion Chambers (CFDCs) measure the ice nucleation ability of sampled aerosol particles under defined temperature and saturation ratio conditions. Several types of CFDC have been developed in the past (e.g., Rogers et al., 2001; Kanji and Abbatt, 2009; Glen and Brooks, 2014; Garimella et al., 2016; Brunner and Kanji, 2021). They differ in geometry, working temperature, and degree of automation, but their working principle is the same. In the following, the two CFDCs of the Karlsruhe Institute of Technology, INKA and mINKA, are presented. Reference experiments are also shown to validate their performance.

3.4.1 Working principle

The following description and calculations refer to the work from Rogers (1988). In a CFDC, two parallel, ice covered plates are kept at different sub-zero temperatures (T_{cold} and T_{warm}), and thereby generate linear gradients of temperature and water vapor partial pressure in the narrow gap between them (as shown in Figure 3.6 panels I). The boundary conditions at the plates ($x = 0$ and $x = 1$) are defined by the cooling system of the instrument (for the temperature) and by an ice coating on the walls (for the water vapor partial pressure):

$$
\begin{aligned}
T(x = 0) &= T_c & T(x = 1) &= T_w \\
e(x = 0) &= e_{sat, ice}(T = T_c) & e(x = 1) &= e_{sat, ice}(T = T_w)
\end{aligned}
\tag{3.7}
$$

The ice and liquid water saturation vapor pressures that establish between the walls ($e_{sat,ice}$ and $e_{sat,water}$) are calculated with equations 3.4 and 3.5 (Murphy and Koop, 2005), and depicted in panels II in Figure 3.6. The resulting saturation ratio profiles (S_{ice} and S_{water}) are shown in panels III. Figure 3.6a and Figure 3.6b refer to different temperature gradients between the instrument walls ($\Delta T = 8\,°C$ and $\Delta T = 13\,°C$).

The investigated aerosol particles flow through the gap between the plates and are thus exposed to supersaturated conditions. Since the ice nucleation ability of the particles critically depends on temperature and saturation ratio, the aerosol particles need to experience a narrow range of thermodynamic conditions. To ensure that, the flow has to be laminar and the aerosol particles confined in a defined section within it. In fact, the aerosol sample flow, also called aerosol lamina, usually represents a small fraction (5 to 10 %) of the total flow ($10 - 12.5\,stdL\,min^{-1}$). The aerosol lamina is encased by a constant flow of particle-free, dry synthetic air. The lamina position is calculated according to Rogers (1988), it depends on the walls temperature difference ΔT, the gap width d, the total flow, and the aerosol flow. The lamina position is indicated by the gray shaded areas in Figure 3.6.

The flow velocity profiles for a total flow of $10\,stdL\,min^{-1}$ between vertically oriented plates are shown in Figure 3.6 panels IV. The velocity profiles are skewed toward the cold plate due to the development of a buoyant flow close to the warm plate. When large temperature gradients are applied the buoyant flow can eventually perturb the laminar flow and generate turbulence (Richardson, 2009). In this case the aerosol flow is not constrained anymore in a thin flow section, and the aerosol particles experience a wider range of thermodynamic conditions (Garimella et al., 2017).

By increasing ΔT with appropriate values for T_w and T_c, the aerosol lamina can be exposed to increasing saturation ratios while kept at constant temperature, performing a so-called saturation scan (Schiebel, 2017).

3.4.2 INKA and mINKA

The two continuous flow diffusion chambers of the Karlsruhe Institute of Technology, INKA and mINKA, base their design on the CFDC developed by Rogers (1988). INKA was developed and described by Schiebel (2017), mINKA is its mobile version[3].

---

3 mINKA has been described for the first time in the Master Thesis "Measurements of the ice nucleating ability of Secondary Organic Aerosol at the CERN CLOUD experiment" from Pia Bogert (2020).
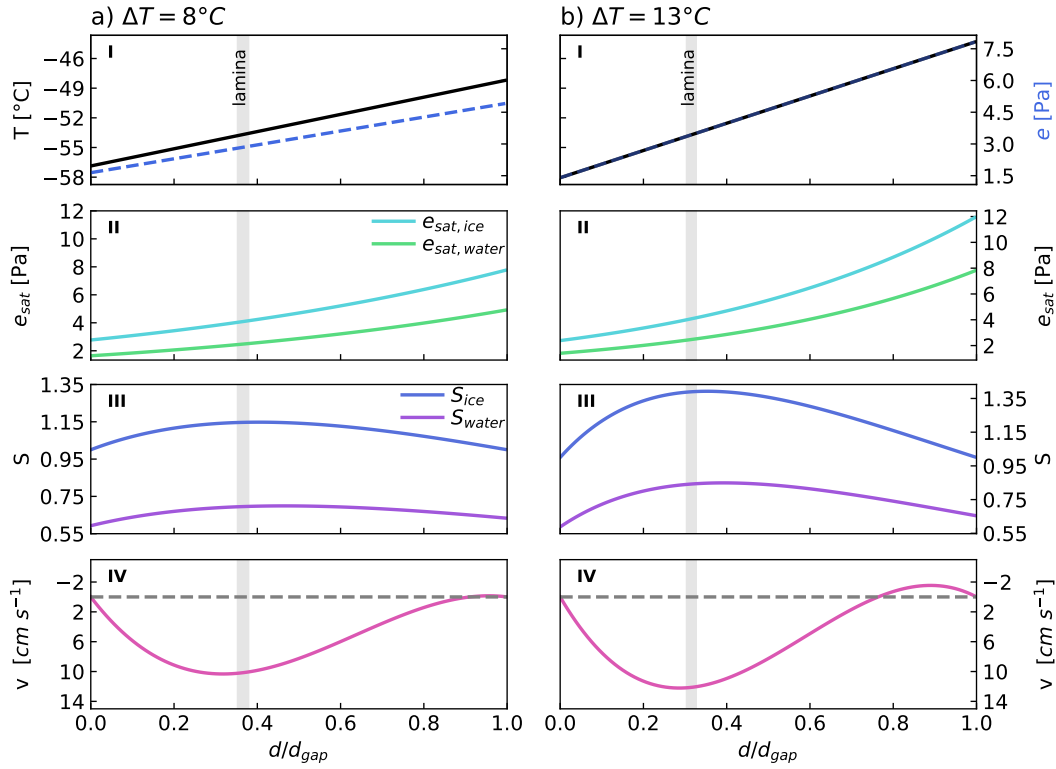
Figure 3.6: Thermodynamic conditions between two vertically oriented ice covered plates kept at different temperatures and with a total flow of $10\,\mathrm{L\,min^{-1}}$. Panels a and b represent the conditions for temperature differences between the walls of $\Delta T = 8\,°\mathrm{C}$ and $\Delta T = 13\,°\mathrm{C}$, respectively. Panels **I** shows the steady state temperature (left axis, black) and water vapor pressure (right axis, dark blue) profiles. Panels **II** report the saturation vapor pressure e_{sat} with respect to ice ($e_{sat,\,ice}$, cyan) and supercooled liquid water ($e_{sat,\,water}$, green) calculated with the parametrization by Murphy and Koop (2005). The saturation ratios S with respect to ice and liquid water are shown in panels **III**. Panels **IV** illustrate the velocity profiles inside the annular gap. The gray shaded areas correspond to the position of the aerosol lamina for an aerosol flow of $0.5\,\mathrm{L\,min^{-1}}$.

In those instruments, two concentric and vertically oriented copper cylinders of different diameters form an annular gap of width $d \approx 1\,\mathrm{cm}$. The outer and inner cylinders correspond to the warm and cold plates, respectively. Copper pipes are welded to the surface of the cylinders and connected to two chillers to control their temperature (from -70 to $20\,°\mathrm{C}$, Proline LAUDA). The copper cylinders of INKA and mINKA are $150\,\mathrm{cm}$ and $85\,\mathrm{cm}$ long, respectively. A total of 24 thermocouples (T-type, $\pm 0.5\,°\mathrm{C}$) are attached to the inner and outer walls of each instrument. Figure 3.7 shows the technical drawings of the two instruments (side view and cross-section), the position of the temperature sensors is also indicated. The sensors can be sorted into six different levels depending on their height along the columns (Figure 3.7).

In the upper 2/3 of INKA, the cylinder walls are kept at two different temperatures to generate supersaturated conditions as described in the previous section (so-called *diffusion section*). In the lower third of the chamber, instead, the walls are kept at the same temperature (so-called *evaporation section*). Without a temperature gradient, the relative humidity in the evaporation section drops to sub-saturated conditions with respect to liquid water, but the ice coated walls ensure $S_{ice} = 1$. The evaporation section is critical for experiments performed at mixed-phase cloud conditions when supercooled droplets and ice crystals can co-exist. In this section of the instrument, in fact, the droplets evaporate while the ice crystals continue to grow, facilitating their discrimination in the analysis. mINKA was set up to measure at low temperatures and $\mathrm{RH}_w < 100\,\%$, and for this reason, it was operated without an evaporation section in the experiments presented in this thesis. Furthermore, this configuration maximizes the residence time of the particles in the section where ice nucleation can occur.
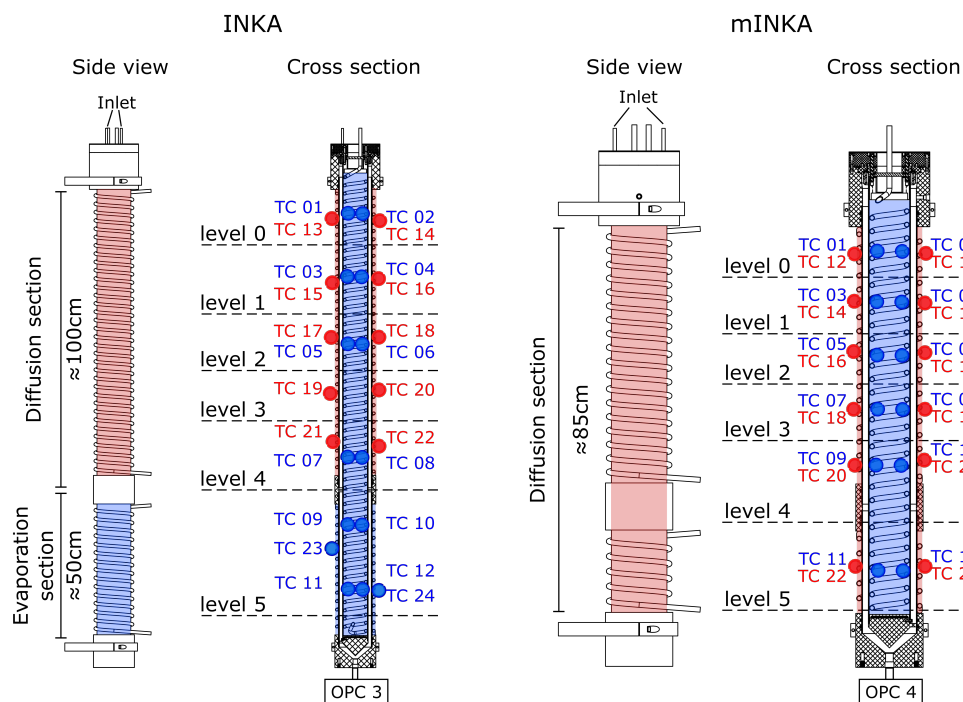
Figure 3.7: Technical drawings of INKA (left) and mINKA (right). The warm and cold walls are colored in red and blue, respectively. The position of the thermocouples is indicated with red and blue circles. The sensors are divided into different levels depending on their height along the columns. Note that the drawings have different scales.

The outlet of the chambers can be connected (i) to a vacuum pump for cleaning purposes and water vapor removal, (ii) to a water pump to flood the chambers with pure water during the chamber icing process, or (iii) to an optical particle counter during the measurements.

Before each measurement period, the chambers are evacuated by connecting their outlet to the vacuum pump to remove both water vapor and aerosol particles. The pressure inside INKA can go as low as $\approx 1\,mbar$ with a leak rate lower than about $2\,mbar\,min^{-1}$. In mINKA, instead, the minimum reachable pressure is $\approx 150\,mbar$ due to the presence of a leak in a weld joint of the inner wall. To minimize the infiltration of ambient air from the leak, the chamber is thus cleaned by flushing synthetic air while evacuating with the vacuum pump. The icing procedure (i.e., the procedure to create the ice layer on the walls of the instrument) consists in (1) cooling the instrument walls to $\approx -27.5\,°C$ while keeping the chamber at low pressure, (2) re-filling the chamber to ambient pressure with particle-free, dry synthetic air, and (3) flooding the annular gap with deionized water (Schiebel, 2017). The chamber is then again evacuated for about $5\,min$ to smooth the ice coating. The ice layer on the inner wall of mINKA is thick enough to seal the leak, however if the chamber is completely evacuated the leak tends to open again. For this reason, a flow of $5\,stdL\,min^{-1}$ of particle free dry synthetic air is kept during the evacuation. After re-filling to ambient pressure, the optical particle counter (OPC) is connected to the outlet of the instrument, and the sampling started. The sample flow can be directly injected into the chamber or can first pass through a HEPA filter (Whatman) to remove the sampled particles. During the measurement period the sample flow is regularly passed through the filter to quantify the background signal in the OPC coming from frost falling from the instrument's walls.

A home-build LabView software controls the wall temperature and mass flow rates, thus determining the aerosol lamina temperature and relative humidity. Ice nucleation experiments can be performed either (i) at constant temperature and increasing the ice saturation ratio, (ii) at constant ice saturation ratio and decreasing the sample temperature, or (iii) at fixed temperature and ice saturation ratio. A typical experiment is presented in section 3.4.6 a

3.4.3 INP concentration

Aerosol particles, droplets and, ice crystals that exit the CFDC are detected with a modified Climet optical particle counter (CI-3100) (Schiebel, 2017). The sensor detects and amplifies the intensity of the light scattered by each particle in the range $0.05 - 4.5\,V$. In order to associate the output voltage to a diameter, a rough size calibration was performed. The calibration experiments were carried out with mono-disperse silicon dioxide particles of known size, which were dispersed into the AIDA chamber and then sampled by the CFDCs. Particles with two different nominal diameters and same refractive index (m = 1.43) were used, CalDust1100 ($0.9\,\mu m$, Palas GmbH) and CalDust2000 ($2\,\mu m$, Palas GmbH). Figure 3.8 shows the results of the calibration experiments. Panels a and b refer to OPC3, connected to INKA; panels c and d refer to OPC4 installed on mINKA. The measured scattering intensities are divided into 20 logarithmically spaced bins and the number concentration dn in each bin calculated. To filter out electrical noise, it is possible to set an intensity lower cutoff in the OPC recordings. The signals with an intensity lower than the defined noise threshold are discarded. In each panel, the gray shaded areas correspond to the defined noise threshold, usually set at $0.2\,V$ or $0.3\,V$. The counting efficiency (CE), reported in each panel, is the ratio of the total number of particles detected by the OPC to the number concentration measured by a CPC. About 70 % of the particles larger than $0.9\,\mu m$ are detected. However, it's important to mention that for these experiments the CPC and the CFDCs were sampling with different sampling lines from the AIDA chamber. In particular, the CPC was sampling with a shorter sampling line, while the CFDCs shared the sampling line from the chamber untill a flow splitter close to their inlets. The reported counting efficiencies likely represent a lower limit estimate due to different losses in the sampling lines of the instruments. The two OPCs agree well among them. The OPC4 shows a size distribution slightly shifted towards larger sizes (i.e., intensity) and has a higher counting efficiency compared to OPC3. The limit of detection of the Climet OPCs is thus estimated at $\approx 0.9\,\mu m$, with an intensity lower cutoff at $0.3\,V$. However, these calibrations refer to particles with a refractive index of m = 1.43, higher than those for water and ice, for which a lower limit of detection is thus expected. Particles larger than $\approx 5\,\mu m$ are detected and counted in the highest intensity bin.

The ice crystals number concentration, and thus the INP number concentration, is assessed by defining an intensity (~size) threshold (called ice threshold) in the OPC records to distinguish between the unactivated aerosol particles and the ice crystals. The uncertainty associated with the calculated ice number concentration depends on (i) the error in the concentration measured by the OPC, (ii) the user-defined ice threshold, and (iii) the experiment dependent background signal. Analogously to other optical particle counters, the error in the concentration measured by the Climet OPCs is assumed to be 20 % (Wagner and Möhler, 2013). The ice threshold is a critical parameter that needs to be evaluated for each experiment. In general, for measurements performed at $RH_w < 100\,\%$ and low temperatures (as for the experiments presented in this thesis), the ice threshold is defined as the lowest intensity that excludes the majority of the detected aerosol particles. The background signal comes from the detection above the ice threshold of ice crystals and large aerosol particles when the ice saturation ratio is still low (i.e., before the start of the saturation scan). In fact, after several hours of measurements the ice layer on the walls can deteriorate, with the formation of frost on the cold wall that eventually falls. To account for the background signal, the number concentration of particles and ice crystals measured above the ice threshold, before the start of each saturation scan, is subtracted from the total ice number concentration (more details are provided in Section 3.4.6).

3.4.4 Lamina calculations

As the ice nucleation ability of aerosol particles strongly depends on temperature and saturation ratio, it is important to correctly evaluate the thermodynamic conditions inside the CFDC and the associated uncertainty. The thermodynamic conditions of the aerosol lamina are calculated according to Rogers (1988) and Schiebel (2017).

Figure 3.9 shows the calculated lamina conditions at the different height levels (defined in Figure 3.7) for an experiment performed at the nominal temperature of $-44\,°C$ in INKA (panels a and c) and mINKA (panels b and d). Results for the lowest level of INKA (i.e., level 5) are not reported
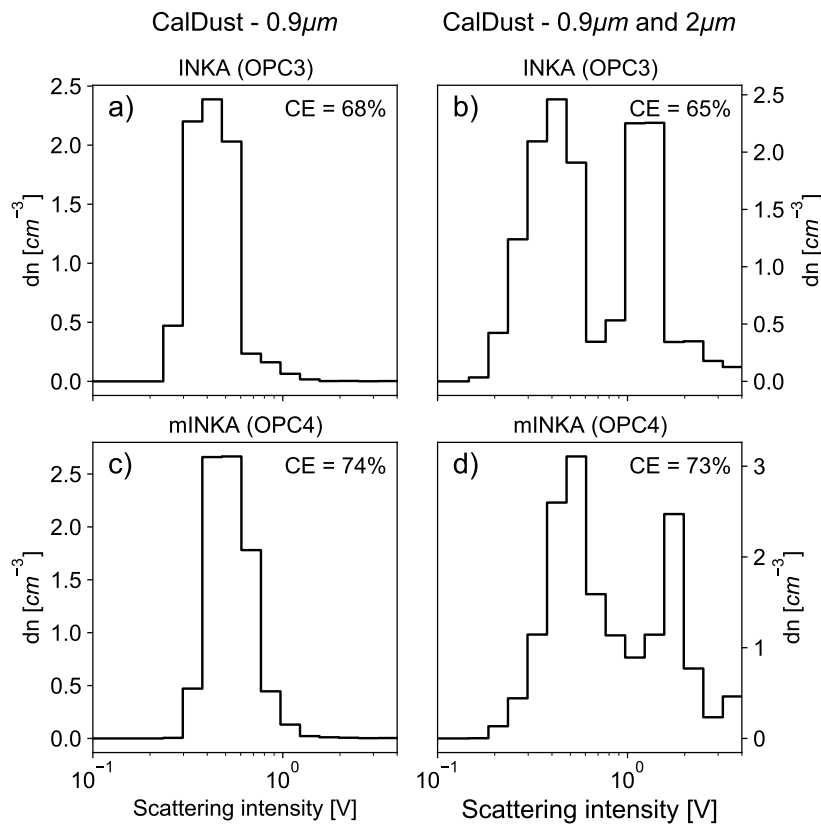
Figure 3.8: Number particle distributions obtained with the Climet CI-3100 OPCs. Panels a and b refer to OPC3, installed on INKA; panels c and d refer to OPC4, installed on mINKA. CalDust1100 particles (0.9 μm) are shown on the left (panels a and c), CalDust1100 together with CalDust2000 (2 μm) particles are shown on the right (panels b and d).

as they relate to the evaporation section. The temperature of the lamina in the upper part of the instruments (level 0) is clearly higher than the average conditions. In both instruments, in fact, the cooling fluid flows from the bottom to the top of the cylinders, gradually heating up (Schiebel, 2017). The lamina saturation ratio at level 0 is also affected, resulting in lower values compared to the average conditions (panels c and d). Since the ice nucleation process is expected to occur in the region with the lowest temperature and highest saturation ratio, only sensors from levels 1 to 4 in INKA and from 1 to 5 in mINKA are used in the mean wall temperature calculation ($\overline{T_w}$ and $\overline{T_c}$). The lamina conditions (T and S) calculated considering the mean value of only those sensors are reported with black dashed lines in Figure 3.9.

The errors associated to the thermocouples ($\pm 0.5\,°C$) and the estimate of the annular gap width affect the evaluation of the aerosol lamina position and its thermodynamic conditions. The uncertainty in the gap width was estimated by Schiebel (2017). The nominal gap width from the technical drawings ($d_{nominal} = 1.14\,cm$) is reduced during the CFDC operation due to the presence of the ice layer on the walls. The gap width with a fresh ice layer on the walls was estimated to be $d_{iced} = 0.99\,cm$ (Schiebel, 2017). For the aerosol lamina calculations, the average value of $\overline{d} = 1.06\,cm$ is used, as the initial ice layer depth is reduced in the course of an experiment.

To take into account those uncertainty in the lamina calculations, the errors on the temperature and gap width are combined to provide the larger deviations from the average conditions. Table 3.2 reports the combination of values used for the lamina and error estimate.

3.4.5 Critical nucleation rates

The critical homogeneous nucleation rate coefficients J_{hom}^{crit} correspond to the estimate of the lower homogeneous freezing rate coefficients measurable with a specific instrument or technique (Möhler
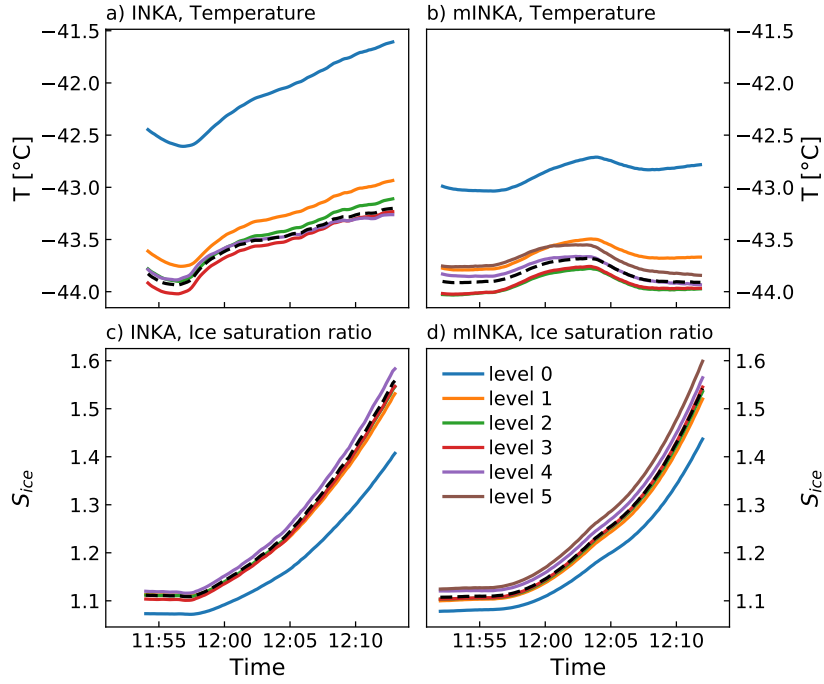
Figure 3.9: Temperature (panels a and b) and saturation ratio with respect to ice (panels c and d) of the aerosol lamina at the different heights along the diffusion section of INKA (panels a and c) and mINKA (panel b and d). See Figure 3.7 for the definition of the different height levels.

Table 3.2: Parameters used for the lamina calculations and associated errors.

	T_w	T_c	d
T,S	$\overline{T_w}$	$\overline{T_c}$	$\overline{d}$
T_{max}	$\overline{T_w} + 0.5$	$\overline{T_c} + 0.5$	d_{iced}
T_{min}	$\overline{T_w} - 0.5$	$\overline{T_c} - 0.5$	$d_{nominal}$
S_{max}	$\overline{T_w} + 0.5$	$\overline{T_c} - 0.5$	d_{iced}
S_{min}	$\overline{T_w} - 0.5$	$\overline{T_c} + 0.5$	$d_{nominal}$

et al., 2003). Equation 2.10 is used for their evaluation (Möhler et al., 2003). The parameters involved are the activation probability n_{hom}/n (i.e., the fraction of frozen solution droplets), the observation time Δt (i.e., the time the particles are exposed to supersaturated conditions), and the volume V of a solution droplet.

To estimate the time interval Δt, it is necessary to evaluate the length of the section of the instruments in which the droplets are exposed to supersaturated conditions and can thus nucleate ice. As discussed in Section 3.4.4, the effective nucleation section has a length of about 80 cm in INKA (levels 1 to 4 in Figure 3.7) and of about 70 cm in mINKA (levels 1 to 5 in Figure 3.7). The residence time of the particles in the so defined nucleation section (Δt) is calculated by using the flow velocity at the lamina position. Figure 3.10 shows the residence time for particles inside the aerosol lamina as a function of the temperature difference between the two walls ΔT (left panel), and as a function of the ice saturation ratio S_{ice} for different aerosol lamina temperatures (colors).

The J_{hom}^{crit} obtained for solution droplets of diameter 0.5 µm and 1 µm, representative for the majority of the aerosol particles investigated in this thesis, are reported as a function of the ice saturation ratio S_{ice} in Figure 3.11 . Solid and dashed lines refer to the freezing probabilities P_{crit} of 0.5 and 0.3, respectively. Panels a and c refer to INKA, panels b and d refer to mINKA. The critical nucleation rate coefficients estimated, for the considered diameters and freezing probabilities, are in the range between 10^{11} and $10^{12} cm^{-3} s^{-1}$.
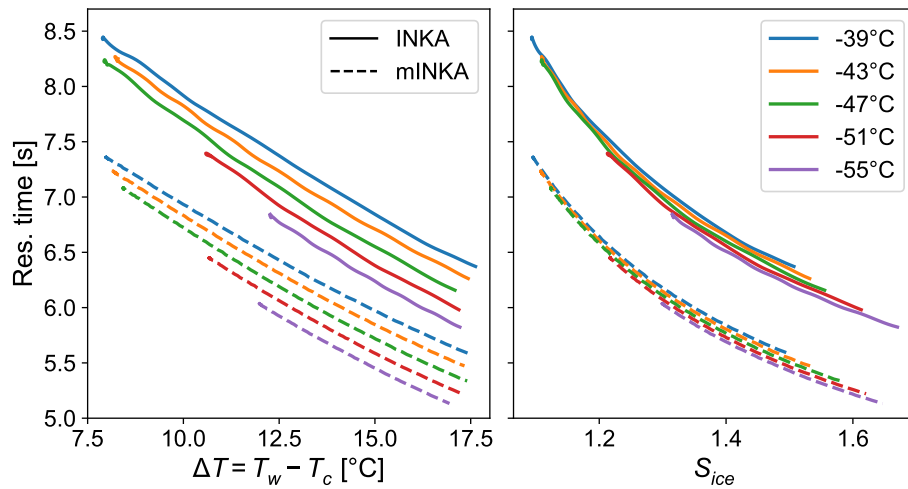
Figure 3.10: Residence time for particles inside the aerosol lamina in INKA (solid lines) and mINKA (dashed lines) for different aerosol lamina temperatures (colors) as a function of the temperature difference between the walls ΔT (left plot) and the ice saturation ratio S_{ice} (right plot).
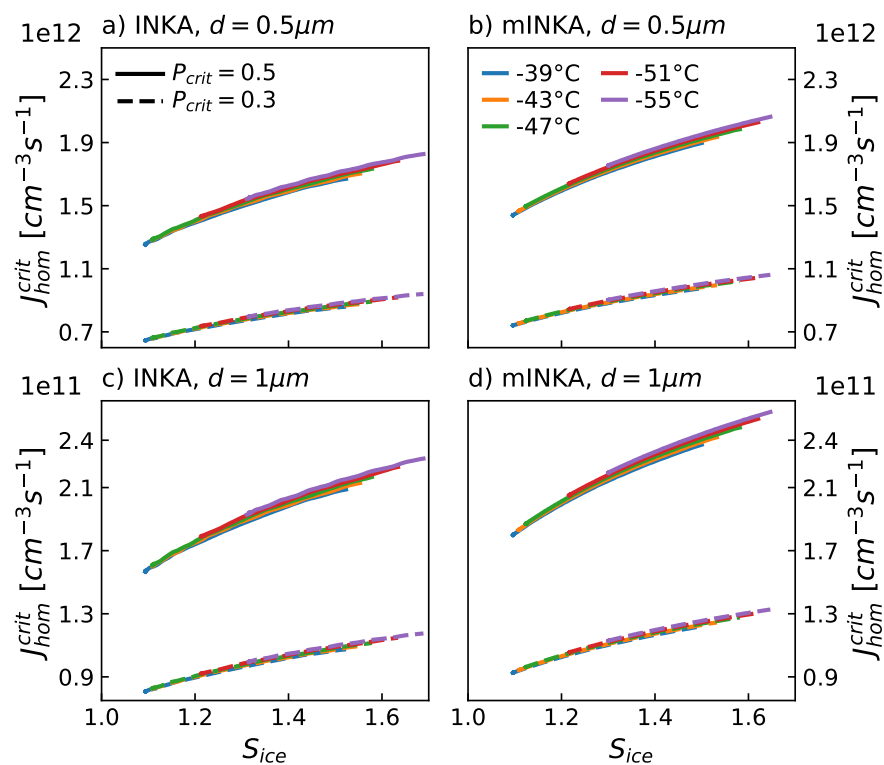

Figure 3.11: Critical nucleation rate coefficients for INKA (panels a and b) and mINKA (panels c and d) for a freezing probability of 0.5 (solid lines) and 0.3 (dashed lines) and solution droplets diameters of $0.5\,\mu m$ (left panels) and $1\,\mu m$ (right panels).

3.4.6 Typical experimental procedure

A typical INKA saturation scan, performed at the nominal temperature of $-54\,°C$ with solid ammonium sulfate particles sampled from the AIDA chamber, is shown in Figure 3.12. Aerosol particles were generated with an ultrasonic nebulizer (described in Section 3.2.2) from a $1\,wt\%$ solution of ammonium sulfate in deionized water. The particles had a median diameter of about $400\,nm$. The particles were injected into the AIDA chamber held at $-50\,°C$ and ice saturated conditions ($S_{ice} = 1$).

Figure 3.12a shows the temperature time series of the warm wall (red), the cold wall (blue), and the aerosol lamina (black). In a saturation scan the temperature of the walls are continuously adjusted in order to keep the lamina temperature constant while increasing the ice saturation ratio. The saturation ratio with respect to ice S_{ice} and liquid water S_{water} are reported in Figure 3.12b. Panel c shows the normalized single particle data from OPC3. Each black dot corresponds to an aerosol particle or ice crystal. The green horizontal line corresponds to the user-defined ice threshold for the experiment under consideration. The ice number concentration is reported in panel c, right axis. The background concentration is calculated as the average concentration of particles or ice crystals above the ice threshold detected before the start of the measurement (gray shaded area, $\approx 2\,min$).
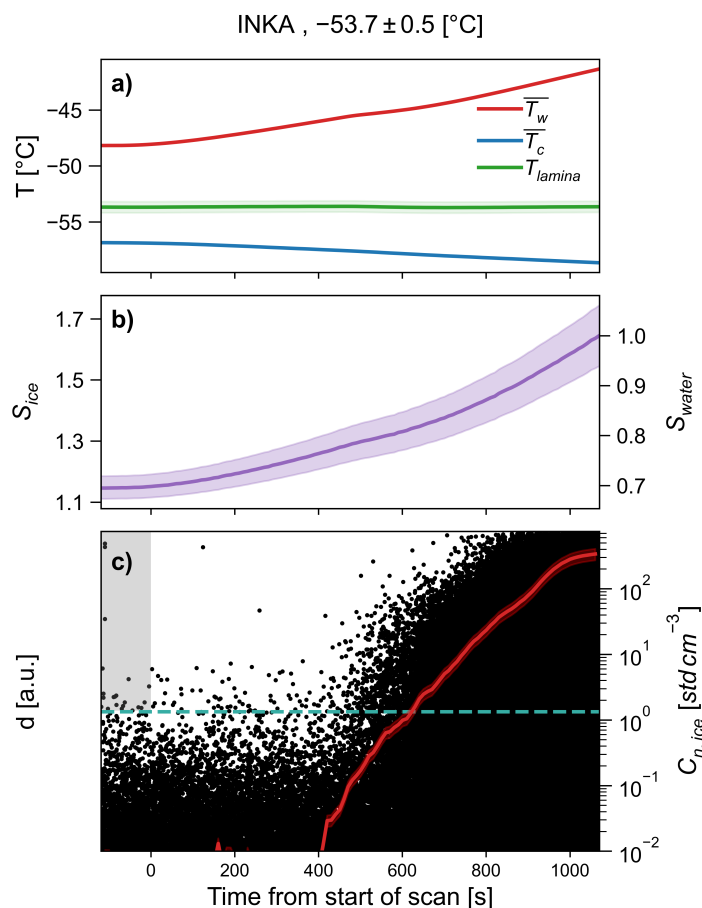
Figure 3.12: Ice saturation ratio scan performed with INKA at the nominal temperature of $-54\,°C$ with crystalline ammonium sulfate particles. **a)** Temperature of the walls and aerosol lamina. **b)** Saturation ratios with respect to ice and liquid water (purple). The associated error is shown as shaded area. **c)** Normalized single particle data from OPC3 (left axis), each black dot corresponds to an aerosol particle or ice crystal. The green horizontal line is the ice threshold. The ice crystal number concentration is also reported in panel c (red, right axis). The gray shaded area highlight the data used to evaluate the background ice concentration.

At low saturation ratios, only the larger aerosol particles are detected by the OPC. As soon as a critical saturation value is reached, after $\approx 400\,s$, ice starts to form heterogeneously on the crystalline ammonium sulfate particles and ice crystals are detected at larger sizes (i.e., higher

scattering intensities) in the OPC records. A further increase in the saturation ratio leads to an increase of the detected nucleation events.

A CPC (model 3772, TSI) is usually operated together with the CFDCs to measure the aerosol number concentration directly before the inlet of the instruments. The ratio of the ice crystal number concentration to the total number of aerosol particles provides the fraction of aerosol particles that nucleated ice (ice nucleating fraction, INF).

3.4.7 Proof of concept

In this section, proof of concept studies performed to validate INKA and mINKA performing features are presented. In particular, experiments on the (i) homogeneous freezing onset of aqueous solution droplets, (ii) deliquescence, and (iii) heterogeneous ice nucleation of crystalline ammonium sulfate particles are shown. Homogeneous freezing of solution droplets and deliquescence of inorganic salts are typical experiments performed to validate the performances of continuous flow diffusion chambers (e.g., DeMott et al., 2003; Kanji and Abbatt, 2009; Richardson, 2009; Kong et al., 2018; Brunner and Kanji, 2021). These phenomena, in fact, occur at defined relative humidity and ice saturation values as a sudden growth of the aerosol particles (deliquescence) or appearance of the ice crystals (homogeneous freezing). In the following, the three types of experiments are presented separately. Finally, a summary overview with the comparison to literature data is shown in Figure 3.17.

HOMOGENEOUS FREEZING OF SOLUTION DROPLETS   Figure 3.13 shows two saturation scans performed with liquid ammonium bisulfate particles (NH_4HSO_4) generated with an ultrasonic nebulizer from a $8\,wt\%$ solution in deionized water. The generated particles had a median diameter of about $1\,\mu m$ (measured with an aerodynamic particle sizer, APS). The measurements were performed at the nominal temperature of $-48\,°C$. Data from the INKA and mINKA instruments are reported in panel a and b, respectively. The single particle data from the OPCs are color-coded by the aerosol number concentration, calculated from the OPC data divided in 20 log-normally distributed size bins. In both instruments, the ice crystals appear only at the end of the measurement period at high ice saturation ratio values. The ice nucleation onsets, defined for an ice-active fraction of 0.1 %, are estimated at 1.57 and 1.55 in INKA and mINKA, respectively (vertical dashed lines in Figure 3.13).

The influence of the evaporation section, present in INKA and not in mINKA, is well visible when comparing the evolution of the particle size distribution as a function of the ice saturation ratio. To facilitate the distinction between aqueous droplets and ice crystals in the OPC records, the lower third section of INKA is kept at subsaturated conditions with respect to liquid water (here at $RH_w \approx 63\,\%$) to evaporate the cloud droplets, but still at ice saturated conditions to avoid the sublimation of the ice crystals. mINKA, instead, is operated without evaporation section and the aerosol particles experience the same supersaturated conditions through the whole chamber. As the ice saturation ratio (and relative humidity) increases during the measurement, the particles are detected at progressively larger sizes due to their hygroscopic growth (Figure 3.13b).

A summary of the homogeneous freezing onsets of sulfuric acid and ammonium bisulfate aqueous solution droplets is presented in Figure 3.17a. For all the experiments, the aerosol particles were sampled from the AIDA chamber held at low temperature ($T < -30\,°C$). The reported onset values correspond to the ice saturation ratio at which an ice nucleating fraction of 0.1 % was reached. In Figure 3.13a, INKA and mINKA results are compared to literature data and parametrizations.
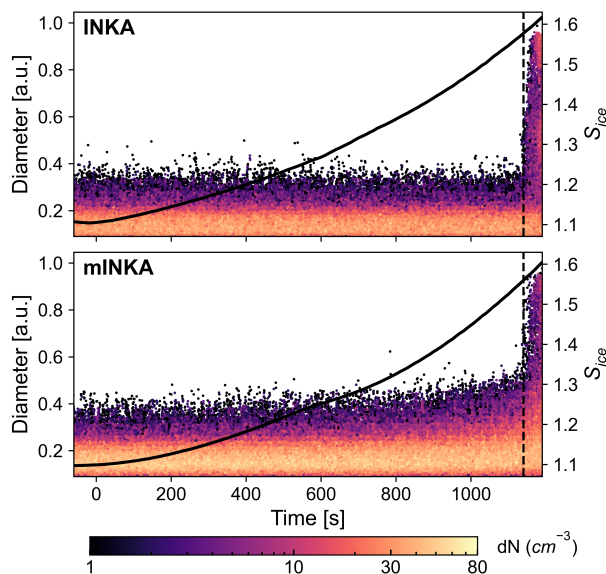
Figure 3.13: Homogeneous freezing experiment performed with liquid NH_4HSO_4 at $-48\,°C$ with INKA (upper panel) and mINKA (lower panel). Each dot corresponds to an aerosol particle or ice crystal at the corresponding normalized diameter. Data are colored by the number concentration calculated from the OPC data divided in 20 log-normally distributed size bins.

DELIQUESCENCE RELATIVE HUMIDITY OF AMMONIUM SULFATE The deliquescence relative humidity (DRH) is detected in the CFDCs as a sudden increase in particle size due to their hygroscopic growth (e.g., Kong et al., 2018; Wagner et al., 2020; Brunner and Kanji, 2021). As for the ice nucleation experiments, to detect the DRH of the investigated aerosol particles the relative humidity is gradually increased while the aerosol temperature is held constant. Figure 3.14 shows a typical deliquescence experiment performed at the nominal temperature of $-35\,°C$ with initially crystalline ammonium sulfate particles $((NH_4)_2SO_4,\ AS)$. The particles were generated with an ultrasonic nebulizer from a $8\,wt\%$ solution of AS in deionized water. The generated particles had a median diameter of about $1\,\mu m$ (measured with an aerodynamic particle sizer, APS). To crystallize the aerosol particles before injection into the AIDA chamber, the aerosol flow was exposed to a relative humidity lower than the efflorescence relative humidity of ammonium sulfate by passing through a series of diffusion dryers. Panels A and C refer to INKA results, mINKA data are shown in panels B and D. The normalized single particle data from the OPCs are reported in panels A and B, color-coded by the number concentration dN calculated from the OPC data divided in 20 log-normally distributed size bins. The relative humidity experienced by the aerosol particles during the scans in INKA and mINKA is reported in panels A and B (right axes, black curves). The aerosol number concentration measured by the OPCs in the size bins shaded in gray is shown in panels C and D (right axes, blue curves). Panels C and D show 5 particle size distributions measured at the outlet of the CFDCs at the times indicated with vertical lines in panels A and B, and corresponding to the relative humidity indicated in the legend. For $RH_w > 88\%$, the hygroscopic growth of the particles is visible in the size distribution plots (panels C and D, red curves) as an increase in the concentration of the larger aerosol particles. The procedure to detect the DRH has been standardized by defining the following criteria: (i) to avoid empty size bins, only the bins whose total concentration sum up to 99% of the total concentration are considered; (ii) only the size bins on the right side of the distribution are considered (because the size bins on the left side would measure a decreasing concentration after the deliquescence); (iii) the two central size bins among those previously identified are selected; (iv) the deliquescence is detected when the aerosol concentration, in both the selected size bins, exceeds their initial values by 2 or 3 standard deviations. For the experiment reported in Figure 3.14, the DRH is detected at $RH_w = 88\%$ in both instruments. As already mentioned in Section 3.4.3, from the size distributions shown in panels c and d, it is visible that OPC4 (installed on mINKA) is sensitive to smaller particles compared to OPC3 (installed on INKA).

The effect of the evaporation section (present in INKA and not in mINKA) is clearly visible. In INKA, although the particles deliquesce at their characteristic DRH in the upper part of the instrument, they re-equilibrate to the conditions of the evaporation section (here $RH_w \approx 70\%$) before exiting the instrument. In mINKA, instead, the particles continue to grow as the relative humidity in the aerosol lamina increases (for RH>DRH).

A summary of the ammonium sulfate deliquescence relative humidity values for ammonium sulfate particles measured at different temperatures is presented in Figure 3.17b.
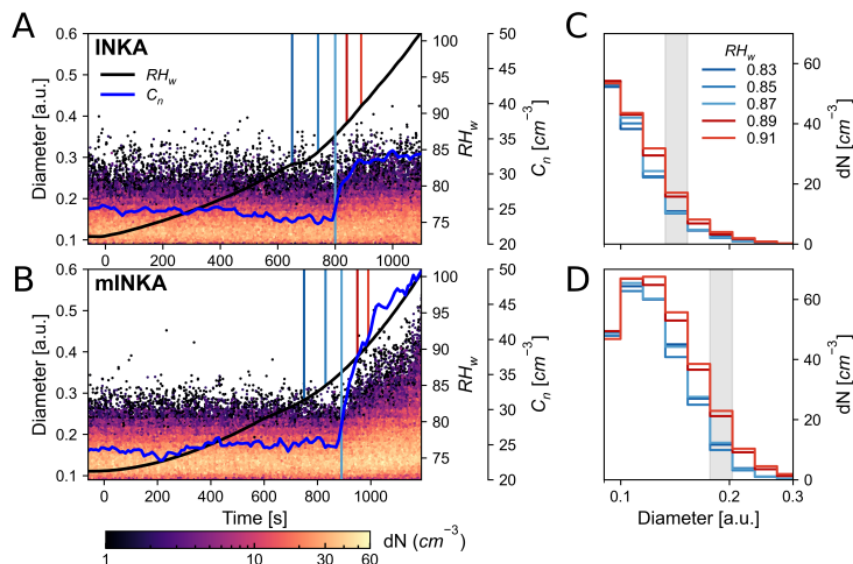
Figure 3.14: Deliquescence experiment performed with crystalline $(NH_4)_2SO_4$ at the nominal temperature of $-35\,°C$. INKA results are shown in panels **A** and **C**, mINKA results are shown in panels **B** and **D**. Panels **A** and **B** report the OPC single particle data recorded during the saturation scan. Panels **C** and **D** illustrate the particle size distributions measured at different relative humidities. The evolution of the aerosol number concentration in the size bins highlighted with a gray shaded area in panels C and D is shown in panels A and B (blue curve, right axes). The relative humidity experienced by the aerosol particles during the measurement is shown in panels A and B with black curves (right axes).

HETEROGENEOUS FREEZING OF CRYSTALLINE AMMONIUM SULFATE   During the various experimental campaigns presented in this thesis, several ice nucleation measurements were performed with crystalline ammonium sulfate (AS) particles. These measurements provide a good data set to compare the heterogeneous ice nucleation onsets measured with INKA and mINKA. As a reference, AIDA expansion cooling experiments performed with crystalline AS particles are also shown.

Particles were generated with an ultrasonic nebulizer from bulk solutions of AS in deionized water or from the neutralization reaction inside the AIDA chamber of acidic particles (sulfuric acid or ammonium bisulfate) with ammonia. The in situ neutralization procedure is described in details in Chapter 4. The AS particles were exposed to a relative humidity below their efflorescence relative humidity value to ensure their crystallization. The crystalline state of the particles inside the AIDA chamber was measured with a Fourier transform infrared sprectrometer and with the SIMONE instrument (see Section 3.2). The median diameter of the particles was about $1\,\mu m$ for the in situ neutralization experiments, and $\approx 0.5\,\mu m$ or $\approx 1\,\mu m$ for the bulk solution experiments (for $1\,wt\%$ and $5-8\,wt\%$ solution concentrations, respectively).

The ice activation curves, i.e. the ice nucleating fraction (INF) of the aerosol population as a function of the ice saturation ratio (S_{ice}), of the crystalline AS particles at temperatures between $-48\,°C$ and $-56\,°C$ are summarized in Figure 3.15. INKA results are shown in the left panels (a-d), mINKA data are reported in the right panels (e-h). Colors represent different aerosol particle generation methods and thermodynamic conditions inside the AIDA or APC chambers (see legend). The ice activation curves of the corresponding AIDA expansion cooling experiments, when available,

are reported with dashed lines. As a reference, the homogeneous freezing of ammonium bisulfate particles is shown in black.
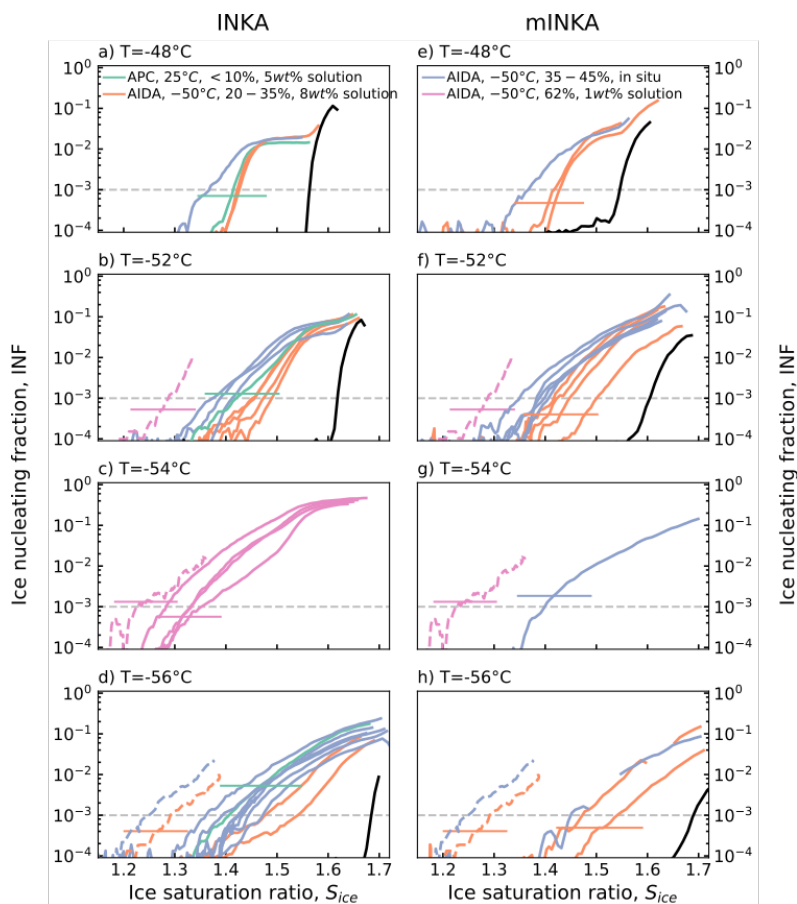
Figure 3.15: Ice nucleating fraction as a function of the ice saturation ratio for crystalline ammonium sulfate particles measured with INKA (**a-d**) and mINKA (**e-h**). Results from AIDA expansion cooling experiments are shown with dashed lines. Homogeneous freezing activation curves for aqueous ammonium bisulfate solution droplets are shown in black. Colors indicate different generation method of the particles (from bulk solution or from the neutralization of acidic particles) and thermodynamic conditions (temperature and relative humidity) of the chambers (APC or AIDA) from which the particles were sampled.

In all the experiments, the number of ice-active particles gradually increased with increasing ice saturation ratio, as typical for heterogeneous ice nucleation. This gradual increase in the number of formed ice crystals is interpreted as the increasing number of surface sites that activate at their corresponding critical ice saturation ratio (Möhler et al., 2006). The ice activation curves corresponding to the homogeneous freezing of the aqueous ammonium bisulfate particles are steeper, indicating that most of the particles nucleated ice at almost the same ice saturation ratio. Additionally, the ice nucleation onsets (defined here for an ice-active fraction of 0.1 %) of the crystalline AS particles are well below the homogeneous freezing onsets measured for the aqueous ammonium bisulfate solution droplets (at $-52\,°C$, $S_{ice} = 1.39 - 1.49$ and $S_{ice} = 1.62$, respectively). These results show the ability of INKA and mINKA to detected and distinguish heterogeneous and homogeneous ice formation.

Although the shape of the heterogeneous ice activation curves is similar for all the AS experiments, the measurements show a certain variability in the detected ice nucleation onsets. However, the ice nucleation measurements performed with INKA and mINKA on the same experimental day and with the same aerosol particles show a good agreement, suggesting that the instrument preparation (e.g. the icing of the walls) is not the cause of the variability in the ice nucleation measurements. The overall variability of the measured ice nucleation onsets at the different temperatures is summarized

in Figure 3.16. The widest range of heterogeneous ice nucleation onsets, from $S_{ice} = 1.36$ to $S_{ice} = 1.54$, is observed in the INKA data at $-56\,°C$.

The variability of the heterogeneous ice nucleation onsets measured with the CFDCs could originate from the different aerosol particle generation methods and thermodynamic conditions of the chambers in which the particles were suspended. Indeed, Zuberi et al. (2001) investigated the heterogeneous ice nucleation ability of aqueous particles with inclusions of crystalline ammonium sulfate and found that the morphology of the solid component (i.e. composed of several microcrystals or of a few larger crystals) can significantly change the critical ice saturation ratio at which ice nucleation occurs. However, more systematic studies are needed to better constrain the source of the measured variability, i.e. if it has an instrumental origin or if the aerosol generation method influences the morphology and ice nucleation ability of the crystalline ammonium sulfate particles.

For some of the measurements, the ice nucleation onset conditions measured with the CFDCs and with AIDA expansion cooling experiments (dashed lines in Figure 3.15) agree within the respective errors. However, a systematic offset between the two techniques is visible, with higher ice saturation ratio onsets measured by the CFDCs (see Figure 3.16). The difference in the median ice saturation ratio onsets measured with the CFDC and AIDA ranges from 0.07 to 0.2. A comparable offset between INKA and AIDA results was already reported by Wagner et al. (2020) with reference to the heterogeneous ice nucleation ability of solid ammonium nitrate particles.
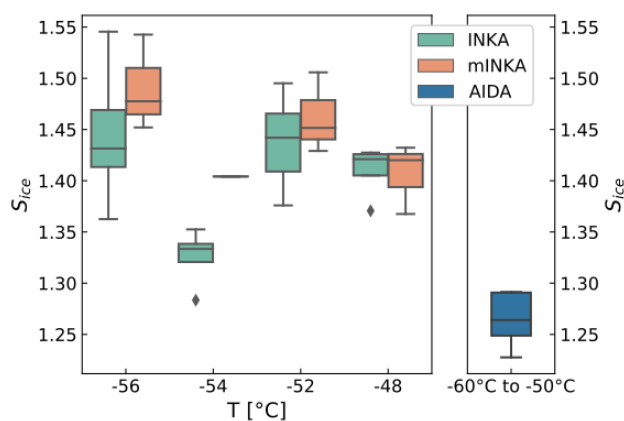
Figure 3.16: Distribution of the ice nucleation onsets measured in the CFDCs and AIDA expansion cooling experiments shown in Figure 3.15. The box shows the quartiles of the data, the horizontal line inside the box is the median value of the distribution, and the whiskers extend to show the rest of the distribution. Outliers are shown with diamonds.

SUMMARY The results of the homogeneous freezing (panel a), deliquescence (panel b), and heterogeneous ice nucleation (panel c) experiments presented in the previous section are summarized in Figure 3.17. INKA results are reported with squares, mINKA data with circles, and literature data are shown in black. The solid black line indicates water saturation ($RH_w = 100\,\%$). The homogeneous freezing parameterizations for aqueous solution droplets from Koop et al. (2000) and for aqueous sulfuric acid particles from Schneider et al. (2021) are also shown. The black dashed line is the ammonium sulfate deliquescence relative humidity calculated with the Extended Aerosol Inorganic Model (E-AIM, Clegg et al., 1998). The parametrizations from Murphy and Koop (2005) (equations 3.5 and 3.4) are used to express the relative humidity with respect to liquid water as a function of the ice saturation ratio.

The CFDCs homogeneous freezing onsets, defined for a 0.1 % activated fraction, are shown in Figure 3.17a. Colors indicate different chemical composition of the particles (sulfuric acid or ammonium bisulfate) and AIDA thermodynamic conditions (see legend). The parametrization by Schneider et al. (2021), obtained from AIDA expansion cooling experiments, better represents the CFDCs data compared to the parametrization suggested by Koop et al. (2000). However, most of the measured ice onsets are at higher ice saturation ratio than the parametrization by Schneider et al. (2021). Various motivations could explain the measured bias. First, the two measuring techniques (i.e., expansion cooling vs CFDC) have different critical nucleation rates, for AIDA experiments

$J_{crit}^{hom} = 10^8 - 10^{13} cm^{-3} s^{-1}$ (Möhler et al., 2003), while for the CFDCs $J_{crit}^{hom} = 10^{11} - 10^{12} cm^{-3} s^{-1}$. The smaller J_{hom}^{crit} of the AIDA experiments reflects in a lower limit of detection of the homogeneous freezing onset (see Figure 2.2), consistent with the lower values measured in the AIDA experiments. Additionally, the residence time inside the CFDCs at such low temperatures and high saturation ratios is $\approx 5 - 6 s$, while an AIDA expansion cooling experiment can last $\approx 100 - 600 s$. Therefore, in the CFDCs particles have less time to equilibrate to the instrument conditions and this, together with possible kinetic limitation of water diffusion at low temperatures, could delay the detected homogeneous freezing onset. Finally, as indicated by the exemplary errorbars shown in Figure 3.17, the error associated to the ice saturation ratio S_{ice} experienced by the aerosol particles becomes progressively larger at low temperature and high S_{ice}, due to the large wall temperature gradients required to achieve such conditions. The large temperature gradients also increase the buoyant flow in proximity of the warm wall, compromising the laminar condition of the flow (see Section 3.4.1 for more details). Black diamonds indicate the homogeneous freezing onset of H_2SO_4 solution droplets measured by Richardson (2009) with a CFDC similar to INKA (i.e., with the same geometry) and at comparable operational conditions (i.e., with a total flow rate of $10 \, stdL min^{-1}$). The values from the three CFDCs are consistent, with the results from Richardson (2009) also being slightly higher that the AIDA parametrization (Schneider et al., 2021) and largely offset from the homogeneou sfreezing parametrization from Koop et al. (2000). Richardson (2009) measured notably lower homogeneous freezing onsets when operating the CFDC with a total flow rate of $5 \, stdL \, min^{-1}$, and suggested that the longer residence time (from $\approx 8 s$ to $\approx 11 s$ at $T_w = -32 \, °C$ and $T_c = -49.5 \, °C$) allows the solution droplets to dilute more, thus to nucleate ice at a lower S_{ice}, and the ice crystals to grow larger, thus to be detected more easily, compared to the experiments performed with a higher flow rate. Nevertheless, by operating vertically oriented CFDCs with such low flow rates a significant buoyant flow could develop close to the warm wall and induce the transition from a laminar to a turbulent flow regime, especially at low temperatures and high S_{ice} values. Which is why all the experiments presented in this thesis have been performed with a total flow rate of $10 \, stdL min^{-1}$.

The deliquescence relative humidity (DRH) of ammonium sulfate particles results are shown in Figure 3.17b. Colors refer to two different experiments performed sampling the aerosol particles from the AIDA chamber held at two different thermodynamic conditions (see legend). DRH values measured by INKA and mINKA at different temperatures agree among them and with previous measurements performed at low temperatures (Braban et al., 2001; Fortin et al., 2002; Brunner and Kanji, 2021). The studies from Braban et al. (2001) and Fortin et al. (2002) are based on infrared spectroscopy experiments, while the study from Brunner and Kanji (2021) is based on CFDC measurements. For temperatures lower than $\approx -38 \, °C$ the data from the three CFDCs start to deviate from the E-AIM results, indicating a possible stronger temperature dependency of the ammonium sulfate DRH than predicted by the model. However, it's important to mention that the DRH values calculated with the E-AIM are expressed here in term of S_{ice} by using the parametrizations from Murphy and Koop (2005) (equations 3.4 and 3.5). A low bias in the parametrization used for the saturation vapor pressure of supercooled liquid water ($e_{sat, w}$), as suggested by Nachbar et al. (2019), would eventually lead to an underestimate of the deliquescence S_{ice} as retrieved from E-AIM, with a consequent shift of the dashed black line to higher ice saturation ratios.

Figure 3.17c shows the heterogeneous ice nucleation onsets already described in the previous section. Colors refer to different generation methods of the particles and different thermodynamic conditions at which the particles were suspended (see legend). Black symbols refer to literature data on the heterogeneous ice nucleation of crystalline ammonium sulfate particles obtained from different techniques and particles with different diameters. Despite the evident offset between the CFDC results and the other techniques and the variability in the ice onset conditions measured with the CFDCs, the clear distinction between the homogeneous and heterogeneous $INF - S_{ice}$ curves showed in the previous sections prove the validity of this techniques in low-temperature ice nucleation measurements.

INKA has already been operated in several experimental campaigns and compared to other instruments and techniques at different working conditions, resulting in a good agreement with the other ice nuclei counters (DeMott et al., 2018; Hiranuma et al., 2019). These results indirectly also validate mINKA results.
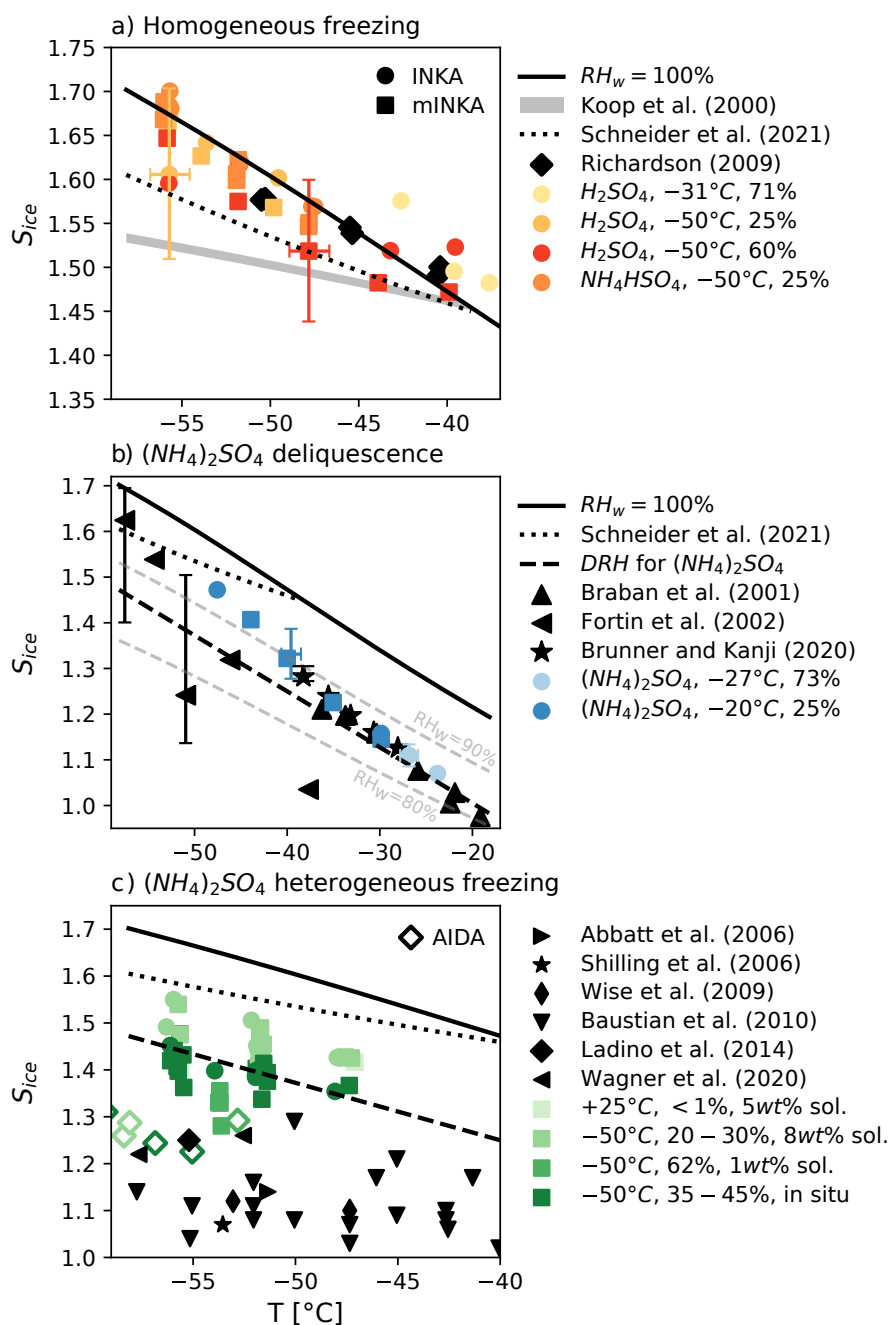
Figure 3.17: Summary of the proof of concept studies. Literature results are shown in black. The black solid line indicates water saturation, black dashed line is the DRH of ammonium sulfate (AS) modeled with the E-AIM (Clegg et al., 1998). The gray shaded area corresponds to the homogeneous freezing onset of aqueous solution droplets (Koop et al., 2000). The black dotted line is the parametrization for the homogeneous freezing of sulfuric acid solution droplets by Schneider et al. (2021). **a)** Ice onsets of homogeneous freezing of solution droplets. Colors indicate different particle chemical composition and AIDA thermodynamic conditions (see legend). **b)** DRH of crystalline AS particles. Colors refer to different thermodynamic conditions at which the aerosol particles were suspended (see legend). **c)** Heterogeneous freezing ice onsets (for INF = 0.1 %) for crystalline AS particles. Colors refer to different generation methods of the particles and different thermodynamic conditions at which the aerosol particles were suspended (see legend).

4 AMMONIATED SULFATE PARTICLES

4.1 INTRODUCTION

Aqueous sulfuric acid (H_2SO_4) is a key component in upper tropospheric aerosol particles. It originates from the oxidation of sulfur dioxide (SO_2) via both gas- and aqueous-phase processes. SO_2 sources are both natural (e.g., from volcanic eruptions and oxidation of dimethyl sulfide) and anthropogenic (e.g., from fossil fuel combustion). Since the 1980s, policies to reduce anthropogenic SO_2 emissions have led to a decrease of its atmospheric concentrations. Anthropogenic activities have substantially modified the nitrogen cycle (Erisman et al., 2008), leading to an increase of about 20% of the ammonia concentration in the Northern hemisphere over the last decades (e.g., Warner et al., 2017).

Based on the relative abundance of gas phase sulfuric acid and ammonia, particles with different ammonium-to-sulfate ratios (ASR), and thus with different physical-chemical properties, can form in the atmosphere. In particular, three different salts can form in the $H_2SO_4/NH_3/H_2O$ system: ammonium bisulfate (AHS, NH_4HSO_4, $ASR = 1.0$), letovicite (LET, $(NH_4)_3H(SO_4)_2$, $ASR = 1.5$), and ammonium sulfate (AS, $(NH_4)_2SO_4$, $ASR = 2.0$). However, the temporal and spatial distribution of ammonia sources as well as atmospheric processing of aerosol particles likely result in aerosol populations with a range of compositions (i.e., ammonium-to-sulfate ratios) rather than uniform stoichiometry.

As inorganic salts, ammoniated sulfate particles can be found in the atmosphere in solution or crystallized form. It is important to determine the phase state of the particles to evaluate their direct radiative effect, heterogeneous reaction rates, and contribution to ice nucleation. Once effloresced, ammonium sulfate particles are solid up to high relative humidities ($\approx 85\%$ at about $-30\,°C$) and can thus be found in a crystalline state in the upper trosposphere, where they can initiate cirrus cloud formation via heterogeneous ice nucleation (Abbatt et al., 2006). A few studies have investigated the thermodynamic properties of partially neutralized particles (i.e. with $ASR < 2.0$) at room temperature (e.g., Spann and Richardson, 1985; Tang and Munkelwitz, 1994; Schlenker et al., 2004; Schlenker and Martin, 2005), but low temperature studies of the $H_2SO_4/NH_3/H_2O$ system relevant for upper tropospheric conditions are still missing. A detailed description of the thermodynamic behavior of the system investigated in this chapter and of the potential role of inorganic salts in cirrus cloud formation can be found in Section 2.4.

This chapter focuses on the crystallization behavior, phase state, and ice nucleation ability at cirrus cloud conditions ($T < -38\,°C$) of ammoniated sulfate particles with $1.0 \leqslant ASR \leqslant 2.0$. A summary of the performed experiments is provided in Table 4.1. The first series of experiments ($1-8$) investigated particles generated from aqueous solutions with pre-defined ammonium-to-sulfate ratios. Similarly to the experimental procedure of Schlenker et al. (2004), the crystallization behavior of particles generated from bulk solutions was measured by exposing the particles to a defined relative humidity history. The aqueous solution droplets, generated with a nebulizer at room temperature and $RH_w = 100\%$, were first exposed to low relative humidity conditions in a diffusion dryer ($RH_w \approx 3\%$) and then to the AIDA cloud chamber at low temperature ($-50\,°C$) and intermediate relative humidity ($RH_w \approx 35\%$), which is clearly below the deliquescence relative humidity of the particles (see Figure 2.10). Thanks to the hysteresis behavior in the water uptake of inorganic salts, particles that eventually crystallize at low RH_w in the injection line remain in a solid state at the final intermediate RH_w in the AIDA chamber. The low temperature deliquescence behavior and ice nucleation ability of the particles were investigated by means of expansion cooling experiments in the AIDA chamber and with humidity scans with two continuous flow diffusion chambers (INKA and mINKA).

The final experiment 9 was designed to simulate the neutralization process at upper tropospheric conditions in the AIDA chamber ($-50\,°C$, $RH_w = 25\%$). For this experiment, aqueous sulfuric

acid droplets were injected into the AIDA chamber, and then gradually neutralized by injecting gas-phase ammonia. Changes in the chemical composition and phase state of the particles were measured by infrared spectroscopy and light scattering depolarization measurements. During the neutralization procedure, the ice nucleation ability of the particles was probed with repeated ice saturation ratio scans performed at $-52\,°C$ and $-56\,°C$. Two AIDA expansion cooling experiments were also performed to measure the ice nucleation ability of partially and fully neutralized particles.

The description of the AIDA facility and of the standard experimental setup can be found in Section 3.2 and will only briefly be mentioned here. In the following, the preparation and characterization of the aerosol particles are described. Section 4.3 and 4.4 report the experimental procedure and results on the crystallization, deliquescence and ice nucleation ability of particles derived from aqueous bulk solutions with pre-defined ammonium-to-sulfate ratios. Finally, the in situ neutralization experiment is introduced and commented in Section 4.5.

Table 4.1: Summary of the experiments performed with ammonium-sulfate particles and main parameters of the aerosol particle populations. ASR is the ammonium-to-sulfate ratio, RH_w^{inj} is the relative humidity in the aerosol injection line, T and RH_w correspond to the conditions inside the AIDA chamber before the start of the expansion cooling experiments. ρ is the density of the particles calculated with the E-AIM (Clegg et al., 1998) at the thermodynamic conditions of the AIDA chamber by forcing the phase state and composition of the particles to the observed one. The listed solid and liquid phases correspond to the composition of the particles upon injection in the AIDA chamber as determined by infrared spectroscopy. AHS: ammonium bisulfate; LET: letovicite; AS: ammonium sulfate.

Exp.	ASR	RH_w^{inj} [%]	T [°C]	RH_w [%]	ρ [g cm^{-3}]	solid phase	liquid phase
1	1.0	$\leqslant 1$	-50	37	1.59	—	Yes
2	1.1	$\leqslant 1$	-51	31	1.78	AHS+LET	Yes
3	1.2	$\leqslant 1$	-50	38	1.78	AHS+LET	—
4	1.35	≈ 18	-50	31	1.78	AHS+LET	—
5	1.5	≈ 3	-51	36	1.77	AHS+AS and LET	—
6	1.6	≈ 3	-51	36	1.77	LET+AS	—
7	1.8	≈ 3	-50	32	1.77	LET+AS	—
8	2.0	$\leqslant 1$	-51	36	1.77	AS	—
9	$0 \to 1.9$	$\leqslant 1$	-51	25	1.45	AHS+LET$\to$LET$\to$AS	Yes

4.2 AEROSOL PREPARATION AND CHARACTERIZATION

For experiments $1-8$, particles were generated with an ultrasonic nebulizer (see Section 3.2.2) from bulk solutions of predefined chemical composition. The aqueous solutions were prepared by dissolving different amounts of ammonium sulfate and ammonium bisulfate in ultra-pure water to obtain overall $8\,wt\%$ solute concentrations with defined ammonium-to-sulfate ratios (ASR, see Table 4.1). A carrier flow of dry synthetic air ($f = 5\,L\,min^{-1}$) was used to inject the aerosol particles into the AIDA chamber.

The crystallization behavior of the particles was investigated by following the experimental procedure used by Schlenker et al. (2004). The generated aqueous solution aerosols were first exposed to low relative humidity conditions by passing them through a series of diffusion dryers before injection to the AIDA chamber. To assess whether the particles crystallized at low relative humidity in the injection line, the relative humidity in the AIDA chamber was kept at an intermediate value below the expected partial deliquescence relative humidity (PDRH) of the particles (about 40% at room temperature, see Section 2.4). However, to also probe the ice nucleation ability of those particles in expansion cooling experiments, a minimum relative humidity is necessary to reach high ice supersaturation during the experiments. The AIDA chamber was thus prepared at $-50\,°C$ and about 35% relative humidity with respect to liquid water (see Table 4.1).

At low temperature it is difficult to accurately control the relative humidity in the AIDA chamber because its humidification is achieved by adding pure water vapor for a few seconds from a heated

water reservoir. When this procedure led to a too low relative humidity the diffusion dryers in the injection line were removed to increase the chamber relative humidity by injecting more humid air together with the aerosol particles. This was the case for experiment 4.

The water vapor pressure e_{inj} the aerosol particles were exposed to in the injection line at 25 °C was calculated from the variation in the water vapor pressure Δe (from the in situ TDL APicT data) and the total volume of injected air (V_{inj}):

$$e_{inj} = \Delta e \frac{V_{AIDA}}{V_{inj}} = \Delta e \frac{V_{AIDA}}{f \cdot \Delta t}$$

$$RH_w^{inj} = \frac{e_{inj}}{e_{s,w}(25\,°C)}$$

with $V_{AIDA} = 84\,300\,L$, $f = 5\,L\,min^{-1}$, and the injection time Δt in minutes. The calculated RH_w^{inj} values are reported in Table 4.1. During experiment 4, the diffusion dryers were removed to inject more humid air to increase the relative humidity in the AIDA chamber, resulting in a relative humidity in the injection line of about 18 %. However, that relative humidity value was sufficient to completely crystallize the particles with an ASR = 1.35, as shown by their infrared spectrum.

For the in situ neutralization experiment (experiment 9), sulfuric acid (SA) solution droplets were generated as described in Section 3.2.2. In brief, a dry and particle-free synthetic air flow is saturated with gas-phase sulfuric acid by flowing over a heated liquid sulfuric acid reservoir. Homogeneous nucleation and subsequent condensation growth of SA particles is then induced by the cooling of the flow to ambient temperature. The final particle diameter is regulated by adjusting the temperature of the reservoir and the flow rate of the carrier flow. When injected into the cold AIDA chamber, the gas-phase sulfuric acid remaining in the aerosol flow caused the nucleation of further aerosol particles. However, once neutralized with ammonia, those small particles (usually with diameter < 30 nm) are not expected to contribute to the heterogeneous ice nucleation activity of the whole population (with median diameter $\approx$ 1 μm), or represent a negligible fraction due to their small total surface area.

The normalized particle number size distributions measured by an aerosol particle sizer (APS) as a function of the volume equivalent diameter D_{ve} are shown in Figure 4.1. To convert the particle aerodynamic diameter to the volume equivalent diameter (see section 3.1 for more details), a shape factor $\chi = 1.0$ was used for fully or partially liquid particles, while $\chi = 1.1$ was chosen for crystalline particles. The density values used for the diameter conversion of the different particles are reported in Table 4.1. As shown in the next section, ammonium bisulfate particles (experiment 1) did not crystallize and remained in a supersaturated liquid state in the AIDA chamber (as also shown by Cziczo and Abbatt, 2000; Schlenker et al., 2004). The equilibrium concentration and density at the AIDA chamber conditions for the aqueous particles of experiments 1 and 9 (with sulfuric acid) were calculated with the Extended Aerosol Inorganic Model (E-AIM, Clegg et al., 1998). The median diameter of the particles was determined with a log-normal fit to the measured size distribution, yielding similar count median diameters in the narrow range $0.91 - 0.99$ μm for all the experiments.

After injection into the AIDA chamber, the phase state of the particles was measured with the SIMONE instrument (Schnaiter et al., 2012) and by means of a Fourier transform infrared (FTIR) spectrometer[1] (Wagner et al., 2006). In the infrared spectra, the intensity and position of specific absorption bands allow to infer the water content, phase state, and chemical composition of the particles (Onasch et al., 1999; Schlenker et al., 2004; Zawadowicz et al., 2015). The SIMONE instrument measures the intensity of the linearly polarized laser light ($\lambda = 488$ nm) scattered by the aerosol particles in the forward (2°) and backward (178°) directions. In the backward direction, the scattered light intensity is detected for the components parallel and perpendicular to the polarization plane of the incident laser light, so that the linear depolarization ratio of the scattered light can be determined. Non-spherical and inhomogeneous particle morphologies can induce a change of the incident polarization state of the laser light, thereby causing a non-zero value for the depolarization ratio. In contrast, homogeneously mixed, spherical aqueous solution droplets show a depolarization ratio of zero.

---

1 FTIR data collection and analysis were performed by Dr. Robert Wagner.
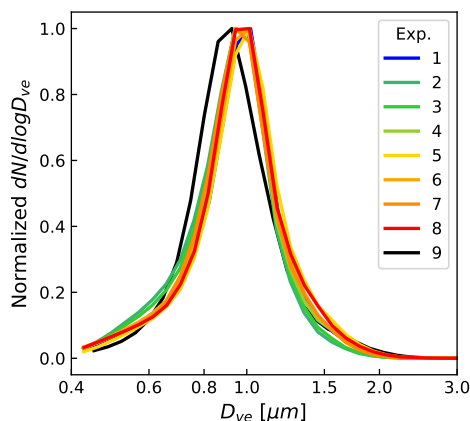
Figure 4.1: Normalized particle size distributions measured with an Aerodynamic Particle Sizer (APS) as a function of the volume equivalent diameter. Particles from experiments 1 to 8 (colored lines) were generated from bulk solutions with an ultrasonic nebulizer, particles from experiment 9 (black line) were generated from sulfuric acid gas-to-particle conversion outside of the AIDA chamber. All the distributions are characterized by a similar median diameter in the range $0.91 - 0.99\,\mu$m.

As indicated in Table 4.1, only particles with an ammonium-to-sulfate ratio (ASR) lower or equal to 1.1 were fully or partially liquid after injection in the AIDA chamber (experiments 1, 2, and 9). Ammonium bisulfate particles (AHS, experiment 1) showed a depolarization ratio comparable to the background value observed for spherical particles ($\approx 4\,\%$) and revealed liquid water signatures in the FTIR spectra (not shown), indicating that the salts did not crystallize during the few seconds residence time in the injection line at $RH_w \leqslant 1\,\%$ or when suspended for longer times at the AIDA chamber conditions. This observation is in agreement with previous studies, in which liquid ammonium bisulfate particles did not crystallize homogeneously at temperatures between $25\,^{\circ}$C and $-35\,^{\circ}$C, and relative humidity down to $2\,\%$ (Cziczo and Abbatt, 2000; Schlenker et al., 2004).

After injection in the AIDA chamber at $RH_w \approx 30\,\%$, particles with an ASR of 1.1 (experiment 2) showed a high depolarization value ($\approx 9\,\%$), indicative of an inhomogeneous morphology, but at the same time also contained liquid water signatures in the infrared spectrum. The particle population could thus have been composed of internally or externally mixed solid/liquid particles. The depolarization ratio of the particles steadily increased to about $15\,\%$ while suspended in the AIDA chamber for about $1.5\,$h, suggesting that the liquid component gradually crystallized at the AIDA conditions. Probably, the small fraction of letovicite present in the particles crystallized homogeneously in the injection line or at the low temperature of the AIDA chamber and then slowly triggered the heterogeneous crystallization of the AHS component at the AIDA chamber conditions. A similar heterogeneous crystallization behavior was observed by Schlenker and Martin (2005) in AHS/LET particles but for particles with a higher ASR (1.4). The crystallization behavior of particles with an ASR = 1.1 was already investigated by Schlenker and Martin (2005) at $20\,^{\circ}$C. In their study, the particles were initially exposed to $RH_w = 60\,\%$, then to $3\,\%$ for about 3 minutes, and finally to $30\,\%$, condition at which the particles were still completely aqueous.

For particles with an ASR $\geqslant 1.2$, efflorescence already occurred in the injection line and completely solid particles were detected in the AIDA chamber. Rosenoern et al. (2008) observed that aqueous LET particles (ASR = 1.5) crystallized as an external mixture of pure LET and internally mixed AS and AHS particles. The infrared spectra (not shown) and the deliquescence behavior (described in the next section) of the particles with an ASR = 1.5 (experiment 5) suggest an externally mixed particle population similar to the one observed by Rosenoern et al. (2008).

In experiment 9, the gradual neutralization of aqueous sulfuric acid particles was simulated by first adding the acidic aerosol particles to the AIDA chamber at $-51\,^{\circ}$C and $RH_w \approx 25\,\%$, and then slowly injecting gas-phase ammonia ($\approx 2\%$ NH$_3$ in air). To completely neutralize the particles (i.e., to obtain an ASR ≈ 2), excess of ammonia was injected in the chamber during two injection periods, corresponding to a total concentration of about $80\,$ppb. The evolution of the chemical composition of the particles was monitored with FTIR spectra, and indications of their phase state was also provided by the SIMONE instrument. The ice nucleation ability of the particles was continuously

monitored with ice saturation ratio scans in the CFDCs, and with two AIDA expansion runs. More details on the experimental procedure and the results are given in Section 4.5.

4.3 LOW–TEMPERATURE DELIQUESCENCE BEHAVIOR

Understand at which thermodynamic conditions aerosol particles are solid and when they start to absorb water is not only important to assess their direct radiative effect (Martin et al., 2004), but also to identify which ice nucleation mechanism they can promote (Wise et al., 2012). At cirrus cloud conditions, solid or internally mixed solid/liquid particles can promote heterogeneous ice nucleation at lower ice saturation ratios compared to aqueous solution droplets that only freeze homogeneously.

The deliquescence relative humidity (DRH) of the particles was determined with three different techniques: infrared spectroscopy, laser light scattering and depolarization, and by measuring the hygroscopic growth of the particles with optical particle counters (OPCs). The appearance of water signatures in the infrared spectra of the particles, as well as changes in the position and shape of specific absorption peaks, indicate when particles start to take up water. The hygroscopic growth of the particles by the water uptake also leads to an increased scattering cross section, which is detected in the optical particle counters and with laser light scattering measurements (SIMONE instrument).

In the AIDA chamber, aerosol particles can be exposed to increasing relative humidity by performing expansion cooling experiments (see section 3.2.3). All experiments were started at a temperature of $\approx -50\,°C$ and a relative humidity with respect to liquid water of $\approx 35\,\%$. Similar cooling rates were used to obtain comparable thermodynamic trajectories $(T - RH_w)$. The peak relative humidity that can be reached during the expansion cooling experiments depends on the microphysical processes taking place. Strong heterogeneous freezing modes, i.e. with a large number of nucleated ice crystals, might limit the peak RH_w to a lower value, because depositional ice growth depletes the water vapor supersaturation. In the continuous flow diffusion chambers (CFDCs), instead, new aerosol particles are continuously sampled and exposed to defined relative humidity conditions at constant temperature (see Section 3.4). Due to the ice-coated walls, the lowest relative humidity in the CFDCs is forced to ice-saturated conditions (corresponding to $RH_w \approx 60\,\%$ at $-50\,°C$) and particles with a lower deliquescence relative humidity will immediately take up water upon entering the instrument. Ideally, CFDCs have no upper limit for the achievable relative humidity, as this parameter only depends on the applied temperature difference between the two walls.

At room temperature, the partial deliquescence relative humidity is expected at $RH_w \approx 40\,\%$ for particles with $1.0 < ASR < 1.5$, and at $RH_w \approx 70\,\%$ for particles with $1.5 < ASR < 2.0$ (see Section 2.4). Particles with $ASR < 1.5$ are thus expected to start to take up water at ice sub-saturated conditions and to have a liquid component at ice saturated conditions. The deliquescence behavior of these particles was thus tested in AIDA expansion experiments, where the initial relative humidity can be set below $40\,\%$. Particles with higher ASR, instead, can efficiently nucleate ice below their deliquescence relative humidity (as shown in the next section), thus limiting the peak relative humidity during the AIDA experiments to a value below the deliquescence relative humidity of the particles that have not yet acted as ice nucleating particles. The deliquescence behavior of these particles was investigated with the CFDCs. AIDA expansion runs and CFDC saturation scans are thus two complementary techniques that allow to investigate the deliquescence behavior of aerosols particles in a wide range of upper tropospheric conditions.

Three representative AIDA experiments performed with particles with ammonium-to-sulfate ratios equal to 1.0 (experiment 1), 1.2 (experiment 3), and 1.6 (experiment 6) are shown in Figure 4.2. Time series of the forward scattering intensity (I_{for}, panels 1, black curves), the depolarization ratio (δ, panels 2, green curves), and the concentration in three custom-defined size bins of the welas OPC 1 (panels 3, purple traces) are shown as a function of the relative humidity in the AIDA chamber during the expansion experiments. As already mentioned, ammonium bisulfate particles (experiment 1) did not crystallize and were aqueous at the AIDA chamber conditions. The initial depolarization ratio had a small background value of $4\,\%$ (panel a2) which is typically observed for spherical particles, and the particles immediately started to take up water when the relative humid-

ity increased. This is shown by the continuous increase of the forward scattering intensity (panel a1) and by the increasing concentration in the OPC size channels corresponding to growing aerosol particles ($1.26 - 1.58\,\mu m$ in violet, and $1.58 - 2.00\,\mu m$ in pink, panel a3). The decreasing concentration measured in the OPC size bin $1.00 - 1.26\,\mu m$ (panel a3, purple trace) is the combined effect of the shift of the particle size distribution to larger sizes and the dilution of the total aerosol concentration due to the evacuation of the AIDA chamber. As the relative humidity further increased, the homogeneous freezing threshold of solution droplets was reached ($\approx 90\,\%$) and aspherical ice crystals formed, leading to a sharp increase in the depolarization value.

Experiment 3, shown in Figure 4.2b, was performed with particles with ASR = 1.2, but it is representative for all the experiments performed with particles with $1.1 \leqslant$ ASR < 1.5 (composed of AHS+LET). As shown by the high depolarization ratio ($\approx 14\,\%$, panel b2), the particles were initially solid in the AIDA chamber. At a relative humidity of about $60\,\%$, the forward scattering intensity I_{for} (panel b1) and the bin-resolved concentration measured by the OPC (violet and pink traces in panel b3) exceeded their initial values by 2 standard deviations, indicating that the fraction of AHS in the particles had deliquesced and the particles had started to take up water. At the same relative humidity, the depolarization ratio δ (panel b2) showed an oscillation, probably due to a re-arrangement of the particle morphology, followed by a steady decrease, indicating that the particles were approximating a more symmetrical geometry. Finally, the sharp increase in I_{for} and δ at $RH_w \approx 80\,\%$ indicate the onset of ice nucleation.

Experiment 6, shown in Figure 4.2c, was performed with particles with ASR = 1.6, but it is representative for all experiments performed with particles with $ASR \geqslant 1.5$ (composed of pure LET, pure AS or LET+AS). These initially solid particles (depolarization at $\approx 15\,\%$, panel c2) did not show any water uptake before ice nucleation took place at $RH_w \approx 80\,\%$ (as seen by the increase in I_{for}). Since a large fraction of particles nucleated ice in the expansion cooling experiments performed with LET, LET+AS, and AS, the ice supersaturation inside the AIDA chamber was quickly depleted and the deliquescence threshold of the particles could not be exceeded anymore.

Similarly to what reported by (Rosenoern et al., 2008), particles generated from aqueous solution with the exact letovicite stoichiometry ($ASR = 1.5$, experiment 5) crystallized as an external mixture with the majority of the particles composed of pure LET and a minor fraction formed of AHS+AS. Indeed, a small drop was measured in the depolarization ratio (from $15\,\%$ to $13\,\%$) at about $RH_w = 55\,\%$. Likely, this was originated by the deliquescence of the ammonium bisulfate component in the AHS+AS crystalline particles. Due to the small fraction of particles that crystallized as AHS+AS, their deliquescence was not observed in the forward scattering intensity measurements or in the OPC data.

The measured partial deliquescence relative humidities, as determined by the increase in the forward light scattering intensity (2 standard deviations above its initial value), are summarized in Figure 4.4 as a function of the ammonium-to-sulfate ratio of the particles.

Typical deliquescence measurements performed with INKA and mINKA are presented in section 3.4.7. In brief, the partial or initial deliquescence of the particles is measured during relative humidity scans as a sudden increase in the number concentration of particles detected at larger diameters by the optical particle counter of the instrument. The experiments presented in this section were performed at the nominal temperature of $-52\,°C$, thus limiting the initial relative humidity to about $60\,\%$. Figure 4.3 shows the particle number concentration measured in the range $0.84 - 0.94$ V by the OPCs mounted at the outlet of INKA (panels a and c) and mINKA (panels b and d) [2]. The number concentration of the detected particles is shown as a function of the relative humidity. The deliquescence relative humidity is determined when the concentration in selected size bins exceeds the initial value by 2 or 3 standard deviations (see Section 3.4.7 for more details).

The results for particles with $ASR < 1.5$ are shown in Figures 4.3a and 4.3b. The continuous water uptake measured in mINKA (panel b) indicates that all these particles contained a liquid fraction already at the lowest achievable relative humidity ($RH_w \approx 60\,\%$). As described in Section 3.4.2, the walls in the lower part of INKA are kept at the same temperature (so-called evaporation section), and, although the particles are exposed to increasing relative humidity in the upper section of the instrument, they always re-equilibrate to ice saturated conditions (thus to a lower relative humidity) in the evaporation section before exiting the instrument. In mINKA, instead, the walls are kept

---

2 A detailed description of the custom-modified Climet OPCs can be found in Section 3.4.3
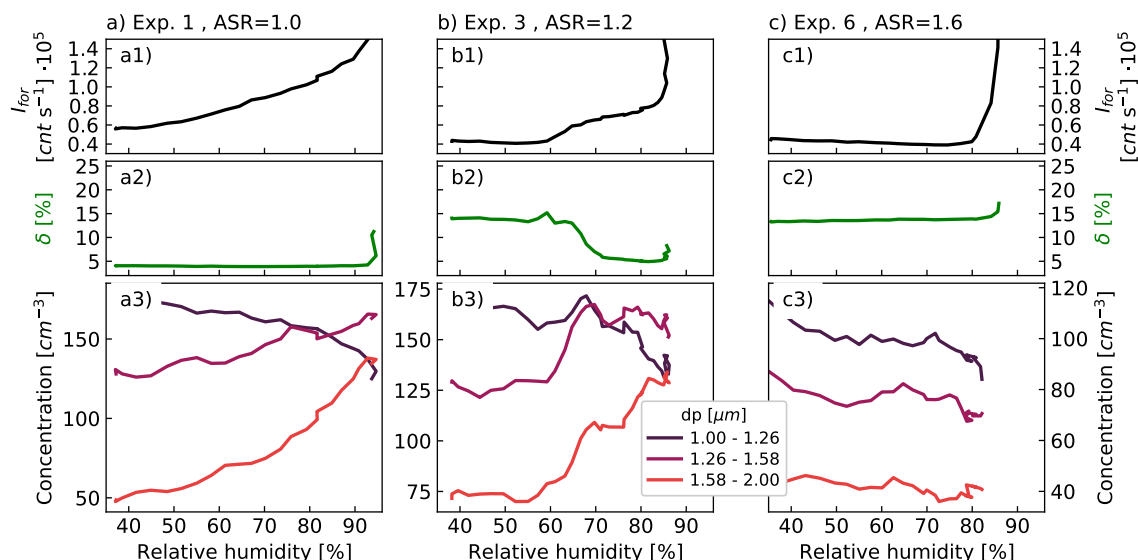
Figure 4.2: Detection of the deliquescence relative humidity with respect to liquid water in three AIDA expansion cooling experiments. Panels 1 and 2 show the forward scattering intensity I_{for} and depolarization ratio δ from the SIMONE instrument. Panels 3 show the aerosol concentration measured by the welas OPC 1 in three custom-defined size bins. **a)** ammonium bisulfate (AHS) particles (experiment 1, ammonium-to-sulfate ratio ASR equal to 1.0). **b)** Internally mixed AHS and letovicite (LET) particles (experiment 3, ASR = 1.2). **c)** Internally mixed LET and ammonium sulfate particles (experiment 6, ASR = 1.6). Particles from experiment 1 show a continuous water uptake with increasing R_w, in experiment 2 particles start to uptake water (PDRH) at about 60 %, while no deliquescence is observed during experiment 6.

at different temperatures for their entire length, and the particles experience a constant saturation along the entire instrument. The presence of the evaporation section explains the different behavior observed in INKA for particles with a liquid component (panel a). The sharp increase observed in INKA at $RH_w = 100\%$ in INKA corresponds to the homogeneous freezing of the solution droplets and will be addressed in the next section.

Particles with an $ASR \geqslant 1.5$ (Figure 4.3c and d), instead, appeared to be crystalline at the initial relative humidity ($RH_w = 60\%$), and started to take up water only at $RH_w \approx 90\%$.

The deliquescence relative humidity values measured in the AIDA and CFDCs experiments are summarized in Figure 4.4 as a function of the ASR of the particles (markers). The results from the Extended Aerosol Inorganic Model (E-AIM, Clegg et al., 1998) computed at $-50\,°C$ are also shown (solid lines). To correctly interpret the model results, it is important to highlight that the model does not allow, by default, supersaturated conditions. As soon as a solution becomes supersaturated with respect to a solid phase (i.e. when RH < DRH), the model forces its crystallization. However, aerosol particles are often found in supersaturated conditions and their homogeneous crystallization only occurs at a high supersaturation[3]. To simulate supersaturated conditions in the E-AIM, it is possible to prevent the formation of specific solids, e.g. the formation of ice in aqueous solution droplets at low temperature and ice supersaturated conditions. For all the model simulations presented here, the formation of solid sulfuric acid hydrates ($H_2SO_4 \cdot nH_2O$) was inhibited, as previous AIDA studies did not show the formation of those crystals even at temperatures as low as $\approx -80\,°C$ (Möhler et al., 2003; Wagner et al., 2006).

For an $ASR = 1.0$, the E-AIM predicts the particles to be composed of solid ammonium bisulfate (AHS) up to a relative humidity of $RH_w = 38\%$ (green line in Figure 4.4). Then, letovicite (LET) immediately precipitates from the deliquesced salt, because the relative humidity is still below the DRH of LET (DRH $\approx 80\%$ at $-50\,°C$). Solid AHS particles thus transforms into solid/liquid particles at 38 %, which then fully dissolve at $RH_w \approx 80\%$ (blue line). However, the formation of

---

3 see Section 2.4 for more details on the thermodynamic behavior of atmospheric inorganic salts
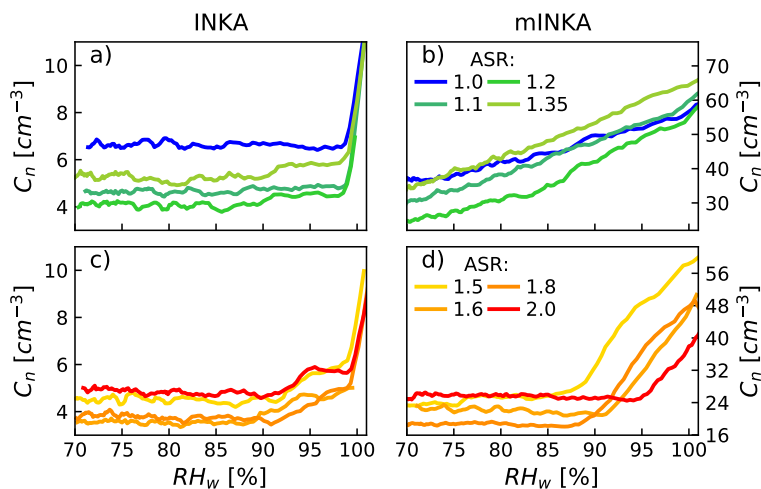
Figure 4.3: Deliquescence relative humidity measurements performed with INKA (panels a and c) and mINKA (panels b and d) at the nominal temperature of $-52\,^\circ$C. The aerosol number concentration measured in a selected size bin by the OPCs are shown as a function of the relative humidity. Particles with $ASR < 1.5$ already had a liquid component upon entering the instruments ($RH_w \approx 60\%$), particles with $ASR \geqslant 1.5$ were initially solid and deliquesced at $RH_w \approx 90\%$.

a solid component in the pure ammonium bisulfate particles was not observed in experiment 1, indicating that LET or AHS did not precipitate in the liquid solution, neither in the injection line (at $RH_w \leqslant 1\,\%$ and $25\,^\circ$C) nor in the AIDA chamber (at $RH_w = 37\,\%$ and $-50\,^\circ$C).

For particles with $1.0 < ASR < 1.5$, composed of AHS+LET, the model predicts that the particles start to take up water when the ammonium bisulfate component deliquesces at $RH_w = 38\,\%$ (green line), and that the particles are fully liquid at $RH_w \approx 80\,\%$ (blue line). The AIDA results for particles with the same ASR (squares in Figure 4.4) localize the start of the deliquescence at a higher relative humidity compared to the E-AIM results (at RH_w approx60 %).

In the E-AIM, particles with a stoichiometric composition (i.e., LET with $ASR = 1.5$ and AS with $ASR = 2.0$) are expected to deliquesce in only one step, while particles composed of LET+AS ($1.5 < ASR < 2.0$) show the partial and full deliquescence relative humidities in a very narrow humidity range at about 83 % (green and blue lines in Figure 4.4). The results from both CFDCs localize the deliquescence relative humidity at slightly higher relative humidities than predicted by the thermodynamic model.
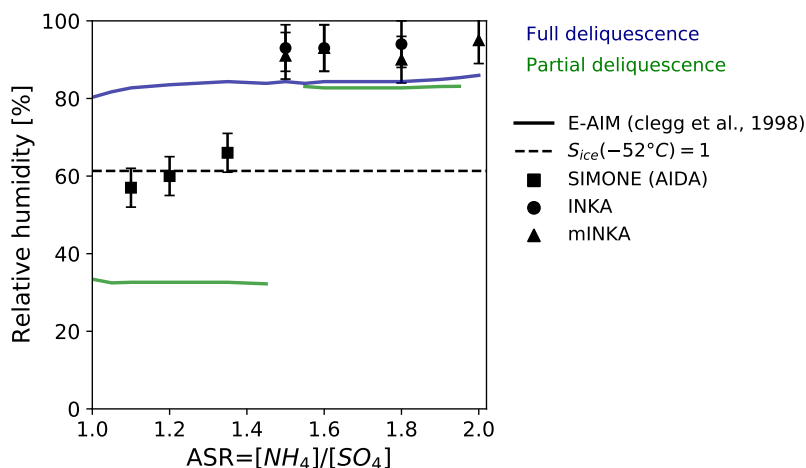
Figure 4.4: Summary of the deliquescence results from the AIDA expansion cooling experiments (squares) and the CFDCs relative humidity scans (circles and triangles for INKA and mINKA data, respectively). Results from the Extended Aerosol Inorganic Model (E-AIM, Clegg et al., 1998) are reported as solid lines. The partial and full deliquescence relative humidities are shown in green and blue, respectively. The AIDA results correspond to temperatures between $-55\,°C$ and $-60\,°C$, the CFDC measurements were performed at a nominal temperature of $-52\,°C$, and the model was evaluated at $-50\,°C$. The relative humidity corresponding to ice-saturation at $-52\,°C$ is indicated with a black dashed line.

4.4 ICE NUCLEATION MEASUREMENTS

The ice nucleation ability of the particles as a function of their ammonium-to-sulfate ratio (ASR) was probed in situ by means of expansion cooling experiments inside the AIDA chamber, and ex situ with two continuous flow diffusion chambers (CFDC) by sampling the aerosol particles from the AIDA chamber.

Exemplary time series of different variables during three AIDA expansion cooling experiments are shown in Figure 4.5. Here, experiment 1 investigated ammonium bisulfate (AHS) aqueous solution particles (Figure 4.5a), experiment 3 was performed with particles with an $ASR = 1.2$ composed of AHS and letovicite (Figure 4.5b), and experiment 6 was performed with particles with an $ASR = 1.6$ composed of letovicite and ammonium sulfate (Figure 4.5c). Time series of temperature (in red) and pressure (in black) inside the AIDA chamber are shown in upper panels; the ice saturation ratio from the in situ TDL measurements (APicT) are reported in middle panels (dark blue traces); the depolarization ratio δ from the laser light scattering instrument SIMONE is shown below (in green); the single particle data from the welas optical particle counters (OPC 1 and 2) are shown in lowest panels, left axis. Each blue dot in the lowest panels corresponds to an aerosol particle or ice crystal measured by the OPC at the corresponding optical diameter D. The fraction of ice-active aerosol particles (i.e., the ice nucleating fraction, INF) is shown in panels 4 (right axes, black trace). The three experiments are exemplary for the three different groups of particles investigated, namely with $ASR = 1.0$, $1.0 < ASR < 1.5$, and $ASR \geqslant 1.5$, corresponding to liquid, internally mixed liquid/solid, and fully solid particles at ice saturated conditions, respectively, as discussed in the previous section.

Liquid AHS particles (experiment 1, panels a) nucleated ice via homogeneous freezing at a high saturation ratio, with the onset (for an ice-active fraction of 0.1%) at $S_{ice} = 1.62$, as indicated by the vertical dashed line at $\approx 215\,s$ after the start of the expansion. The ice nucleation event is detected by the sharp increase of the depolarization ratio δ (panel a3) due to the formation of aspherical ice crystals, and by the appearance of the ice crystals in the OPC at large optical diameters (blue dots in panel a4).

Particles with an $ASR = 1.2$ (experiment 3, panels b) were completely solid at the initial conditions of the AIDA chamber ($RH_w = 38\,\%$), but the ammonium bisulfate component deliquesced at ice sat-

urated conditions (as described in the previous section and visible by the drop in the depolarization at $S_{ice} = 1$ in panel b3). At an ice saturation ratio of 1.47, about 315 s after the start of the expansion, a distinct mode of heterogeneously formed ice crystals appeared in the OPC records and induced an increase of the depolarization ratio.

Since the particles have a liquid component when the ice crystals form, the measured heterogeneous nucleation mode can be classified as immersion freezing on the not yet fully dissolved letovicite fraction. By further increasing the cooling rate, an additional increase of the ice saturation ratio was achieved, allowing to reach the homogeneous freezing threshold measured in experiment 1 (dashed horizontal lines at $S_{ice} = 1.62$ in panels 2). The homogeneous freezing mode appears as a second step in the ice-active fraction curve (second vertical line).

Particles with an $ASR = 1.6$ (experiment 6, panels c) composed of LET+AS were solid at the initial AIDA chamber conditions and only deliquesced at $RH_w \approx 90\%$, as measured with the CFDCs and shown in the previous section. At $S_{ice} \approx 1.3$, the first ice crystals were detected, reaching an ice-active fraction of 0.1% at $S_{ice} = 1.39$ (dashed vertical line). As the LET+AS particles were still solid when heterogeneous ice nucleation initiated, deposition or pore condensation and freezing must be the prevalent ice nucleation modes.

Figure 4.6 summarizes the ice activation curves, i.e. the ice nucleating fraction as a function of the ice saturation ratio, of the AIDA experiments for particles with ammonium-to-sulfate ratios from 1.0 to 2.0 (experiments 1 to 8 in Table 4.1). The ice nucleation results can be classified in three different groups, according to the ice nucleation mode taking place and to the ice nucleation efficiency of the aerosol particles. Particles with $ASR = 1.0$ are liquid and nucleate ice via homogeneous freezing, as shown by the sharp activation threshold at $S_{ice} = 1.62$ of the AHS particles (blue data). Particles with $1.0 < ASR < 1.5$ (green data) form internally mixed solid/liquid particles and can induce heterogeneous ice nucleation in the immersion freezing mode at a lower ice saturation ratio ($S_{ice} \approx 1.5$) compared to homogeneous freezing. Finally, particles with an $ASR \geqslant 1.5$ (yellow, orange, and red data) are solid up to high relative humidities and their ice nucleation onset (defined as the ice saturation ratio at which 0.1% of the particles are activated as ice crystals) shifts to much smaller ice supersaturation. With the fully neutralized ammonium sulfate particles ($ASR = 2$, red data) being the most ice-active ones in the $H_2SO_4/NH_3/H_2O$ system. These results clearly show that the degree of neutralization of ammonium-sulfate particles impacts their ice nucleation ability.

Figure 4.7 shows the ice nucleation results from INKA (panels a and c) and mINKA (panels b and d) at $-52\,°C$ (panels a and b) and $-56\,°C$ (panels c and d). Similarly to Figure 4.6, the ice nucleating fraction (INF) is shown as a function of the ice saturation ratio S_{ice}. The particle classification in three different groups according to their neutralization state (i.e., $ASR \leqslant 1$, $1.0 < ASR < 1.5$, and $ASR \geqslant 1.5$) and corresponding ice nucleation ability (i.e., homogeneous freezing, immersion freezing, and deposition and/or PCF), is also clearly visible in the CFDCs measurements.

Ammonium bisulfate particles (in blue) froze homogeneously, showing a sudden increase in the ice-active fraction of particles. The ice nucleation onsets, defined for an ice nucleating fraction of particles of 0.1% was measured at $S_{ice} \approx 1.60$ and $S_{ice} \approx 1.69$ at $-52\,°C$ and $-56\,°C$, respectively.

Particles with $1.0 < ASR < 1.5$ (green data) had a liquid component at ice saturated conditions (see previous section) and showed an intermediate ice nucleation ability. Similarly to the AIDA experiments, the two different ice nucleation modes, i.e. heterogeneous nucleation at low S_{ice} values and homogeneous freezing at higher S_{ice}, are well discernible also in the CFDCs measurements. As only a minor fraction of the aerosol particles initiated heterogeneous ice formation, the ice onsets for this group of particles is still in correspondence of the homogeneous freezing threshold for the aqueous ammonium bisulfate. Slightly lower values ($S_{ice} \approx 1.6$) were obtained only in the measurements performed with INKA at $-56\,°C$.

Particles with an ASR in the range $1.5 - 1.8$ showed the highest ice nucleation efficiency, with the ice nucleation onsets at $S_{ice} = 1.4 - 1.45$. Unlike in the AIDA results, the ammonium sulfate particles ($ASR = 2$, red curve) showed a similar or lower ice nucleation onset compared to particles composed of AS+LET or pure LET (orange and yellow curves, respectively). However, as reported in Section 3.4.7, a certain variability has been observed in the CFDCs results when comparing the heterogeneous ice nucleation ability of crystalline ammonium sulfate particles measured in several different experiments. The measured variability is shown in Figure 4.7 as red shaded area. The
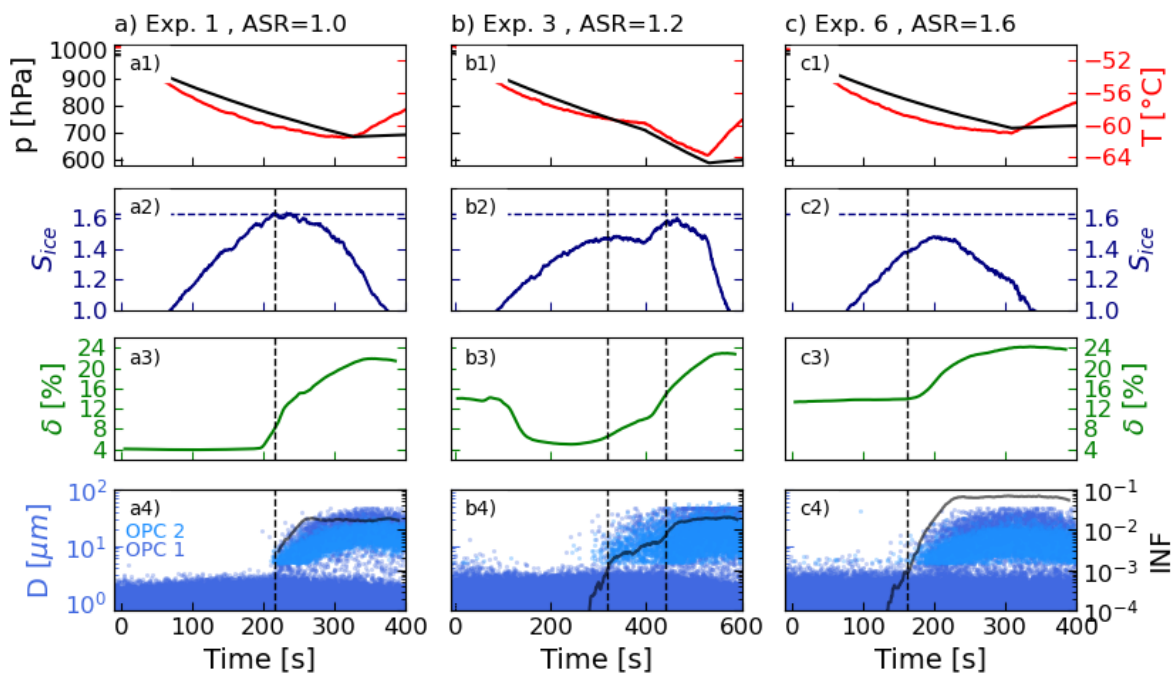
Figure 4.5: Time series of different AIDA records during three expansion cooling experiments performed with ammonium bisulfate particles (experiment1, panels a), mixed ammonium bisulfate (AHS) and letovicite (LET) particles (experiment 3, panels b), and mixed LET and ammonium sulfate (AS) particles (experiment 6, panels c). Panels 1 report pressure (black trace, left axes) and temperature (red trace, right axes) inside the AIDA chamber; panels 2 show the evolution of the ice saturation ratio S_{ice}; panels 3 present the depolarization ratio δ; panels 4 display the welas OPC single particle data on the left axes (each blue dot corresponds to an aerosol particle or ice crystal detected at the corresponding optical diameter) and the ice nucleating fraction (INF) on the right axes. Aqueous AHS solution particles with ASR = 1.0 formed ice via homogeneous nucleation at S_{ice} = 1.62 (vertical lines in panels a), particles with ASR = 1.2 formed ice via immersion freezing on the solid LET inclusions at S_{ice} = 1.47 (first vertical line in panels b) and via homogeneous freezing at a higher saturation ratio (second vertical lines), and particles with ASR = 1.6 induced heterogeneous ice nucleation via deposition or pore condensation and freezing on the solid LET+AS at S_{ice} = 1.39 (vertical lines in panels c).

ice nucleation ability of the ammonium sulfate particles investigated here fall in the lower range of expected conditions, with the ice nucleation onset at $S_{ice} \approx$ 1.50 and 1.54 at −52 °C and −56 °C, respectively.

For particles with a liquid component (i.e., with $1.0 < ASR < 1.5$), the INKA results are more robust than those from mINKA. The absence of the evaporation section in mINKA and the large size of the investigated particles makes it difficult to identify an appropriate ice threshold in the OPC data to distinguish between the large droplets and the small ice crystals. The ice threshold in the OPC data from mINKA was defined in order to definitely exclude any solution droplets, probably leading to an underestimation of the ice crystal concentration.
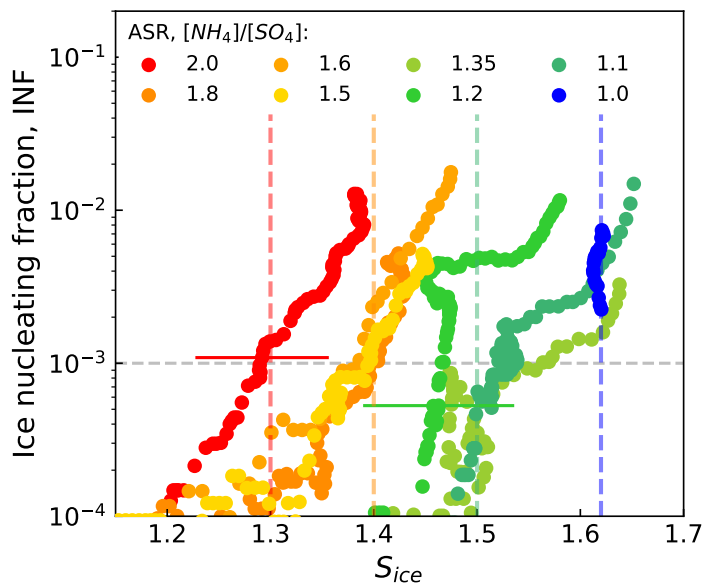
Figure 4.6: Ice nucleating fraction (INF) of aerosol particles as a function of the ice saturation ratio S_{ice} measured during the AIDA expansion cooling experiments. The horizontal line indicates the ice onset condition defined for an activation of 0.1% of the aerosol particles as ice crystals.
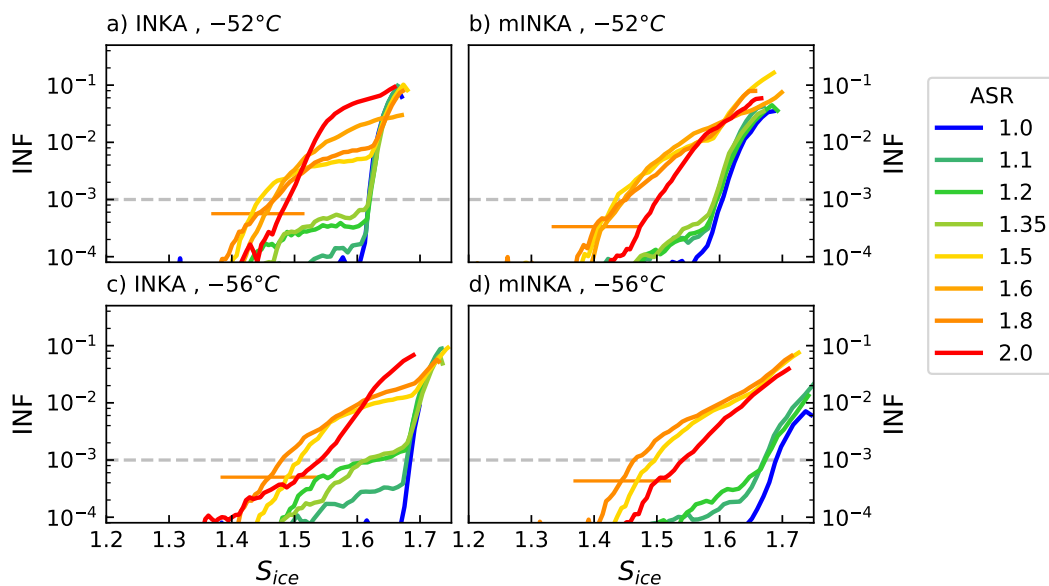
Figure 4.7: Ice nucleating fraction (INF) as a function of the ice saturation ratio S_{ice} for particles with ammonium-to-sulfate ratios (ASR) between 1.0 and 2.0 measured at $-52\,°C$ and $-56\,°C$ with INKA and mINKA. The red shaded area corresponds to the range of conditions at which INKA and mINKA measured the heterogeneous ice nucleation ability of crystalline ammonium sulfate particles (ASR = 2.0) during previous experiments.

4.5   IN SITU NEUTRALIZATION EXPERIMENT

To simulate the gradual neutralization process that sulfuric acid solution droplets may experience in the upper troposphere, an in situ neutralization experiment was performed in the AIDA chamber (experiment 9 in Table 4.1). The experiment time series is shown in Figure 4.8.

Sulfuric acid particles ($ASR = 0$) were injected in the AIDA chamber, followed by two periods of slow and steady injection of gas-phase ammonia (shaded areas in Figure 4.8a) to gradually neutralize the particles. The ice nucleation ability of the particles was measured every $\approx 30\,\mathrm{min}$ with the CFDCs and with two AIDA expansion cooling experiments performed at the end of each injection period of ammonia. Figure 4.8a shows the depolarization ratio δ (green trace, left axis) and the AIDA chamber relative humidity (blue trace, right axis) during the experiment. The initial depolarization value is consistent with a background value also observed for homogeneous, spherical particles (about 3 %). The two sharp increases in relative humidity and depolarization (at 13:15 and 18:15) indicate the two AIDA expansion cooling experiments. The average composition of the particles, in terms of their ammonium-to-sulfate ratio derived from infrared extinction spectra, is shown in Figure 4.8b. The ice saturation ratio scans performed with INKA (at $-56\,°C$) and mINKA (at $-52\,°C$) are shown in panels d and e, respectively. The S_{ice}-time trajectories of the CFDCs measurements are color-coded by the measured ice nucleating fraction. The black horizontal dashes mark the threshold of 0.1% aerosol particles activated as ice crystals. The ice onsets measured during the two AIDA experiments are also reported in panel d with black dashes (at about 13:00 and 18:00). The $INF - S_{ice}$ curves are reported in Figure 4.9 with the corresponding color of the circles in panels c and d.

The injected aqueous sulfuric acid particles induced ice nucleation predominantly at the homogeneous freezing threshold ($S_{ice} = 1.61$). However, as shown in Figure 4.9a and 4.9b, already during the first saturation scans both CFDCs detected a small heterogeneous ice nucleation mode, probably caused by an early uptake of background ammonia in the particles. The average particle composition at the end of the first ammonia injection period (at about 12:20) reached $ASR \approx 1.4$ and the particles were likely crystalline. The predominant crystalline state of the particles is inferred by the high depolarization ratio (about 8 %) and by the deliquescence behavior of the particles during the first AIDA expansion (not shown). Indeed, the particles did not take up water until the deliquescence relative humidity of ammonium bisulfate was reached ($RH_w \approx 55\,\%$). The ice nucleation measurements performed with the CFDCs just before the AIDA expansion (olive green lines in Figure 4.9a and 4.9b) revealed a pronounced heterogeneous ice nucleation mode, with a much lower ice onset compared to homogeneous freezing ($S_{ice} = 1.47$). A similar ice nucleation onset was measured during the first AIDA expansion experiment ($S_{ice} = 1.48$), shown with green squares in Figure 4.9a. Since the particles have a liquid component when the ice crystals form, the measured heterogeneous nucleation mode can be classified as immersion freezing, similarly to particles with comparable ASR and obtained from bulk solutions. The ice nucleation results for particles generated from bulk solutions with $ASR = 1.35$ (experiment 4, AHS+LET) and $ASR = 1.5$ (experiment 5, LET) are shown in Figure 4.9c and d for comparison. The ice nucleation ability of the in situ neutralized particles with $ASR \approx 1.4$ appears to be more similar to that of pure letovicite (orange lines in panels c and d) than that of mixed AHS+LET particles (green lines in panels c and d).

After the AIDA expansion run, the particles had a higher degree of neutralization ($ASR \approx 1.6$) and produced a higher depolarization ratio ($\approx 14\,\%$). However, their ice nucleation ability was almost unchanged with the ice nucleation onset measured at $S_{ice} = 1.45$. As the particles were already solid before the expansion, the increase in the depolarization ratio is likely associated to a change in the morphology of the particles.

During the second ammonia injection period, the ASR of the particles further increased and fully neutralized particles were obtained. The lower rate of neutralization clearly visible for the second injection period is most likely due to the different phase state of the particles. At the beginning of the experiment the aerosol aprticles were liquid, while during the second neutralization step they were already in a crystalline state. The ice nucleation ability of the particles increased with their degree of neutralization, confirming the results obtained for particles generated from bulk solutions (experiments $1 - 8$). The ice nucleation onset of the fully neutralized ammonium sulfate particles was measured at $S_{ice} = 1.35 - 1.36$ in the CFDCs (at $-52\,°C$ and $-56\,°C$) and at $S_{ice} = 1.20$ in
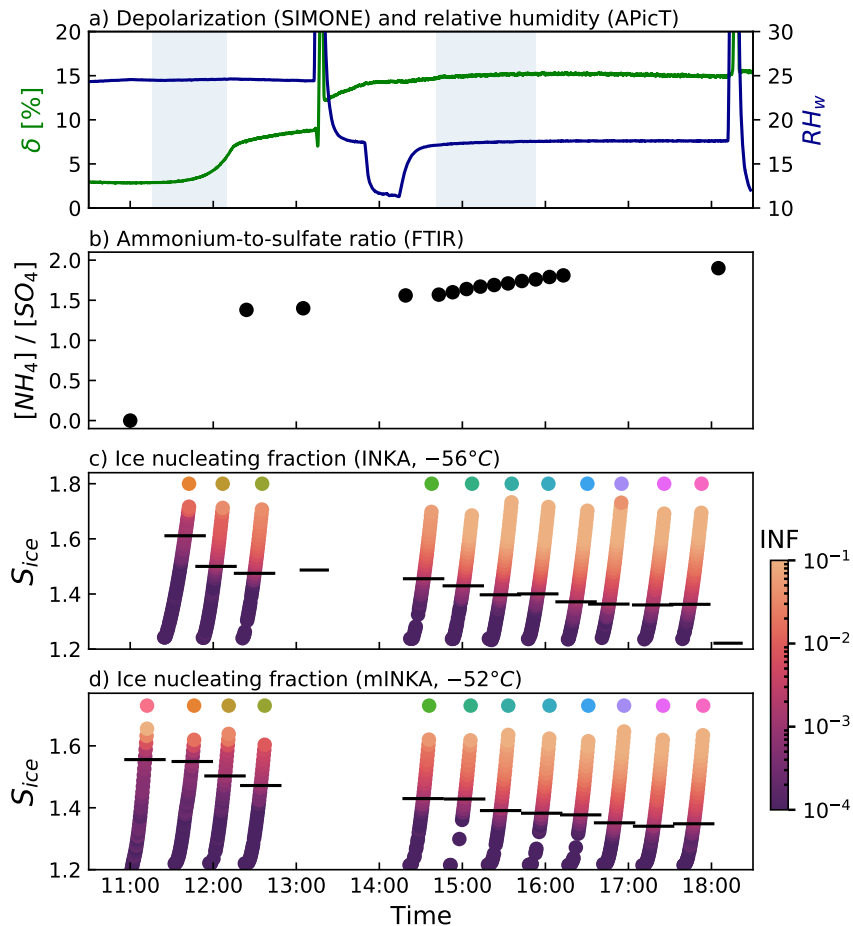
Figure 4.8: Time series of the in situ neutralization experiment. **a)** Depolarization ratio δ (left axis, green line) and relative humidity inside the AIDA chamber (right axis, blue trace). The light blue shaded areas indicate the two ammonia injection periods. **b)** Ammonium-to-sulfate ratio of the particles obtained from the measured infrared spectra. **c)** and **d)** Saturation scans performed with INKA and mINKA at −56 °C and −52 °C, respectively. The trajectories are color-coded by the measured ice nucleating fraction (INF). The black dashes indicate the ice nucleation onset conditions (defined for 0.1 % of the particles activated as ice crystals) measured by the CFDCs and during the two AIDA expansion runs (at about 13:00 and 18:00). The colored circles refer to the ice-activation curves reported in Figure 4.9.

the final AIDA expansion experiment (pink squares in Figure 4.9a). In this experiment, the fully neutralized particles clearly appear as the most active also in the CFDCs measurements. Indeed, their ice activation curves fall in the upper range of conditions expected for crystalline AS particles in the CFDCs measurements (red shaded area in Figure 4.9 panels c and d). The offset of about 0.15 between the ice nucleation onsets measured in AIDA and INKA is consistent with the bias already observed in experiments $1-8$ and in previous measurements performed with crystalline ammonium sulfate (see Section 3.4.7) and ammonium nitrate (Wagner et al., 2020) particles.

The in situ neutralization experiment corroborates the ice nucleation results obtained in experiments $1-8$, showing the composition-dependent ice nucleation ability of the particles in the $H_2SO_4/NH_3/H_2O$ system. Particles with increasing ammonium-to-sulfate ratio nucleate ice at progressively lower ice saturation ratios and through different ice nucleation modes. Initially ($ASR = 0$), ice is formed via homogeneous freezing at $S_{ice} \approx 1.6$, then ($ASR \approx 1.4$) via immersion freezing at $S_{ice} \approx 1.45$, and finally ($ASR \geqslant 1.6$) via deposition or pore condensation and freezing at $S_{ice} \approx 1.25$.

The degree of neutralization measured with the FTIR corresponds to the average composition of the particles, thus when an intermediate ASR of $1.6-1.8$ was measured the particles could have also been composed of a less neutralized core surrounded by a fully neutralized layer. In this case the particles would already show the ice nucleation behavior of the fully neutralized particles obtained in experiment 8 ($ASR = 2.0$). However, the gradual shift of the ice nucleation onsets (from 1.45 to 1.39) together with the measured increase in ASR (from 1.57 to 1.81) correspond to the ice onsets measured in experiments 6 ($ASR = 1.6$) and 7 ($ASR = 1.8$) at $S_{ice} = 1.4-1.45$. This suggests that the in situ neutralized particles have a quite uniform composition, and that the ice nucleation results obtained from particles of pre-defined and uniform composition (experiments $1-8$) also represent the ice nucleation ability of particles neutralized under more atmospherically relevant conditions. The ice nucleation results from experiments $1-8$ can thus be used to infer composition-depended parametrizations for the $H_2SO_4/NH_3/H_2O$ system to be implement in climate models.
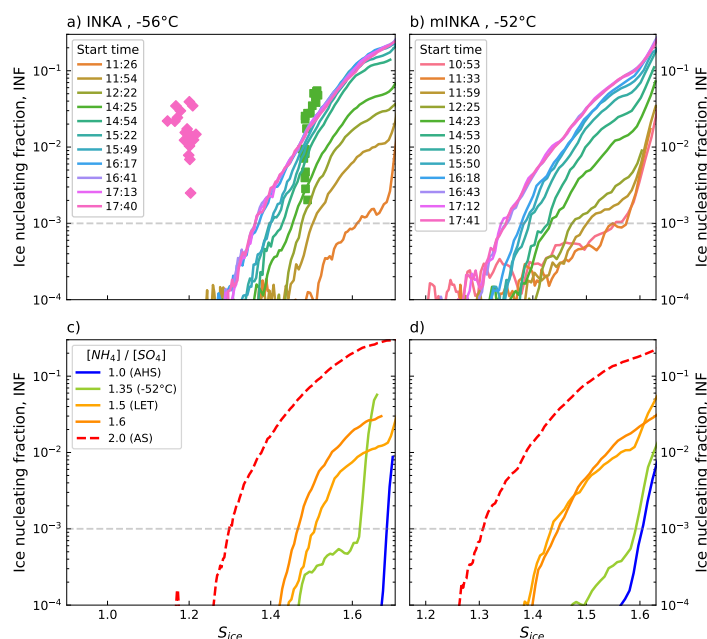
Figure 4.9: Ice nucleating fraction INF as a function of the ice saturation ratio S_{ice}. Measurements at the nominal temperature of $-56\,°C$ from INKA (panels a and c) and at $-52\,°C$ from mINKA (panels b and d) are shown with lines. Panels **a and b** report the results from the in situ neutralization experiment, panels **c and d** show, for comparison, the ice nucleation ability of particles with pre-defined ammonium-to-sulfate ratios obtained from bulk solutions. Results from the two AIDA expansion runs performed during the in situ neutralization experiment are shown with squares and diamonds in panel a. The red shaded areas in panels c and d indicate the range of ice nucleation ability measured for crystalline ammonium sulfate particles with the CFDCs at $-56\,°C$ and $-52\,°C$ in previous experiments.

4.6 CONCLUSIONS

In this chapter, experiments on the low temperature crystallization behavior, deliquescence, and ice nucleation ability of particles in the system $H_2SO_4/NH_3/H_2O$ were presented. The experiments were performed at the AIDA facility by means of expansion cooling experiments (from $-50\,°C$ to $-62\,°C$) and with two continuous flow diffusion chambers at $-52\,°C$ and $-56\,°C$.

The degree of neutralization of atmospheric sulfate particles is regulated by the concentrations of gas phase sulfuric acid and ammonia, likely resulting in particles with a distribution of composition (i.e., ammonium-to-sulfate ratios) rather than in an aerosol population with a uniform degree of neutralization that exactly corresponds to the stoichiometry of one of the three solids in the system (AHS, LET, AS). The thermodynamic properties at upper tropospheric conditions of acidic (i.e., sulfuric acid) and fully neutralized (i.e., ammonium sulfate) particles have been investigated in the past (e.g., Onasch et al., 1999), but little attention was given to the intermediate ranges of compositions. A comprehensive series of studies on the crystallization behavior and hygroscopic growth of particles with intermediate compositions in the $H_2SO_4/NH_3/H_2O$ system were performed at room temperature (Schlenker et al., 2004; Schlenker and Martin, 2005; Rosenoern et al., 2008). However, to more correctly predict the impact of ammonium-sulfate particles on the climate, it is important to know their phase state at low temperatures and the related impact on cirrus formation. The experiments presented in this chapter extend the results from Schlenker et al. (2004) and Schlenker and Martin (2005) to lower temperatures. The ice nucleation ability of particles with intermediate composition is measured for the first time.

An illustrative schematic of the results on the phase state and ice nucleation ability of particles in the $H_2SO_4/NH_3/H_2O$ system is presented in Figure 4.10. Aqueous particles with $ASR = 1.0$ nucleated ice via homogeneous freezing at high saturation ratios ($S_{ice} = 1.62$). Particles with $1.1 \leqslant ASR < 1.5$, composed of LET and AHS, crystallized at the low relative humidity conditions of the injection line, with the initial formation of letovicite that induced the heterogeneous crystallization of AHS. At about $-50\,°C$, the solid AHS component deliquesced at a relative humidity of about $60\,\%$, resulting in internally mixed solid/liquid particles at ice saturated conditions. In LET(solid)+AHS(liquid), the solid LET component initiated heterogeneous ice nucleation via immersion freezing at $S_{ice} \approx 1.55$, at slightly lower ice saturation ratios than required for homogeneous freezing. Zuberi et al. (2001) also found that the freezing conditions for solid letovicite immersed in aqueous ammonium bisulfate particles did not significantly deviate from those required for the homogeneous freezing of pure aqueous AHS.

For $ASR \geqslant 1.5$ the particles fully crystallized as pure letovicite ($ASR = 1.5$), internal mixtures of letovicite and ammonium sulfate ($1.5 < ASR < 2.0$), and pure ammonium sulfate ($ASR = 2.0$). For this group of particles, the deliquescence relative humidity was measured at $RH_w \approx 90\,\%$. These particles initiated heterogeneous ice nucleation in the deposition or pore condensation and freezing modes, with the freezing ice saturation ratios decreasing with increasing degree of neutralization. Pure letovicite ($ASR = 1.5$) or mixed letovicite and ammonium sulfate ($1.5 < ASR < 2.0$) particles showed an intermediate ice nucleation ability, with the ice onset at $S_{ice} \approx 1.4$. The fully neutralized AS particles showed the highest ice nucleation activity in the $H_2SO_4/NH_3/H_2O$ system, with an ice nucleation onset at $S_{ice} \approx 1.2$.

The measurements reported here show that the phase state and ice nucleation ability of particles in the $H_2SO_4/NH_3/H_2O$ system strongly depend on their degree of neutralization. A detailed knowledge of the abundance and neutralization degree of ammonium-sulfate particles in the upper troposphere is thus a key factor to correctly represent cirrus cloud formation and properties. This additional parameter would improve the assessment of the radiative effect of cirrus clouds in climate models.
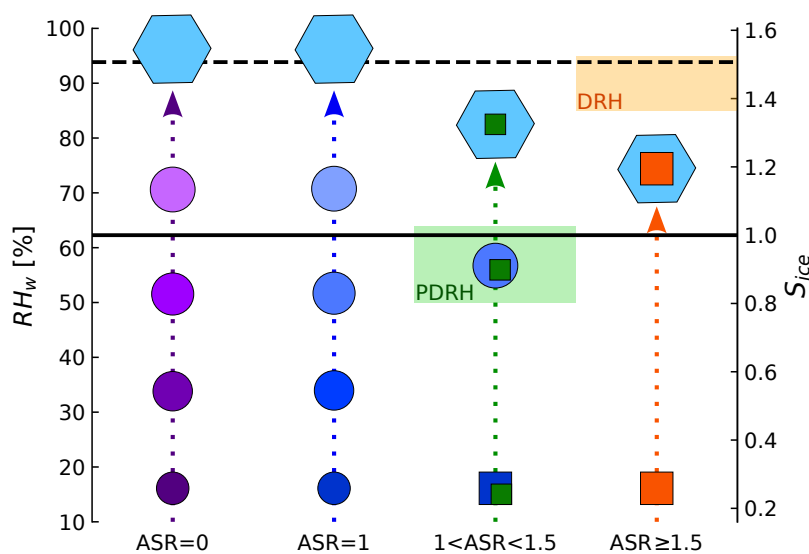
Figure 4.10: Schematic of the different ice nucleation regimes for particles in the $H_2SO_4/NH_3/H_2O$ system as a function of the ammonium-to-sulfate ratio (ASR) at $-52\,°C$. The solid and dashed black lines correspond to $S_{ice} = 1.0$ (ice saturated conditions) and $S_{ice} = 1.52$ (homogeneous freezing threshold, Koop et al., 2000). Pure ammonium bisulfate particles likely remain in an supercooled aqueous state in the atmosphere and initiate ice formation only via homogeneous freezing at $S_{ice} \approx 1.6$, similarly to aqueous sulfuric acid particles (ASR $= 0$, here shown as reference). Particles with $1 < ASR < 1.5$ can be found as liquid/solid internal mixtures of ammonium bisulfate/letovicite at ice supersaturated conditions and can thus initiate ice nucleation via immersion freezing at $S_{ice} \approx 1.55$. For ASR $\geqslant 1.5$, particles can remain in a crystalline state up to $RH_w \approx 90\,\%$ and initiate ice nucleation via deposition or pore condensation and freezing at $S_{ice} \approx 1.4$. Fully neutralized particles (ASR $= 2$) are the most efficient in the system, with the ice nucleation onset at about $S_{ice} = 1.2$.

5 | AMMONIUM NITRATE PARTICLES

5.1 INTRODUCTION

Ammonium nitrate particles (NH_4NO_3, AN) form in the atmosphere from the neutralization reaction of nitric acid (HNO_3) with ammonia (NH_3). Nitric acid mainly originates from the oxidation of nitric oxides (NO_x), which are produced by fossil fuel combustion, biomass burning, and lightning. The partitioning of nitric acid to the particle phase depends on ambient temperature (due to its strong temperature-dependent saturation vapor pressure), relative humidity, and acidity of the particle (Stelson and Seinfeld, 2007). Ammonia is the most abundant base present in the atmosphere and it comes primarily from agricultural sources and cattle farming (Bouwman et al., 1997). Unlike ammonium-sulfate salts, ammonium nitrate is semi-volatile and in reversible phase equilibrium with its gaseous precursors (Matsumoto and Tanaka, 1996). If sulfate ions are also present, nitric acid neutralization with ammonia only occurs under ammonium-rich conditions, that is when the ammonium-to-sulfate molar ratio is larger than 1.5 (Seinfeld and Pandis, 2012; Huang et al., 2011; Ge et al., 2017). Due to the expected increase in nitrate precursor emissions and the decrease of sulfate aerosols, the concentration of nitrate in the particle phase is expected to increase in the next decades (Bauer et al., 2007).

Most of the sources of nitric acid and all the sources of ammonia are located inside the boundary layer. However, convective systems in highly polluted environments can act as efficient transport corridors for aerosol particles and gases to the upper troposphere. The Asian Tropopause Aerosol Layer (ATAL, Vernier et al., 2011), for example, forms during the Asian summer monsoon period from the lifting of boundary layer air. The pollutants lifted from the ground can then accumulate in the upper troposphere and lower stratosphere due to the Asian anticyclone (Vernier et al., 2018). In addition to the uplift of primary aerosol particles (such as carbonaceous, sea salt, and mineral dust particles, Yu et al., 2015), also secondary aerosol particles can form due to the low temperature of the upper troposphere, which facilitates the partitioning of the uplifted gases to the particle phase (Weigel et al., 2021). In addition to sulfate particles and secondary organics (Yu et al., 2015), crystalline ammonium nitrate particles were recently observed within plumes of elevated ammonia concentrations in the ATAL (Höpfner et al., 2019).

The observation by Höpfner et al. (2019) of crystalline ammonium nitrate (AN) particles (as clearly evidenced by infrared measurements) is surprising because pure AN particles tend to remain in a liquid state also at relative humidities close to 0 % at temperatures down to $-35\,°C$ (Cziczo and Abbatt, 2000; Martin, 2000). However, its heterogeneous crystallization can be initiated by various mechanisms, such as by the presence of solid inclusions (Han et al., 2002), by contact with solid particles (Davis et al., 2015), and by the addition of salts that crystallize more readily (Schlenker et al., 2004). In particular, the crystallization of ammonium nitrate particles was observed for a small fraction of ammonium sulfate (AS) present in the particles (about 10 mol%, Schlenker et al., 2004; Schlenker and Martin, 2005). Mass spectrometric measurements showed that the AN particles detected by Höpfner et al. (2019) also contained sulfate, suggesting that their heterogeneous crystallization was initiated by the sulfate component. The occurrence of crystalline AN particles in the upper troposphere makes them likely candidates for heterogeneous ice formation. Indeed, it has already been shown that crystalline inorganic salts of different chemical compositions can

---

The results of the experiment performed at the CLOUD chamber presented in this chapter are included in the manuscript "Synergistic particle formation in the upper troposphere by nitric acid, sulfuric acid and ammonia" by Wang, Xiao, Bertozzi et al. (under review).

contribute to heterogeneous ice formation at low temperatures (see e.g. Chapter 4; Abbatt et al., 2006; Shilling et al., 2006; Wise et al., 2012).

The crystallization and ice nucleation ability of mixed AN/AS particles was investigated by Höpfner et al. (2019) and Wagner et al. (2020). In their studies, the aerosol particles were generated from bulk solutions with different mole fraction of ammonium sulfate, from 33.3 mol% down to 0.6 mol%. The crystallization experiments were performed in the AIDA chamber at temperatures between $-60\,°C$ and $-30\,°C$, and relative humidities with respect to liquid water between 18 % and 68 %. It was found that a fraction of 0.6 mol% of ammonium sulfate, much smaller than the 10 mol% investigated by Schlenker and Martin (2005), is already sufficient to induce the crystallization of the AN particles at $-50\,°C$ and $RH_w = 22\,\%$. The ice nucleation measurements, performed with AIDA expansion cooling experiments and INKA saturation scans, showed that at temperatures above $-43\,°C$, the AN particles deliquesce and nucleate ice by homogeneous freezing, while at temperatures below $-43\,°C$ crystalline AN is able to induce heterogeneous ice nucleation at lower ice saturation ratios ($S_{ice} = 1.1 - 1.2$) before reaching the deliquescence point.

In this chapter, the work of Wagner et al. (2020) is extended to investigate a different crystallization pathway of ammonium nitrate/sulfate particles. Instead of directly starting with pre-mixed AN/AS particles, in these new experiments the uptake of sulfate from the gas phase onto pure, initially aqueous ammonium nitrate particles was mimicked. Sulfuric acid (H_2SO_4) was generated in the gas phase in the presence of ammonia and was allowed to condense on the AN particles. The experiments were performed in the AIDA and CLOUD chambers. The AIDA experiments aimed to accurately characterize the phase state of the particles during the heterogeneous crystallization process, for which it was necessary to control the particle size of the pre-added AN particles to about $1\,\mu m$. In the experiment performed at the CLOUD chamber, particles in a more atmospherically relevant size range ($40 - 300\,nm$) were generated by simulating hotspot conditions within the Asian monsoon anticyclone. The accurate control of the gas precursor concentration allowed to gradually increase the sulfuric acid concentration and to measure the particle composition when the AN crystallization occurred. The ice nucleation ability of the aqueous and crystalline AN particles was investigated in both experiments.

In the AIDA experiment, ammonium nitrate particles with a median diameter of about $1\,\mu m$ were generated ex situ from the nebulization of a bulk solution of AN. Gas phase sulfuric acid was produced inside the AIDA chamber held at $-50\,°C$ and $RH_w = 62\,\%$. The phase state of the particles was continuously monitored with a Fourier Transform Infrared (FTIR) Spectrometer[1] and with laser light linear depolarization measurements (SIMONE instrument). The ice nucleation behavior of the aqueous and crystalline AN particles was measured with two continuous flow diffusion chambers (INKA and mINKA) at temperatures between $-40\,°C$ and $-56\,°C$. Crystalline particles were also probed in an AIDA expansion cooling experiment.

In the CLOUD experiment, ammonium nitrate particles with a median diameter of about $100\,nm$ were generated in situ from the gas-to-particle conversion of nitric acid and ammonia at about $-40\,°C$ and $15 - 30\,\%$ relative humidity with respect to liquid water. To induce the crystallization of the particles, the concentration of gas phase sulfuric acid was then slowly increased, with an excess of ammonia in the gas phase. The accurate control of concentration of the gas precursors and the measurements performed with several mass spectrometers allowed to accurately quantify the sulfate concentration in the particles and its effect on the ice nucleation ability of the AN particles. The ice nucleation ability of the particles was continuously measured with ice saturation ratio scans performed with two continuous flow diffusion chambers (mINKA and SPIN) at $-58\,°C$ and $-53\,°C$.

5.2 AEROSOL PREPARATION AND CHARACTERIZATION

AIDA EXPERIMENT The description of the AIDA chamber and the standard instrumentation used can be found in Section 3.2.

An overview of the AIDA crystallization experiment is presented in Figure 5.1. Ammonium nitrate particles were generated with an ultrasonic nebulizer from an $8\,wt\%$ solution . The particles were injected into the AIDA chamber at about $-50\,°C$ and ice saturated conditions ($S_{ice} = 1.0$,

---

1 FTIR data collection and analysis were performed by Dr. Robert Wagner.

$RH_w = 62\%$). Before injection into the AIDA chamber, the aerosol flow was exposed to low relative humidity conditions ($RH_w \leqslant 3\%$) by passing through a series of diffusion dryers. In agreement with previous studies, pure AN particles did not crystallize during aerosol injection (i.e., in the few seconds of residence time in the injection line at $RH_w \leqslant 3\%$) or when suspended for longer times at the AIDA chamber conditions. The low backscattering linear depolarization ratio of the particles ($\delta \approx 3\%$, Figure 5.1a) corresponds to the background value that is typically observed for homogeneous liquid particles. Additionally, the habitus of the $\nu_3(NO_3^-)$ absorption band at $1500 - 1300\,cm^{-1}$ in the infrared spectrum of the particles (shown in blue in Figure 5.1b) resembles that of supercooled liquid ammonium nitrate measured by Höpfner et al. (2019). To initiate the heterogeneous crystallization of the AN particles, gas phase sulfuric acid was produced inside the chamber from the oxidation of SO_2 by $\cdot OH$ radicals. Hydroxyl radicals were generated in the dark from the reaction of ozone and tetramethylethylene (TME, C_6H_{12}). The injection order of the gases and the respective time of injection are indicated in the upper part of Figure 5.1a. (i) Ozone ($\approx 741\,ppb$) and (ii) SO_2 ($\approx 7\,ppb$) were injected first, indicated in blue and orange in Figure 5.1a. To produce gas phase sulfuric acid, (iii) TME was then injected in two steps, marked in gray. Sulfuric acid both condensed on the ammonium nitrate particles and homogeneously nucleated new particles. Finally, (iv) ammonia was injected ($3.9\,ppb$) to neutralize the sulfuric acid component (light blue shaded area). The phase state of the particles was continuously monitored with a Fourier Transform Infrared Spectrometer (FTIR) and with laser light linear depolarization measurements (SIMONE instrument). As described by Höpfner et al. (2019), aqueous and crystalline ammonium nitrate particles have different characteristic infrared extinction spectra, which allows distinguishing the phase state of the particles. Additionally, changes in the polarization of the light scattered by the aerosol particles, expressed in terms of the depolarization ratio δ, allow inferring the morphology of the particles. A depolarization ratio of zero is associated with spherical aqueous solution droplets, while a non-zero value is characteristic of non-spherical and inhomogeneous particles. A discussion of the crystallization behavior of the particles is provided in the result section.

The size distribution of the particles was measured with an aerodynamic particle sizer (APS). The volume equivalent diameter of the particles was calculated assuming a shape factor of 1.0 or 1.1, and a density of $1.44\,g\,cm^{-3}$ or $1.72\,g\,cm^{-3}$ for aqueous and crystalline AN particles, respectively. Equilibrium mass concentration and density of the aqueous ammonium nitrate particles at the thermodynamic condition of the AIDA chamber were calculated with the Extended Aerosol Inorganic Model (E-AIM, Clegg et al., 1998). The median diameter of the particle size distribution before and after the crystallization process was 980 and $933\,nm$, respectively, as fitted by a log-normal distribution.

The ice nucleation ability of the ammonium nitrate particles before and after the crystallization process was measured with ice saturation scans performed with mINKA and INKA at the nominal temperature of $-52\,°C$ and $-56\,°C$. Additional measurements were performed to investigate the temperature-dependent ice nucleation ability of the crystalline AN particles at temperatures between $-40\,°C$ and $-56\,°C$. The ice nucleation ability of the crystalline AN particles was also measured with an AIDA expansion cooling experiment at the starting temperature of about $-50\,°C$. The sampling line shared by the two CFDCs was cooled to about $-30\,°C$ to prevent the warming of the aerosol particles during the transfer from the AIDA chamber to the instruments. During the crystallization procedure (i.e. during injection of the gas precursors), changes in the ice nucleation ability of the aqueous ammonium nitrate particles were monitored with INKA by measuring the number concentration of ice crystals forming at the constant conditions of $-55.6\,°C$ and $S_{ice} = 1.34$. Additionally, the particle size distribution at the constant conditions of $-51.8\,°C$ and $RH_w = 79\%$ (i.e. below the deliquescence relative humidity of crystalline AN particles, $DRH = 97\%$ at $-50\,°C$, Clegg et al., 1998) was continuously measured with the optical particle counter at the outlet of the mINKA instrument. Unlike INKA, mINKA was operated without an evaporation section, thereby facilitating the detection of the hygroscopic growth of the aerosol particles (see Sections 3.4.2 and 3.4.7 for more details).

The fraction of particles inducing heterogeneous ice nucleation (ice nucleating fraction, INF) is computed as the ratio of the ice crystal number concentration to the aerosol particle number concentration measured by the APS. The ice nucleation active surface site density n_S (INAS density, see Section 2.2) is calculated as the ratio of the ice crystal number concentration to the total surface area
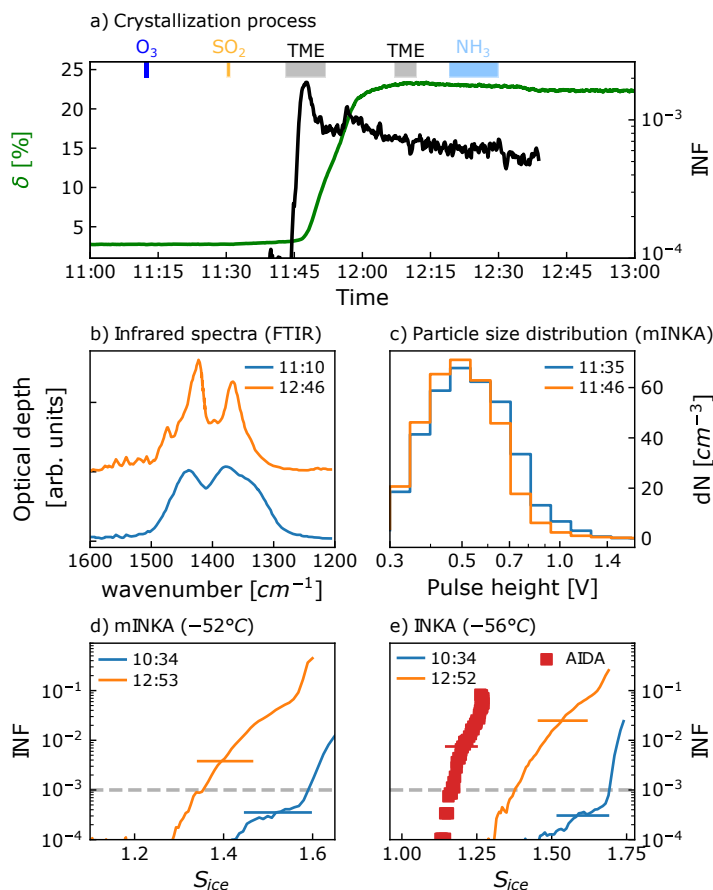
Figure 5.1: Overview of the ammonium nitrate crystallization experiment performed in the AIDA chamber at about $-50\,°C$ and $RH_w = 62\,\%$. **a)** Time series of the crystallization process. The gas injection periods are highlighted in the upper part of the plot. The linear depolarization ratio δ is shown in green (left axis), the evolution of the ice nucleating fraction (INF) at $-56\,°C$ and $S_{ice} = 1.34$ measured by INKA is shown in black (right axis). **b)** Infrared spectra of AN particles measured before (blue) and after (orange) their crystallization. The spectra are offset for clarity. **c)** Particle size distribution of the aqueous AN (blue) and the crystalline AN particles (orange) measured by mINKA at about $-52\,°C$ and $RH_w = 79\,\%$. **d)** and **e)** Ice nucleating fraction (INF) as a function of the ice saturation ratio (S_{ice}) measured by mINKA, INKA, and AIDA (in red). Blue curves show the homogeneous nucleation of aqueous AN particles; orange and red curves present the heterogeneous ice nucleation ability of crystalline AN.

of the aerosol particles measured by the APS. The newly formed aerosol particles that nucleated in the AIDA chamber during the production of sulfuric acid are not included in the total aerosol particle concentration, because their small size prevents a significant contribution to a heterogeneous ice nucleation mode (median diameter of about $30\,nm$ measured with a scanning mobility particle sizer, SMPS).

CLOUD EXPERIMENT The description of the CLOUD chamber and the list of instruments operated during the CLOUD14 campaign can be found in Section 3.3.

An overview of the experiment presented here is shown in Figure 5.2. Pure ammonium nitrate particles were formed via homogeneous nucleation of nitric acid and ammonia vapors at about $-40\,°C$ and $RH_w = 15 - 30\,\%$. Gas phase nitric acid was directly injected into the chamber and its concentration was progressively increased to induce the homogeneous nucleation and growth of the aerosol particles. The nitric acid concentration, measured with a chemical ionization mass spectrometer[2] (CIMS, with bromide as the reagent ion) is shown in Figure 5.2a. Ammonia was continuously injected during the whole experiment to ensure the full neutralization of nitric and

---

2 Br^--CIMS data were collected and analyzed by Dr. Mingyi Wang (Carnegie Mellon University).

sulfuric acid. The ammonia concentration was measured with a proton transfer reaction mass spectrometer[3] (PTR-MS) and ranged between 160 and 320 ppt (Figure 5.2a). Once the median diameter of the AN particles leveled off at about 100 nm, the nitric acid concentration was stabilized and the growth of the particles was stopped. The evolution of the particle size distribution measured with a scanning mobility particle sizer (SMPS) is shown in Figure 5.2d. Gaseous sulfuric acid was generated from the oxidation of sulfur dioxide (SO_2) by hydroxyl radicals ($\cdot OH$). First, the production of $\cdot OH$ radicals was initiated via ozone photolysis by turning on the UV lights inside the chamber (at about 3:30, black vertical line). The ozone concentration was about $180 - 200$ ppb. Then, SO_2 was injected and oxidized to sulfuric acid (Figure 5.2b). Gas phase sulfuric acid was measured with a CIMS using nitrate as reagent ion[4]. The SO_2 injection rate was increased 2 times during the experiment, resulting in a step-wise increase of gas phase sulfuric acid (Figure 5.2b, brown trace), with final concentration of about 3.2 ppt. The chemical composition of the particles was monitored with an aerosol mass spectrometer[5] (AMS). The time series of the particle phase nitrate concentration measured by the AMS is shown in Figure 5.2c (dark blue, left axis). The sulfate-to-nitrate molar ratio of the particles is also shown (right axis, in red). The sulfate appeared in the particle phase approximately 1 h after the start of SO_2 injection.

The ice nucleation ability of the particles was monitored with mINKA and SPIN. mINKA was operated at the nominal temperature of $-58\,°C$, SPIN[6] measured at $-53\,°C$. Unlike SPIN, mINKA was operated without an evaporation section to maximize the exposure time of the sampled particles to the defined ice supersaturated conditions (see Section 3.4.2 for more details). A detailed description of the SPIN instrument with its experimental operation and measurement uncertainties can be found e.g. in Garimella et al. (2016), Garimella et al. (2017), Korhonen et al. (2020), and Welti et al. (2020). Ice saturation ratio scans were started approximately every $20 - 30$ min throughout the experiment. To keep the aerosol particles at a constant temperature during the transfer from the CLOUD chamber to the instruments, both CFDCs sampled the aerosol particles from the CLOUD chamber with an actively cooled sampling line. The sampling line of mINKA was set to the CLOUD chamber temperature (about $-40\,°C$), whereas the SPIN sampling line was set to the minimum working temperature of the chiller (about $-30\,°C$).

The fraction of particles that initiated ice nucleation (ice nucleating fraction, INF) is calculated as the ratio of the ice crystal number concentration to the total number of particles with diameters larger than 10 nm, obtained by integration of the particle number size distribution from the SMPS data. To compare the ice nucleation results obtained from particles of different sizes, the ice nucleation active surface site density n_S (INAS density, see Section 2.2) is used. n_S is calculated as the ratio of the ice number concentration to the total surface area of particles with diameters larger than 10 nm, obtained from the SMPS data assuming spherical particles.

---

3 PTR-MS data were collected and analyzed by Wiebke Scholz (University of Innsbruck).
4 NO_3^--CIMS data were collected and analyzed by Guillaume Marie (Goethe University Frankfurt).
5 AMS data were collected and analyzed by Brandon Lopez (Carnegie Mellon University).
6 SPIN data collection and analysis was performed by Dr. Ana A. Piedehierro and Dr. André Welti (Finnish Meteorological Institute).
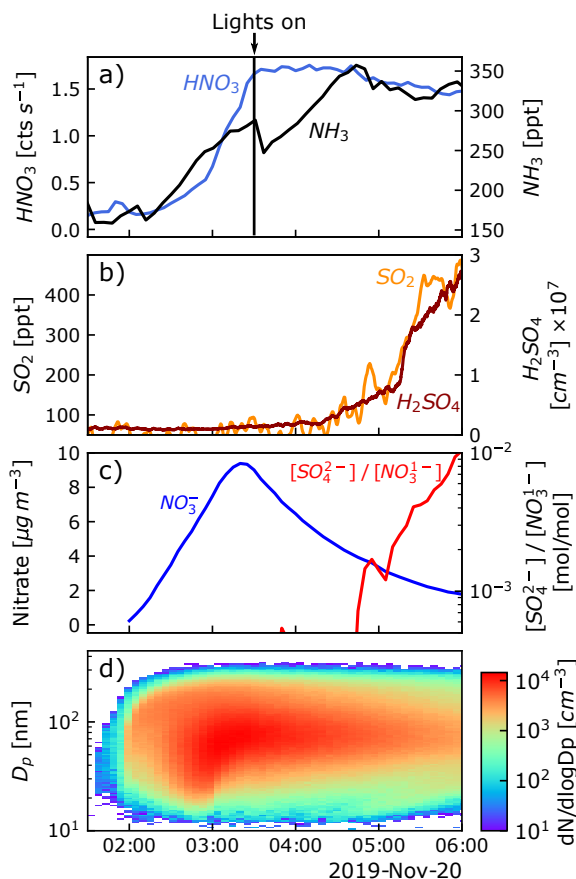
Figure 5.2: Overview of the AN crystallization experiment performed in the CLOUD chamber at about $-40\,°C$ and $RH_w = 15 - 30\,\%$. **a)** Concentration of nitric acid (HNO_3, blue) and ammonia (NH_3, black). **b)** Concentration of sulfur dioxide (SO_2, orange) and gas-phase sulfuric acid (H_2SO_4, red). **c)** Chemical composition of the aerosol particles. The concentration of nitrate (NO_3^-) is shown in blue, the sulfate-to-nitrate molar ratio is shown in red. **d)** Temporal evolution of the particle size distribution.

5.3 RESULTS AND DISCUSSION

AIDA EXPERIMENT The crystallization process and the results from the AIDA experiment are summarized in Figure 5.1. The injection periods of the different gases are indicated in the upper part of panel a: O_3 in blue, SO_2 in orange, C_6H_{12} (TME) in gray, and NH_3 in light blue. The time series of the linear depolarization ratio δ is shown in green in panel a (left axis). Panel a also reports the evolution of the ice nucleating fraction (INF) measured with INKA during the crystallization process at the constant conditions of $-55.6\,°C$ and $S_{ice} = 1.34$ (right axis). At about 11:45, during the first TME injection period, a sharp increase is visible in the depolarization ratio (from about $3\,\%$ to $23\,\%$) and in the ice nucleating fraction (from $< 10^{-4}$ to about $2 \cdot 10^{-3}$). Both depolarization and ice nucleation measurements clearly indicate that the AN particles crystallized upon generation and uptake of gas-phase sulfuric acid (SA). The fact that the heterogeneous crystallization of the AN particles took place before the injection of ammonia could indicate that (i) the condensed sulfuric acid was neutralized by the ammonium ions present in the AN particles, with the immediate crystallization of the ammonium sulfate component, or that (ii) gas phase ammonia was already present as a background in the chamber and co-condensed on the AN particles together with SA. The presence of ammonia contamination in the chamber is likely because high loads of ammonia were used in a series of experiments performed in the previous days.

The change in the phase state of the particles was also visible in the infrared extinction spectra. Figure 5.1b shows the AN infrared spectrum in the regime of the $\nu_3(NO_3^-)$ absorption band measured before (blue) and after (orange) the crystallization. The spectral habitus of the aqueous and

crystalline particles corresponds to the measurements by Höpfner et al. (2019) and Wagner et al. (2020), with the solid particles presenting narrower absorption bands. The spectra were scaled and offset to facilitate their comparison.

Indication of the crystallization of the AN particles is also visible in the particle size distributions measured with the optical particle counter of mINKA during the gas injection period. Figure 5.1c shows the particle size distributions measured by the OPC before (in blue) and after (in orange) the AN crystallization. During the crystallization process, particles were exposed in mINKA to a temperature of $-51.8\,°C$ and a relative humidity of 79 %, below the expected deliquescence relative humidity of AN particles (see Section 2.4). Due to loss of water, the crystalline AN particles appear at smaller diameters compared to the aqueous particles.

The ice nucleation measurements, performed before and after the crystallization of the AN particles, are shown in panels d and e. Measurements were performed with mINKA at the nominal temperature of $-52\,°C$ (panel d) and with INKA at $-56\,°C$ (panel e). The measurements conducted before the gas injections (in blue) show a dominant homogeneous freezing mode, with the ice onset (for an ice nucleating fraction of 0.1 %) at $S_{ice} = 1.59$ (mINKA) and $S_{ice} = 1.69$ (INKA). The visible minor heterogeneous mode could have resulted from a small fraction of already crystalline AN particles, probably due to foreign contamination during the preparation of the solution or the injection procedure in the AIDA chamber. The crystalline AN particles (in orange) show a clear heterogeneous ice nucleation mode with the ice onset at $S_{ice} = 1.35$ (mINKA) and $S_{ice} = 1.38$ (INKA). The ice nucleation ability of the crystalline particles was also measured with an AIDA expansion cooling experiment. The AIDA result, shown in red in Figure 5.1e, locate the heterogeneous ice nucleation onset at an even lower ice saturation ratio, $S_{ice} = 1.17$. A similar difference in the ice nucleation onsets measured with expansion cooling experiments and CFDC scans at cirrus cloud conditions has been observed in other experiments performed with AN (Wagner et al., 2020) and ammonium-sulfate particles (see Sections 3.4.7 and 4.4).

To investigate the ice nucleation ability of crystalline AN particles at different temperatures, a second heterogeneous crystallization experiment was performed in the AIDA chamber at the same thermodynamic conditions. The ice nucleation ability of the crystalline AN particles was tested at temperatures between $-40\,°C$ and $-56\,°C$ with INKA and mINKA measurements. The $INF - S_{ice}$ curves are shown in Figure 5.3a, and the ice onset conditions (for an ice nucleating fraction of 0.1 %) are summarized in Figure 5.3b. In Figure 5.3b, the ice nucleation onsets of AN/AS mixed particles from the study of Wagner et al. (2020) are also reported (black empty symbols). The AIDA data (diamonds) refer to particles with ammonium sulfate concentrations from 0.6 to 33 mol%, the INKA data (circles) only show the results for particles with 0.6 mol% of ammonium sulfate. The new results from INKA and mINKA show a good agreement and are consistent with the INKA measurements from the study of Wagner et al. (2020). The ice onsets corresponding to the aqueous and crystalline AN particles from the experiment presented in Figure 5.1 are also included in gray. The theoretical deliquescence relative humidity (DRH) of crystalline AN calculated with the E-AIM is shown as the blue dashed line. Parameterizations for homogeneous freezing of aqueous solution droplets (Koop et al., 2000) and for aqueous sulfuric acid particles (Schneider et al., 2021) are shown as gray shaded area and black dotted line, respectively. Two ice nucleation regimes, as typical of inorganic salt particles, can be identified. At temperatures higher than $\approx$ $-43\,°C$, the AN particles first deliquesce and then freeze homogeneously at high ice saturation ratios ($S_{ice} \approx 1.4$, red symbols) in agreement with the parameterizations for homogeneous freezing (Koop et al., 2000; Schneider et al., 2021). At temperatures below $-43\,°C$, instead, the crystalline particles can act as ice nucleating particles (INPs) and initiate heterogeneous ice formation before their DRH is reached. The CFDC results show a shift of the ice nucleation onsets towards higher values for decreasing temperature, while the AIDA results from Wagner et al. (2020) suggest a weak temperature-dependent ice nucleation ability of the crystalline AN particles. However, the low temperature CFDC measurements could be affected by the short residence time of the particles in the instrument, which could limit the time for the particles to equilibrate to the ice supersaturated conditions and to grow to large sizes. The better agreement between the CFDC and AIDA data at temperatures above $-50\,°C$ supports the hypothesis of an instrumental bias at low temperatures.

The AIDA experiments show that co-condensation of sulfuric acid and ammonia on aqueous ammonium nitrate particles is an effective heterogeneous crystallization pathway at $-50\,°C$ and
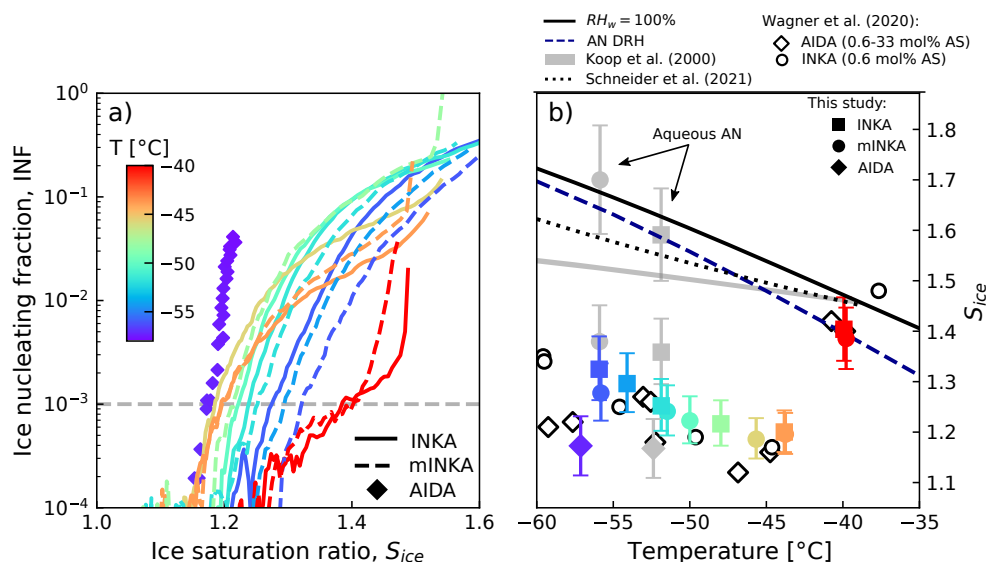
Figure 5.3: Summary of the ice nucleation results from the AIDA experiments for crystalline ammonium nitrate (AN) particles as a function of the ice saturation ratio and the temperature. **a)** $INF - S_{ice}$ curves measured with INKA (solid lines), mINKA (dashed lines), and AIDA (diamonds) during the second heterogeneous crystallization experiment, color-coded by the investigated temperature. **b)** Ice onset conditions (for an $INF = 10^{-3}$) for the same measurements as in panel a. The ice onset results from the first crystallization experiment presented in Figure 5.1 for aqueous and crystalline AN particles are shown in gray. Results from Wagner et al. (2020) for mixed AN/AS particles are reported with empty black symbols; AIDA data (diamonds) refer to AS concentrations from 0.6 to 33 mol%, INKA data (circles) refer to particles with an AS concentration of 0.6 mol%. Water saturation, AN deliquescence relative humidity (DRH) (Clegg et al., 1998), and parameterizations for the homogeneous freezing of aqueous solutions and aqueous sulfuric acid particles (Koop et al., 2000; Schneider et al., 2021) are also shown.

high relative humidity conditions $RH_w = 62\%$. The ice nucleation ability of the so-crystallized AN particles agrees with previous measurements performed with AN/AS particles generated from pre-mixed AN/AS bulk solutions (Wagner et al., 2020).

In the AIDA experiment, AN particles with a median diameter of about $1\,\mu m$ were used in order to achieve a sufficiently high aerosol mass concentration to be able to characterize the phase state of the particles by FTIR spectroscopy and to obtain a clear depolarization ratio signal from the SIMONE instrument. However, newly formed AN particles are unlikely to reach such large sizes in the upper troposphere. The experiment performed at the CLOUD chamber helps addressing this issue by investigating smaller AN particles, using precursor concentrations that correspond to hotspot conditions within the monsoon anticyclone and yielded a median particle diameter of only about $0.1\,\mu m$. Additionally, the fraction of sulfuric acid particles that homogeneously nucleated during the generation of gas-phase sulfuric acid in the AIDA chamber could have reacted with background ammonia and became crystalline ammonium sulfate particles. These tiny crystalline AS seed particles could have partially contributed to the heterogeneous crystallization of the AN particles via a collision-efflorescence mechanism (Davis et al., 2015). In the CLOUD experiment, the accurate control of the concentration of the gas precursors avoided the formation of new particles during the production of sulfuric acid. Moreover, the mass spectrometer measurements made it possible to determine the minimum amount of sulfate that had to be condensed in order to initiate the crystallization of the AN particles.

CLOUD EXPERIMENT The ice nucleation results from the CLOUD experiment are summarized in Figure 5.4. The ice nucleating fractions (INF) as a function of the ice saturation ratio S_{ice} measured by mINKA (at $-58\,°C$) and SPIN (at $-53\,°C$) are shown in panel a and b, respectively. The curves are color-coded by the sulfate-to-nitrate molar ratio of the particles measured with the Aerosol Mass Spectrometer (AMS). The time at which each saturation scan was started is also reported. At the

beginning of the experiment, pure ammonium nitrate particles nucleated ice only at high saturation ratios ($S_{ice} = 1.56 - 1.6$, dark blue curves). The sharp increase in the ice crystal number concentration at a defined ice saturation ratio is typical of the homogeneous freezing mode (see Section 3.4.7). The high ice nucleation onsets of the pure AN particles confirm their initial auqoues phase, similarly to the AIDA experiments where the phase state of the particles was directly measured. When the sulfate concentration reached a value of about 0.15 mol% (at about 04:55, the light blue curve in Figure 5.4a), the ice crystals appeared in the mINKA instrument already at about $S_{ice} = 1.34$ (for an $INF = 10^{-5}$), and their concentration gradually increased over a wider range of S_{ice} values. The slower increase in the INF with S_{ice} is indicative of a heterogeneous ice nucleation mode and implies the presence of a solid component in the particles. However, at this point, only a tiny fraction of the particles nucleated ice heterogeneously, and the ice nucleation onset, defined as the ice saturation ratio at which 0.1 % of the particles activated as ice crystals, still corresponds to the homogeneous freezing threshold. A sulfate concentration of about 0.15 mol% was probably sufficient to initiate the crystallization only of a small fraction of the AN particles.

The ice nucleation onset progressively shifted to lower values ($S_{ice} = 1.4$ and $S_{ice} = 1.3$) as the sulfate concentration rose to 0.4 mol% and 1.4 mol%, respectively. The minor changes in the ice nucleation ability of the particles with a sulfate concentration greater than 0.4 mol% suggest that most of the AN particles were already crystalline. This result is in very close agreement with the result of Wagner et al. (2020), which measured the crystallization of larger AN particles ($\approx 0.9\,\mu m$) with a sulfate concentration of 0.6 mol% at about $-50\,°C$ and $RH_w = 22\,\%$. The ice nucleation ability of crystalline AN particles with different sizes obtained in the AIDA and CLOUD experiments is compared in terms of ice nucleation active surface site (INAS) density in the conclusions section.

In the measurements performed with SPIN at $-53\,°C$ (Figure 5.4b), the heterogeneous ice nucleation mode appears only at a higher sulfate-to-nitrate molar ratio (0.5 mol%) and is less pronounced than in the mINKA measurements. However, the transition from the sharp activation at the homogeneous freezing threshold for the aqueous AN particles to the gradual increase in the INF of the heterogeneous ice nucleation mode is visible also in the SPIN measurements. The gray shaded area in Figure 5.4b corresponds to the background concentration of ice crystals in the SPIN instrument (in the mINKA instrument the background ice counts were lower than 10^{-5} fraction of the aerosol particles). The differences in the heterogeneous ice nucleation ability measured with the two CFDCs could result from a different sensitivity of the two instruments towards the formation of ice crystals via heterogeneous ice nucleation. In view of the results presented in the previous section, the small temperature difference between the SPIN ($-53\,°C$) and mINKA ($-58\,°C$) scans is not a likely reason to explain the difference in the measured ice nucleation behavior. The INKA and mINKA heterogeneous ice nucleation measurements compared well (see Sections 3.4.7, 4.4), but systematic intercomparison studies between CFDCs with different geometries and characteristics at cirrus cloud conditions are still missing. In Chapter 6, a first comparison of the homogeneous freezing threshold measured by mINKA and SPIN for a different aerosol system will be presented.
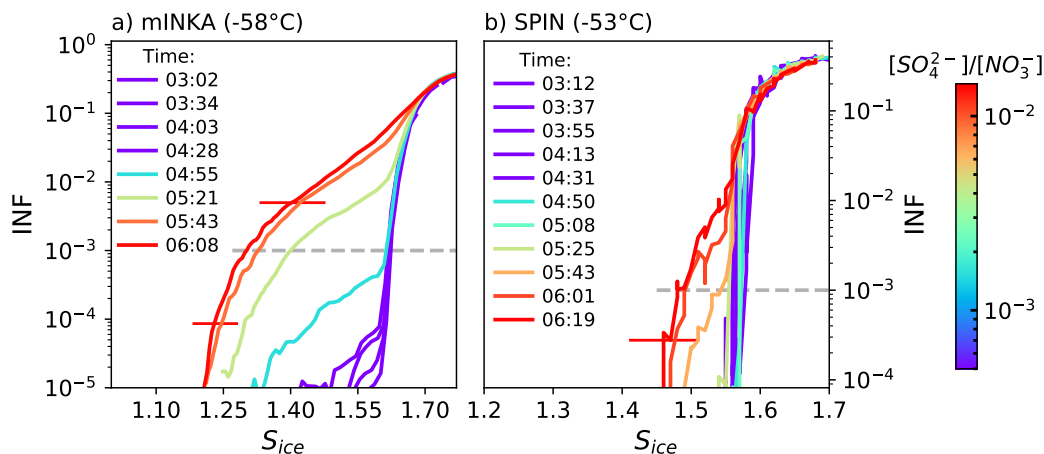
Figure 5.4: Overview of the ice nucleation measurements performed during the CLOUD experiment. The ice nucleating fraction INF is shown as a function of the ice saturation ratio S_{ice}. The curves are color-coded by the sulfate-to-nitrate molar ratio measured by the AMS. The time at which each saturation scan was performed is indicated in the legend.

5.4 CONCLUSIONS

Strong convective systems that develop during the Asian summer monsoon season can uplift primary aerosol particles as well as trace gases, leading to the formation of the so-called Asian Tropopause Aerosol Layer (ATAL, Vernier et al., 2011). In the upper troposphere, the formation of new aerosol particles from the condensation of gaseous precursors is facilitated by the low temperatures that induce supersaturated conditions for several gaseous species. Crystalline ammonium nitrate (AN) particles were recently observed within plumes of elevated NH_3 concentrations in the ATAL (Höpfner et al., 2019). Additionally, due to the expected increase in nitrate precursor emissions and the decrease of sulfate aerosols, the concentration of nitrate in the particle phase is expected to increase (Bauer et al., 2007).

The phase state of the AN particles, or of the AN coating on pre-existing seed particles, is of great importance in defining their direct and indirect radiative effect. Liquid AN particles can nucleate ice only via homogeneous freezing at high ice saturation ratios. In the crystalline state, however, AN particles remain solid up to $RH_w = 97\%$ (at $-50\,°C$, corresponding to $S_{ice} = 1.56$) and can thus initiate ice nucleation via heterogeneous nucleation at low ice saturation ratios ($S_{ice} \approx 1.2$) (Wagner et al., 2020). Which of the two ice nucleation modes dominates (i.e., homogeneous or heterogeneous) influences the microphysical properties of the cloud, and thus its optical thickness (see Section 1.1.3).

Pure ammonium nitrate particles are known to exist as supercooled aqueous solution droplets even at very low relative humidity (Martin, 2000; Cziczo and Abbatt, 2000). However, the crystallization of aqueous salt droplets can be induced by various heterogeneous mechanisms (e.g., Han et al., 2002; Davis et al., 2015), including the addition of salts that more readily crystallize (Ge et al., 1996). In particular, the addition of sulfate has been shown to initiate the crystallization of AN (Schlenker and Martin, 2005). This multicomponent crystallization mechanism has already been explored in previous studies, but generally using pre-mixed bulk solutions with different mole ratios of ammonium nitrate and ammonium sulfate for aerosol generation (Schlenker and Martin, 2005; Höpfner et al., 2019; Wagner et al., 2020). In this chapter, the work from Wagner et al. (2020) was extended by investigating the heterogeneous crystallization and ice nucleation ability of ammonium nitrate particles after co-condensation of gas-phase sulfuric acid and ammonia. The crystallization experiments were performed at the AIDA and the CLOUD chamber. The ice nucleation ability of the liquid and crystalline particles was probed with continuous flow diffusion chambers (INKA, mINKA, and SPIN) and with AIDA expansion cooling experiments at temperatures between $-40\,°C$ and $-56\,°C$.

In both the AIDA and CLOUD chamber experiments, the heterogeneous crystallization of AN particles with median diameters of about 1 μm and 100 nm was observed after the co-condensation of a small amount of sulfuric acid and ammonia. In particular, the CLOUD experiment showed that a sulfate concentration of 0.4 mol% in the AN particles is sufficient to initiate their crystallization and to turn the particles into efficient ice nucleating particles. This result is in agreement with the study of Wagner et al. (2020), where the AN crystallization was observed for particles with similar sulfate concentration (0.6 mol%) but larger diameter (≈ 0.9 μm).

The ice nucleation active surface site density n_S (INAS, see Section 2.2) calculated from the ice nucleation results presented in the previous sections is shown in figure 5.5. The n_S parameterization proposed by Wagner et al. (2020) for crystalline ammonium nitrate particles is shown as a gray shaded area. The new measurements agree with this parameterization, although particles with different diameters were used in the different experiments, supporting the validity of the INAS density approach for this particle type. n_S values for desert dust particles for a similar temperature range are also reported for comparison (Ullrich et al., 2017). The similar ice nucleation activity between the crystalline AN and desert dust particles, a recognized and well-studied INP type under cirrus conditions (Hoose and Möhler, 2012), highlights the importance of AN as a potential seed for cirrus cloud formation. Increasing concentrations of AN in the upper troposphere would lead to an increase of ice nucleating particles that can modify the formation mechanism and microphysical properties of cirrus clouds.
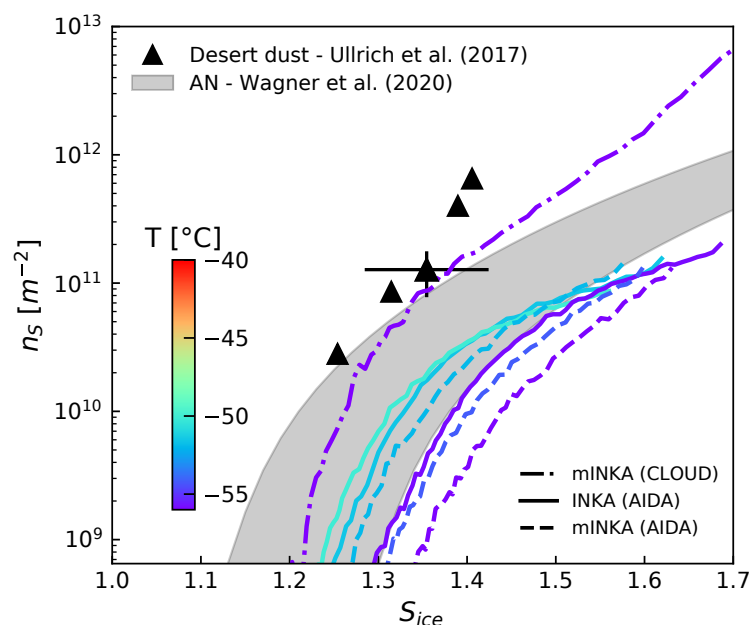
Figure 5.5: Ice nucleation active surface site density (n_S) versus ice saturation ratio (S_{ice}) for crystalline ammonium nitrate (AN) particles measured at temperatures between $-50\,°C$ and $-56\,°C$ (color-coded). The parameterization for crystalline AN particles presented by Wagner et al. (2020) is shown as a gray shaded area. The INAS density values for desert dust particles measured in a similar temperature range are also reported for comparison (Ullrich et al., 2017).

6 | SECONDARY ORGANIC AEROSOL PARTICLES

6.1 INTRODUCTION

Secondary organic aerosol (SOA) particles form directly in the atmosphere from the oxidation and gas-to-particle conversion of volatile organic compounds (VOCs). SOA particles represent an important component of the atmospheric aerosol, accounting for $50 - 85\%$ of the total organic aerosol burden (Jimenez et al., 2009).

Globally, atmospheric VOCs are dominated by biogenic sources such as plants, with isoprene (C_5H_8, IP) being the most abundant VOC (Seinfeld and Pandis, 2012; Steiner and Goldstein, 2007). Although the emission rate of α-pinene ($C_{10}H_{16}$, αP) is ten times lower compared to isoprene (60 vs $600\,Tg\,yr^{-1}$) the mass yield of compounds derived from terpenes, especially αP, is higher (Guenther et al., 2006). Pure αP and αP together with IP are investigated in this chapter as representative systems for biogenic SOA.

SOA particles from the oxidation of α-pinene are a well-characterized system often used as a reference for new particle formation, growth, hygroscopicity, and ice nucleation studies. In particular, growth rates and chemical composition of αP SOA particles formed under a range of tropospheric temperatures (from $25\,°C$ to $-25\,°C$) were investigated by Kristensen et al. (2017), Stolzenburg et al. (2018), and Huang et al. (2018). They found that at low temperatures a higher fraction of less oxidized and thus more volatile compounds partition to the particle phase compared to experiments performed at higher temperatures. Since compounds with lower volatility are believed to have a higher viscosity (Champion et al., 2019), uplifted SOA particles, i.e., particles formed at a higher temperature (e.g. in the boundary layer) and then transported to lower temperatures (e.g. to the upper troposphere), could be more viscous compared to those directly formed at low temperature.

The effect of relative humidity on the chemical composition of the particles is still largely unknown. Several studies have shown that relative humidity influences aerosol yield (e.g., Tillmann et al., 2010), but a detailed understanding of the effect on the chemical composition of the particles is still missing (Kidd et al., 2014; Huang et al., 2018). Kidd et al. (2014) investigated changes in the viscosity of αP SOA particles formed at different relative humidity (RH_w). Higher RH_w conditions at particle formation were associated with a decrease in the concentration of high molecular mass compounds, thus leading to a decrease in particle viscosity. Similar results were obtained by Huang et al. (2018).

The presence of isoprene leads to a reduction in the nucleation rate of new particles and in the aerosol yield (Kiendler-Scharr et al., 2009; McFiggans et al., 2019). Heinritzi et al. (2020) showed that the addition of isoprene leads to a reduction in the gas-phase concentration of molecules with 20 carbon atoms and to the appearance of molecules with a lower molecular weight (i.e. with 15 carbon atoms), which then also contribute to the growth of the particles. The presence of compounds with lower molecular weight could thereby decrease the viscosity of the particles (Koop et al., 2011).

The main sources of anthropogenic VOCs are fossil fuel production and combustion (about 40%), biomass burning (25%), use of biofuel (17%), and industrial processes (18%) (Koppmann, 2007). Major classes of anthropogenic VOCs are alkanes, alkenes, aromatic hydrocarbons, and oxygenated VOCs (Atkinson and Arey, 2003). Naphthalene ($C_{10}H_8$, NAPH), investigated in this chapter as representative for anthropogenic SOA, is a polycyclic aromatic hydrocarbon. Polycyclic aromatic hydrocarbon have a lower volatility compared to biogenic precursors and are classified as intermediate-volatility organic compounds (IVOC, see Section 2.3 and Donahue et al., 2009). Photooxidation of

---

Part of the results presented in this chapter have already been presented in the Master Thesis "Measurements of the ice nucleating ability of Secondary Organic Aerosol at the CERN CLOUD experiment" from Pia Bogert (2020).

naphthalene results in compounds with high molecular weight and low volatility that contribute to SOA formation (Chan et al., 2009; Xiao et al., 2021). Oxidation products of NAPH have been identified in urban particulate matter (Arey et al., 1989).

The phase state of organic particles is an important property that strongly affects climate, air quality, and health (see e.g. Section 2.3, Pöschl and Shiraiwa, 2015; Reid et al., 2018). Traditionally, atmospheric SOA particles were considered to be liquid but recent studies have found that they can also be in a glassy phase state (i.e., in an amorphous solid phase) at low temperature and/or relative humidity (e.g., Virtanen et al., 2010; Shiraiwa et al., 2017). The phase state of the SOA particles depends on their composition and the environmental conditions, resulting in a viscosity that spans several orders of magnitude for different atmospheric SOA particles (Koop et al., 2011; Shiraiwa et al., 2011). Viscosity determines the hygroscopic behavior of aerosol particles and defines their ability to form clouds (e.g., Mikhailov et al., 2009; Murray et al., 2010). Due to the slow diffusion of water and its plasticizing effect, steep radial gradients in water concentration, called diffusion fronts, develop in the particles (O'Meara et al., 2016; Bastelberger et al., 2017). Depending on their viscosity and the time scale under consideration, highly viscous particles can thus be in non-equilibrium with the surrounding conditions.

How this complex water uptake behavior influences the ice nucleation ability of glassy particles in the atmosphere is still not fully understood. If organic aerosol particles remain in a glassy phase state at ice supersaturated conditions, heterogeneous ice nucleation can occur on their solid surface. For example, it has been shown that some classes of highly viscous single organic compounds (e.g., citric acid, raffinose, and levoglucosan) can initiate heterogeneous ice nucleation at low temperatures ($T < -55\,°C$), with ice saturation ratios for the nucleation onset well below the homogeneous freezing limit ($S_{ice} = 1.2 - 1.5$) (e.g., Murray et al., 2010; Wilson et al., 2012). If the particles start to take up water and an aqueous shell forms, ice nucleation can either occur heterogeneously at low ice saturation ratios via immersion freezing or at higher S_{ice} via homogeneous freezing of the aqueous, sufficiently diluted shell (Berkemeier et al., 2014; Knopf et al., 2018). Fowler et al. (2020) suggested that the homogeneous freezing onsets of viscous SOA particles deviate from the water-activity based parameterization for aqueous solution droplets (Koop et al., 2000) depending on the size of the particles and the humidification rate.

The majority of previous ice nucleation measurements performed with αP SOA particles showed ice formation only at or above the homogeneous freezing threshold for aqueous solution droplets (Möhler et al., 2008; Prenni et al., 2009; Ladino et al., 2014; Wagner et al., 2017; Charnawskas et al., 2017). However, Ladino et al. (2014) showed that αP SOA have an enhanced ice nucleation ability if pre-cooled, suggesting that their viscosity may play a role in defining their ice nucleation behavior. Recently, Piedehierro et al. (2021) measured the ice nucleation ability of αP SOA particles generated with a range of different oxidation mechanisms (i.e. with ozone or hydroxyl radicals), different oxidation levels, and exposure to different relative humidity conditions. In all cases, the measured ice nucleation onset was at or above the homogeneous freezing threshold. Only Ignatius et al. (2016) measured lower ice nucleation onsets for αP SOA particles compared to aquoues sulfuric acid solution droplets and suggested that heterogeneous freezing was the dominant ice nucleation mechanism. Also oxidation products of isoprene, namely isoprene-epoxydiol (IEPOX) and 2-Methyltetrol, have been recently identified as efficient ice nucleating particles at about $-46\,°C$ (Wolf et al., 2020). Regarding anthropogenic SOA, Wang et al. (2012) investigated the water uptake and ice nucleation ability of naphthalene-derived SOA particles at temperatures between $-25\,°C$ and $-70\,°C$. The particles were generated in a flow reactor at room temperature and $RH_w \approx 35\,\%$, collected on hydrophobically coated glass plates, and exposed to controlled temperature and relative humidity conditions in an ice nucleation cell. At temperatures between $-31\,°C$ and $-43\,°C$, the NAPH SOA particles took up water at about $80 - 85\,\%$ and initiated ice nucleation via immersion freezing. At lower temperatures, the particles nucleated ice heterogeneously at lower ice saturation ratios ($S_{ice} = 1.36 - 1.52$) compared to the onset for homogeneous freezing of aqueous solution droplets.

The experiments presented in this chapter were performed at the CLOUD facility during the CLOUD14 campaign and investigated the ice nucleation ability of secondary aerosol particles derived from three different systems: α-pinene (αP), mixtures of α-pinene and isoprene (αP+IP), and

naphthalene (NAPH) (see Table 6.1). The ice nucleation ability of the particles was measured with three continuous flow diffusion chambers (CFDCs) through ice saturation ratio scans performed at temperatures between $-40\,°C$ and $-65\,°C$. Experiments with αP SOA were performed at different temperatures ($5\,°C$, $-10\,°C$, $-31\,°C$, and $-50\,°C$) and relative humidities ($RH_w = 2\,\%$, $20\,\%$, and $60\,\%$) to investigate how the thermodynamic conditions at which the SOA particles form may influence their chemical composition and thus their ice nucleation ability. Since SOA particles in the atmosphere are likely to be mixtures of several compounds, the effect of isoprene admixture to the αP system was investigated in two experiments performed at $-10\,°C$ and $-30\,°C$. These experiments are the first ice nucleation measurements of mixed αP and IP SOA particles. Finally, two experiments were performed with NAPH SOA particles as representative system for anthropogenic SOA. NAPH-derived SOA particles were generated at $6\,°C$ and $-10\,°C$ and low relative humidity conditions.

6.2 EXPERIMENTAL METHODS

6.2.1 Aerosol generation and characterization

The aerosol particles were generated in the CLOUD chamber from the oxidation and gas-to-particle conversion of gaseous precursors. The description of the CLOUD chamber, the list of instruments used during the CLOUD14 campaign, and the description of a typical experiment can be found in Section 3.3. A list of the experiments presented in this chapter can be found in Table 6.1, summarizing the thermodynamic conditions inside the CLOUD chamber and the range of gas precursor concentrations used in each experiment. The nucleation and growth of the SOA particles to certain size was controlled by increasing the concentration of the gas precursors and by initiating the production of hydroxyl radicals ($\cdot$OH) upon activation of the light system. After the nucleation and growth period ($2-3\,h$), the ice nucleation measurements were started and lasted for about $4-7\,h$.

During the measurement period, the aerosol number concentration constantly decreased due to wall and sampling losses (see Section 3.3.2). Because the aerosol particles serve as a condensation sink for the gas precursors, an excessive decrease in the particle concentration can lead to the nucleation of new particles. Such behavior was observed in a couple of runs, leading to the transformation of the particle size distribution from a uni-modal to a multi-modal log-normal distribution. To limit this effect, the concentration of the gas precursors was reduced once the particles reached a size of about $100\,nm$. The injection of the gas precursors was never completely stopped to prevent the evaporation of semi-volatile compounds from the particles.

The gas-phase concentration of the precursor vapors was measured with a proton transfer reaction mass spectrometer[1] (PTR-MS). The aerosol number concentration and particle size distribution were measured with a condensation particle counter (CPC) and a scanning mobility particle sizer (SMPS), respectively. The chemical characterization of the formed particles was performed with different aerosol mass spectrometers. The bulk composition of the aerosol particles was measured with an Aerosol Mass Spectrometer (AMS). The chemical characterization at the molecular level was performed with three different instruments, (i) a Filter Inlet for Gases and AEROsols (FIGAERO) coupled with a time-of-flight chemical ionization mass spectrometer (CIMS), (ii) an Extractive ElectroSpray Ionization time-of-flight mass spectrometer (EESI-TOF), and (iii) a Thermal Desorption-Differential Mobility Analyzer (TD-DMA) coupled to a nitrate CIMS. The full list of instruments employed during the CLOUD14 campaign can be found in Table 3.1. Results on the chemical composition of the particles will not be presented in this thesis and will be analyzed in relation to the ice nucleation ability of the particles in a future study.

---

1 PTR-MS data were collected and analyzed by Wiebke Scholz (University of Innsbruck).

Table 6.1: List of the experiments presented in this chapter. Temperature (T), relative humidity (RH$_w$), and ozone concentration correspond to the average values measured during the experiments. Concentrations of α-pinene (αP), isoprene (IP), and naphthalene (NAPH) refer to the peak values.

Run number	T [°C]	RH$_w$	O$_3$ [ppb]	αP [ppb]	IP [ppb]	NAPH [ppb]
2201	5	2 %	70	10.7	–	–
2211	−10	10 %	112	2	–	–
2221	−31	20 %	102	5.7	–	–
2222	−50	18 %	100	5.0	–	–
2224	−29	62 %	107	6.1	–	–
2223	−48	65 %	110	8.4	–	–
2210	−10	39 %	110	2.6	21.1	–
2220	−30	21 %	100	6.7	33	–
2238	6	18 %	263	–	–	23
2240	−10	2 %	497	–	–	35

6.2.2 Ice nucleation measurements

The ice nucleation measurements were performed with three continuous flow diffusion chambers (CFDCs), namely mINKA, SPIN[2] (SPectrometer for Ice Nuclei), and PINCii[3] (Portable Ice Nucleation Chamber II). The description of the CFDC working principle and mINKA can be found in Sections 3.4.1 and 3.4.2, respectively. SPIN (Stetzer et al., 2008; Garimella et al., 2016) and PINCii (Chou et al., 2011) are two vertically-oriented parallel-plate CFDCs. Both chambers have a 100 cm long diffusion section. The evaporation sections of SPIN and PINCii are 25 cm and 44 cm long, respectively. To maximize the exposure time of the sampled particles to the supersaturated conditions, mINKA was operated without an evaporation section (see Section 3.4.2 for more details). In all instruments, the plate-to-plate distance is 1 cm (without ice-coating layer). SPIN is equipped with a linear depolarization optical particle counter (OPC) that uses four optical detectors for counting, sizing, and differentiating unactivated aerosol particles, droplets, and ice crystals in the $0.4 - 15\,\mu m$ size range. In PINCii, aerosol particles and ice crystals are detected using a Lighthouse OPC (Remote 3104). The OPC counts and classifies the particles into four different size channels ($0.3 - 1\,\mu m$, $1 - 3\,\mu m$, $3 - 5\,\mu m$, and $> 5\,\mu m$). The details of the OPC mounted on mINKA and its custom-made calibration have been described in Section 3.4.3. During the CLOUD14 campaign, the minimum obtainable aerosol lamina temperature was about −65 °C, −60 °C, and −50 °C for mINKA, SPIN, and PINCii, respectively. A description of the uncertainties related to temperature and ice saturation ratio of the aerosol lamina in mINKA measurements can be found in Section 3.4.4; for the uncertainties in SPIN and PINCii measurements the reader is referred to Korhonen et al. (2020).

Ice nucleation measurements were performed sampling the polydispersed aerosol particles from the CLOUD chamber with insulated and actively cooled sampling lines (see Section 3.3.1). The ice nucleation ability of the particles was measured at temperatures between −40 °C and −65 °C with ice saturation ratio scans (each lasting $\approx 20\,min$) for a time period of $4 - 7\,h$. The CFDCs were operated with different experimental protocols developed to get the best performance from each instrument, thus obtaining stable temperature conditions in the instrument and minimizing the background ice counts. Subsequent saturation ratio scans at different temperatures were performed by progressively decreasing the aerosol lamina temperature in mINKA and PINCii. In SPIN, instead, the measurements were performed by increasing the aerosol lamina temperature. When comparing the ice nucleation ability measured by the CFDCs during the same experiment and at the same aerosol lamina temperature, it is therefore necessary to consider that the individual measurements may partly have a time offset of a few hours, so that changes in the chemical composition or size distribution of the particles must be taken into account in the interpretation of the results.

The ice particle number concentration was measured with optical particle counters. All particles larger than $1\,\mu m$ detected by the OPCs are interpreted as ice crystals. During the CFDCs ice

---

2 SPIN data collection and analysis was performed by Dr. Ana A. Piedehierro and Dr. André Welti (Finnish Meteorological Institute).

3 PINCii data collection and analysis was performed by Zoé Brasseur (Helsinki University).

saturation ratio scans, the hygroscopic growth of the SOA particles above $1\,\mu m$ can be excluded because of the small size of the investigated particles (smaller than $400\,nm$ in diameter) and the low hygroscopic growth factor (ratio of the wet to dry particle diameter) typically observed for SOA particles ($D_{RH_w=95\%}/D_{dry} < 1.3$, Varutbangkul et al., 2006). The background ice concentration was evaluated before each single humidity scan in mINKa and PINCii, and once before the start of each experiment in SPIN, by measuring the ice number concentration while filtered particle-free air was sampled in the instruments. The fraction of particles that initiated ice nucleation (ice nucleating fraction, INF) is calculated as the ratio of the ice crystal number concentration to the total number of particles with diameter larger than $10\,nm$, obtained by integration of the particle number size distribution from the SMPS data.

To directly compare the performance of the three CFDCs, measurements with a large time offset were discarded and only ice nucleation measurements performed at a similar temperature ($\pm 2\,°C$) and time interval ($\pm 30\,min$) were selected among all the experiments performed during the CLOUD14 campaign. Additionally, only experiments in which the particles nucleated ice at or above the homogeneous freezing limit are considered. The comparison between mINKA and SPIN comprises 22 ice saturation ratio scans performed at temperatures between $-38\,°C$ and $-54\,°C$; the comparison between PINCii and SPIN comprises 10 scans performed at temperatures between $-42\,°C$ and $-46\,°C$. Figure 6.1a shows two exemplary comparisons among SPIN and mINKA (blue and green curves, respectively). Figure 6.1b shows the comparison between SPIN and PINCii (blue and red curves, respectively).
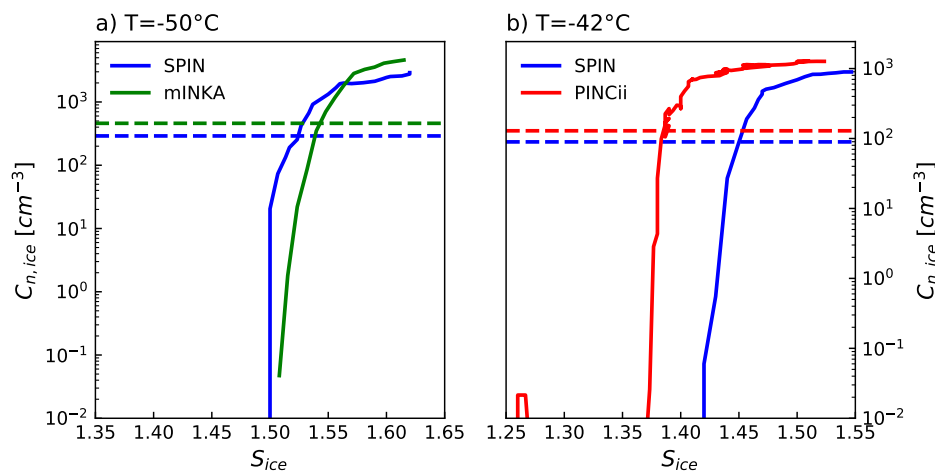
Figure 6.1: Ice crystal number concentration $C_{n,ice}$ measured as a function of the ice saturation ratio S_{ice}. **a)** Comparison between two ice saturation ratio scans performed with mINKA (green) and SPIN (blue) at the nominal temperature of $-50\,°C$ and with the same aerosol particles. **b)** Comparison between two measurements of PINCii (red) and SPIN (blue) at $\approx -42\,°C$. The horizontal dashed lines correspond to the ice number concentration equal to $10\,\%$ of the peak values reached at the end of the ice saturation ratio scans of the respective instruments.

The measured ice number concentration $C_{n,ice}$ is shown as a function of the ice saturation ratio S_{ice}. The sudden nucleation of a large number of ice crystals at a critical ice saturation ratio suggests that the particles froze homogeneously (see Section 3.4.7). The term homogeneous freezing referred to highly viscous particles is here used to indicate either the freezing of the completely liquefied particles or the homogeneous freezing of an outer aqueous shell. The horizontal dashed lines denote the ice number concentration that corresponds to $10\,\%$ of the peak value reached at the end of the ice saturation ratio scans of the respective instruments. The associated ice saturation ratio value is identified in the following as the ice onset condition. The ice-activation curves presented in Figure 6.1 are representative of all the experiments selected for the comparison. The homogeneous freezing onsets of the selected experiments are reported in Figure 6.2a as a function of temperature. Different symbols identify the three different CFDCs and colors correspond to the different experiments. Corresponding ice onsets are shown with the same color and connected with lines to facilitate the comparison. The conditions corresponding to water saturation ($RH_w = 100\,\%$) and the
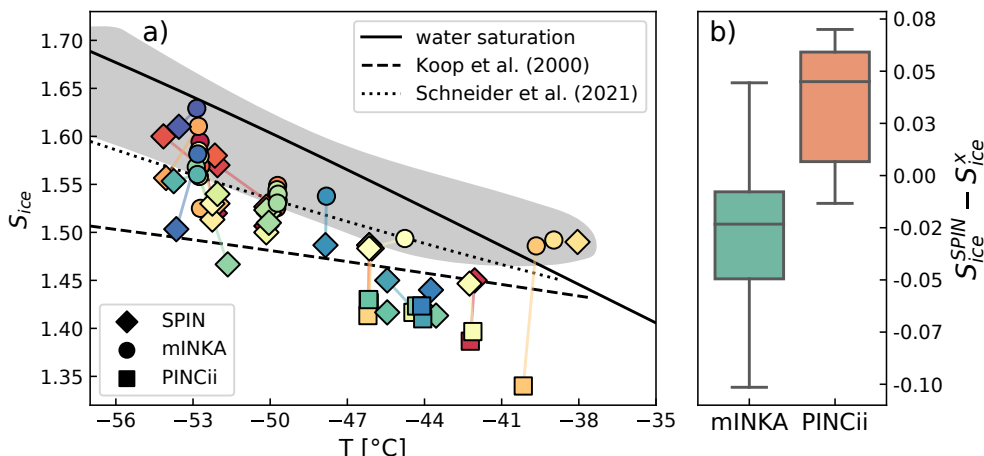
Figure 6.2: a) Ice onset conditions as a function of temperature for the selected experiments (see main text for more details). Symbols identify the instrument (see legend) and colors represent different CLOUD experiments. Corresponding ice onsets are plotted with the same color and connected with lines. The gray shaded area corresponds to the range of conditions at which homogeneous freezing of aqueous solution droplets was measured in previous experiments with INKA and mINKA. **b)** box plot of the difference between the homogeneous ice onset measured by SPIN and mINKA (green) and by SPIN and PINCii (red). The box shows the quartiles of the data, the horizontal line inside the box is the median value of the distribution, and the whiskers extend to show the rest of the distribution.

two homogeneous freezing parameterizations suggested by Koop et al. (2000) and Schneider et al. (2021) (specifically derived for sulfuric acid solution droplets) are also shown. The range of $S_{ice} - T$ conditions at which homogeneous freezing of aqueous solution droplets (H_2SO_4 and NH_4HSO_4, median particle diameter 1 μm) was measured with mINKA and its laboratory-based version INKA is shown as gray-shaded area (see Section 3.4.7 for more details). Overall, the instruments show a good agreement, with most of the measurements (> 95 %) falling inside the uncertainty ranges (not shown for clarity). Figure 6.2b shows the overall statistics obtained from the inter-comparison experiments in a box plot. The ice onset measured by SPIN is chosen as reference and compared to the values obtained by mINKA ($S_{ice}^{SPIN} - S_{ice}^{mINKA}$, green box) and PINCii ($S_{ice}^{SPIN} - S_{ice}^{PINCii}$, red box). The ice onsets measured with mINKA are, on average, slightly higher compared to those measured by SPIN, with a median difference equal to -0.02 (see Figure 6.2b). The ice onsets measured with PINCii, instead, are slightly lower compared to the SPIN measurements, with a median difference of $+0.04$ (see Figure 6.2b).

6.3 ICE NUCLEATION RESULTS

6.3.1 Biogenic SOA

In the first four experiments, the αP SOA particles were formed at different temperatures and low relative humidity to simulate different nucleation conditions (experiments 2201, 2211, 2221, and 2222 in Table 6.1). In all those experiments, the particles were likely in a glassy state inside the CLOUD chamber (Järvinen et al., 2016; Petters et al., 2019). The ice activation curves from the four experiments are summarized in Figure 6.3 with different colors (see legend). The results are divided by instrument (columns) and by the temperature at which the ice nucleation ability was measured (rows). Regardless of the thermodynamic conditions inside the CLOUD chamber, the sharp increase in the ice number concentration at a certain critical ice saturation ratio indicates that all the generated αP SOA particles froze homogeneously at all the investigated temperatures in all the three CFDCs.
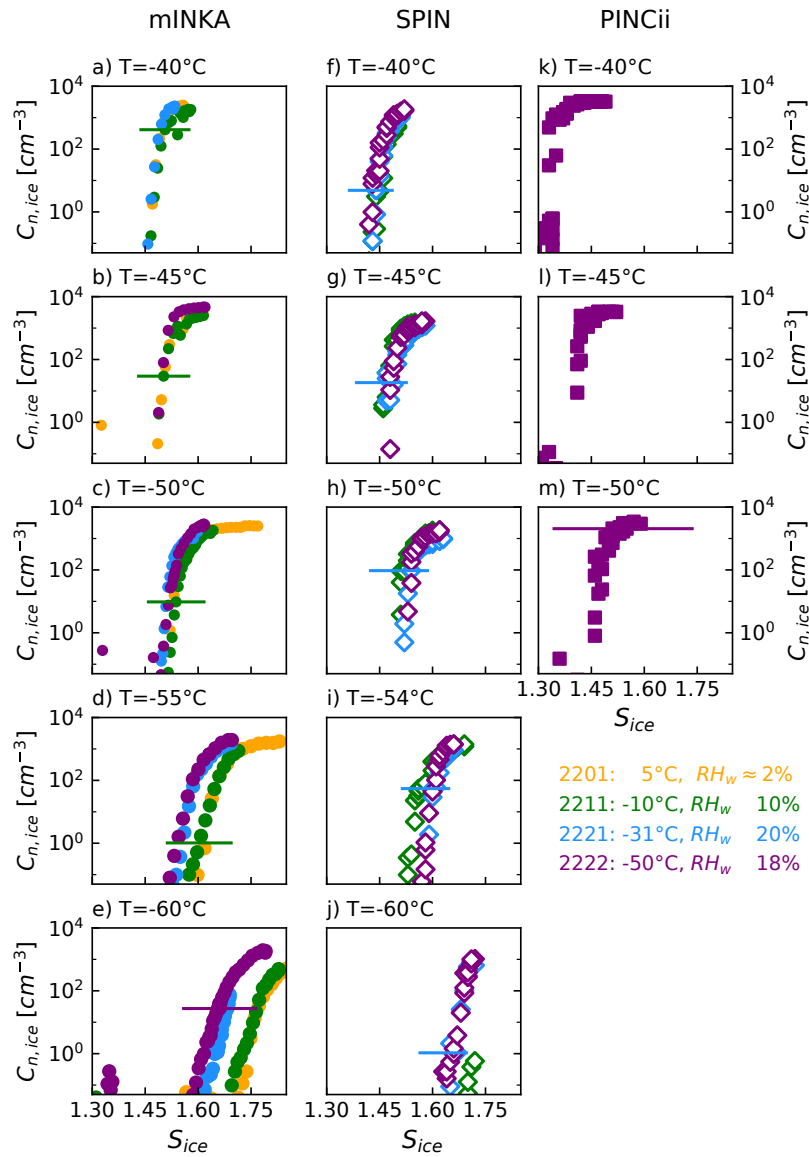
Figure 6.3: Ice number concentration $C_{n,\,ice}$ as a function of the ice saturation ratio S_{ice} measured with mINKA (**a-e**), SPIN (**f-j**), and PINCii (**k-m**) at temperatures between $-40\,°C$ and $-60\,°C$ for αP SOA particles formed at $5\,°C$ (yellow), $-10\,°C$ (green), $-30\,°C$ (blue), and $-50\,°C$ (purple) in the CLOUD chamber. The sharp increase in the ice number concentration at a certain critical ice saturation ratio indicates that all the generated αP SOA particles froze homogeneously.

The ice onset conditions, defined as the ice saturation ratio at which the ice crystal number concentration reaches 10 % of the peak value, are summarized in Figure 6.4. Similar to the experiments selected for the inter-comparison presented in the previous section, the ice onset values measured by PINCii (squares) are slightly lower than those measured by mINKA (circles) and SPIN (empty diamonds), especially at temperatures above −45 °C. However, the shape of the ice-activation curves measured by PINCii (Figure 6.3k-m) suggests that ice nucleation occurred via homogeneous freezing, in agreement with the other instruments. The measurements from mINKA and SPIN nicely overlap over the whole temperature range covered by the two instruments.

For $T > −55$ °C, no significant difference is detected between the different experiments and the ice onsets are in agreement with the homogeneous freezing parameterization developed for aqueous sulfuric acid solution droplets by Schneider et al. (2021) (black dotted curve). For $T < −55$ °C, the ice onset conditions start to deviate from the homogeneous freezing parameterization towards higher S_{ice} values. A larger offset is observed for the particles formed at a higher temperature in the CLOUD chamber (green and yellow symbols).

The deviation from the homogeneous freezing parameterization at low temperatures could be partially explained by the technical limitations of the CFDCs. At low temperature and high ice saturation ratios, the temperature difference between the instrument walls is large (about 17 °C at −60 °C for $S_{ice} = 1.8$) and a turbulent flow is likely to develop in the instrument due to buoyancy effects. A turbulent flow inside the instrument leads the aerosol sample to spread outside of the ideal aerosol lamina section and to experience a wider range of thermodynamic conditions (Garimella et al., 2017). Indeed, the more tilted slope of the activation curves at low temperatures, as visible in Figure 6.3, could be an indication that an increasingly larger fraction of the aerosol particles is outside of the aerosol lamina and experiences a lower ice saturation ratio. Furthermore, the residence time of the aerosol particles in the instrument also depends on the thermodynamic conditions. At −45 °C and $S_{ice} = 1.1$, the residence time in mINKA is about 8 s, while it drops to about 5 s at −60 °C and $S_{ice} = 1.8$. The shorter residence time implies that only higher ice nucleation rates can be measured (see Section 3.4.5 for more details) and that the particles have less time to equilibrate to the thermodynamic conditions inside the instrument. The deviation towards higher S_{ice} onsets at $T < −55$ °C could therefore be related to the incomplete liquefaction of the initially glassy SOA particles on the experimental time scale of the CFDC measurements. However, measurements performed under the same S_{ice} and T conditions and with the same flow settings are affected by the same systematic uncertainties, so that relative variations between experiments with different aerosol types or aerosol nucleation conditions can still be indicative.

The higher ice onsets measured at low temperature by mINKA for particles nucleated at 5 °C and −10 °C could indicate a higher viscosity of the particles due to their different chemical composition. Chemical composition analysis from particle-phase mass spectrometers will be considered in future analyses to elucidate the potential role of particle composition.

The results from the previous literature studies performed with αP SOA particles are reported in black in Figure 6.4. The low S_{ice} onsets measured by Ignatius et al. (2016), attributed to a heterogeneous freezing mode, agree with PINCii measurements, but the shape of the activation curves in PINCii indicate that homogeneous freezing was the most likely ice nucleation mechanism. At lower temperatures, previous measurements indicate that the particles nucleated ice at lower ice saturation ratios, in better agreement with the parameterization by Schneider et al. (2021). However, the comparison between different studies is difficult due to the different methods of generation of the SOA particles (e.g. in cloud chambers or flow tubes) and the different techniques used for the ice nucleation measurements (e.g. with expansion cooling experiments or with CFDCs). During an AIDA expansion run, for example, the thermodynamic conditions inside the chamber change relatively slow and the particles have more time to adjust to the changing saturation ratios, and for the, at least, partial liquefaction of the particles in the outer layers. In a CFDC, instead, new particles are continuously sampled and only have a few seconds to equilibrate to the increasing saturation ratios.

Based on the literature results presented in Section 6.1, the experiments performed at low relative humidity with pure αP are expected to originate the particles with the highest viscosity among the biogenic systems investigated here, and thus with the highest propensity to heterogeneously form

ice crystals. Nevertheless, the pure αP SOA particles formed at low RH_w only froze homogeneously at high ice saturation ratios. High relative humidity conditions inside the CLOUD chamber are expected to decrease the viscosity of the particles through the plasticizing effect of water (Gordon and Taylor, 1952) and the decrease in the concentration of high molecular weight compounds (Kidd et al., 2014). The occurrence of a heterogeneous ice nucleation mode for the pure αP SOA particles formed at high relative humidity in the CLOUD chamber is thus not likely.

The relative humidity effect was investigated in experiments 2223 and 2224, αP SOA particles were generated in the CLOUD chamber at $-50\,°C$ and $-30\,°C$, and about 60 % relative humidity with respect to liquid water. At such low temperatures, αP SOA particles are expected to be in a glassy state even at high relative humidity conditions (Järvinen et al., 2016; Petters et al., 2019). The shape of the ice-activation curves for the experiments performed at high relative humidity (not shown) resemble those reported in Figure 6.3, indicating that, as expected, also these particles only froze homogeneously. The ice onset conditions are reported in Figure 6.5 (light green and pink) together with the ice onsets for particles nucleated at the same temperatures but low relative humidity (blue and purple). In agreement with the experiments at low RH_w, PINCii measured lower ice onsets (squares) compared to the other two CFDCs (circles for mINKA and empty diamonds for SPIN). For $T > -55\,°C$, the ice onsets from mINKA and SPIN agree with the homogeneous freezing parameterization for aqueous sulfuric acid particles from (Schneider et al., 2021). For $T < -55\,°C$, similarly to the previous experiments, the ice onset values start to deviate towards higher S_{ice} values from the parameterizations. The ice nucleation onsets of the SOA particles formed at high relative humidity (light green and pink symbols) deviate from the homogeneous freezing parameterizations even more that those of the SOA particles formed at low RH_w and thus expected to be more viscous. This result suggests that the incomplete liquefaction of the particles on the experimental time scale less likely explains the offset from the homogeneous freezing parametrizations.

To simulate particles with a more atmospherically relevant composition, isoprene (IP) was added to the αP system in two experiments performed at $-10\,°C$ (experiment 2210) and $-30\,°C$ (experiment 2220). On the one hand, Heinritzi et al. (2020) have shown that the addition of isoprene introduces in the system compounds with a lower molecular weight that are thus expected to decrease the viscosity of the formed particles (Champion et al., 2019; Galeazzo et al., 2021). On the other hand, Wolf et al. (2020) suggested that isoprene-derived organic compounds can initiate heterogeneous ice formation at low temperatures.

The effect of IP on the chemical composition of the particles formed at $-30\,°C$ is presented in Caudillo et al. (2021). In particular, compounds with a lower molecular weight were found in the particles when IP was added to the αP system. However, as summarized in Figure 6.6, no evident changes were detected in the ice nucleation ability of the particles. The observed ice onsets are in the same range of conditions at which pure αP particles nucleated ice. Furthermore, no heterogeneous ice formation was measured, indicating that either the isoprene-derived compounds present in the particles investigated here have a different ice nucleation ability compared to those investigated by Wolf et al. (2020), or that the presence of αP have suppressed their ice nucleation ability.

The ice nucleation onsets of the particles containing isoprene-derived compounds are still largely offset from the homogeneous freezing parametrizations, although particles with a lower viscosity are expected to form in the αP+IP system compared to the pure αP SOA. This result, together with the results for pure αP SOA particles formed at high RH_w, suggests that the incomplete liquefaction of the particles on the experimental time scale less likely explains the offset from the homogeneous freezing parametrizations.

6.3.2 Anthropogenic SOA

The ice nucleating fraction (INF) as a function of the ice saturation ratio measured by mINKA for SOA particles derived from αP and NAPH is compared in Figure 6.7. The curves are color-coded by the temperature at which the ice nucleation ability was measured. In contrast to the biogenic system, the INF of the NAPH-derived particles slowly increases with increasing ice saturation ratio. Also, two different regimes are visible in the INF of the NAPH-derived particles for $T < -52\,°C$. The first ice nucleation mode, which was not detected in the biogenic system, only involves a small fraction
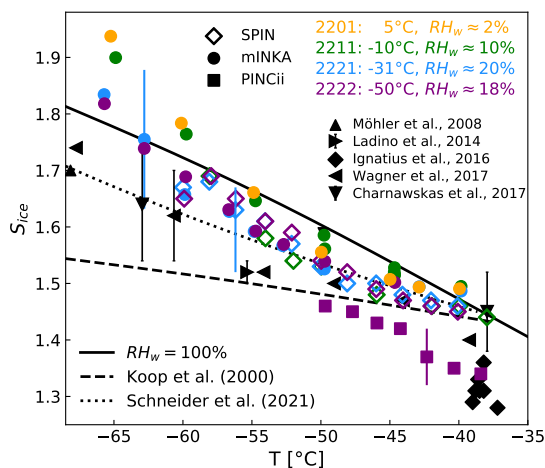
Figure 6.4: Comparison of the ice onset conditions for homogeneous freezing of αP SOA particles formed at different temperatures in the CLOUD chamber (colors). The measurements were performed by three continuous flow diffusion chambers (CFDCs, symbols). Literature results are reported in black.
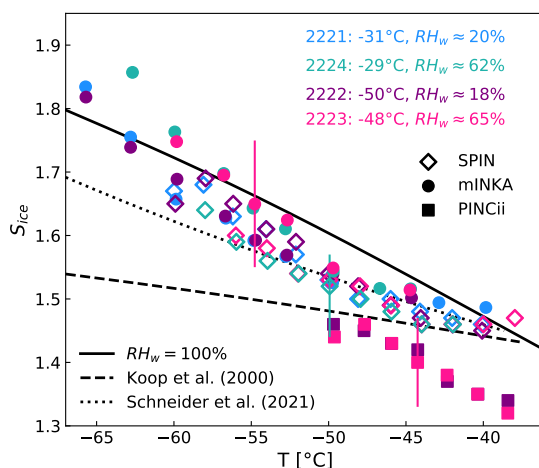
Figure 6.5: Comparison of the ice onset conditions for homogeneous freezing of αP SOA particles formed at two different temperatures, and low and high relative humidity in the CLOUD chamber (colors), as measured by the three CFDCs (symbols).
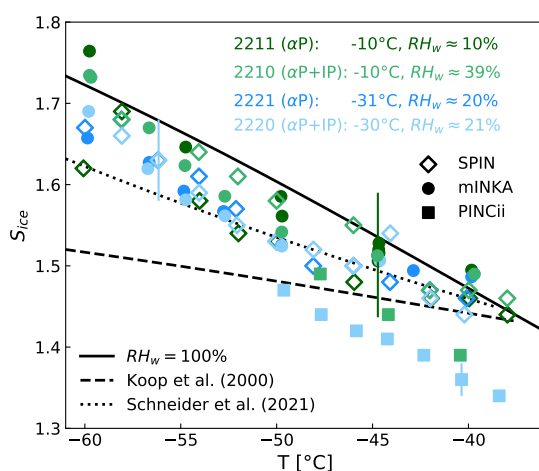
Figure 6.6: Comparison of the ice onset conditions for homogeneous freezing of αP and αP+IP SOA particles formed at −30 °C and −50 °C in the CLOUD chamber (colors) measured by the three CFDCs (symbols).
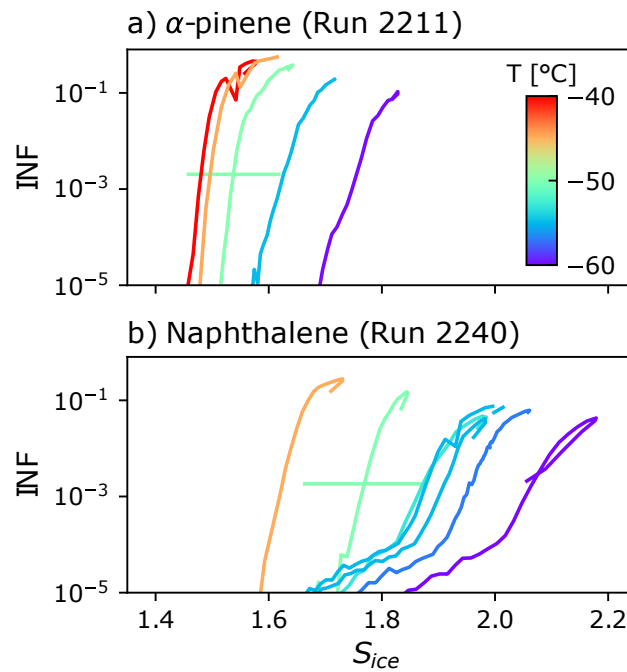
Figure 6.7: Ice nucleating fraction (INF) as a function of the ice saturation ratio (S_{ice}) measured by mINKA for **a)** α-pinene and **b)** NAPH-derived SOA particles.

of the particles and might be interpreted as a weak heterogeneous ice nucleation mode. The second nucleation mode at higher ice saturation ratios, i.e., the homogeneous nucleation mode, is sharper and involves a larger fraction of the aerosol population. The onsets of both the heterogeneous and homogeneous freezing modes are at or above water saturation conditions ($RH_w = 100\%$) and are probably explained by the higher viscosity of the NAPH SOA particles compared to the biogenic systems. A higher viscosity of the NAPH-derived SOA particles could also explain the heterogeneous ice nucleation mode, occurring either due to deposition nucleation on the glassy surface or via immersion freezing of the glassy core surrounded by an aqueous shell. If the particles remain in a glassy state at even higher ice saturation ratios, the sharp increase in the ice number concentration, interpreted as homogeneous freezing, could indeed originate from the homogeneous freezing of an aqueous outer shell rather than the whole liquefied particles, or from condensation and freezing of pure water on their still solid surface.

The summary of the two experiments performed with NAPH SOA particles is presented in Figure 6.8. The $S_{ice} - T$ trajectories of the humidity scans from the three CFDCs are color-coded by the ice nucleating fraction (INF). Panels a-c refer to the particles formed at 6 °C and $RH_w = 18\%$ (experiment 2238), panels d-f show the ice nucleation ability of the particles formed at -10 °C and $RH_w = 2\%$ (experiment 2240). The black dashes in Figure 6.8a and 6.8d (i.e. in the mINKA measurements) indicate the ice onset conditions, here defined for an ice nucleating fraction of 0.1 %. In both SPIN and PINCii, the ice crystals also appeared at a higher ice saturation ratio compared to the experiments with biogenic SOA, similar to the measurements with mINKA as discussed above. The difference is especially evident in SPIN measurements for experiment 2240 (panel e), for which at temperatures below about -50 °C no ice nucleation is detected in the range of ice supersaturation investigated (up to water saturation).

Previous ice nucleation measurements with NAPH-derived SOA particles, with similar diameters and in the same temperature range investigated here, were performed by Wang et al. (2012). The authors also reported of a heterogeneous ice nucleation mode at temperatures below about -45 °C. The ice onset conditions, defined in correspondence of the first ice nucleation event observed, ranged from $S_{ice} = 1.36$ to $S_{ice} = 1.52$.
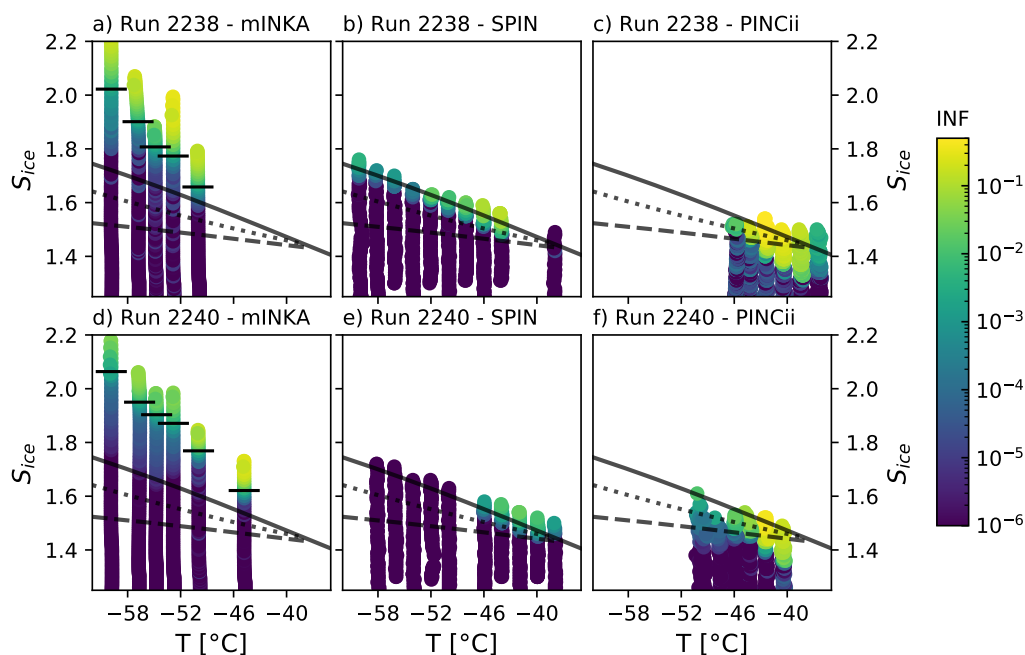
Figure 6.8: $S_{ice} - T$ trajectories color-coded by the ice nucleating fraction (INF) measured by mINKA (**a, d**), SPIN (**b, e**), and PINCii (**c, f**) for NAPH-derived SOA particles. Results for the particles formed at 6 °C and $RH_w = 18\%$ (run 2238) are shown in the upper panels (**a-c**), results for the particles formed at −10 °C and $RH_w = 2\%$ (run 2240) are shown in the lower panels (**d-f**). Black dashes in panels a and d indicate the ice onsets defined for INF = 0.1 %.

6.4 CONCLUSIONS

The ice nucleation ability of secondary organic aerosol (SOA) particles formed from the oxidation of three different systems, namely from α-pinene (αP), α-pinene and isoprene (αP+IP), and naphthalene (NAPH), was investigated in this chapter. Particles were generated and characterized in the CLOUD chamber, a unique facility for aerosol nucleation studies. Ice nucleation measurements were performed at temperatures between −40 °C and −65 °C with three different continuous flow diffusion chambers (mINKA, SPIN, and PINCii). For the first time, the comparison of homogeneous ice nucleation onsets measured with three CFDCs of different geometry was performed at temperatures between −38 °C and −54 °C. Overall the measurements are in good agreement, with a median difference in the ice saturation ratio onsets of less than 0.05. mINKA and SPIN compared better, while the ice onsets measured by PINCii are probably affected by a small negative offset.

The experiments were designed to investigate how changes in the chemical properties of SOA particles, generated at different thermodynamic conditions and from different organic compounds, influence their ice nucleation ability. αP-derived SOA particles, a well-characterized system often considered as a reference for SOA studies, were formed at 5 °C, −10 °C, −31 °C, and −50 °C and low relative humidity conditions. Experiments at −30 °C and −50 °C were performed also at high relative humidity ($RH_w \approx 60\%$). Although it is to be expected that particles formed at different thermodynamic conditions are composed of molecules with different molecular weights and volatility (e.g., Stolzenburg et al., 2018; Kidd et al., 2014), there was no significant effect on their ice nucleation ability. In fact, all the αP-derived SOA particles here investigated nucleated ice only via homogeneous freezing at high ice saturation ratios ($S_{ice} = 1.5 - 1.9$ in the temperature range from −45 °C to −65 °C). The range of ice saturation ratios at which the αP-derived SOA particles nucleated ice is comparable to the homogeneous freezing onsets previously measured for aqueous solution droplets.

The addition of isoprene to the αP system was accompanied by the occurrence of compounds with a lower molecular weight in both the gas and particle phase (Caudillo et al., 2021), suggesting that less viscous particles were formed. Homogeneous ice nucleation onsets similar to those for the pure αP system were measured.

The parameterization for the homogeneous freezing of aqueous sulfuric acid droplets suggested by Schneider et al. (2021) nicely describes the homogeneous freezing onsets presented in this chapter for temperatures above about $-55\,°C$. For lower temperatures, the measured ice onsets are higher than the parameterization and cover a larger range of ice saturation ratios. Although the αP SOA particles formed at high relative humidity or in presence of isoprene were expected to have a lower viscosity compared to the αP SOA particles formed at low relative humidity, their homogeneous freezing onsets still showed a positive offset from the parameterizations for homogeneous freezing. This result suggests that the short residence time of the particles in the instrument and their incomplete liquefaction is less likely to be the cause of the deviation.

A small fraction of naphthalene SOA particles initiated ice nucleation heterogeneously but at relatively high ice saturation ratios (about $S_{ice} = 1.9$ at $-58\,°C$). The majority of the NAPH particles nucleated ice at higher ice saturation ratios compared to the biogenic SOA, pointing to a higher viscosity of the NAPH-derived SOA particles.

The experiments presented here indicate that regardless of the fomration conditions (e.g. in the boundary layer or in the upper troposphere) the ice nucleation ability of glassy αP SOA particles does not significantly change. Similar ice nucleation onsets were also obtained for the more atmospherically relevant system composed of αP and isoprene. This indicates that the changes observed in the chemical composition of the particles did not substantially alter the ice nucleation ability in comparison with the pure αP particles. Naphthalene SOA particles showed a weak heterogeneous ice nucleation mode, but at ice saturation ratios where biogenic SOA particles or aqueous solution droplets would have already frozen via homogeneous freezing. The SOA particles investigated in this chapter are thus not expected to contribute to cirrus cloud formation via heterogeneous ice nucleation but only at high ice saturation ratios comparable to those of the ubiquitous aqueous sulfuric acid solution droplets.

7 | AMMONIUM SULFATE AND SECONDARY ORGANIC MATERIAL INTERNALLY MIXED PARTICLES

7.1 INTRODUCTION

Sulfate and organics are among the most abundant aerosol components in the troposphere and have also been found in cirrus ice crystal residuals (Murphy et al., 2006; Froyd et al., 2009). Airborne measurements performed with a single particle mass spectrometer showed that most of the particles were found to be internal mixtures of sulfate and organics, and the sulfate component was often partially or fully neutralized (Froyd et al., 2009). A recent study, spanning 10 years of filter measurements, showed a dominant contribution of sulfate or organics depending on location, altitude, and season (Martinsson et al., 2019).

The experiments presented in this chapter focus on internally mixed particles composed of ammonium sulfate (the most ice-active compound in the $H_2SO_4/NH_3/H_2O$ system) and secondary organic material. The current knowledge on the ice nucleation ability of the individual compounds and their internal mixtures is briefly summarized here.

The ice nucleation ability at cirrus conditions of ammonium sulfate particles depends on their phase state (see Section 2.4). Liquid ammonium sulfate particles nucleate ice homogeneously at saturation ratios which are in good agreement with predictions of the water-activity-based ice nucleation formulation by Koop et al. (2000), e.g. at an ice saturation ratio $S_{ice} = 1.55$ at $-51\,°C$ (Bertram et al., 2000). Crystalline ammonium sulfate particles, however, which form below the efflorescence relative humidity of $40 - 45\,\%$ (Gao et al., 2006), can induce heterogeneous ice formation below about $-50\,°C$, e.g. at $S_{ice} = 1.20$ at about $-55\,°C$ (see e.g. Chapter 4 and Abbatt et al., 2006). At these low temperatures, the deliquescence relative humidity of ammonium sulfate is higher than the onset relative humidity for heterogeneous ice nucleation, which then occurs at much lower ice saturation ratios than homogeneous freezing of fully deliquesced aqueous particles (e.g., Abbatt et al., 2006; Shilling et al., 2006; Wise et al., 2010). A similar ice nucleation behavior, with the competition between deliquescence and heterogeneous ice nucleation, is also observed for other inorganic salts like sodium chloride (Wise et al., 2012; Wagner and Möhler, 2013) and ammonium nitrate (see Chapter 5 and Wagner et al., 2020).

The phase state is also a critical parameter for the ice nucleation ability of organic particles. Some organic compounds, e.g. oxalic acid, are able to crystallize and act as ice nucleating particles in the immersion freezing (Zobrist et al., 2006; Wagner et al., 2015) and deposition nucleation mode (Kanji et al., 2008). Recently, atmospheric secondary organic aerosol particles have been found in a glassy phase state at low temperatures and/or relative humidity (Virtanen et al., 2010; Shiraiwa et al., 2017) and glassy particles have shown to promote heterogeneous ice formation (Murray et al., 2010; Wilson et al., 2012). These observations have led to an increased number of studies focusing on the ice nucleation ability of secondary organic particles originating from different gas precursors (see e.g. Chapter 6, Wang et al., 2012; Ladino et al., 2014; Ignatius et al., 2016; Charnawskas et al., 2017; Wagner et al., 2017; Wolf et al., 2020). Heterogeneous ice nucleation on glassy particles was mainly observed in experiments with single organic compounds, whereas the majority of the studies performed with secondary organic aerosol particles from the oxidation of α-pinene showed ice formation only at or above the homogeneous freezing threshold (see Chapter 6).

Only a few studies explored the ice nucleation ability of internally mixed particles composed of organic compounds and crystalline ammonium sulfate (AS). Shilling et al. (2006) showed that, at temperatures between $-33\,°C$ and $-83\,°C$, the heterogeneous ice nucleation onset of pure crystalline

---

This Chapter is an adapted version of the manuscript "Ice nucleation ability of ammonium sulfate aerosol particles internally mixed with secondary organics" by Bertozzi et al. (2021)

AS was not altered by the addition of maleic acid in a 1 : 1 ratio by weight. Wise et al. (2010), Schill and Tolbert (2013), and Baustian et al. (2013) investigated how the addition of palmitic acid, organic polyols, sucrose, citric acid, and glucose changed the heterogeneous ice nucleation ability of crystalline AS in an environmental cell coupled with an optical microscope and a Raman spectrometer. The organic to inorganic particle mass ratio in these studies varied from 1 : 1 to 2 : 1. These studies show that the organic components only minimally affect the efflorescence and deliquescence relative humidity of the AS particles (at temperatures between $-33\,°C$ and $-3\,°C$), and also that their intrinsic heterogeneous ice nucleation ability almost remains unchanged (at temperatures between $-63\,°C$ and $-43\,°C$). More recently, Ladino et al. (2014) and Schill et al. (2014) investigated the effect on the ice nucleation ability when more atmospherically relevant organic components are mixed with AS, namely secondary organic material (SOM) from the oxidation of α-pinene and from the reaction of methylglyoxal with methylamine. Ladino et al. (2014) probed the ice nucleation ability of AS particles mixed with α-pinene SOM with inorganic to organic mass ratios of 1 : 1 and 4 : 1 at $-55\,°C$. The mixed particles were generated by atomizing a liquid solution of AS mixed with the water soluble fraction of the SOM. The particles passed a diffusion dryer and were size selected (170 nm) for the ice nucleation measurement. The ice saturation ratio required for 0.1 % of the mixed particles to nucleate ice was found to be 1.40, a value between the nucleation onsets of the pure AS particles (at $S_{ice} = 1.25$) and the pure organic particles ($S_{ice} = 1.52$). Schill et al. (2014) started their ice nucleation experiments with liquid solution droplets composed of methylglyoxal, methylamine, and AS, which were deposited on a silica disk. Particles were then exposed to low relative humidity to induce efflorescence of the AS component. Optical microscope images revealed that the AS crystallized in numerous isolated islands embedded in the organic matrix. For the mixed particles, the ice onset at $-58\,°C$ occurred at $S_{ice} = 1.36$, which is below the ice onset saturation ratio for pure organic particles ($S_{ice} = 1.52$). The authors suggested that immersion freezing on the crystalline ammonium sulfate islands was the main ice nucleation mode for this system.

The experiments presented in this chapter were conducted in the AIDA cloud chamber, a unique platform to investigate phase changes of aerosol particles during temperature and relative humidity cycles or during cloud processing (Wagner et al., 2017). Formation and dissipation of clouds, as well as cycles of humidification and drying are examples of processes commonly occurring in the atmosphere (Pruppacher and Jaenicke, 1995; Hoose et al., 2008), but their effects on the physical properties of the so-processed aerosol particles are still poorly understood. In particular, the effect of several aging and cloud processing mechanisms on the ice nucleation ability of the mixed particles was investigated. The ice nucleation ability was either tested in situ by expansion cooling experiments in the AIDA chamber, or ex situ by sampling the particles and probing them in the INKA continuous flow diffusion chamber. At first, two types of reference experiments were performed, shown in the schematic of Figure 7.1 as experiments of type A and B. In experiment A, the ice nucleation ability of pure crystalline ammonium sulfate (AS) particles is shown as reference. In experiment B, an external aerosol preparation chamber was used to generate crystalline AS particles thickly coated with secondary organic material (SOM) derived from α-pinene. The organic coating completely suppressed the heterogeneous ice nucleation ability of the AS core. Based on these data, a dedicated coating experiment was performed in the AIDA chamber, where the organic coating thickness was gradually increased to quantify the effect of the organic material condensing on the AS surface (experiments of type C).

Particles investigated in experiments of type B and C probably had a core-shell morphology, with the ice nucleation (IN) active ammonium sulfate core shielded by the condensed, not IN active organic material. However, phase state and morphology of the particles present in the atmosphere might differ from such idealized core-shell geometries. Mixtures of organics and ammonium sulfate can also form at higher temperature and relative humidity conditions at which the particles are fully mixed, as e.g. in liquid clouds. In such a situation, the important question is: what would be the particle morphology if the crystallization of the ammonium sulfate component is only induced at a later stage, when the particle is subjected to a sufficiently low relative humidity? Would this process also inevitably lead to evenly coated particles where the heterogeneous IN activity of the AS component is strongly suppressed? An important process that needs to be considered is that initially homogeneously mixed aqueous particles can undergo the so-called liquid-liquid phase separation when the relative humidity is reduced (Marcolli and Krieger, 2006). For mixed particles

of AS and organics, several studies have determined the relative humidity at which the liquid-liquid phase separation occurs (separation relative humidity) as function of the temperature, the organic-to-sulfate mass ratio, and the oxygen-to-carbon ratio (O:C) (e.g., Ciobanu et al., 2009; Bertram et al., 2011). For example, Bertram et al. (2011) showed that for mixed AS/SOM derived from α-pinene, isoprene, and β-caryophyllene at about 18 °C and with O:C< 0.5, the separation relative humidity is at about 90 %. The phase separated particles can assume different morphologies depending on temperature, drying rate, viscosity of the organic component (Fard et al., 2017), and size of the particles (You et al., 2014; Freedman, 2020). Apart from a core-shell arrangement, possible particle morphologies also include several islands of the inorganic component in the organic matrix or partially engulfed structures. If the relative humidity is then further reduced to induce the crystallization of the AS, the ice nucleation active inorganic component is not necessarily completely surrounded by the deactivating SOM, with strong implications for the ice nucleation ability of the particles. This processing pathway was investigated in experiment D. The experiment started with the thickly SOM-coated AS particles from the reference experiment B, but they were then activated to cloud droplets in the AIDA chamber at a higher temperature (−5 °C), thereby generating homogeneously mixed aqueous droplets. Finally, the relative humidity was reduced to induce the AS crystallization and we probed the ice nucleation ability of the particles at cirrus cloud conditions.

Another pathway that can lead to a morphology change in particles of organic-inorganic mixtures is cloud processing in a convective cloud system. Adler et al. (2013) showed that aerosol particles composed uniquely of natural organic matter, or mixed with ammonium sulfate, assume a highly porous morphology after an atmospheric freeze-drying process that involved droplet activation, freezing, and sublimation of ice crystals. The effect was more visible for the purely organic compared to the internally mixed particles. Wagner et al. (2017) simulated such freeze-drying process by an expansion cooling experiment in the AIDA chamber with secondary organic aerosol particles derived from the ozonolysis of α-pinene and also observed the formation of highly porous particles. In experiment type E, the freeze-drying experiment from Wagner et al. (2017) was repeated with the thickly SOM-coated AS particles to investigate whether the expected change in morphology would also affect the particles' ice nucleation ability. The effect might be twofold: first, the porous organic coating could, by itself, be more ice nucleation active than the non-porous coating due to the recently proposed pore condensation and freezing mechanism (Marcolli, 2014); second, a porous coating layer could less efficiently shield the ice nucleating active AS component from the environment, thereby also enhancing the particles' ice nucleation ability after the freeze-drying process.
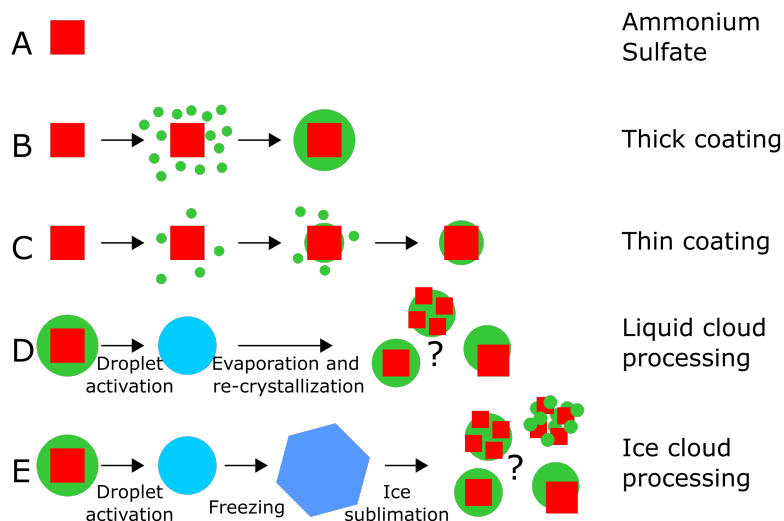
Figure 7.1: Summary of the experiments performed. Experiment A: crystalline ammonium sulfate (AS). Experiment B: AS crystals thickly coated with secondary organic matter (SOM) from the ozonolysis of α-pinene (AP) at 20 °C in the aerosol preparation and characterization (APC) chamber (thick coating). Experiment C: AS crystals stepwise coated with small amounts of SOM from the ozonolyis of AP at upper tropospheric temperature in the AIDA chamber (thin coating). Experiment D: in situ crystallization of the AS component from a homogeneously-mixed, aqueous droplet that was generated by the droplet activation of crystalline AS aerosol thickly coated with SOM (prepared as in experiment B). Experiment E: aerosol prepared in the same way as in B, then subjected to an atmospheric freeze-drying process, involving droplet activation, freezing, and ice sublimation.

7.2 AEROSOL PREPARATION AND CHARACTERIZATION

The aerosol particles were generated, characterized, and aged in the AIDA chamber and in the aerosol preparation and characterization (APC) chamber. A detailed description of the AIDA facility and of the standard aerosol instrumentation used for the experiments here presented can be found in Section 3.2. The coating procedure performed in the APC chamber aimed at generating a thick organic coating layer on the AS seed particles with high reproducibility. The ice nucleation ability of these particles was either directly probed in a reference experiment (experiments of type B) or after subjecting the particles to different processing steps (experiments of type D and E). The coating experiments performed in the AIDA chamber, instead, aimed at quantifying the effect of a thin coating on the inorganic seeds (experiments of type C). In this case, the coating procedure consisted of several steps, each with a small amount of organics condensing on the seed aerosol particles. The coating procedure in the APC chamber was performed at ambient temperature and low relative humidity, and in the AIDA chamber at low temperature and ice saturated conditions. Table 7.1 provides a list of the performed experiments together with information on the thermodynamic conditions at which the particles were generated, the concentration of the gas precursors, the median diameter of the seed particle size distributions before the coating procedure, and the organic mass fraction after the coating procedure.

An aqueous solution was prepared by dissolving ammonium sulfate in ultra-pure water to obtain a 1 % solute concentration. The solution was then aerosolized by means of an ultrasonic nebulizer. A series of diffusion dryers ensured a relative humidity with respect to water in the injection line lower than 1 %, well below the efflorescence relative humidity of ammonium sulfate (Onasch et al., 1999; Gao et al., 2006). Secondary organic material (SOM) was generated from the ozonolysis of α-pinene. Another important pathway for the formation of α-pinene SOM in the atmosphere are photo-oxidation reactions, but the ice nucleating ability of the organic material generated via dark ozonolysis or photooxidation of α-pinene was found to be very similar (Piedehierro et al., 2021). Ozone was produced with a silent discharge generator in pure oxygen.

Table 7.1: Summary of the experiments performed and main parameters of the aerosol particle populations. D_p^{median} is the median diameter of the lognormal fit to the aerosol size distribution measured right before the coating procedure. The α-pinene concentration corresponds to the total amount added during the injection periods. For the in situ coating experiments (experiments type C), the organic mass fraction f_{org} refers to the value measured at the end of the coating procedure. The coating thickness is estimated from a combined analysis of the SMPS and the AMS data, the first number refers to the coating thickness evaluated at the median diameter, and the range in the parenthesis to the values at 300 and 500 nm particle diameter (see text for more details).

Exp. ID	Type	$D_p^{median}{}_*$ [nm]	Coating T [°C]	Coating RH [%]	O_3 [ppm]	α-Pinene [ppb]	Coating time	$f_{org} \cdot 100$ [wt%]	Coating thickness [nm]
A1	Amm. Sulfate	395	-	-	-	-	-	-	-
B1	Thick coating	380	+25	$\leqslant 1$	1.6	110.9	33 min	26.9	28 (22 − 37)
B2	Thick coating	415	+25	$\leqslant 1$	2.6	325.1	1 h 4 min	39.1	50 (36 − 60)
C1	Thin coating	403	−50	60	0.2	0.6	4 h 10 m	5.7	6 (4 − 7)
C2	Thin coating	430	−60	57	0.2	1.2	2 h 45 min	4.8	5 (3 − 6)
C3	Thin coating	403	−45	61	0.2	0.7	5 h 10 min	8.3	8 (6 − 10)
D1	Liquid cloud	380	+25	$\leqslant 1$	1.8	238.7	1 h	39.1	46 (36 − 60)
D2	Liquid cloud	365	+25	$\leqslant 1$	1.6	110.4	33 min	24.3	24 (20 − 33)
E1	Freeze-drying	345	+25	$\leqslant 1$	1.8	235.1	1 h 1 min	47.3	54 (47 − 79)

* Assuming a shape factor $\chi = 1.1$

The generation of AS particles with thick SOM coating was started by injecting crystalline AS particles ($\approx 10^5$ cm^{-3}) into the APC chamber. Then ozone was added (about 2 ppm), followed by a continuous flow of α-pinene for approximately 30 minutes (experiments B1 and D2) or 1 hour (experiments B2, D1 and E1), resulting in a total concentration between 100 and 300 ppb of injected precursor gas (see Table 7.1 for the concentrations used in each experiment). The high initial aerosol concentration in the APC chamber during the α-pinene injection provided a sufficiently large total surface area for the organic reaction products to condense on the existing AS particles, and to suppress, in the majority of cases, the nucleation and growth of pure organic aerosol particles. At the end of the coating procedure, a fraction of the aerosol particles were transferred into the AIDA chamber.

For the thin coating experiments performed in the AIDA chamber (experiments of type C), the coating was performed in three to four steps, with the injection of smaller amounts of α-pinene. Each step consisted in the injection of 100 to 700 ppt of organic gas precursor, summing up to a total concentration of approximately 1 ppb (see Table 7.1 for the concentrations used in each experiment). A new injection step of gas precursor was performed approximately every hour, to allow the reaction to be completed and to simultaneously perform the ice nucleation measurements with the CFDC.

A high resolution time of flight aerosol mass spectrometer (HR-ToF-AMS, Aerodyne) measured the chemical composition of the particles, with an uncertainty of 5.3 % regarding the measured mass concentrations (based on ionization efficiency calibration) [1]. The organic content of the particles was measured after the transfer of the particles from the APC chamber to the AIDA chamber (experiments type B, D, and E) or continuously during the thin coating experiments in AIDA (experiments of type C). During the coating procedure of experiments B2 and C2, some pure organic particles nucleated and eventually grew to a size detectable in the SMPS and the mass spectrometer. For these experiments, to obtain the organic mass concentration of the organic coating on the AS particles, the total organic mass measured by the AMS was corrected for the mass of the smaller mode of nucleated pure organic particles. This was done by independently deriving the total mass concentration of the smaller particle mode from the size distribution measured with the SMPS (estimating the density of the organic material as $\rho_{org} = 1.25$ g cm^{-3} (Saathoff et al., 2009)) and then subtracting it from the total mass concentration measured with the AMS. The organic mass fraction values f_{org} reported in Table 7.1 refer to the organic content at the end of the coating procedures, i.e., regarding experiments of type C, they refer to the organic content after the last coating step. The size-resolved measurements of the chemical composition of the particles by the AMS indicate that the organic mass fraction is constant and not a function of the particle size.

---

1 Data collection and analysis was performed by Junwei Song

To estimate the thickness of the organic coating, d, the size distribution of the pure crystalline AS particles from the SMPS measurements and the organic mass fraction f_{org} from the AMS were combined. Thereby, the crystalline AS seeds are assumed to be spherical particles with diameter D_p, and the organic material to be evenly distributed on their surface, leading to a spherical organic shell. The coating thickness d is thus calculated assuming a perfectly concentric core shell morphology as follows:

$$d = \frac{D_p^{coated} - D_p}{2}$$

The diameter of the coated particles D_p^{coated} is calculated by considering the size-dependence of the particles' organic mass $M_{org}(D_p)$:

$$D_p^{coated}(D_p) = \left[D_p^3 + \frac{6}{\pi} \frac{M_{org}(D_p)}{\rho_{org}} \right]^{\frac{1}{3}},$$

with:

$$M_{org}(D_p) = \frac{f_{org}}{1 - f_{org}} \cdot \rho_{AS} \cdot \frac{\pi}{6} D_p^3$$

The resulting estimated organic coating thickness corresponding to the median diameter of the particle population is reported in Table 7.1. In Table 7.1, it is also indicated between brackets the estimated coating thickness for seed particles with diameters of 300 and 500 nm, i.e., the size range which comprises the major particle mode in the number size distribution (see below and Figure 7.2 for the number size distribution measurements). The thickness estimated for the thickly SOM-coated AS particles (experiments of type B, D and E) ranged from 24 nm to 54 nm. Thinner coatings were obtained at the end of the coating experiments performed in the AIDA chamber (experiments of type C) with 6 nm, 5 nm, and 8 nm coating thicknesses.

Exemplary particle size distributions for the pure crystalline AS and for the SOM-coated AS particles are reported in Figure 7.2. The effect of the organic coating on the particle diameter is clearly visible for the thickly coated particles (Figure 7.2a, experiment D1). Instead, no change is detectable in the SMPS measurements for the thin coating experiments, in which a lower amount of organic material was produced and condensed on the particles (Figure 7.2b, experiment C3). However, due to the numerous processes taking place during the coating procedures (e.g., change of the shape factor of the particles) it is not possible to directly infer the coating thickness from the SMPS measurements.

The phase state of the ammonium sulfate content in the mixed particles (i.e., crystalline or liquid) has been determined with depolarization measurements of back-scattered laser light and the analysis of infrared extinction spectra recorded by means of a Fourier transform infrared spectrometer[2] (FTIR) (Wagner et al., 2006). The presence or absence of specific liquid water absorption bands and changes in the peak position and band width of the ν_3 sulfate mode at about $1100\,cm^{-1}$ between crystalline and liquid AS allowed to infer the phase state of the AS content in the mixture (Onasch et al., 1999; Zawadowicz et al., 2015). The SIMONE instrument (Schnaiter et al., 2012) measures the intensity of the light scattered by the aerosol particles in the forward (2°) and backward (178°) directions from a linearly polarized laser ($\lambda = 488\,nm$). In the backward direction, the polarization-resolved scatter light intensity is detected so that the linear depolarization ratio of the aerosol particles can be determined. Non-spherical and inhomogeneous particle morphologies, like a crystalline core of AS or islands of crystalline AS in the mixed particles, can induce a change of the incident polarization state of the laser, thereby causing a non-zero value for the depolarization ratio. In contrast, homogeneously mixed, spherical aqueous solution droplets would show a depolarization ratio of zero.

---

2 Data collection and analysis was performed by Dr. Robert Wagner.
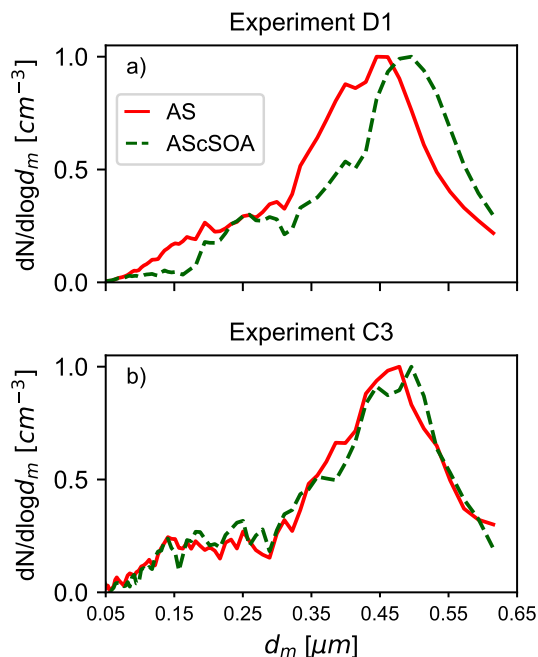
Figure 7.2: Comparison of the normalized particle number size distribution before and after the coating procedure. The x-axes represent the electrical mobility diameter d_m. **a)** Particle number size distribution for experiment D1 before (red) and after (green) the coating process. The thick organic coating was performed in the APC chamber. **b)** particle number size distribution for experiment C3 before (red) and at the end (green) of the in situ coating procedure. The thin coating experiments were performed step-wise and with lower concentrations of the gas precursor in the AIDA chamber. No apparent shift in the particle number size distribution was detected for experiments of type C.

7.3 RESULTS AND DISCUSSION

The results from the different types of experiments are presented in three different subsections. The reference experiments with pure and thickly SOM-coated crystalline AS particles, as well as the gradual thin coating experiments performed in the AIDA chamber are presented first (Sect. 7.3.1). The results on the ice nucleation ability of initially thickly SOM-coated AS crystals, which were temporarily activated to homogeneously mixed, aqueous droplets and then recrystallized are presented in Sect. 7.3.2 (experiment D). Finally, the experiments where the initially thickly SOM-coated AS crystals were subjected to freeze-drying processing in the AIDA chamber are presented in Sect. 7.3.3 (experiment E).

7.3.1 Organic coating effect

The ice nucleation ability of pure and SOM-coated solid ammonium sulfate particles at cirrus cloud conditions was probed with experiments of type A, B, and C (Figure 7.1). The particles were coated in the APC chamber for experiments of type B and in the AIDA chamber for experiments of type C. In both cases, it can be assumed that the coating procedure led to particles with a core-shell morphology, with the solid AS as the core and the organic material surrounding it. This hypothesis is supported by the ice nucleation measurements as discussed below. Experiment of type B was conducted two times with different coating time and amount of α-pinene added to the APC chamber. In experiment B1, SOM-coated AS particles were generated with an organic mass fraction of $26.9\,wt\%$ and a coating thickness of $28\,nm$; in experiment B2, the organic mass fraction was $39.1\,wt\%$ and the coating thickness $50\,nm$. As already mentioned, these coating thicknesses were computed for the median particle diameters assuming a uniform coating.

Time series of the AIDA expansion cooling runs for experiments A1 (pure crystalline AS) and B2 are presented in Figure 7.3. The upper panels show the pressure and temperature drop during the expansion runs. The middle panels show the saturation ratio with respect to ice (S_{ice}) and the homogeneous freezing threshold (Koop et al., 2000). The lower panels depict the fraction of aerosol particles activated as ice crystals (ice nucleating fraction, INF). Black dotted vertical lines indicate when the INF reaches the threshold of 0.1 %, defined here as the ice nucleation onset. Crystalline AS particles induce heterogeneous ice nucleation at saturation values lower than those required for the homogeneous freezing of solution droplets. For crystalline AS the ice onset is measured at $S_{ice} = 1.29$ (Figure 7.3a middle panel). For SOM-coated AS particles, instead, the ice onset is measured at $S_{ice} = 1.44$ (Figure 7.3b middle panel). The organic coating clearly suppresses the ice nucleation activity of the crystalline AS core and shifts the ice nucleation onset close to the homogeneous freezing threshold. The strong decrease of the ice nucleation ability of the particles suggests that most of the IN active sites of the bare AS have been shielded by the condensed organic material distributed in a core-shell morphology.
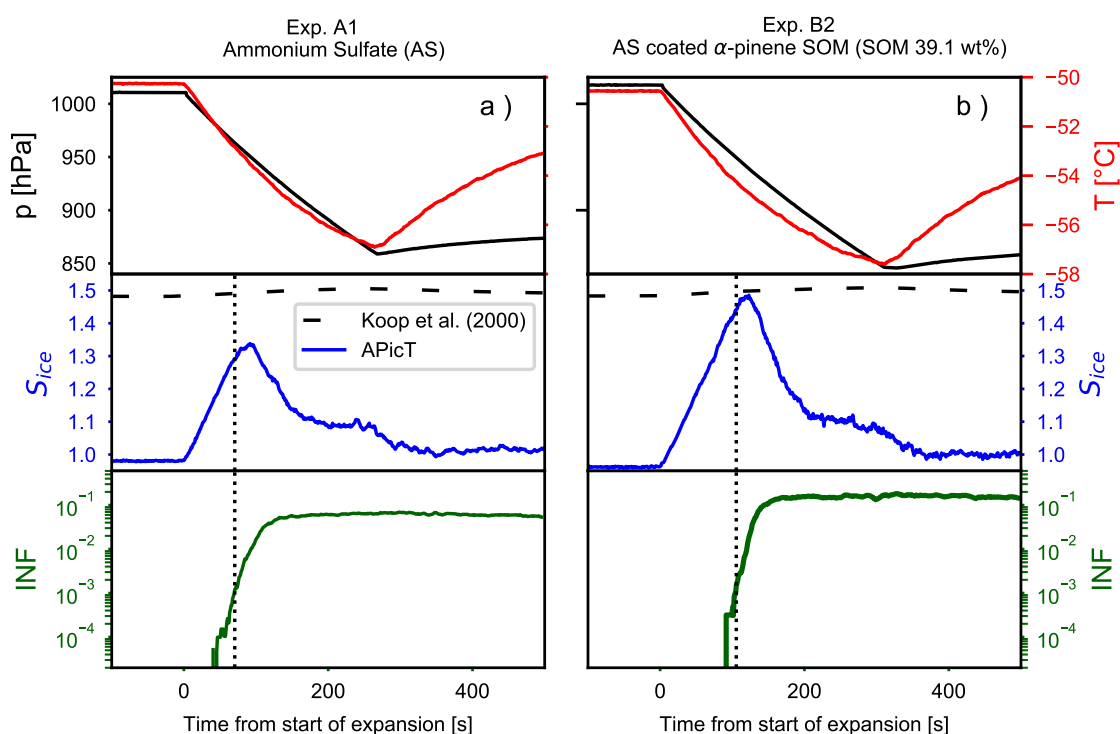
Figure 7.3: Time series of the AIDA expansion cooling experiment for pure crystalline ammonium sulfate (experiment A1, panel a) and ammonium sulfate crystals coated with SOM from the ozonolysis of α-pinene (experiment B2, panel b). The upper panels show pressure (black lines, left axis) and temperature (red lines, right axis). The middle panels show the increase of the saturation ratio with respect to ice (blue line). The homogeneous freezing threshold computed for a Δa_w of 0.3 of the ice-melting curve (Koop et al., 2000) is indicated with the horizontal dashed lines. The lower panels show the fraction of aerosol particles that induced ice formation (ice nucleating fraction, INF). The vertical dotted lines indicate when 0.1 % of the aerosol particles acted as INPs.

Figure 7.4a summarizes the ice onset saturation ratios for pure and thickly SOM-coated crystalline AS particles from this study (experiments A1, B1, and B2). The water saturation ($RH_w = 100\%$), the homogeneous freezing threshold for $\Delta a_w = 0.3$ (Koop et al., 2000), and the AS deliquescence relative humidity (Clegg et al., 1998) are also shown in the figure. Results from AIDA and INKA are shown as squares and circles, respectively, and the symbol colors refer to the different aerosol types used in the different experiments (orange for pure AS particles and light and dark green for experiments B1 and B2, respectively). Both methods clearly show the suppression of the heterogeneous ice nucleation activity of the crystalline ammonium sulfate core by the organic coating. The AIDA

results show lower ice onset saturation ratios for both pure and SOM-coated AS particles compared to the INKA results. A similar offset between the two techniques (expansion cooling experiments and CFDC saturation scans) has been observed in several measurements performed at cirrus cloud conditions with crystalline inorganic salts and presented in this Thesis (see e.g. Section 3.4.7, Section 4.4, Section **??**, and Wagner et al., 2020). It is worth mentioning that secondary organic material is more viscous at low temperature and this also affects water diffusion. Therefore, different experimental techniques could be subjected to different kinetic limitations, inducing ice nucleation at different conditions. During an AIDA expansion run, for example, the thermodynamic conditions inside the chamber change relatively slow and allow long equilibration times. However, inside the continuous flow diffusion chamber, new particles are continuously sampled, suddenly exposed to a supersaturated environment, and only have a few seconds ($\approx 10\,s$) to activate as ice crystals.

In Figure 7.4b, the data from experiments A and B are compared to literature results of S_{ice} at the ice nucleation onset for pure crystalline AS particles (red colored symbols) and pure secondary organic aerosol (SOA) particles (green colored symbols). One can see that the pure AS and pure SOA data form clearly separated blocks on the S_{ice} vs. T diagram, with the heterogeneous nucleation onsets for AS ranging from 1.1 to 1.3 and for pure SOA from 1.4 to 1.7. With regard to the experiments with the thickly SOM-coated AS particles, experiment B1 shows a slightly lower ice onset saturation ratio ($S_{ice} = 1.4$, AIDA experiment) compared to the measurements of the pure SOA particles. However, this early onset was only representative of a small fraction of the aerosol particle population and if an INF of 1% had been chosen as the onset condition, the related S_{ice} value had already increased to 1.46.
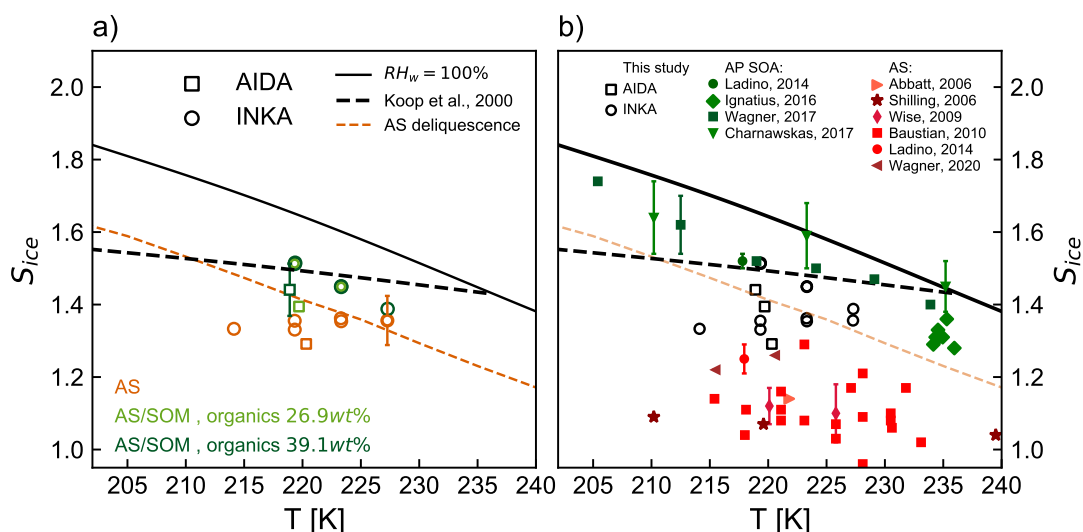
Figure 7.4: Summary of the ice nucleation onsets for crystalline ammonium sulfate (AS), pure secondary organic aerosol (SOA) particles and, crystalline AS coated with secondary organic matter as a function of temperature T. The solid black line indicates water saturation ($RH_w = 100\,\%$), the dashed black line indicates the homogeneous freezing threshold ($\Delta a_w = 0.3$, Koop et al. (2000)), and the dashed orange line is the ammonium sulfate deliquescence relative humidity (Clegg et al., 1998). **a)** Results from this study (corresponding to an ice nucleating fraction of 0.1%) for pure, crystalline AS (orange symbols) and for AS coated with α-pinene SOM (green symbols). Light green symbols refer to experiment B1 (organic mass fraction 26.9 wt%), dark green symbols refer to experiment B2 (organic mass fraction 39.1%). Results from the AIDA expansion cooling experiments are reported with squares, circles refer to INKA results. **b)** Results from this study (open symbols) are compared to literature data for crystalline AS (red symbols) and α-pinene SOA particles (green symbols).

Experiments B1 and B2 have shown that thick SOM-coating layers almost completely suppress the heterogeneous ice nucleation ability of the AS component and shift the particles' ice nucleation onset close to that observed for the pure SOA particles. Experiments of type C were thus conducted to investigate and quantify the effect of a thin organic coating layer on the ice nucleation activity of crystalline AS particles. As previously described, the coating procedure for these experiments was

performed directly in the AIDA chamber at different temperatures ($-45\,°C$, $-50\,°C$, and $-60\,°C$) and at ice saturated conditions by step-wise oxidizing small amounts of α-pinene. After each coating step, the aerosol particles were sampled and their ice nucleation ability measured with the continuous flow diffusion chamber at the same, or slightly lower, temperature of the AIDA chamber (at the nominal values of $-50\,°C$, $-54\,°C$, and $-60\,°C$). Figure 7.5a shows the ice nucleating fraction (INF) as a function of the saturation ratio with respect to ice for humidity ramps performed at $-54\,°C$ with particles characterized by different organic mass fractions with INKA. The activation curves from experiments C1 and C3 are shown with solid symbols (circles and down-pointing triangles, respectively), data from experiments B1 and B2 are shown as empty circles. The gradual shift of the ice onset towards higher saturation values with the increase of the condensed organic material is clearly visible. Already after the second coating step of experiment C1, that corresponded to an organic mass fraction of only 2.4 wt%, most of the ice crystals that had formed at $S_{ice} < 1.4$ on the pure crystalline AS particles have disappeared from the records. After the fourth coating step of experiment C1, when the organic mass fraction has reached a value of 5.7 wt%, the ice nucleation onset was shifted close to the value observed for pure α-pinene SOA particles. The ice nucleation ability of particles with ≈ 8 wt% organic material (experiment C3) is almost identical to the one of the thickly coated particles from experiments B1 and B2 (with 27 wt% and 39 wt% organic mass fractions, respectively), indicating that such a low organic content, if uniformly distributed, is sufficient to suppress the ice nucleation ability of the solid AS particles. The progressive increase in the ice onset saturation ratios measured by the continuous flow diffusion chamber highlights its sensitivity to detect the effect of the organic coating.

Figure 7.5b summarizes the ice onset saturation ratios, corresponding to an INF of 0.1 %, obtained from the INKA measurements as function of the organic mass fraction of the particles. Results for experiment A1 (left side) and for all experiments of type C (right side) are shown. Different symbols correspond to different experiments, colors indicate at which temperature the ice nucleation ability was measured. The data confirm the results from the experiments presented in Fig. 7.5a, showing that the ice nucleation ability of the solid AS component is gradually suppressed with the increase of organic material condensed on its surface. In most cases organic mass fractions of only $4-8$ wt% (yielding estimated coating thicknesses of $5-8$ nm) shift the ice nucleation onsets of the coated AS particles to values above $S_{ice} = 1.45$ at temperatures between $-45\,°C$ and $-55\,°C$, i.e. to the regime where also pure SOA particles would nucleate ice. These small organic mass fractions were sufficient to completely suppress the heterogeneous ice nucleation ability of the crystalline AS core. The suppression of the particles' ice nucleation ability during and at the end of the coating procedure suggests, as for experiments of type B, that the organic material is evenly distributed on the AS surface and progressively covers its IN-active sites.

The temperature trend of the ice nucleation onsets for organic mass fractions larger than about 4 wt% revealed by experiments C, i.e., higher S_{ice} values with decreasing temperature, could point to a homogeneous ice nucleation pathway of the coated particles, meaning that at least the outer layer of the organic material has liquefied during the residence time of the particles in INKA. A similar temperature trend has been observed for all the experiments performed with SOA particles presented in Chapter 6, and in previous ice nucleation studies with pure α-pinene SOA particles (e.g., Ladino et al., 2014; Wagner et al., 2017; Charnawskas et al., 2017).

7.3.2 Liquid cloud processing

In view of the results from the previous section, that the ice nucleation onset saturation ratios of SOM-coated crystalline AS particles are already at or above $S_{ice} = 1.45$ for small organic mass fractions of 10 wt%, one might ask the question whether this type of internally mixed particles should still be considered as candidates for inducing heterogeneous ice nucleation in cloud models. Furthermore, mass spectrometer measurements by Froyd et al. (2009) show that the average organic mass fraction of internally mixed particles is even higher (ranging from 30 to 70 wt%). Experiments of type C, however, just tested one specific pathway for the formation of the mixed particles, where the crystalline AS was already present and then coated with the organic substances. As already discussed in the introduction, different particle morphologies, like partially engulfed structures, might form when the particles are initially homogeneously mixed, aqueous mixtures of sulfate and
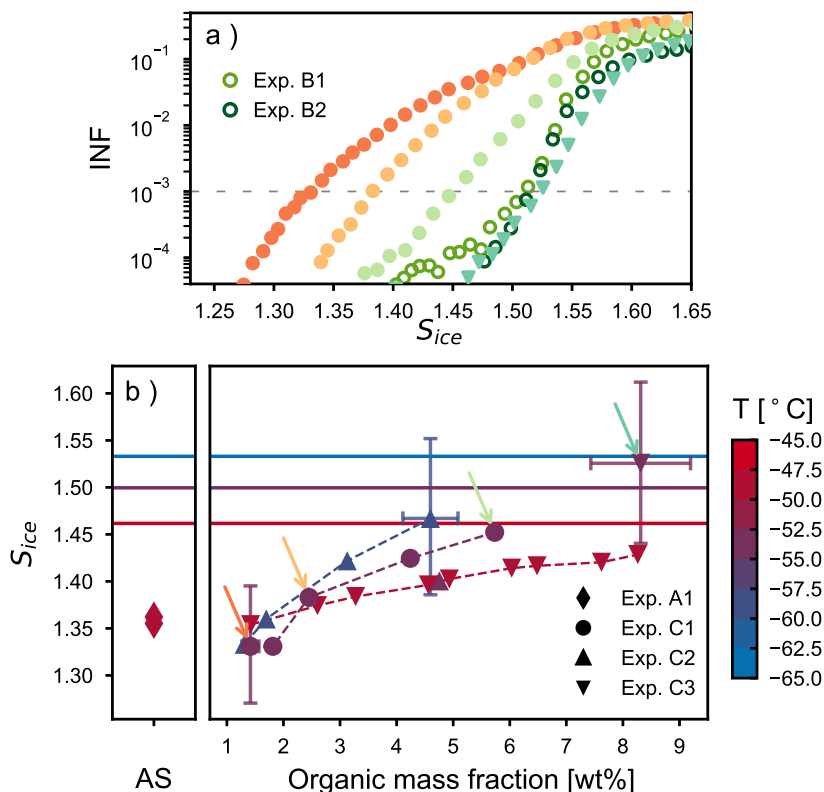
Figure 7.5: Ice nucleation results for the thin coating experiments (type C). **a)** Ice nucleating fraction as function of S_{ice} for humidity scans performed with INKA at the nominal temperature of $-54\,°C$ during experiments C1 (solid circles), C3 (down-pointing triangles), and B (empty circles). **b)** Ice onsets saturation ratio (defined for an INF of 0.1 %) for all INKA measurements during experiments C1, C2, and C3. Colors indicate the temperature at which the ice nucleation measurements have been performed in INKA. The horizontal lines indicate the threshold for homogeneous freezing of solution droplets at three different temperatures ($\Delta a_w = 0.3$, Koop et al., 2000). In all experiments, a gradual increase in the ice onset saturation ratios with increasing organic mass fraction was measured (dashed lines to guide the eyes). The colored arrows indicate the measurements reported in panel a.

organics, and then the AS component crystallizes. This pathway was investigated with experiments of type D, where liquid cloud processing is simulated. Here, the experiment starts from thickly SOM-coated AS crystals as investigated in experiments of type B, these particles are then temporarily activated to homogeneously mixed, aqueous droplets in a short expansion run conducted in the AIDA chamber at warm and humid conditions, and finally they are exposed to low relative humidity to induce the re-crystallization of the ammonium sulfate component.

Figure 7.6a shows a schematic of the liquid cloud processing together with the possible phase states and morphologies of the particles during the experiment. The thickly coated ammonium sulfate particles were generated in the APC chamber (stage I in Figure 7.6a) and then transferred into the AIDA chamber (stage II), which was held at $-5\,°C$ and $RH_w = 85\,\%$. These are conditions where the ammonium sulfate component is already in a liquid state (the AS deliquescence relative humidity at $-5\,°C$ is $RH_w = 83\,\%$ (Clegg et al., 1998)), but where the entire particle is probably still in a liquid-liquid phase separated state (separation relative humidity can be as high as $\approx$ 90 % (You et al., 2014)). Figure 7.6b presents the time series of the AIDA pressure (black line), AIDA temperature (red line), AIDA relative humidity with respect to water (blue line), and linear depolarization ratio measured with the SIMONE instrument (green line) during the liquid cloud processing experiment. The liquid state of the ammonium sulfate fraction upon transfer from the APC chamber into the AIDA chamber is verified by the FTIR measurements, reported in Figure 7.6c. Spectrum A (in orange) is a reference spectrum of crystalline ammonium sulfate particles

from Experiment A1 in the regime of the ν_3 (SO_4^{2-}) mode at about $1114\,cm^{-1}$. Spectrum B (in blue) was recorded after addition of the organic-coated AS crystals into the AIDA chamber. Here, the ν_3 mode is clearly broadened and shifted to lower wavenumbers. These spectral changes are indicative of the transition of AS from the solid to the liquid state (Zawadowicz et al., 2015). Also the low value of the depolarization ($\delta \approx 1\%$) is indicative of a particle morphology that is close to that of a homogeneous sphere. However, the nonzero value of δ indicates that some particle inhomogeneity still remains. We suggest that the particles are characterized by two phase-separated, slightly eccentrically arranged liquid components, because δ would also be zero for concentric spheres (Bohren and Huffman, 1998).

To then transform the phase-separated particles in the AIDA chamber into homogeneously mixed liquid particles, a short expansion run wa performed in order to reach $RH_w = 100\%$ and thereby exceed the relative humidity threshold for the liquid-liquid phase separation (stage III in Figure 7.6a). During the expansion run, the depolarization δ indeed dropped to the background value of about 0 % when the relative humidity increased above 90 %, indicating that the initially SOM-coated AS crystals successfully transformed to homogeneously mixed aqueous droplets. After the expansion, the AIDA chamber was refilled to ambient pressure and the recrystallization of the AS component was induced by reducing the relative humidity to 32 % (stage IV). This was done by extracting the humid air from the chamber and refilling it at the same rate with dry synthetic air. Note that in this specific experiment the chamber walls were not ice-coated, because the ice layer would have acted as a source of water vapor and prevented the reduction of the relative humidity. To support the reduction in relative humidity, the AIDA chamber was also slightly warmed to $-3.5\,°C$. The recrystallization of the AS fraction becomes evident from the increase of the depolarization δ over time and the associated change in the infrared signature of the particles. Spectrum C in Figure 7.6c (in purple), which was recorded at $RH_w = 32\%$ at the end of the recrystallization step, clearly shows that the ν_3 mode of particles has shifted back to the peak position typical for crystalline AS. This procedure has been applied in two experiments with particles of different organic mass fraction (experiments D1 and D2, see Table 7.1).

The ice nucleation ability of the in situ crystallized particles has been probed with INKA at $-54\,°C$ immediately after the AS crystallization (for experiments D1 and D2), and with an expansion cooling experiment after overnight cooling of the AIDA chamber to $-50\,°C$ (for experiment D2). As the INKA measurements were performed by sampling from the AIDA chamber at $-5\,°C$ and $RH_w \approx 32\%$, a diffusion dryer was used to prevent frost formation in the instrument inlet. To infer the possible effect of the dryer on the ice nucleation ability of the recrystallized particles, an additional INKA measurement was performed after the cooling of the AIDA chamber, thus without the need of a diffusion dryer. The ice nucleation ability measured with and without the dryer (i.e., before and after the cooling) are comparable (not shown), indicating that the dryer did not influence the ice nucleation ability of the particles. Figures 7.6d and 7.6e present the ice nucleating fraction (INF) as a function of the saturation ratio with respect to ice S_{ice} for pure AS crystals (orange data, experiment A1), unprocessed thickly SOM-coated AS crystals (green, experiment B1), and for the internally mixed particles that were subjected to the droplet activation and in situ crystallization process (yellow data, experiment D2). Very similar results were obtained for experiment D1. The AIDA and INKA results indicate that the ice nucleation ability of the processed particles lies between those of the pure crystalline AS and of the thickly SOM-coated AS crystals. The onset of the heterogeneous ice nucleation mode of the processed particles is observed at $S_{ice} \approx 1.35$. The in situ crystallization of initially homogeneously mixed aqueous AS/SOM particles can therefore lead to particle morphlgies that are heterogeneously ice nucleation active, even if the organic mass fraction is as high as $39.1\,wt\%$ or $24.3\,wt\%$ (Experiments D1 and D2, respectively). Most probably, the particles adopt a partially engulfed structure, where some ice nucleating sites of the AS component remain uncovered by the organic material (Freedman, 2020). This result again supports the hypothesis of a core-shell morphology for the coated particles of experiments B, for which the heterogeneous ice nucleation ability of the AS component was completely masked by the condensed organic material.

The measured ice onsets agree with previous measurements of Ladino et al. (2014) and Schill et al. (2014). As noted in the introduction, Ladino et al. (2014) investigated mixed particles composed of AS and the water soluble fraction of SOM derived from α-pinene. The particles were generated

from liquid solutions with inorganic to organic mass ratios of 1 : 1 and 4 : 1, dried, and then probed in a CFDC on their ice nucleation ability at $-55\,°C$. They also found an intermediate ice nucleation onset of the mixed particles (at $S_{ice} = 1.4$) compared to reference experiments with pure crystalline AS (ice onset at $S_{ice} = 1.25$) and pure secondary organic particles (ice onset at $S_{ice} = 1.52$). The results from Ladino et al. (2014) are shown for comparison with the INKA data in Figure 7.6e (triangles, AS in orange, mixed particles in yellow, and pure SOA in green). The results for the pure SOA particles from Ladino et al. (2014) and for the thickly SOM-coated particles from this study agree, confirming that the coated particles have an ice nucleation behavior similar to the purely organic particles, consistent with the assumption of a core-shell morphology. Also the ice nucleation behavior of the mixed particles obtained from homogeneously mixed aqueous AS/SOM solutions upon crystallization of the AS component nicely agree. Schill et al. (2014) have shown that complex particle morphologies are formed when AS crystallizes from solution droplets composed of methylglyoxal, methylamine, and AS. In their experiment, the ice nucleation onset of the internally mixed particles was lower compared to the pure organics, in agreement with results presented here.

However, the underlying heterogeneous ice nucleation mode might be different in the various studies. In addition to deposition nucleation, crystalline AS particles might also be ice nucleation active in the immersion freezing mode (Zuberi et al., 2001). This activity may be controlled by the viscosity and water solubility of the organic material (Schill and Tolbert, 2013; Schill et al., 2014). The finding that α-pinene SOM mass fractions greater than $\approx 5 - 10\,wt\%$ completely suppress the heterogeneous ice nucleation ability of crystalline AS (as shown in the previous section) rules out that immersion freezing is a prevalent nucleation mode in the experiments presented in this section. The higher heterogeneous ice nucleation activity of internally mixed AS/SOM particles formed by cloud droplet activation and recrystallization of the AS component must therefore be related to a change in the particle morphology to a partially engulfed structure. For organic materials with a lower viscosity and higher water solubility, however, the mixed particles might also be heterogeneously ice nucleation active in a core-shell morphology due to immersion freezing by the crystalline AS core. Schill et al. (2014) assumed that immersion freezing was indeed responsible for the heterogeneous ice nucleation mode observed in their experiments. As Ladino et al. (2014) only used the water soluble fraction of the generated SOM, its hygroscopic behavior might be different compared to these experiments so that their observed heterogeneous ice nucleation mode of the mixed particles after the AS crystallization might also be due to immersion freezing. The viscosity and amount of the organic material will also determine whether the crystallization of AS in internally mixed aqueous AS/SOM particles can occur at all. In particular, at lower temperatures and/or higher amounts of organics, the AS efflorescence could also be inhibited (Bodsworth et al., 2010). If re-crystallization of the AS component and the formation of a partially engulfed particle morphology did not occur at lower temperatures (in contrast to the $-5\,°C$ condition simulated in this study), liquid cloud processing would not increase the ice nucleation ability of the AS/SOM particles.

The enhanced ice nucleation ability of the liquid cloud processed particles compared to the pure organic and organic-coated particles clearly indicates that the ice nucleation ability of atmospheric aerosol particles can strongly change during their lifetime in the atmosphere. Cloud processing of internally mixed aerosol particles is a common phenomenon, whose impacts on the microphysical properties of the particles need to be investigated in future studies.
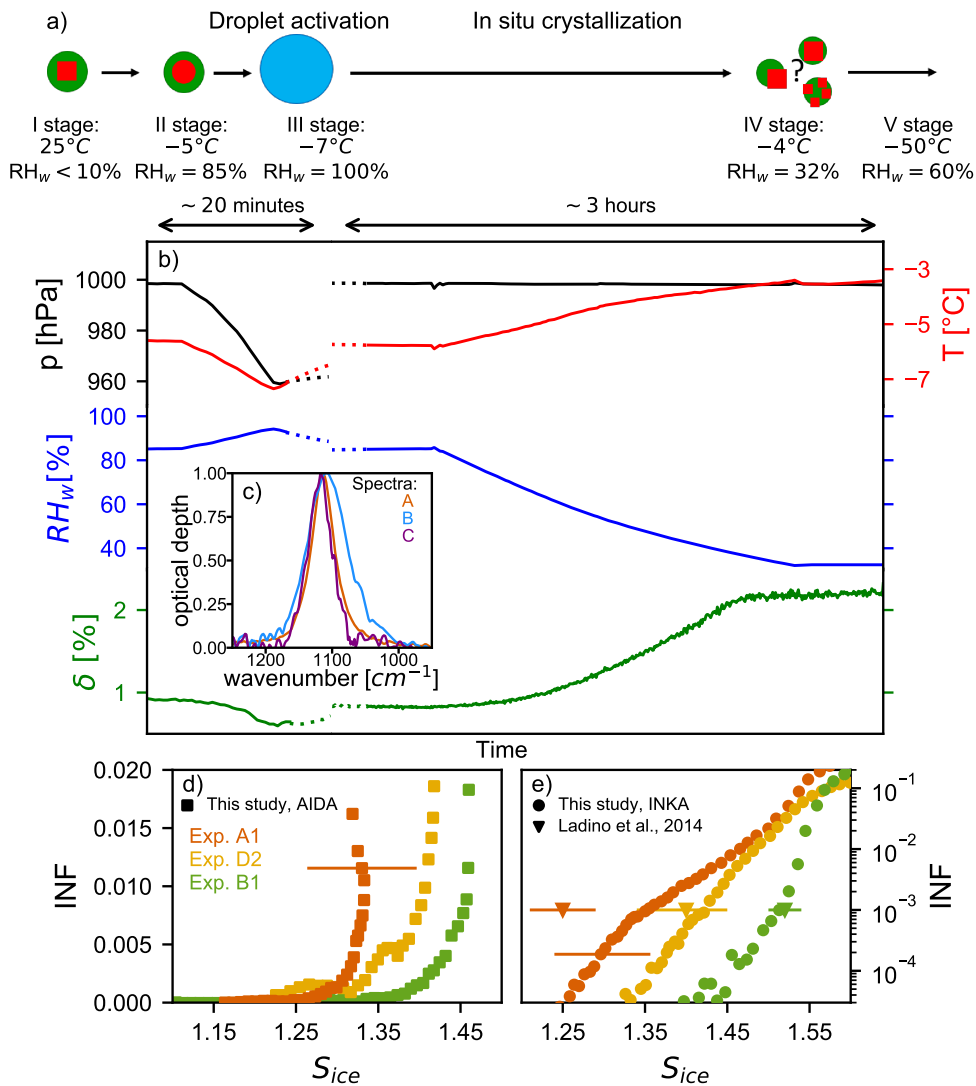
Figure 7.6: Liquid cloud processing, re-crystallization, and ice nucleation results (experiment type D). **a)** Schematic of the phase state and possible morphology of the particles after the in situ crystallization process. **b)** Time series of pressure (black line), temperature (red line), relative humidity with respect to water (blue line), and backscattering linear depolarization ratio (green line) during the in situ crystallization for experiment D2. The left part of the plot shows the short expansion run started at $-5\,°C$ and $RH_w = 85\%$ to activate the seed aerosol particles to homogeneously mixed, aqueous droplets. After refilling of the AIDA chamber to ambient pressure (not shown in the figure), the relative humidity was reduced to $RH_w = 32\%$ to induce the AS efflorescence. **c)** Normalized infrared spectra in the regime of the ν_3 (SO_4^{2-}) mode obtained after transfer of the particles into the AIDA chamber (spectrum B) and after the in situ crystallization (spectrum C) in comparison with a reference spectrum of pure AS crystals (spectrum A). **d)** and **e)** Ice nucleating fraction as function of S_{ice} for the AIDA and INKA experiments with pure AS crystals (experiment A1, orange symbols), unprocessed AS crystals with thick SOM coating (experiment B1, green symbols), and in situ crystallized mixed AS/SOM particles (experiment D2, yellow symbols). Ice onset results from Ladino et al. (2014) are reported in panel e as triangles: pure AS in orange, mixed AS/SOM particles in yellow, and pure SOA particles in green.

7.3.3 Freeze-drying processing

After an atmospheric freeze-drying process in a convective cloud system (described below), organic particles can adopt a highly porous morphology (Adler et al., 2013; Wagner et al., 2017). The porous morphology results from the fact that the initially liquid organic material concentrates and vitrifies upon ice formation, leaving behind a porous structure when the ice sublimates. This might provide a pathway to increase the ice nucleation ability of internally mixed AS/SOM particles with high organic mass fraction, because a porous organic coating might less efficiently cover the ice-active sites of the crystalline AS component. This pathway is investigated in experiment of type E.

The freeze-drying process of the thickly SOM-coated AS particles was started at $-30\,°C$ in the AIDA chamber. At this temperature, it is possible to run through the droplet activation (liquefaction of the organic material) and freezing (re-vitrification of the organic material) within a single expansion cooling experiment. Figure 7.7a summarizes the cloud processing steps and the potential phase and morphology changes of the particles. The time series of the AIDA records during the freeze-drying expansion run, started at time $0\,s$, are shown in Figure 7.7b. When the relative humidity exceeded the water saturation (first vertical line in Figure 7.7b), aerosol particles were activated as cloud droplets, detected by their larger diameter in the optical particle counter data. When the temperature approached the homogeneous freezing threshold (at about $-36\,°C$), a further fast drop in pressure was achieved by opening a valve in the pipe connection between the AIDA chamber and the evacuated APC chamber. This additional fast drop in pressure almost instantly reduced the gas temperature by another $2.5\,K$ and caused the entire droplet population to freeze homogeneously. The ice crystal formation is clearly visible in the optical particle counter data (second vertical line in Figure 7.7b). The chamber was then refilled to ambient pressure with dry synthetic air and the ice crystals thereby quickly sublimated. To probe the ice nucleation ability of the freeze-dried aerosol particles at cirrus cloud conditions the AIDA chamber was further cooled to $-50\,°C$. After the chamber cooling, the infrared spectrum of the freeze-dried AS/SOM particles in the regime of the ν_3 (SO_4^{2-}) mode was similar to spectra A and C in Figure 7.6c, indicating that the sulfate was effloresced. The AIDA expansion run started at $-50\,°C$ and the INKA supersaturation scan was performed at $-54\,°C$ with the particles sampled from the AIDA chamber at $-50\,°C$. The results are shown in Figures 7.7c and 7.7d with yellow symbols. As a reference, the ice nucleating fraction (INF) curves for pure ammonium sulfate crystals (Experiment A1, orange symbols), and unprocessed, thickly SOM-coated AS crystals (Experiment B2, green symbols) are shown. The ice nucleation ability of the freeze-dried particles lies between those of the reference systems, similar to the in situ crystallized particles (experiment of type D). The heterogeneous ice nucleation mode of the freeze-dried particles has the ice onset for an ice nucleating fraction of 1% at a saturation ratio S_{ice} of 1.41, while the ice onset saturation ratio is 1.33 for pure AS crystals and 1.48 for thickly SOM-coated AS crystals.

The activation curve of the freeze-dried particles measured with INKA (Figure 7.7d, yellow data) has a different profile compared, for example, to the thickly-coated particles (green data). The slower increase of the ice nucleating fraction as a function of the ice saturation ratio (similar to the activation curve for AS in orange) suggests that heterogeneous freezing is the dominant ice nucleation mechanism occurring in INKA up to $S_{ice} \approx 1.6$. This effect could be related to the limited residence time of the particles in the INKA instrument, which together with a slower water uptake from the particles could have shifted the detected homogeneous freezing onset to higher S_{ice} values. This kinetic limitation is not evident in the AIDA data, probably due to longer equilibration time during the expansion run. Particles in experiment E1 will likely be more viscous than particles from experiment B2 due to their larger organic mass fraction and/or due to a change of the chemical-physical properties of the particles after the freeze-drying process.

The enhanced ice nucleation ability of the freeze-dried particles may be explained by morphology changes. First, as already suggested above, a porous organic coating could less efficiently cover the ice nucleating active sites of the crystalline AS core. Second, the organic material might have been redistributed during the freeze-drying process, so that a similar morphology change as discussed in Experiment D could have occurred (like the formation of partially engulfed structures). The similar heterogeneous ice onsets measured in experiments D and E support this hypothesis. Third, the porous organic material formed during the freeze-drying process could be a better ice nucleus on its own via the pore condensation and freezing mechanism or by retaining an imprint
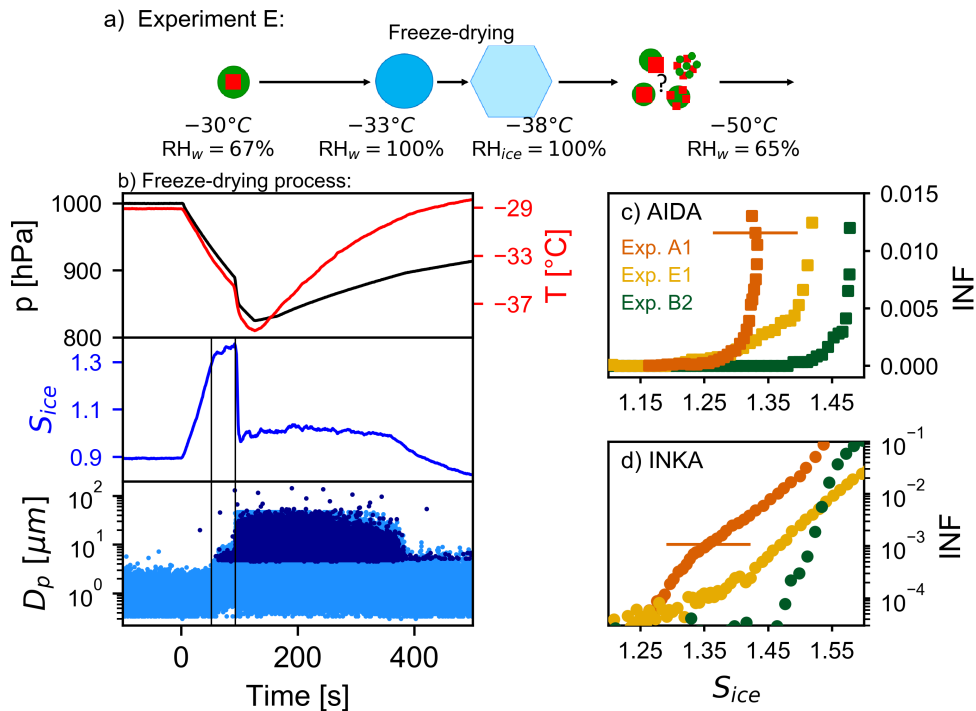
Figure 7.7: Results for the freeze-drying experiment (experiment E1). **a)** Scheme of the freeze-drying process together with the possible phase state and morphology of the particles during the experiment. **b)** Time series of the AIDA data during the freeze-drying process. Upper panel: pressure and temperature inside the AIDA chamber (black and red traces). Middle panel: saturation ratio with respect to ice (blue trace). Lower panel: single particle data from the welas optical particle counters (OPC1 and OPC2), each dot corresponds to an aerosol particle, droplet, or ice crystal at the corresponding optical diameter. **c)** and **d)** Ice nucleating fraction as function of the saturation ratio with respect to ice measured by AIDA and INKA. Data for pure AS crystals are reported in orange (experiment A1), unprocessed AS crystals with thick SOM coating in green (experiment B2), and freeze-dried SOM-coated AS crystals in yellow (experiment E1). Note the different scale in panels c and d.

of the sublimated ice on the highly viscous organic material. Previous studies observed an efficient pre-activation of glassy organic aerosol particles after ice-cloud processing (Wagner et al., 2012; Kilchhofer et al., 2021). Wagner et al. (2012) investigated in the AIDA chamber four different organic solutes, raffinose, 4-hydroxy-3-methoxy-DL-mandelic acid (HMMA), levoglucosan, and a multicomponent mixture of raffinose with five dicarboxylic acids and ammonium sulfate, and observed that the ice-cloud processed glassy aerosol particles catalyzed ice formation at ice saturation ratios between 1.05 and 1.30. Kilchhofer et al. (2021) confirmed the improved ice nucleation ability of cirrus-cloud processed raffinose particles in dedicated CFDC ice nucleation measurements. This raises the question of why the ice-cloud processed AS/SOM particles (observed ice onset at $S_{ice} = 1.41$) do not reveal an even better ice nucleation ability. However, repeated ice nucleation experiments with secondary organic aerosol particles produced from the ozonolysis of α-pinene performed by Wagner et al. (2017) showed a much lower susceptibility towards pre-activation compared to the above mentioned organic solutes. For example, the ice nucleation onset of the ice-cloud processed α-pinene SOA particles at about $-50\,°C$ was at an ice saturation ratio of about 1.45. A similar ice nucleation threshold was found in an experiment where highly porous α-pinene SOA particles were formed by a freeze-drying process at about $-30\,°C$ (as in the current study) and then cooled to cirrus temperatures to probe their ice nucleation ability. Furthermore, Adler et al. (2013) showed that in mixed AS/OM particles with a 1 : 1 molar ratio, the formation of a porous structure was reduced compared to the pure organic particles, adding to the effect that the freeze-dried AS/SOM particles are not extremely efficient INPs.

In spite of the strong effect of thin SOM coating layers revealed by experiments of type C, the ice nucleation ability of AS/SOM internally mixed particles is also strongly linked to their thermodynamic history. Uplifting of particles to the upper troposphere via convective clouds, for example, could lead to particles with an enhanced ice nucleation ability.

7.4 CONCLUSIONS

In this chapter, the ice nucleation ability of internally mixed particles composed of crystalline ammonium sulfate (AS) and secondary organic material (SOM) from the ozonolysis of α-pinene was investigated. The ice nucleation ability of the particles was probed at temperatures between $-50\,°C$ and $-65\,°C$, with expansion cooling experiments in the AIDA chamber and with a continuous flow diffusion chamber.

Mixed particles composed of sulfate and organics represent a major type of aerosol particles in the upper troposphere and may contribute a significant fraction of ice nucleating particles (INPs) involved in cirrus cloud formation (Froyd et al., 2009).

Crystalline AS particles are recognized efficient INPs at cirrus conditions, as shown in Chapter **??** and by previous studies (e.g., Abbatt et al., 2006). However, secondary organic material condensed on the AS surface progressively shifts the ice nucleation onset to higher ice saturation ratios. A small amount of SOM, corresponding to an organic mass concentration of $5-8\,wt\%$, is sufficient to increase the ice nucleation onset of the coated particles to $S_{ice} > 1.45$ (experiment of type C). Thus, a thin coating layer of secondary organic material is able to greatly reduce the ability of crystalline AS to act as INP. Möhler et al. (2008) also measured the suppression of the heterogeneous ice nucleating ability of mineral dust aerosol particles caused by a coating of SOM derived from the ozonolysis of α-pinene. The ozonolysis of α-pinene is not the only mechanism responsible for upper tropospheric SOM, as photolysis also plays a crucial role during daytime. However, the nucleation and growth mechanisms does not influence the ice nucleation ability of α-pinene derived organic material (Piedehierro et al., 2021).

Internally mixed particles can form in the atmosphere through different pathways and can experience various aging and cloud-cycling processes, leading to particles with more complex morphologies than the idealized core-shell case, as simulated in experiments of type C. Two experiments were performed to investigate whether there are pathways by which the ice nucleation ability of mixed AS/SOM particles with high organic weight fractions ($25-50\,wt\%$), as often found in the upper troposphere (Froyd et al., 2009), could be increased. Different particle morphologies, such as partially engulfed structures, might form, for example, when homogeneously mixed, aqueous mixtures of sulfate and organics undergo the crystallization of the AS component (experiments of type D). Results show that the processed particles have an ice nucleation ability lying between those of the pure and the SOM-coated AS particles in a core shell morphology, with the ice onset at $S_{ice} \approx 1.35$ at $-53\,°C$.

Another possible atmospheric process that can modify the ice nucleation ability of SOM-coated AS particles is the freeze-drying process. Previous studies have shown that highly viscous organic particles can adopt a porous morphology after a freeze-drying process, which could influence their ice nucleation ability. The freeze-drying process was simulated in the AIDA chamber at $-30\,°C$ and then probed the ice nucleation ability of the mixed processed particles at $-50\,°C$ (experiment type E). Also in this case, the processed mixed particles show an intermediate ice nucleation ability compared to the reference systems (i.e., ice nucleation ability between pure AS and AS with a compact SOM coating in a core shell morphology).

Results from experiments D and E suggest that internally mixed particles, that undergo liquid or ice cloud processing, have unevenly distributed organic coating. The solid AS component is thus partially uncovered and able to catalyze the ice nucleation at lower S_{ice} compared to the unprocessed, uniformly coated particles.

In summary, the experiments presented in this chapter highlight the difficulty to represent the ice nucleation ability of internally mixed particles with just a single parametrization. The presence of an organic coating can suppress the ice nucleation ability of the seed particle at cirrus cloud conditions, but the ice nucleation ability of the same particle can substantially change if subjected to

atmospheric processing. Since cloud processing is a common phenomenon, especially for particles uplifted in a convective system, their morphology changes and the enhancement of their ice nucleation ability need to be carefully characterized, also for internally mixed particles with different compositions (e.g., mineral dust particles coated with organic material).

8 | COATED MINERAL DUST PARTICLES

8.1 INTRODUCTION

Mineral dust is an important atmospheric aerosol component, with the global annual emission mass estimated to be about $1500\,\mathrm{Tg\,yr^{-1}}$ (Usher et al., 2003; Ginoux et al., 2012). On a global scale, the most active dust sources are located in arid regions such as North Africa, which contributes to 55 % of the global emissions, Middle East, and central Asia (Ginoux et al., 2012). In the Southern Hemisphere, dust emissions are much lower, with the major source located in Australia. Atmospheric mixing and circulation can transport plums of dust particles far away from their strong sources. Ryder et al. (2013) estimated that most of the particles with diameters larger than about $30\,\mathrm{\mu m}$ remain suspended in the atmosphere for less than a day before they deposit due to gravitational settling or wet deposition. Smaller particles, instead, can have an atmospheric lifetime of the order of several weeks and can be transported over thousands of kilometers (Prospero, 1999; Schepanski, 2018). Saharan dust plumes, for example, can reach Northern Europe (Ansmann et al., 2003), Iceland (Varga et al., 2021), the United States (Prospero, 1999), and eventually the Southern Ocean (Li et al., 2008).

Mineral dust play a key role in cloud ice formation by facilitating heterogeneous ice formation in a wide range of temperatures and ice saturation ratios (e.g., Pruppacher and Klett, 1997; DeMott et al., 2003; Sassen et al., 2003; Möhler et al., 2006; Hoose and Möhler, 2012). Dust particles are efficient ice nucleating particles (INPs) in the immersion freezing mode at a temperature above $-38\,^\circ\mathrm{C}$, and in the water-subsaturated regime in the deposition nucleation or pore condensation and freezing modes (Hoose and Möhler, 2012; Marcolli, 2014; Vali et al., 2015). Natural dust particles have complex mineralogy that varies among the different sources, and they are usually composed of aggregates of different minerals (Claquin et al., 1999). Clay minerals (such as illites and kaolinites) are believed to constitute the major fraction of the dust aerosol mass (about 62 %), followed by quartz (16 %), feldspars (11 %), and calcite (3 %) (Atkinson et al., 2013).

Feldspar particles have shown a high ice nucleation ability compared to the other minerals both at mixed-phase cloud conditions for $T > -38\,^\circ\mathrm{C}$ (Atkinson et al., 2013; Peckhaus et al., 2016) and in the cirrus cloud temperature range (Yakobi-Hancock et al., 2013). Atkinson et al. (2013) suggested that feldspar components may dominate the overall ice nucleation behavior of mixed natural samples despite their low mass concentration due to their high ice nucleation ability. The higher ice nucleation ability of feldspar minerals, in particular of potassium feldspar (K-feldspar) (Harrison et al., 2016), has been associated to their micro-textures and topographic features (Kiselev et al., 2017; Whale et al., 2017) or to the weak interaction energy of the surface cations with water molecules (Zolles et al., 2015). Recently, Kumar et al. (2021) have tried to identify the mechanism behind the high ice nucleation ability of K-feldspar with molecular dynamics simulations. In the simulations, ice nucleation did not occur on the planar pristine surface of the mineral at about $-40\,^\circ\mathrm{C}$ suggesting that they are not responsible for the ice nucleation ability of K-feldspar particles.

While suspended in the atmosphere, mineral dust particles may undergo several aging processes such as cloud cycles (Wurzler et al., 2000), heterogeneous reactions (e.g., Dentener et al., 1996), and condensation of different chemical species (Levin et al., 1996; Kandler et al., 2007). Several field studies have documented the internal mixing state of dust particles with acidic components (e.g., sulfuric and nitric acid) and organic compounds (e.g., oxidized secondary organics), especially in the upper troposphere (e.g., Murphy, 1998; Murphy, 2005; Murphy et al., 2006; Kojima et al., 2006). Chemical coating or other atmospheric aging processes can modify the surface properties of the particles and thus their direct and indirect effect on the climate. For example, coatings with soluble materials can modify the optical properties of the mineral dust particles, and may enhance their ability to act as cloud condensation nuclei (Levin et al., 1996). It is important to study the effect of different aging processes on the ice nucleation ability of mineral dust particles in order to fully infer their role in cloud formation. Additionally, understanding the impact of particle surface property

changes on their ice nucleation ability can improve our knowledge of the microphysical processes involved in the heterogeneous ice formation on the pristine particles.

Several studies have investigated the effect of different aging processes (e.g., coatings and exposure to oxidants) on the ice nucleation ability of mineral dust particles (Hoose and Möhler, 2012). Most of the past literature studies that investigated the effect of coatings were performed in the mixed-phase cloud regime. In those studies, mixed and pure mineral dust samples, including K-feldspar, were coated with several different compounds commonly found in the atmosphere (e.g., sulfuric and nitric acid, carboxylic acids, levoglucosan, and secondary organic material) (e.g., Zobrist et al., 2008b; Niedermeier et al., 2010; Yang et al., 2011; Kulkarni et al., 2014; Augustin-Bauditz et al., 2014; Kumar et al., 2018). It was found that coatings have a minor effect on the initial ice nucleation ability of the bare particles in the immersion freezing mode, while they have a stronger deactivation effect on the deposition and pore condensation and freezing modes (e.g., Cziczo et al., 2009; Eastwood et al., 2009; Chernoff and Bertram, 2010; Sullivan et al., 2010; Kulkarni et al., 2014).

Only a few studies investigated the effects of coatings on mineral dust particles in the cirrus cloud temperature range (T < −38 °C). Archuleta et al. (2005) measured the ice nucleation ability of bare and sulfuric acid (SA) coated surrogates of mineral dust particles (i.e., aluminum oxide, alumina-silicate, and iron oxide) with a continuous flow diffusion chamber at temperatures between −45 °C and −60 °C. The SA coatings, estimated to be in the $1.6 − 7 \, wt\%$ range, affected the ice nucleation ability of the different particles in different ways. The ice saturation ratio at ice formation onset of the coated particles was found to be lower (iron oxide particles), unchanged (aluminum oxide particles), or higher (alumina-silicate particles) compared to the initial value. Möhler et al. (2008) investigated the effect of coatings of secondary organic material (SOM) derived from the ozonolysis of α-pinene on illite and Arizona test dust (ATD) particles in AIDA expansion cooling experiments at about −65 °C. The ice nucleation onsets (defined for 1% of ice-active particles) shifted from an ice saturation ratio $S_{ice} \approx 1.05$ for the uncoated samples to about 1.15 and 1.65 for the SOM-coated ATD and illite particles, respectively. The difference in the ice onset conditions between the two SOM-coated samples was explained by the different amounts of condensed organic material, about $17 \, wt\%$ and $41 \, wt\%$ for the coated ATD and illite particles, respectively. Koehler et al. (2010) also investigated SOM-coated ATD particles but in a wider temperature range (from −40 °C to −60 °C) with a continuous flow diffusion chamber. Similarly to Möhler et al. (2008), the secondary organic material was derived from the ozonolysis of α-pinene, but the organic mass fraction condensed on the particles was not estimated. The SOM-coated ATD particles only froze at or above the homogeneous freezing threshold of aqueous solution droplets (Koop et al., 2000). Comparing the different experiments investigating coating effects on the ice nucleation ability of mineral dust particles is difficult because of the different aerosol generation methods, nature of the seed particles, coating procedures, and the different ice nucleation measurement methods applied.

The experiments presented in this chapter aimed at investigating for the first time the effect of thin coatings of sulfuric acid and secondary organic material on the heterogeneous ice nucleation ability of feldspar particles at cirrus cloud conditions. Two samples of feldspar with slightly different mineralogical compositions were investigated. To simulate upper tropospheric aging of the particles, the coating procedure was performed inside the AIDA chamber at about −44 °C. The ice nucleation ability of the particles was probed with expansion cooling experiments. The experiments were conducted at the AIDA chamber during the Fifth Ice Nucleation Workshop - part 1 (FIN01, 2014).

8.2 AEROSOL PREPARATION AND CHARACTERIZATION

Two different mineral samples of feldspar were used. The same two samples had already been investigated in the immersion freezing regime by Peckhaus et al. (2016). By following the same name convention of Peckhaus et al. (2016) the samples are here addressed as FS01 and FS04. Both samples were prepared by ball milling of single-crystal mineral specimens. The composition of the two samples is dominated by potassium feldspar (K-feldspar), but the overall mineralogical composition is slightly different, as reported in Table 8.1. The bulk mineralogical composition was determined by X-ray powder diffraction (XRD). A detailed description of the two samples, in terms of morphology and mineralogical composition, can be found in the work of Peckhaus et al. (2016).

Table 8.1: Mineral composition of the feldspar samples used in the presented ice nucleation experiments. Table adapted from Peckhaus et al. (2016).

Sample	Source	Mineral composition (XRD)
FS01	Minas Gerais (Brazil), supplied by IAG TU Darmstadt	76 % K-feldspar (microcline) 24 % Na/Ca-feldspar (albite)
FS04	Mt. Maloso area (Malawi), supplied by IAG TU Darmstadt	80 % K-feldspar (microcline) 18 % Na/Ca-feldspar (albite) 2 % quartz

A detailed description of the AIDA chamber and its standard instrumentation can be found in Section 3.1 and Section 3.2. The dry feldspar samples were dispersed with a rotating brush generator (RBG, RBG1000, Palas). Dry and particle-free synthetic air was used as carrier gas from the RBG to the AIDA chamber. Two cyclone impactors in the transfer line removed particles larger than about 1 to 2 μm from the aerosol flow. The aerosol particle number concentration was measured with a condensation particle counter (CPC). The number size distribution of the particle population was measured with a scanning mobility particle sizer (SMPS), for mobility diameters in the range $10 - 800$ nm, and with an aerodynamic particle sizer (APS), for aerodynamic diameters in the range $0.7 - 20$ μm. To combine the SMPS and APS measurements, the mobility and the aerodynamic diameters were converted to volume equivalent diameters. For the uncoated particles, a dynamic shape factor of 1.3 and a density of 2.6 g cm^{-3} were used for this conversion. For the coated particles, the same density of the bare feldspar particles was used, assuming that the applied thin coating layers (see below) did not significantly modify the initial density of the particles. The morphology of the coated particles, instead, is expected to exhibit more smooth surface structures and the dynamic shape factor was thus reduced to 1.2.

To simulate atmospheric aging processes in the upper troposphere, the feldspar particles were coated in the AIDA chamber at low temperature (about -44 °C) and almost ice saturated conditions ($S_{ice} \approx 1$, RH$_w \approx 65$ %). During different experiments, coatings of sulfuric acid (H_2SO_4, SA) or secondary organic material (SOM) derived from the ozonolysis of α-pinene were applied. A list of the performed experiments is presented in Table 8.2.

Table 8.2: Summary of the experiments performed and main parameters of the aerosol particle populations. T_0 and $S_{ice,\,0}$ indicate the thermodynamic conditions inside the AIDA chamber during the coating procedure and also correspond to the initial conditions of the expansion cooling experiments. D_{ve}^{median} is the volume equivalent median diameter of the lognormal fit to the aerosol size distribution measured right before the expansion cooling experiments. The ice nucleation onset temperature $T_{0.1\,\%}$ and ice saturation ratio $S_{ice,\,0.1\,\%}$ correspond to an ice-active aerosol particle number fraction of 0.1 %.

Exp.	Sample	Coating	T_0 [°C]	$S_{ice,\,0}$	D_{ve}^{median} [μm]	$T_{0.1\,\%}$ [°C]	$S_{ice,\,0.1\,\%}$
1	FS01	—	−43.8	0.97	0.21	−45.8	1.19
2	FS01	H_2SO_4	−43.8	0.98	0.22	−47.8	1.44
3	FS04	—	−44.7	0.97	0.23	−46.0	1.10
4	FS04	SOM	−44.9	0.97	0.24	−49.2	1.48
5	FS04	H_2SO_4	−45.0	0.97	0.27	−49.0	1.46

The effect of a thin coating of sulfuric acid on the ice nucleation ability of the mineral dust particles was investigated for both feldspar samples (experiments 2 and 5 with FS01 and FS04 as seed particles, respectively). The SOM coating was tested only for the sample FS04 (experiment 4).

The formation of sulfuric acid in the AIDA chamber was initiated from the oxidation of sulfur dioxide (SO_2) with hydroxyl radicals ($\cdot$OH). Hydroxyl radicals were generated from the dark ozonolysis of tetramethylethylene (TME, C_6H_{12}). After injection of the feldspar particles FS01 ($c_n \approx 700$ cm^{-3}) at the beginning of experiment 2, the gaseous precursors were injected in the following order: ozone (≈ 900 ppb), TME (≈ 8 ppb), sulfur dioxide (≈ 2.5 ppb), and again TME (≈ 5 ppb) to convert all the sulfur dioxide to sulfuric acid. A similar procedure was performed for
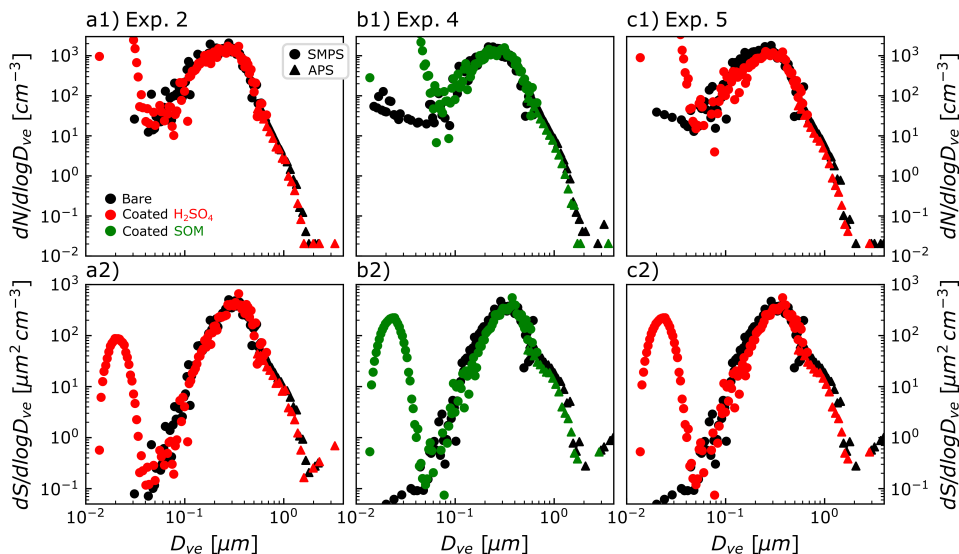
Figure 8.1: Number (upper panels) and surface (lower panels) size distributions as a function of the volume equivalent diameter measured with an SMPS (circles) and APS (triangles). Measurements performed before coating are shown in black and after the coating in red (for sulfuric acid coating) and green (for SOM coating). After the coating procedure, nucleation of aqueous sulfuric acid and secondary organic aerosol particles resulted in bi-modal distributions with the nucleation modes at about 25 nm.

experiment 5 by adding FS04 particles ($c_n \approx 550 \, cm^{-3}$), ozone ($\approx 1 \, ppm$), sulfur dioxide ($\approx 5 \, ppb$), and TME ($\approx 11 \, ppb$).

Because of the low saturation pressure, most of the sulfuric acid molecules formed in the gas-phase condense and stick to the particle surface, or undergo nucleation together with water molecules to form new nanometer-sized aqueous sulfuric acid particles. The newly formed particles grew to a median diameter of about 25 nm with the larger particles at about 50 nm. For these particles, a shape factor of 1.0 was used to convert the mobility diameter of the SMPS measurements to the volume equivalent diameter.

Coating of the feldspar particles with secondary organic material was achieved by first adding the mineral dust particles of the sample FS04 ($c_n \approx 650 \, cm^{-3}$), followed by ozone ($\approx 240 \, ppb$) and α-pinene ($\approx 600 \, ppt$). The oxidation products of α-pinene condensed on the feldspar particles and also initiated the nucleation of secondary organics containing particles. The newly formed organic particles grew to a median diameter of about 25 nm with the larger particles at about 70 nm. For these particles, a shape factor of 1.0 was used to convert the mobility diameter of the SMPS measurements to the volume equivalent diameter. Figure 8.1 shows the number and surface size distributions measured before (in black) and after (in red or green) the coating procedure for experiments 2 (panels a), 4 (panels b), and 5 (panels c). The condensation of the secondary material on the feldspar particles did not result in a detectable shift of the particle size distributions, indicating that only a thin coating layer condensed on the particles for all the experiments. The median diameter D_{ve}^{median} of the bare (experiments 1 and 3) and coated feldspar particles (experiments 2, 4, and 5) is reported in Table 8.2.

8.3 ICE NUCLEATION EXPERIMENTS

The ice nucleation ability of the bare and coated mineral dust particles was investigated with expansion cooling experiments inside the AIDA chamber at the initial temperature of about −44 °C (T_0 in Table 8.2). A detailed description of a typical AIDA expansion cooling experiment can be found in Section 3.2.3.

Data time series from ice nucleation experiments performed with bare, SA-coated, and SOM-coated FS04 feldspar particles (experiments 3, 4, and 5) are compared in Figure 8.2. These examples are also representative of the experiments performed with FS01 (experiments 1 and 2). The upper panels show the time series of pressure (in black) and temperature (in red) during the expansion inside the AIDA chamber. Middle panels report the evolution of the ice saturation ratio S_{ice}. The parameterizations from Murphy and Koop (2005) are used to calculate the saturation vapor pressure over liquid water and ice. The horizontal dashed line corresponds to the homogeneous freezing threshold for aqueous solution droplets according to the parameterization of Koop et al. (2000) (for $\Delta a_w = 0.3$, see Section 2.1). The single-particle data from the two optical particle counters (OPC) installed inside the thermal housing of the AIDA chamber are shown in the bottom panels. Each blue dot corresponds to an aerosol particle or ice crystal at the corresponding optical diameter (left axis). The ice crystals are detected at larger sizes compared to the initial aerosol particles due to their irregular shapes and higher refractive index. The ice-active fraction of the aerosol population (i.e., the ice nucleating fraction, INF) is reported in black (right axis). The ice nucleating fraction is calculated as the ratio of the measured ice crystal concentration to the number concentration of the pristine or coated dust particles only, excluding the nucleation mode of particles formed during the coating procedure. The pure SA and SOA particles do not influence the ice nucleation measurements because they only contribute to ice nucleation at or above the homogeneous freezing threshold for aqueous solution droplets (Möhler et al., 2003; Wagner et al., 2017). Therefore, differences between the experiments performed with uncoated and coated particles only relate to changes in the surface features of the mineral dust particles.

There is a pronounced difference in the ice nucleation behavior of the bare (experiment 3, panel a) and coated (experiments 4 and 5, panels b and c) feldspar particles. The ice nucleation by pure mineral particles starts at a low ice saturation ratio ($S_{ice} = 1.10$ for an $INF = 0.1\,\%$, vertical dashed line), well below the homogeneous freezing threshold for aqueous solution droplets (horizontal dashed lines in the middle panels of Figure 8.2). A large fraction of aerosol particles nucleated ice at low S_{ice}, and the ice supersaturation is quickly depleted due to the diffusional growth of ice crystals, limiting the peak ice saturation ratio during the expansion experiment to about 1.16. The SOM-coated and SA-coated particles, instead, started to nucleate ice only for an ice saturation ratio inside the chamber approaching the homogeneous freezing threshold value at about $S_{ice} = 1.45$. The ice onset conditions for experiments 1 (with FS01) and 2 (SA-coated FS01) are reported in Table 8.2.

The ice nucleation active surface site (INAS) density n_s (shown in the next section) is calculated by dividing the ice crystal number concentration by the total surface area of the particles derived from the combined SMPS and APS size distributions excluding the nucleation mode aerosol particles.
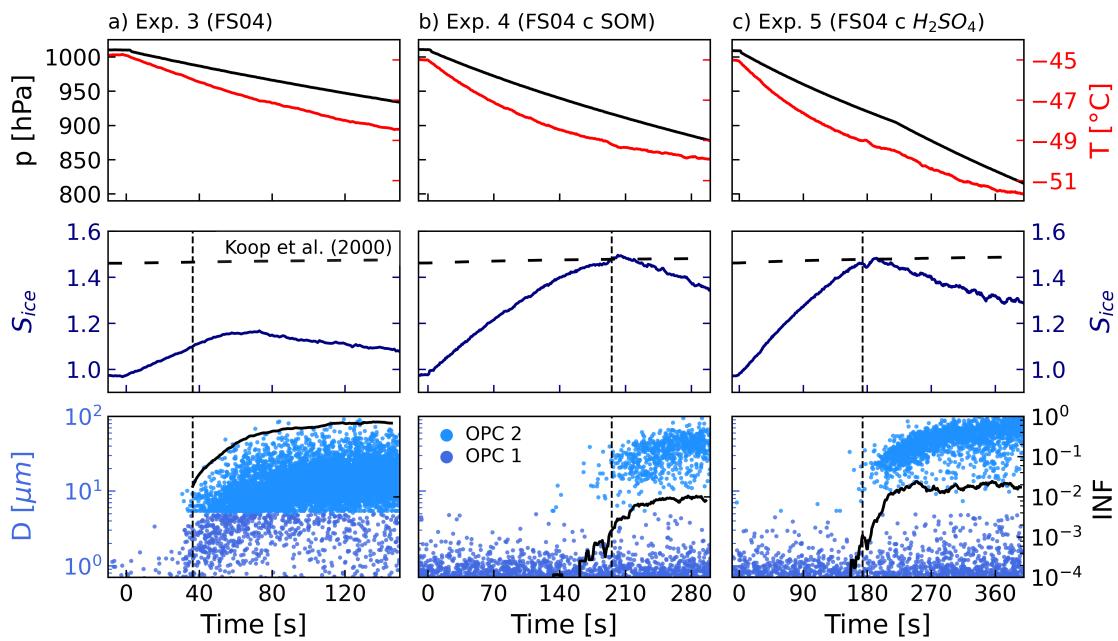
Figure 8.2: Time series of three AIDA expansion cooling experiments performed with bare FS04 (experiment 3, panel a), FS04 coated with secondary organic material from the ozonolysis of α-pinene (experiment 4, panel b), and FS04 coated with sulfuric acid (experiment 5, panel c). Upper panels report the reduction in pressure (black traces, left axes) and temperature (red traces, right axes) inside the AIDA chamber. Middle panels show the evolution of the ice saturation ratio S_{ice} and the homogeneous freezing threshold for aqueous solution droplets (black horizontal dashed lines, Koop et al., 2000). Lower panels show the single-particle data from the optical particle counters (OPC), each blue dot corresponds to an aerosol particle or ice crystal at the corresponding optical diameter (left axis). The ice nucleating fraction (INF) is also shown in the lower panels (black traces, right axes).

8.4 RESULTS

A summary of the ice nucleation results is provided in Figure 8.3, where the ice nucleating particle fraction is shown as a function of the ice saturation ratio for all the experiments performed. Data for the bare feldspar samples are shown in black, experiments with SA-coated particles are shown in red, and results for SOM-coated FS01 in green. For comparison, the ice nucleation onset (for INF = 0.1 %) measured at −40 °C with a continuous flow diffusion chamber by Yakobi-Hancock et al. (2013) for a different sample of K-feldspar particles (size selected at a diameter of 200 nm) is also shown (gray diamond).

The increasing number of ice-active particles measured with increasing ice saturation ratio for the uncoated particles is typical for heterogeneous ice nucleation. This gradual increase in the number of formed ice crystals is interpreted as the increasing number of surface sites that activate at their corresponding critical ice saturation ratio (Möhler et al., 2006). Both feldspar samples show a high ice nucleation ability and initiate ice crystal formation at ice saturation ratios well below the homogeneous freezing threshold for aqueous solution droplets (Koop et al., 2000). The ice nucleation onsets, defined for 0.1 % of ice-active particles, were measured at S_{ice} = 1.19 and 1.10 for the samples FS01 and FS04, respectively. A higher ice nucleation activity of the sample FS04 compared to FS01 was also evident in the immersion freezing experiments from Peckhaus et al. (2016). The ice nucleation onset from Yakobi-Hancock et al. (2013) is at a slightly higher ice saturation ratio (S_{ice} = 1.27), but still in agreement with the results of the sample FS01. The ice nucleation onset of the thinly coated feldspar particles is shifted to about S_{ice} = 1.45 and the shape of the ice-activation curves is steeper, suggesting that most of the particles nucleated ice at almost the same ice saturation ratio. The effect of different coating materials (SA or SOM) and seed particles (FS01 or FS04) is not discernible.

The ice nucleation results of experiments 3, 4, and 5 are summarized in terms of ice nucleation active surface sites (INAS) density n_s in Figure 8.4. The parameterization for natural desert dust suggested by Ullrich et al. (2017) is also shown for comparison (colored lines). The $T - S_{ice}$ trajectories of the AIDA experiments are shown with gray lines. The calculated n_s values are shown with circles whose size and color identify the n_s values. Water saturation and homogeneous freezing threshold for aqueous solution droplets are shown with solid and dashed black lines.

The INAS density values of the bare feldspar sample FS04 (Figure 8.4a) are much higher than the parameterization for the mixed natural dust particles from Ullrich et al. (2017). The higher ice nucleation ability of the feldspar particles compared to the mixed natural samples could be related to their mineralogy or to the presence on the surface of the particles of artificial features originated from the ball milling of the original single crystal sample. The INAS density values for the coated particles, instead, are much higher than the parameterization. Ice nucleation occurs close to the homogeneous freezing threshold, suggesting that the ice nucleation mode changes from heterogeneous to homogeneous nucleation of the diluted coating material.

The high fraction of ice-active feldspar particles at very low ice saturation ratios and the strong suppression of their ice nucleation ability by thin coatings hint at the potential importance of pore condensation and freezing in the measured heterogeneous ice formation on the bare feldspar particles. The high ice nucleation activity of the bare particles could be explained by a pre-activation effect similar to that measured for illite particles by Wagner et al. (2016). At low temperatures, pores or cracks present on the surface of the particles can fill with ice at ice subsaturated conditions (pre-activation), thus leading to the spontaneous growth of the ice crystals once ice saturated conditions are achieved. When the particles are coated, the pores are filled with the condensed material and water vapor cannot condense anymore preventing the formation, or growth, of the initial ice germ formed in the pores. The strong suppression in the ice nucleation ability of SOM-coated illite particles reported by Möhler et al. (2008) could also be explained by the suppression of the pre-activation effect measured by Wagner et al. (2016).
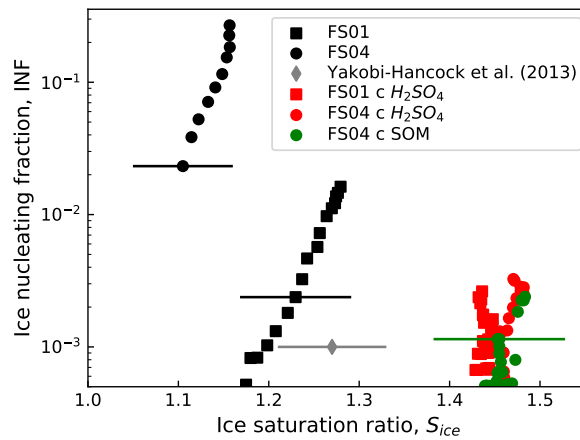
Figure 8.3: Ice nucleating fraction as a function of the ice saturation ratio for bare feldspar samples (black symbols) and coated with sulfuric acid (red symbols) or secondary organic material from the ozonolysis of α-pinene. The ice nucleation onset from the experiment of Yakobi-Hancock et al. (2013) with a different sample of K-feldspar is shown in gray.
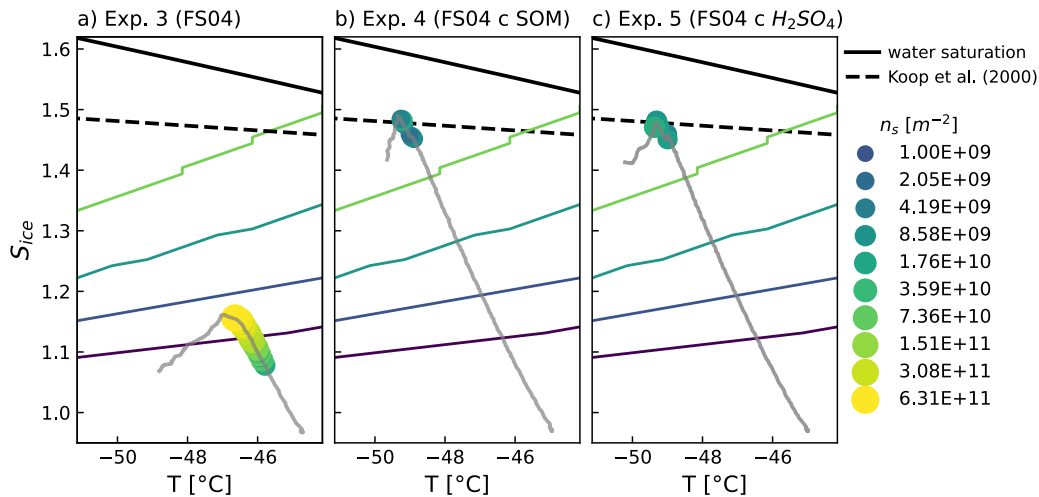
Figure 8.4: $T - S_{ice}$ trajectories of the AIDA expansion cooling experiments (gray lines). The size and color of the superimposed circles indicate the ice-active surface site density values corresponding to the color bar. Contour lines of n_s from the parameterization for desert dust from Ullrich et al. (2017) are also shown. Water saturation and homogeneous freezing threshold for solution droplets are shown as solid and dashed black lines.

8.5 CONCLUSIONS

To investigate the effect of atmospheric aging under upper tropospheric conditions, bare feldspar samples were coated inside the AIDA chamber at about $-44\,^{\circ}\text{C}$ and ice saturated conditions ($\text{RH}_w \approx 65\,\%$) with sulfuric acid and secondary organic material derived from the ozonolysis of α-pinene. The coating experiments showed for the first time that the ice nucleation ability of feldspar particles at cirrus cloud conditions is strongly suppressed already by thin coatings layers. The ice onset, corresponding to an ice-active fraction of aerosol particles of $0.1\,\%$, was shifted from an ice saturation ratio of about $S_{\text{ice}} = 1.10 - 1.20$ for the bare particles to $S_{\text{ice}} \approx 1.5$ for the coated particles, a value close to the homogeneous freezing threshold for aqueous solution droplets (Koop et al., 2000).

Both the low ice nucleation onset of the bare particles and the strong suppression of their ice nucleation ability by small amounts of condensed material suggest that pores and cracks are responsible for the high ice nucleation ability of the uncoated particles. Assuming that the feldspar content in natural mineral dust aerosol particles has similar surface features to the samples investigated here, it is possible to conclude that the contribution of feldspar components to heterogeneous formation of cirrus clouds is strongly suppressed by thin coating layers of sulfuric acid and secondary organic material. To better understand and quantify the role of pre-activation in pores and its suppression by coating materials, further experiments with different types of natural mineral dust samples should be performed.

Field studies have shown that dust particles are often found internally mixed with acidic components and organic compounds, especially in the upper troposphere. The experiments presented in this chapter highlight the potential importance of pore condensation and freezing for feldspar containing mineral dust particles, and demonstrate the strong effect that aging processes can have on their ice nucleation ability. By describing ice crystal formation with parametrizations formulated only for pristine mineral dust particles, the occurrence of heterogeneously formed cirrus clouds may be overestimated.

9 | SUMMARY

This thesis investigates several atmospheric aerosol systems for their ice nucleation behavior, which is of relevance for ice formation in clouds. Clouds play an important role in the Earth's energy budget by interacting with both short- and long-wave radiation. Their net radiative contribution, or rather, their warming or cooling effect on the planet, depends on their altitude, geographical location, occurrence frequency, and optical properties. The latter, in turn, are defined by the microphysical properties of the clouds, such as phase state, number concentration, and size of the hydrometeors. The focus of this thesis is on cirrus clouds, whose net radiative effect is still poorly quantified.

Cirrus are clouds composed only of ice particles that form in the upper troposphere at temperatures below about $-38\,°$C. Two different ice nucleation mechanisms compete in cirrus cloud formation, namely homogeneous freezing of ubiquitous aqueous solution droplets or heterogeneous ice formation with the contribution of rare ice nucleating particles (INPs). The different number concentrations of aqueous solution droplets and INPs present in the atmosphere lead to the formation of cirrus clouds with different optical properties depending on the relative contribution of the two ice formation mechanisms. Which pathway dominates in cirrus cloud formation is determined by dynamic processes (e.g. updraft velocity), and availability and type of INPs present in the atmosphere. Detailed knowledge of the ice nucleation ability of atmospheric particles is therefore crucial to correctly formulate and model cirrus formation mechanism, their microphysical properties, and finally their impact on the present and future climate.

The experiments presented in this thesis were performed at the AIDA chamber at the Karlsruhe Institute of Technology and at the CLOUD experiment at the European Organization for Nuclear Research (CERN). The AIDA chamber is a unique facility to perform aerosol-cloud interaction studies in a wide range of thermodynamic conditions and to simulate chemical and physical processing of the aerosol particles, such as chemical aging and cloud cycling. The CLOUD experiment is especially designed for aerosol nucleation studies. The accurate control of the concentration of the gas precursors, along with the employment of different state of the art aerosol mass spectrometers, allow an accurate chemical characterization of the formed aerosol particles. The ice nucleation measurements were performed at temperatures between $-40\,°$C and $-65\,°$C with expansion cooling experiments in the AIDA chamber and with continuous flow diffusion chambers. In particular, the ice nucleation ability of secondary aerosol particles was studied with regard to changes in their chemical composition, phase state, surface properties, and morphology. Inorganic and organic compounds of biogenic and anthropogenic origin, at pristine or aged conditions, were investigated.

Sulfuric acid and ammonia are among the most abundant acids and bases present in the atmosphere. Their concentrations, which are predominantly controlled by anthropogenic emissions, determine the relative abundance of sulfate and ammonium (i.e., neutralization degree) in the particle phase. Small changes in the neutralization degree of ammonium-sulfate particles were shown to define their phase state, deliquescence behavior, and ice nucleation ability (Chapter 4). The ammonium-to-sulfate ratio (ASR) of the particles was found to be a useful parameter to classify their ice nucleation ability. As a general trend particles with higher ASR form ice at lower ice saturation ratios. Aqueous sulfuric acid particles ($ASR = 0$) and their fully neutralized salt (ammonium sulfate, $ASR = 2.0$) have been thoroughly investigated in previous ice nucleation studies. However, the results presented in Chapter 4 are the first ice nucleation measurements of partially neutralized particles composed of mixed ammonium bisulfate and letovicite ($1.0 < ASR < 1.5$), pure letovicite ($ASR = 1.5$), and mixed letovicite and ammonium sulfate ($1.5 < ASR < 2.0$).

Ammonium bisulfate particles ($ASR = 1.0$) remain in a supercooled aqueous phase state in the atmosphere and initiate ice nucleation only via homogeneous freezing at an ice saturation ratio of

about 1.62 at −52 °C, similarly to other aqueous solution droplets. Particles with a higher neutral-ization degree can have a component (either letovicite or ammonium sulfate) that is crystalline at ice supersaturated conditions for temperatures below about −50 °C. Such particles are therefore able to initiate heterogeneous ice formation at lower ice saturation ratios. Mixtures of ammonium bisulfate and letovicite prevail as internally-mixed solid/liquid particles. They initiate ice forma-tion on the crystalline letovicite component immersed in the deliquesced ammonium bisulfate at an ice saturation ratio of ≈ 1.55. Crystalline letovicite, mixed letovicite and ammonium sulfate, and pure ammonium sulfate particles remain in a crystalline state up to very high ice saturation ratios (≈ 1.5) and initiate heterogeneous ice formation in the range $S_{ice} = 1.2 − 1.4$. The fully neutralized crystalline ammonium sulfate particles were shown to be the most ice nucleation active compound in the system.

Our knowledge of the neutralization degree of upper tropospheric particles is very limited as aerosol chemical composition measurements are scarce and limited to few geographical locations. The expected increase in the neutralization degree of ammonium-sulfate particles due to decreasing sulfur dioxide and increasing ammonia emissions could increase the number of heterogeneously formed cirrus clouds in the future. These results show that the detailed knowledge of the abundance and neutralization degree of ammonium-sulfate particles in the upper troposphere is a key factor to correctly represent cirrus cloud formation and properties. This additional parameter would improve the assessment of the radiative effect of cirrus clouds in climate models.

Recent studies have documented the efficient transport of polluted boundary layer air to the upper troposphere during the Asian summer monsoon season over India and China and the resulting formation of the Asian Tropopause Aerosol Layer (ATAL) (e.g., Vernier et al., 2009). Remote and in situ measurements have shown that high loads of ammonia can reach the upper troposphere and induce the formation of crystalline ammonium nitrate particles (Höpfner et al., 2019). Pure ammonium nitrate particles are known to remain in a supercooled aqueous phase even at low relative humidity, however, their heterogeneous crystallization can be initiated by a small amount of ammonium sulfate (Schlenker and Martin, 2005). Recently, Wagner et al. (2020) showed that crystalline ammonium nitrate particles can initiate heterogeneous ice formation at temperatures below about −50 °C.

The heterogeneous crystallization of ammonium nitrate particles from the co-condensation of sulfuric acid and ammonia is investigated here for the first time (Chapter 5). A sulfate concentration of about 0.4 mol% was found to be sufficient to trigger the crystallization of supercooled ammonium nitrate particles at about −40 °C and at a relative humidity with respect to liquid water of 15 − 30 %. The initially aqueous particles froze homogeneously at $S_{ice} ≈ 1.6$. At about −55 °C, the crystallized particles instead initiated heterogeneous ice formation at $S_{ice} ≈ 1.2$, in agreement with the results from Wagner et al. (2020). The calculated ice nucleation active surface site (INAS) density is in agreement with the parametrization suggested by Wagner et al. (2020), although smaller particles were investigated in this work (0.1 − 0.3 μm compared to 1 μm). The agreement between the two studies validates the INAS density approach for these types of particles in the investigated size range.

The fact that a tiny amount of sulfate is sufficient to trigger the heterogeneous crystallization of ammonium nitrate suggests that most of the ammonium nitrate particles are likely to crystallize in the upper troposphere at low relative humidity. Primary particles that are uplifted together with gaseous components could also influence the crystallization behavior and ice nucleation ability of the ammonium nitrate component. Internally mixed particles consisting e.g. of mineral dust or sea salt and ammonium nitrate should be further investigated in terms of heterogeneous crystallization, water uptake, and ice nucleation ability. A few measurements of the deliquescence behavior of ammonium nitrate particles internally mixed with ammonium sulfate were presented by Wagner et al. (2020), but additional studies on the low temperature deliquescence of pure and mixed crystalline ammonium nitrate particles are needed to correctly assess their phase state and thus their potential to act as ice nucleating particles at upper tropospheric conditions.

Besides inorganic species, oxidized volatile organic compounds also contribute to the formation and growth of secondary aerosol particles in the atmosphere. Traditionally, atmospheric secondary

organic aerosol (SOA) particles were considered to be liquid but recent studies have shown that they can also be found in an amorphous solid phase state in the atmosphere, thus having the potential to act as ice nucleating particles. The experiments presented in Chapter 6 were designed to investigate how changes in the chemical properties of SOA particles, generated at different thermodynamic conditions and from different organic compounds (α-pinene, α-pinene with isoprene, and naphthalene) influence their ice nucleation ability.

SOA particles derived from α-pinene were chosen as a reference system because of their abundance in the atmosphere. Temperature and relative humidity at which the α-pinene SOA particles were formed and grew were altered in a series of experiments to investigate how related changes in their chemical composition could affect their phase state and ice nucleation ability. Because in the atmosphere several different organic compounds participate in the growth of SOA particles, isoprene was added to the α-pinene system to simulate more atmospherically relevant conditions. Recent studies have shown that the addition of isoprene leads to the formation of compounds with a lower molecular weight, which can also partition to the particle phase (Heinritzi et al., 2020; Caudillo et al., 2021). Changes in the molecular weight of the compounds present in the particles modify their viscosity and could thus also change their ability to nucleate ice (Koop et al., 2011).

The results shown in Chapter 6 indicate that the investigated biogenic SOA particles initiate ice nucleation only at or above the ice saturation ratio threshold for homogeneous freezing of aqueous solution droplets regardless of whether isoprene is added to the system or whether the thermodynamic conditions for the formation of the α-pinene particles are varied.

Naphthalene-derived particles were chosen as representative for anthropogenic SOA. Berkemeier et al. (2014) identified naphthalene as the volatile organic compound with the highest possibility to generate heterogeneous ice nuclei due to its high viscosity and low hygroscopicity. Naphthalene SOA particles showed a weak heterogeneous ice nucleation mode, but at ice saturation ratios where biogenic SOA particles or aqueous solution droplets would have already frozen via homogeneous freezing. The majority of the naphthalene SOA particles nucleated ice at higher ice saturation ratios ($S_{ice} \approx 1.9$ at $-56\,°C$) compared to the biogenic SOA ($S_{ice} \approx 1.6$ at the same temperature), pointing to a higher viscosity of the naphthalene-derived SOA particles. The SOA particles investigated in this thesis likely do not contribute significantly to heterogeneous cirrus formation, because they nucleate ice only at high ice saturation ratios comparable or higher than the freezing threshold of the ubiquitous aqueous sulfuric acid solution droplets.

Aerosol particles have a long residence time in the upper troposphere and often undergo aging processes that can modify their chemical and physical properties. For example, particles can be coated by condensable materials (e.g. sulfate and organics) or undergo cloud processing. Mixed particles composed of sulfate and organics represent a major type of aerosol particles in the upper troposphere and may constitute a significant fraction of ice nucleating particles involved in cirrus cloud formation (Froyd et al., 2009). Internally mixed particles composed of ammonium sulfate (AS) and secondary organic material (SOM) from the oxidation of α-pinene were investigated in Chapter 7. The experiments show that a thin coating layer of SOM, corresponding to an organic mass concentration of about $5-8\,wt\%$, is sufficient to greatly reduce the ability of the crystalline ammonium sulfate to act as ice nucleating particle, with an increase of the ice onset saturation ratio from 1.25 to 1.5 at about $-52\,°C$.

Internally mixed particles can form in the atmosphere through different pathways and can experience various cloud-cycling processes, leading to particles with more complex morphologies than the idealized core-shell case. Experiments were performed to investigate whether liquid or ice cloud processing could modify the ice nucleation ability of mixed AS/SOM particles in a core-shell morphology and with high organic weight fractions of about $25-50\,wt\%$, as often found in the upper troposphere (Froyd et al., 2009). The processed particles showed an intermediate ice nucleation ability between that of the pure and the SOM-coated AS particles in a core-shell morphology, with the ice onset at $S_{ice} \approx 1.35$ at $-53\,°C$. The viscous organic material is probably redistributed during cloud processing and the AS component partially uncovered and able to initiate ice nucleation at lower S_{ice} compared to the unprocessed, uniformly coated particles.

The experiments presented in Chapter 7 highlight the difficulty to represent the ice nucleation ability of internally mixed particles with parameterizations based only on their chemical composi-

tion. The presence of an organic coating can suppress the ice nucleation ability of the seed particle at cirrus cloud conditions, but the ice nucleation ability of the same particle can substantially change if subjected to atmospheric processing. Cloud processing is a common phenomenon in the atmosphere, especially for particles uplifted in convective systems. Hence, it is important to consider the effect of this process on the morphology of atmospheric particles to properly assess their ice nucleation ability.

The effect of atmospheric aging has been investigated also for another type of atmospherically relevant aerosol particles, namely mineral dust. Mineral dust particles are widely known to play a key role in cloud formation, facilitating the heterogeneous formation of ice crystals under a wide range of temperatures and ice saturation ratios (e.g., Hoose and Möhler, 2012). While suspended in the atmosphere, mineral dust particles may undergo several aging processes, such as coating with different chemical species that can alter their surface properties and features.

The experiments presented in Chapter 8 aim at characterizing the effect of a thin coating of sulfuric acid or secondary organic material (SOM) from the ozonolysis of α-pinene on the heterogeneous ice nucleation ability of two feldspar samples in the cirrus temperature range. The ice nucleation ability of the feldspar samples was strongly suppressed by the thin coatings. The initially low ice saturation ratio onsets of the bare feldspar particles shifted from $S_{ice} = 1.1 - 1.2$ to about 1.45 at $\approx -46\,°C$ after both sulfuric acid and SOM coating, similar to the homogeneous freezing onset of aqueous solution droplets. The high ice nucleation ability of the bare feldspar particles and its strong suppression by a thin coating point to the potential importance of surface features of the particles, such as cracks and pores, in the underlying ice nucleation mechanism. The coating material had probably filled the ice nucleation active sites so that they could no longer host condensed water and initiate the nucleation of a stable ice germ.

These results indicate that the effect of aging processes on the ice nucleation ability of mineral particles, at least those including feldspar components, should be considered when calculating or predicting cirrus cloud formation. The occurrence of heterogeneously formed cirrus clouds may be overestimated if ice crystal formation is described with parametrizations formulated only for pristine mineral dust particles.

In conclusion, the results presented in this thesis improve our understanding of the role of secondary aerosol particles in the formation of cirrus clouds. The chemical composition has a critical effect on the ice nucleating ability of aerosol particles, but aging and cloud-cycling processes should also be considered to correctly predict changes in the ice nucleation ability of the particles while suspended in the atmosphere. The ice nucleation measurements presented here should be considered in climate models to assess the atmospheric relevance of the different investigated systems in the heterogeneous formation of cirrus clouds under different precursor emission scenarios.

ACRONYMS

αP   α-pinene

AHS   Ammonium Bisulfate

AIDA   Aerosol Interaction and Dynamics in the Atmosphere

AMS   Aerosol Mass Spectrometer

AN   Ammonium Nitrate

APC   Aerosol Preparation and Characterization

APicT AIDA PCI in-cloud Tunable diode laser

APS   Aerodynamic Particle Sizer

AS   Ammonium Sulfate

ASR   Ammonium-to-Sulfate Ratio

ATAL   Asian Tropopause Aerosol Layer

CCN   Cloud Condensation Nuclei

CFDC   Continuous Flow Diffusion Chamber

CLOUD Cosmics Leaving OUtdoor Droplets

CNT   Classical Nucleation Theory

CPC   Condensation Particle Counter

DRH   Deliquescence Relative Humidity

E-AIM Extended Aerosol Inorganic Model

ERH   Efflorescence Relative Humidity

FTIR   Fourier Transform Infrared (Spectroscopy)

IN   Ice Nucleus

INAS   Ice Nucleation Active (surface) Site (density)

INF   Ice Nucleating Fraction

INKA   Ice Nucleation Instrument of the KArlsruhe Institute of Technology

INPs   Ice Nucleating Particles

IP   Isoprene

LET   Letovicite

LS   Lower Stratosphere

mINKA mobile Ice Nucleation Instrument of the KArlsruhe Institute of Technology

NAPH   Naphthalene

OPC   Optical Particle Counter

PCF   Pore Condensation and Freezing

PDRH Partial Deliquescence Relative Humidity

PINCii Portable Ice Nucleation Chamber II

SA   Sulfuric Acid

SIMONE Streulichtintensitatsmessungen zum optischen Nachweis von Eispartikeln

SMPS   Scanning Mobility Particle Counter

SOA   Secondary Organic Aerosol

SOM   Secondary Organic Matter

SPIN   SPectrometer for Ice Nuclei

TME   Tetramethylethylene

UT   Upper Troposphere

VBS   Volatility Basis Set

VOC   Volatile Organic Compound

BIBLIOGRAPHY

Abbatt, J. P. D. et al. (2006). "Solid Ammonium Sulfate Aerosols as Ice Nuclei: A Pathway for Cirrus Cloud Formation." In: *Science* September, pp. 1770–1773.

Adler, G. et al. (2013). "Formation of highly porous aerosol particles by atmospheric freeze-drying in ice clouds." In: *Proceedings of the National Academy of Sciences* 110.51, pp. 20414–20419. DOI: 10.1073/pnas.1317209110.

Almeida, J. et al. (2013). "Molecular understanding of sulphuric acid–amine particle nucleation in the atmosphere." In: *Nature* 502.7471, pp. 359–363. DOI: 10.1038/nature12663.

Andreae, M. O. et al. (2018). "Aerosol characteristics and particle production in the upper troposphere over the Amazon Basin." In: *Atmospheric Chemistry and Physics* 18.2, pp. 921–961. DOI: 10.5194/acp-18-921-2018.

Angell, C. A. (2002). "Liquid Fragility and the Glass Transition in Water and Aqueous Solutions." In: *Chemical Reviews* 102.8, pp. 2627–2650. DOI: 10.1021/cr000689q.

Ansmann, A. et al. (2003). "Long-range transport of Saharan dust to northern Europe: The 11-16 October 2001 outbreak observed with EARLINET." In: *Journal of Geophysical Research: Atmospheres* 108.D24, n/a–n/a. DOI: 10.1029/2003JD003757.

Archuleta, C. M., P. J. DeMott, and S. M. Kreidenweis (2005). "Ice nucleation by surrogates for atmospheric mineral dust and mineral dust/sulfate particles at cirrus temperatures." In: *Atmospheric Chemistry and Physics* 5.10, pp. 2617–2634. DOI: 10.5194/acp-5-2617-2005.

Arey, J. et al. (1989). "Diurnal concentrations of volatile polycyclic aromatic hydrocarbons and nitroarenes during a photochemical air pollution episode in Glendora, California." In: *Environmental Science & Technology* 23.3, pp. 321–327. DOI: 10.1021/es00180a009.

Atkinson, J. D. et al. (2013). "The importance of feldspar for ice nucleation by mineral dust in mixed-phase clouds." In: *Nature* 498.7454, pp. 355–358. DOI: 10.1038/nature12278.

Atkinson, R. and J. Arey (2003). "Atmospheric Degradation of Volatile Organic Compounds." In: *Chemical Reviews* 103.12, pp. 4605–4638. DOI: 10.1021/cr0206420.

Augustin-Bauditz, S. et al. (2014). "The immersion mode ice nucleation behavior of mineral dusts: A comparison of different pure and surface modified dusts." In: *Geophysical Research Letters* 41.20, pp. 7375–7382. DOI: 10.1002/2014GL061317.

Baron, P. A. et al. (2011). "Real-Time Techniques for Aerodynamic Size Measurement." In: *Aerosol Measurement*. Hoboken, NJ, USA: John Wiley & Sons, Inc., pp. 313–338. DOI: 10.1002/9781118001684.ch14.

Bastelberger, S. et al. (2017). "Diffusivity measurements of volatile organics in levitated viscous aerosol particles." In: *Atmospheric Chemistry and Physics* 17.13, pp. 8453–8471. DOI: 10.5194/acp-17-8453-2017.

Bates, T. S. et al. (1992). "Sulfur emissions to the atmosphere from natural sourees." In: *Journal of Atmospheric Chemistry* 14.1-4, pp. 315–337. DOI: 10.1007/BF00115242.

Bauer, S. E. et al. (2007). "Nitrate aerosols today and in 2030: a global simulation including aerosols and tropospheric ozone." In: *Atmospheric Chemistry and Physics* 7.19, pp. 5043–5059. DOI: 10.5194/acp-7-5043-2007.

Baustian, K. J. et al. (2013). "State transformations and ice nucleation in amorphous (semi-)solid organic aerosol." In: *Atmospheric Chemistry and Physics* 13.11, pp. 5615–5628. DOI: 10.5194/acp-13-5615-2013.

Beaman, R. G. (1952). "Relation between (apparent) second-order transition temperature and melting point." In: *Journal of Polymer Science* 9.5, pp. 470–472. DOI: 10.1002/pol.1952.120090510.

Berkemeier, T. et al. (2014). "Competition between water uptake and ice nucleation by glassy organic aerosol particles." In: *Atmospheric Chemistry and Physics* 14.22, pp. 12513–12531. DOI: 10.5194/acp-14-12513-2014.

Bertozzi, B. et al. (2021). "Ice nucleation ability of ammonium sulfate aerosol particles internally mixed with secondary organics." In: *Atmospheric Chemistry and Physics* 21.13, pp. 10779–10798. DOI: 10.5194/acp-21-10779-2021.

Bertram, A. K. et al. (2011). "Predicting the relative humidities of liquid-liquid phase separation, efflorescence, and deliquescence of mixed particles of ammonium sulfate, organic material, and water using the organic-to-sulfate mass ratio of the particle and the oxygen-to-carbon ele." In: *Atmospheric Chemistry and Physics* 11.21, pp. 10995–11006. DOI: `10.5194/acp-11-10995-2011`.

Bertram, A. K. et al. (2000). "Ice Formation in $(NH_4)_2SO_4 - H_2O$ Particles." In: *The Journal of Physical Chemistry A* 104.3, pp. 584–588. DOI: `10.1021/jp9931197`.

Blundell, S. and K. Blundell (2010). *Concepts in Thermal Physics.* Oxford University Press.

Bodsworth, A., B. Zobrist, and A. K. Bertram (2010). "Inhibition of efflorescence in mixed organic–inorganic particles at temperatures less than 250 K." In: *Physical Chemistry Chemical Physics* 12.38, p. 12259. DOI: `10.1039/c0cp00572j`.

Bohren, C. F. and D. R. Huffman (1998). *Absorption and Scattering of Light by Small Particles*. Wiley. DOI: `10.1002/9783527618156`.

Bossolasco, A. et al. (2021). "Global modeling studies of composition and decadal trends of the Asian Tropopause Aerosol Layer." In: *Atmospheric Chemistry and Physics* 21.4, pp. 2745–2764. DOI: `10.5194/acp-21-2745-2021`.

Boucher, O. et al. (2013). "Clouds and Aerosols." In: *Climate Change 2013: The Physical Science Basis. Contribution of Working Group I to the Fifth Assessment Report of the Intergovernmental Panel on Climate Change*. Ed. by T. Stocker et al. Cambridge, United Kingdom and New York, NY, USA: Cambridge University Press. Chap. 7, pp. 571–658. DOI: `10.1017/CB09781107415324.016`.

Bouwman, A. F. et al. (1997). "A global high-resolution emission inventory for ammonia." In: *Global Biogeochemical Cycles* 11.4, pp. 561–587. DOI: `10.1029/97GB02266`.

Braban, C. F., J. P. D. Abbatt, and D. J. Cziczo (2001). "Deliquescence of ammonium sulfate particles at sub-eutectic temperatures." In: *Geophysical Research Letters* 28.20, pp. 3879–3882. DOI: `10.1029/2001GL013175`.

Brunner, C. and Z. A. Kanji (2021). "Continuous online monitoring of ice-nucleating particles: development of the automated Horizontal Ice Nucleation Chamber (HINC-Auto)." In: *Atmospheric Measurement Techniques* 14.1, pp. 269–293. DOI: `10.5194/amt-14-269-2021`.

Burnett, D., F. Thielmann, and J. Booth (2004). "Determining the critical relative humidity for moisture-induced phase transitions." In: *International Journal of Pharmaceutics* 287.1-2, pp. 123–133. DOI: `10.1016/j.ijpharm.2004.09.009`.

Carslaw, K. S., R. G. Harrison, and J. Kirkby (2002). "Cosmic Rays, Clouds, and Climate." In: *Science* 298.5599, pp. 1732–1737. DOI: `10.1126/science.1076964`.

Caudillo, L. et al. (2021). "Chemical composition of nanoparticles from α-pinene nucleation and the influence of isoprene and relative humidity at low temperature." In: *Atmospheric Chemistry and Physics Discussions*, pp. 1–26. DOI: `10.5194/acp-2021-512`.

Champion, D., M. Le Meste, and D. Simatos (2000). "Towards an improved understanding of glass transition and relaxations in foods: molecular mobility in the glass transition range." In: *Trends in Food Science & Technology* 11.2, pp. 41–55. DOI: `10.1016/S0924-2244(00)00047-9`.

Champion, W. M. et al. (2019). "Volatility and Viscosity Are Correlated in Terpene Secondary Organic Aerosol Formed in a Flow Reactor." In: *Environmental Science & Technology Letters* 6.9, pp. 513–519. DOI: `10.1021/acs.estlett.9b00412`.

Chan, A. W. H. et al. (2009). "Secondary organic aerosol formation from photooxidation of naphthalene and alkylnaphthalenes: implications for oxidation of intermediate volatility organic compounds (IVOCs)." In: *Atmospheric Chemistry and Physics* 9.9, pp. 3049–3060. DOI: `10.5194/acp-9-3049-2009`.

Charlson, R. J. et al. (1992). "Climate Forcing by Anthropogenic Aerosols." In: *Science* 255.5043, pp. 423–430. DOI: `10.1126/science.255.5043.423`.

Charnawskas, J. C. et al. (2017). "Condensed-phase biogenic–anthropogenic interactions with implications for cold cloud formation." In: *Faraday Discussions* 200, pp. 165–194. DOI: `10.1039/C7FD00010C`.

Chen, J.-P., A. Hazra, and Z. Levin (2008). "Parameterizing ice nucleation rates using contact angle and activation energy derived from laboratory data." In: *Atmospheric Chemistry and Physics* 8.24, pp. 7431–7449. DOI: `10.5194/acp-8-7431-2008`.

Cheng, Y.-S. (2011). "Condensation Particle Counters." In: *Aerosol Measurement*. Hoboken, NJ, USA: John Wiley & Sons, Inc. Chap. 17, pp. 381–392. DOI: `10.1002/9781118001684.ch17`.

Chernoff, D. I. and A. K. Bertram (2010). "Effects of sulfate coatings on the ice nucleation properties of a biological ice nucleus and several types of minerals." In: *Journal of Geophysical Research* 115.D20, p. D20205. DOI: 10.1029/2010JD014254.

Chou, C. et al. (2011). "Ice nuclei properties within a Saharan dust event at the Jungfraujoch in the Swiss Alps." In: *Atmospheric Chemistry and Physics* 11.10, pp. 4725–4738. DOI: 10.5194/acp-11-4725-2011.

Ciobanu, V. G. et al. (2009). "LiquidLiquid Phase Separation in Mixed Organic/Inorganic Aerosol Particles." In: *The Journal of Physical Chemistry A* 113.41, pp. 10966–10978. DOI: 10.1021/jp905054d.

Claquin, T., M. Schulz, and Y. J. Balkanski (1999). "Modeling the mineralogy of atmospheric dust sources." In: *Journal of Geophysical Research: Atmospheres* 104.D18, pp. 22243–22256. DOI: 10.1029/1999JD900416.

Clarke, A. D. (1998). "Particle Nucleation in the Tropical Boundary Layer and Its Coupling to Marine Sulfur Sources." In: *Science* 282.5386, pp. 89–92. DOI: 10.1126/science.282.5386.89.

Clegg, S. L., P. Brimblecombe, and A. S. Wexler (1998). "Thermodynamic Model of the System H^+–NH_4^+–SO_4^{2-}–NO_3^-–H_2O at Tropospheric Temperatures." In: *The Journal of Physical Chemistry A* 102.12, pp. 2137–2154. DOI: 10.1021/jp973042r.

Colberg, C. A. et al. (2003). "A novel model to predict the physical state of atmospheric H_2SO_4/NH_3/H_2O aerosol particles." In: *Atmospheric Chemistry and Physics* 3.4, pp. 909–924. DOI: 10.5194/acp-3-909-2003.

Colberg, C. A., U. K. Krieger, and T. Peter (2004). "Morphological Investigations of Single Levitated H_2SO_4/NH_3/H_2O Aerosol Particles during Deliquescence/Efflorescence Experiments." In: *Journal of Physical Chemistry A* 108.14, pp. 2700–2709. DOI: 10.1021/jp037628r.

Connolly, P. J. et al. (2009). "Studies of heterogeneous freezing by three different desert dust samples." In: *Atmospheric Chemistry and Physics* 9.8, pp. 2805–2824. DOI: 10.5194/acp-9-2805-2009.

Contini, D., R. Vecchi, and M. Viana (2018). "Carbonaceous Aerosols in the Atmosphere." In: *Atmosphere* 9.5, p. 181. DOI: 10.3390/atmos9050181.

Crippa, M. et al. (2014). "Organic aerosol components derived from 25 AMS data sets across Europe using a consistent ME-2 based source apportionment approach." In: *Atmospheric Chemistry and Physics* 14.12, pp. 6159–6176. DOI: 10.5194/acp-14-6159-2014.

Crowe, J. H., J. F. Carpenter, and L. M. Crowe (1998). "The role of vitrification in anhydrobiosis." In: *Annual Review of Physiology* 60.1, pp. 73–103. DOI: 10.1146/annurev.physiol.60.1.73.

Cziczo, D. J. and J. P. D. Abbatt (2000). "Infrared Observations of the Response of $NaCl$, $MgCl_2$, NH_4HSO_4, and NH_4NO_3 Aerosols to Changes in Relative Humidity from 298 to 238 K." In: *The Journal of Physical Chemistry A* 104.10, pp. 2038–2047. DOI: 10.1021/jp9931408.

Cziczo, D. J. et al. (1997). "Infrared spectroscopy of model tropospheric aerosols as a function of relative humidity: Observation of deliquescence and crystallization." In: *Journal of Geophysical Research: Atmospheres* 102.D15, pp. 18843–18850. DOI: 10.1029/97JD01361.

Cziczo, D. J. et al. (2009). "Deactivation of ice nuclei due to atmospherically relevant surface coatings." In: *Environmental Research Letters* 4.4. DOI: 10.1088/1748-9326/4/4/044013.

David, R. O. et al. (2019). "Pore condensation and freezing is responsible for ice formation below water saturation for porous particles." In: *Proceedings of the National Academy of Sciences* 116.17, pp. 8184–8189. DOI: 10.1073/pnas.1813647116.

Davis, R. D. et al. (2015). "Contact efflorescence as a pathway for crystallization of atmospherically relevant particles." In: *Proceedings of the National Academy of Sciences of the United States of America* 112.52, pp. 15815–15820. DOI: 10.1073/pnas.1522860113.

Debenedetti, P. G. and F. H. Stillinger (2001). "Supercooled liquids and the glass transition." In: *Nature* 410.6825, pp. 259–267. DOI: 10.1038/35065704.

DeCarlo, P. F. et al. (2004). "Particle Morphology and Density Characterization by Combined Mobility and Aerodynamic Diameter Measurements. Part 1: Theory." In: *Aerosol Science and Technology* 38.12, pp. 1185–1205. DOI: 10.1080/027868290903907.

DeMott, P. J. et al. (2010). "Predicting global atmospheric ice nuclei distributions and their impacts on climate." In: *Proceedings of the National Academy of Sciences* 107.25, pp. 11217–11222. DOI: 10.1073/pnas.0910818107.

DeMott, P. J. et al. (2003). "African dust aerosols as atmospheric ice nuclei." In: *Geophysical Research Letters* 30.14, p. 1732. DOI: 10.1029/2003GL017410.

DeMott, P. J. et al. (2018). "The Fifth International Workshop on Ice Nucleation phase 2 (FIN-02): laboratory intercomparison of ice nucleation measurements." In: *Atmospheric Measurement Techniques* 11.11, pp. 6231–6257. DOI: 10.5194/amt-11-6231-2018.

Dentener, F. J. et al. (1996). "Role of mineral aerosol as a reactive surface in the global troposphere." In: *Journal of Geophysical Research* 101.17, pp. 22869–22889.

Dette, H. P. and T. Koop (2015). "Glass formation processes in mixed inorganic/organic aerosol particles." In: *Journal of Physical Chemistry A* 119.19, pp. 4552–4561. DOI: 10.1021/jp5106967.

Donahue, N. M. et al. (2011). "A two-dimensional volatility basis set: 1. organic-aerosol mixing thermodynamics." In: *Atmospheric Chemistry and Physics* 11.7, pp. 3303–3318. DOI: 10.5194/acp-11-3303-2011.

Donahue, N. M. et al. (2006). "Coupled Partitioning, Dilution, and Chemical Aging of Semivolatile Organics." In: *Environmental Science & Technology* 40.8, pp. 2635–2643. DOI: 10.1021/es052297c.

Donahue, N. M., A. L. Robinson, and S. N. Pandis (2009). "Atmospheric organic particulate matter: From smoke to secondary organic aerosol." In: *Atmospheric Environment* 43.1, pp. 94–106. DOI: 10.1016/j.atmosenv.2008.09.055.

Eastwood, M. L. et al. (2009). "Effects of sulfuric acid and ammonium sulfate coatings on the ice nucleation properties of kaolinite particles." In: *Geophysical Research Letters* 36.2, n/a–n/a. DOI: 10.1029/2008GL035997.

Elbert, W. et al. (2007). "Contribution of fungi to primary biogenic aerosols in the atmosphere: wet and dry discharged spores, carbohydrates, and inorganic ions." In: *Atmospheric Chemistry and Physics* 7.17, pp. 4569–4588. DOI: 10.5194/acp-7-4569-2007.

Erisman, J. W. et al. (2008). "How a century of ammonia synthesis changed the world." In: *Nature Geoscience* 1.10, pp. 636–639. DOI: 10.1038/ngeo325.

Fahey, D. W. et al. (2014). "The AquaVIT-1 intercomparison of atmospheric water vapor measurement techniques." In: *Atmospheric Measurement Techniques* 7.9, pp. 3177–3213. DOI: 10.5194/amt-7-3177-2014.

Fan, J. et al. (2016). "Review of Aerosol–Cloud Interactions: Mechanisms, Significance, and Challenges." In: *Journal of the Atmospheric Sciences* 73.11, pp. 4221–4252. DOI: 10.1175/JAS-D-16-0037.1.

Fard, M. M., U. K. Krieger, and T. Peter (2017). "Kinetic Limitation to Inorganic Ion Diffusivity and to Coalescence of Inorganic Inclusions in Viscous Liquid–Liquid Phase-Separated Particles." In: *The Journal of Physical Chemistry A* 121.48, pp. 9284–9296. DOI: 10.1021/acs.jpca.7b05242.

Fitzner, M. et al. (2015). "The Many Faces of Heterogeneous Ice Nucleation: Interplay Between Surface Morphology and Hydrophobicity." In: *Journal of the American Chemical Society* 137.42, pp. 13658–13669. DOI: 10.1021/jacs.5b08748.

Flagan, R. C. (2011). "Electrical Mobility Methods for Submicrometer Particle Characterization." In: *Aerosol Measurement*. Hoboken, NJ, USA: John Wiley & Sons, Inc., pp. 339–364. DOI: 10.1002/9781118001684.ch15.

Fletcher, N. H. (1958). "Size Effect in Heterogeneous Nucleation." In: *The Journal of Chemical Physics* 29.3, pp. 572–576. DOI: 10.1063/1.1744540.

Fortin, T. J., J. E. Shilling, and M. A. Tolbert (2002). "Infrared spectroscopic study of the low-temperature phase behavior of ammonium sulfate." In: *Journal of Geophysical Research: Atmospheres* 107.D10, pp. 4–1. DOI: 10.1029/2001JD000677.

Fowler, K., P. Connolly, and D. Topping (2020). "Modelling the effect of condensed-phase diffusion on the homogeneous nucleation of ice in ultra-viscous particles." In: *Atmospheric Chemistry and Physics* 20.2, pp. 683–698. DOI: 10.5194/acp-20-683-2020.

Fox, T. G. and P. J. Flory (1950). "Second-Order Transition Temperatures and Related Properties of Polystyrene. I. Influence of Molecular Weight." In: *Journal of Applied Physics* 21.6, pp. 581–591. DOI: 10.1063/1.1699711.

Freedman, M. A. (2020). "Liquid–Liquid Phase Separation in Supermicrometer and Submicrometer Aerosol Particles." In: *Accounts of Chemical Research* 53.6, pp. 1102–1110. DOI: 10.1021/acs.accounts.0c00093.

Fromm, M. et al. (2000). "Observations of boreal forest fire smoke in the stratosphere by POAM III, SAGE II, and lidar in 1998." In: *Geophysical Research Letters* 27.9, pp. 1407–1410. DOI: 10.1029/1999GL011200.

Froyd, K. D. et al. (2009). "Aerosol composition of the tropical upper troposphere." In: *Atmospheric Chemistry and Physics* 9.13, pp. 4363–4385. DOI: 10.5194/acp-9-4363-2009.

Galeazzo, T. et al. (2021). "Estimation of secondary organic aerosol viscosity from explicit modeling of gas-phase oxidation of isoprene and α-pinene." In: *Atmospheric Chemistry and Physics* 21.13, pp. 10199–10213. DOI: 10.5194/acp-21-10199-2021.

Gao, Y., S. B. Chen, and L. E. Yu (2006). "Efflorescence Relative Humidity for Ammonium Sulfate Particles." In: *The Journal of Physical Chemistry A* 110.24, pp. 7602–7608. DOI: 10.1021/jp057574g.

Garimella, S. et al. (2016). "The SPectrometer for Ice Nuclei (SPIN): an instrument to investigate ice nucleation." In: *Atmospheric Measurement Techniques* 9.7, pp. 2781–2795. DOI: 10.5194/amt-9-2781-2016.

Garimella, S. et al. (2017). "Uncertainty in counting ice nucleating particles with continuous flow diffusion chambers." In: *Atmospheric Chemistry and Physics* 17.17, pp. 10855–10864. DOI: 10.5194/acp-17-10855-2017.

Gaston, C. J. (2020). "Re-examining Dust Chemical Aging and Its Impacts on Earth's Climate." In: *Accounts of Chemical Research* 53.5, pp. 1005–1013. DOI: 10.1021/acs.accounts.0c00102.

Ge, X. et al. (2017). "Characteristics and Formation Mechanisms of Fine Particulate Nitrate in Typical Urban Areas in China." In: *Atmosphere* 8.12, p. 62. DOI: 10.3390/atmos8030062.

Ge, Z., A. S. Wexler, and M. V. Johnston (1996). "Multicomponent Aerosol Crystallization." In: *Journal of Colloid and Interface Science* 183.1, pp. 68–77. DOI: 10.1006/jcis.1996.0519.

Ginoux, P. et al. (2012). "Global-scale attribution of anthropogenic and natural dust sources and their emission rates based on MODIS Deep Blue aerosol products." In: *Reviews of Geophysics* 50.3, p. 3005. DOI: 10.1029/2012RG000388.

Glen, A. and S. D. Brooks (2014). "Single Particle Measurements of the Optical Properties of Small Ice Crystals and Heterogeneous Ice Nuclei." In: *Aerosol Science and Technology* 48.11, pp. 1123–1132. DOI: 10.1080/02786826.2014.963023.

Gordon, M. and J. S. Taylor (1952). "Ideal copolymers and the second-order transitions of synthetic rubbers. i. non-crystalline copolymers." In: *Journal of Applied Chemistry* 2.9, pp. 493–500. DOI: 10.1002/jctb.5010020901.

Greer, A. L. (1995). "Metallic Glasses." In: *Science* 267.5206, pp. 1947–1953. DOI: 10.1126/science.267.5206.1947.

Grieshop, A. P., N. M. Donahue, and A. L. Robinson (2007). "Is the gas-particle partitioning in α-pinene secondary organic aerosol reversible?" In: *Geophysical Research Letters* 34.14, p. L14810. DOI: 10.1029/2007GL029987.

Guenther, A. et al. (2006). "Estimates of global terrestrial isoprene emissions using MEGAN (Model of Emissions of Gases and Aerosols from Nature)." In: *Atmospheric Chemistry and Physics* 6.11, pp. 3181–3210. DOI: 10.5194/acp-6-3181-2006.

Guenther, A. et al. (1995). "A global model of natural volatile organic compound emissions." In: *Journal of Geophysical Research* 100.D5, p. 8873. DOI: 10.1029/94JD02950.

Guenther, A. B. et al. (1993). "Isoprene and monoterpene emission rate variability: Model evaluations and sensitivity analyses." In: *Journal of Geophysical Research* 98.D7, p. 12609. DOI: 10.1029/93JD00527.

Hallquist, M. et al. (2009). "The formation, properties and impact of secondary organic aerosol: current and emerging issues." In: *Atmospheric Chemistry and Physics* 9.14, pp. 5155–5236. DOI: 10.5194/acp-9-5155-2009.

Han, J.-H., H.-M. Hung, and S. T. Martin (2002). "Size effect of hematite and corundum inclusions on the efflorescence relative humidities of aqueous ammonium nitrate particles." In: *Journal of Geophysical Research: Atmospheres* 107.D10, pp. 3–1. DOI: 10.1029/2001JD001054.

Harrison, A. D. et al. (2016). "Not all feldspars are equal: a survey of ice nucleating properties across the feldspar group of minerals." In: *Atmospheric Chemistry and Physics* 16.17, pp. 10927–10940. DOI: 10.5194/acp-16-10927-2016.

Heinritzi, M. et al. (2020). "Molecular understanding of the suppression of new-particle formation by isoprene." In: *Atmospheric Chemistry and Physics* 20.20, pp. 11809–11821. DOI: 10.5194/acp-20-11809-2020.

Heintzenberg, J. (1989). "Fine particles in the global troposphere A review." In: *Tellus B: Chemical and Physical Meteorology* 41.2, pp. 149–160. DOI: 10.3402/tellusb.v41i2.15064.

Herbert, R. J. et al. (2014). "Representing time-dependent freezing behaviour in immersion mode ice nucleation." In: *Atmospheric Chemistry and Physics* 14.16, pp. 8501–8520. DOI: 10.5194/acp-14-8501-2014.

Herrmann, H. et al. (2015). "Tropospheric Aqueous-Phase Chemistry: Kinetics, Mechanisms, and Its Coupling to a Changing Gas Phase." In: *Chemical Reviews* 115.10, pp. 4259–4334. DOI: 10.1021/cr500447k.

Hinds, W. C. (1999). *Aerosol Technology: Properties, Behavior, and Measurement of Airborne Particles*. 2nd, p. 504.

Hiranuma, N. et al. (2019). "A comprehensive characterization of ice nucleation by three different types of cellulose particles immersed in water." In: *Atmospheric Chemistry and Physics* 19.7, pp. 4823–4849. DOI: 10.5194/acp-19-4823-2019.

Hodzic, A. et al. (2020). "Characterization of organic aerosol across the global remote troposphere: a comparison of ATom measurements and global chemistry models." In: *Atmospheric Chemistry and Physics* 20.8, pp. 4607–4635. DOI: 10.5194/acp-20-4607-2020.

Hoose, C. et al. (2008). "Global simulations of aerosol processing in clouds." In: *Atmospheric Chemistry and Physics* 8.23, pp. 6939–6963. DOI: 10.5194/acp-8-6939-2008.

Hoose, C. and O. Möhler (2012). "Heterogeneous ice nucleation on atmospheric aerosols: a review of results from laboratory experiments." In: *Atmospheric Chemistry and Physics* 12.20, pp. 9817–9854. DOI: 10.5194/acp-12-9817-2012.

Höpfner, M. et al. (2019). "Ammonium nitrate particles formed in upper troposphere from ground ammonia sources during Asian monsoons." In: *Nature Geoscience* 12.8, pp. 608–612. DOI: 10.1038/s41561-019-0385-8.

Hoppel, W. A., G. M. Frick, and R. E. Larson (1986). "Effect of nonprecipitating clouds on the aerosol size distribution in the marine boundary layer." In: *Geophysical Research Letters* 13.2, pp. 125–128. DOI: 10.1029/GL013i002p00125.

Huang, W. et al. (2018). "α–Pinene secondary organic aerosol at low temperature: chemical composition and implications for particle viscosity." In: *Atmospheric Chemistry and Physics* 18.4, pp. 2883–2898. DOI: 10.5194/acp-18-2883-2018.

Huang, X. et al. (2011). "Evidence of high PM2.5 strong acidity in ammonia-rich atmosphere of Guangzhou, China: Transition in pathways of ambient ammonia to form aerosol ammonium at $[NH_4^+]/[SO_4^{2-}] = 1.5$." In: *Atmospheric Research* 99.3-4, pp. 488–495. DOI: 10.1016/j.atmosres.2010.11.021.

Ickes, L. et al. (2015). "Classical nucleation theory of homogeneous freezing of water: thermodynamic and kinetic parameters." In: *Physical Chemistry Chemical Physics* 17.8, pp. 5514–5537. DOI: 10.1039/C4CP04184D.

Ignatius, K. et al. (2016). "Heterogeneous ice nucleation of viscous secondary organic aerosol produced from ozonolysis of α-pinene." In: *Atmospheric Chemistry and Physics* 16.10, pp. 6495–6509. DOI: 10.5194/acp-16-6495-2016.

Järvinen, E. et al. (2016). "Observation of viscosity transition in α-pinene secondary organic aerosol." In: *Atmospheric Chemistry and Physics* 16.7, pp. 4423–4438. DOI: 10.5194/acp-16-4423-2016.

Jimenez, J. L. et al. (2009). "Evolution of Organic Aerosols in the Atmosphere." In: *Science* 326.5959, pp. 1525–1529. DOI: 10.1126/science.1180353.

Kanakidou, M. et al. (2005). "Organic aerosol and global climate modelling: a review." In: *Atmospheric Chemistry and Physics* 5.4, pp. 1053–1123. DOI: 10.5194/acp-5-1053-2005.

Kandler, K. et al. (2007). "Chemical composition and complex refractive index of Saharan Mineral Dust at Izaña, Tenerife (Spain) derived by electron microscopy." In: *Atmospheric Environment* 41.37, pp. 8058–8074. DOI: 10.1016/j.atmosenv.2007.06.047.

Kanji, Z. A. and J. P. D. Abbatt (2009). "The University of Toronto Continuous Flow Diffusion Chamber (UT-CFDC): A Simple Design for Ice Nucleation Studies." In: *Aerosol Science and Technology* 43.7, pp. 730–738. DOI: 10.1080/02786820902889861.

Kanji, Z. A., O. Florea, and J. P. D. Abbatt (2008). "Ice formation via deposition nucleation on mineral dust and organics: dependence of onset relative humidity on total particulate surface area." In: *Environmental Research Letters* 3.2, p. 025004. DOI: 10.1088/1748-9326/3/2/025004.

Kanji, Z. A. et al. (2017). "Overview of Ice Nucleating Particles." In: *Meteorological Monographs* 58, pp. 1–1. DOI: 10.1175/AMSMONOGRAPHS-D-16-0006.1.

Kidd, C. et al. (2014). "Integrating phase and composition of secondary organic aerosol from the ozonolysis of -pinene." In: *Proceedings of the National Academy of Sciences* 111.21, pp. 7552–7557. DOI: 10.1073/pnas.1322558111.

Kiendler-Scharr, A. et al. (2009). "New particle formation in forests inhibited by isoprene emissions." In: *Nature* 461.7262, pp. 381–384. DOI: 10.1038/nature08292.

Kilchhofer, K., F. Mahrt, and Z. A. Kanji (2021). "The Role of Cloud Processing for the Ice Nucleating Ability of Organic Aerosol and Coal Fly Ash Particles." In: *Journal of Geophysical Research: Atmospheres* 126.10, e2020JD033338. DOI: 10.1029/2020JD033338.

Kirkby, J. (2007). "Cosmic Rays and Climate." In: *Surveys in Geophysics* 28.5-6, pp. 333–375. DOI: 10.1007/s10712-008-9030-6.

Kirkby, J. et al. (2011). "Role of sulphuric acid, ammonia and galactic cosmic rays in atmospheric aerosol nucleation." In: *Nature* 476.7361, pp. 429–435. DOI: 10.1038/nature10343.

Kiselev, A. et al. (2017). "Active sites in heterogeneous ice nucleation – the example of K-rich feldspars." In: *Science* 355.6323, pp. 367–371. DOI: 10.1126/science.aai8034.

Knopf, D. A., P. A. Alpert, and B. Wang (2018). *The Role of Organic Aerosol in Atmospheric Ice Nucleation: A Review.* DOI: 10.1021/acsearthspacechem.7b00120.

Koehler, K. A. et al. (2010). "Laboratory investigations of the impact of mineral dust aerosol on cold cloud formation." In: *Atmos. Chem. Phys* 10, pp. 11955–11968. DOI: 10.5194/acp-10-11955-2010.

Köhler, H. (1936). "The nucleus in and the growth of hygroscopic droplets." In: *Trans. Faraday Soc.* 32, pp. 1152–1161. DOI: 10.1039/TF9363201152.

Kojima, T. et al. (2006). "Sulfate-coated dust particles in the free troposphere over Japan." In: *Atmospheric Research* 82.3-4, pp. 698–708. DOI: 10.1016/j.atmosres.2006.02.024.

Kong, X. et al. (2018). "A continuous flow diffusion chamber study of sea salt particles acting as cloud nuclei: deliquescence and ice nucleation." In: *Tellus B: Chemical and Physical Meteorology* 70.1, pp. 1–11. DOI: 10.1080/16000889.2018.1463806.

Koop, T. et al. (2000). "Water activity as the determinant for homogeneous ice nucleation in aqueous solutions." In: *Nature* 406.6796, pp. 611–614. DOI: 10.1038/35020537.

Koop, T. et al. (2011). "Glass transition and phase state of organic compounds: dependency on molecular properties and implications for secondary organic aerosols in the atmosphere." In: *Physical Chemistry Chemical Physics* 13.43, p. 19238. DOI: 10.1039/c1cp22617g.

Koppmann, R. (2007). *Volatile Organic Compounds in the Atmosphere.* Ed. by R. Koppmann. Oxford, UK: Blackwell Publishing Ltd, pp. 1–500. DOI: 10.1002/9780470988657.

Korhonen, K. et al. (2020). "Ice-nucleating ability of particulate emissions from solid-biomass-fired cookstoves: an experimental study." In: *Atmospheric Chemistry and Physics* 20.8, pp. 4951–4968. DOI: 10.5194/acp-20-4951-2020.

Krämer, M. et al. (2016). "A microphysics guide to cirrus clouds – Part 1: Cirrus types." In: *Atmospheric Chemistry and Physics* 16.5, pp. 3463–3483. DOI: 10.5194/acp-16-3463-2016.

Kristensen, K. et al. (2017). "The effect of sub-zero temperature on the formation and composition of secondary organic aerosol from ozonolysis of α-pinene." In: *Environmental Science: Processes & Impacts* 19.10, pp. 1220–1234. DOI: 10.1039/C7EM00231A.

Kroll, J. H. and J. H. Seinfeld (2008). "Chemistry of secondary organic aerosol: Formation and evolution of low-volatility organics in the atmosphere." In: *Atmospheric Environment* 42.16, pp. 3593–3624. DOI: 10.1016/j.atmosenv.2008.01.003.

Kroll, J. H. et al. (2009). "Physical chemistry of aerosols." In: *Physical Chemistry Chemical Physics* 11.36, p. 7759. DOI: 10.1039/b916865f.

Kulkarni, G. et al. (2014). "Ice nucleation of bare and sulfuric acid-coated mineral dust particles and implication for cloud properties." In: *Journal of Geophysical Research: Atmospheres* 119.16, pp. 9993–10011. DOI: 10.1002/2014JD021567.

Kulkarni, P. et al. (2008). "Features of upper troposphere and lower stratosphere aerosols observed by lidar over Gadanki, a tropical Indian station." In: *Journal of Geophysical Research* 113.D17, p. D17207. DOI: 10.1029/2007JD009411.

Kulmala, M. et al. (2010). "Atmospheric data over a solar cycle: no connection between galactic cosmic rays and new particle formation." In: *Atmospheric Chemistry and Physics* 10.4, pp. 1885–1898. DOI: 10.5194/acp-10-1885-2010.

Kumar, A., A. K. Bertram, and G. N. Patey (2021). "Molecular Simulations of Feldspar Surfaces Interacting with Aqueous Inorganic Solutions: Interfacial Water/Ion Structure and Implications for Ice Nucleation." In: *ACS Earth and Space Chemistry* 5.8, pp. 2169–2183. DOI: 10.1021/acsearth spacechem.1c00216.

Kumar, A. et al. (2018). "Ice nucleation activity of silicates and aluminosilicates in pure water and aqueous solutions – Part 1: The K-feldspar microcline." In: *Atmospheric Chemistry and Physics* 18.10, pp. 7057–7079. DOI: 10.5194/acp-18-7057-2018.

Kupc, A. et al. (2011). "A fibre-optic UV system for H_2SO_4 production in aerosol chambers causing minimal thermal effects." In: *Journal of Aerosol Science* 42.8, pp. 532–543. DOI: 10.1016/j.jaerosci.2011.05.001.

Ladino, L. A. et al. (2014). "Factors controlling the ice nucleating abilities of α-pinene SOA particles." In: *Journal of Geophysical Research: Atmospheres* 119.14, pp. 9041–9051. DOI: 10.1002/2014JD021578.

Levenspiel, O. (1999). "Chemical Reaction Engineering." In: *Industrial & Engineering Chemistry Research* 38.11, pp. 4140–4143. DOI: 10.1021/ie990488g.

Levin, Z., E. Ganor, and V. Gladstein (1996). "The Effects of Desert Particles Coated with Sulfate on Rain Formation in the Eastern Mediterranean." In: *Journal of Applied Meteorology and Climatology* 35.9, pp. 1511–1523. DOI: 10.1175/1520-0450(1996)035<1511:TEODPC>2.0.CO;2.

Levine, J. (1950). *Statistical Explanation of Spontaneous Freezing of Water Droplets*. Tech. rep., pp. 1–27.

Lewis, R. and E. Schwartz (2004). *Sea Salt Aerosol Production: Mechanisms, Methods, Measurements and Models—A Critical Review*. Vol. 152. Geophysical Monograph Series. Washington, D. C.: American Geophysical Union, pp. 1–408. DOI: 10.1029/GM152.

Li, F., P. Ginoux, and V. Ramaswamy (2008). "Distribution, transport, and deposition of mineral dust in the Southern Ocean and Antarctica: Contribution of major sources." In: *Journal of Geophysical Research* 113.D10, p. D10207. DOI: 10.1029/2007JD009190.

Li, Y. et al. (2020). "Predictions of the glass transition temperature and viscosity of organic aerosols from volatility distributions." In: *Atmospheric Chemistry and Physics* 20.13, pp. 8103–8122. DOI: 10.5194/acp-20-8103-2020.

Lienhard, D. M. et al. (2015). "Viscous organic aerosol particles in the upper troposphere: diffusivity-controlled water uptake and ice nucleation?" In: *Atmospheric Chemistry and Physics* 15.23, pp. 13599–13613. DOI: 10.5194/acp-15-13599-2015.

Lighty, J. S., J. M. Veranth, and A. F. Sarofim (2000). "Combustion Aerosols: Factors Governing Their Size and Composition and Implications to Human Health." In: *Journal of the Air & Waste Management Association* 50.9, pp. 1565–1618. DOI: 10.1080/10473289.2000.10464197.

Loeb, N. G. et al. (2009). "Toward Optimal Closure of the Earth's Top-of-Atmosphere Radiation Budget." In: *Journal of Climate* 22.3, pp. 748–766. DOI: 10.1175/2008JCLI2637.1.

Lohmann, U. and J. Feichter (2005). "Global indirect aerosol effects: a review." In: *Atmospheric Chemistry and Physics* 5.3, pp. 715–737. DOI: 10.5194/acp-5-715-2005.

Lohmann, U., F. Luond, and F. Mahrt (2016). *An Introduction to Clouds*. Cambridge: Cambridge University Press, pp. 1–391. DOI: 10.1017/CBO9781139087513.

Lupi, L., A. Hudait, and V. Molinero (2014). "Heterogeneous Nucleation of Ice on Carbon Surfaces." In: *Journal of the American Chemical Society* 136.8, pp. 3156–3164. DOI: 10.1021/ja411507a.

Mahowald, N. M. et al. (2005). "Atmospheric global dust cycle and iron inputs to the ocean." In: *Global Biogeochemical Cycles* 19.4, n/a–n/a. DOI: 10.1029/2004GB002402.

Mahrt, F. et al. (2020a). "Aging induced changes in ice nucleation activity of combustion aerosol as determined by near edge X-ray absorption fine structure (NEXAFS) spectroscopy." In: *Environmental Science: Processes & Impacts* 22.4, pp. 895–907. DOI: 10.1039/C9EM00525K.

Mahrt, F. et al. (2020b). "The Impact of Cloud Processing on the Ice Nucleation Abilities of Soot Particles at Cirrus Temperatures." In: *Journal of Geophysical Research: Atmospheres* 125.3, e2019JD030922. DOI: 10.1029/2019JD030922.

Marcolli, C. et al. (2007). "Efficiency of immersion mode ice nucleation on surrogates of mineral dust." In: *Atmospheric Chemistry and Physics* 7.19, pp. 5081–5091. DOI: 10.5194/acp-7-5081-2007.

Marcolli, C. (2014). "Deposition nucleation viewed as homogeneous or immersion freezing in pores and cavities." In: *Atmospheric Chemistry and Physics* 14.4, pp. 2071–2104. DOI: 10.5194/acp-14-2071-2014.

Marcolli, C. and U. K. Krieger (2006). "Phase Changes during Hygroscopic Cycles of Mixed Organic/Inorganic Model Systems of Tropospheric Aerosols." In: *The Journal of Physical Chemistry A* 110.5, pp. 1881–1893. DOI: 10.1021/jp0556759.

Martin, S. T. et al. (2004). "Effects of the physical state of tropospheric ammonium-sulfate-nitrate particles on global aerosol direct radiative forcing." In: *Atmospheric Chemistry and Physics* 4.1, pp. 183–214. DOI: 10.5194/acp-4-183-2004.

Martin, S. T. (2000). "Phase Transitions of Aqueous Atmospheric Particles." In: *Chemical Reviews* 100.9, pp. 3403–3454. DOI: 10.1021/cr990034t.

Martinsson, B. G. et al. (2019). "Formation and composition of the UTLS aerosol." In: *npj Climate and Atmospheric Science* 2.1, p. 40. DOI: 10.1038/s41612-019-0097-1.

Mason, B. J. and J. Maybank (1958). "Ice-nucleating properties of some natural mineral dusts." In: *Quarterly Journal of the Royal Meteorological Society* 84.361, pp. 235–241. DOI: 10.1002/qj.49708436 104.

Matsumoto, K. and H. Tanaka (1996). "Formation and dissociation of atmospheric particulate nitrate and chloride: An approach based on phase equilibrium." In: *Atmospheric Environment* 30.4, pp. 639–648. DOI: 10.1016/1352-2310(95)00290-1.

McDonald, B. C. et al. (2018). "Volatile chemical products emerging as largest petrochemical source of urban organic emissions." In: *Science* 359.6377, pp. 760–764. DOI: 10.1126/science.aaq0524.

McFiggans, G. et al. (2019). "Secondary organic aerosol reduced by mixture of atmospheric vapours." In: *Nature* 565.7741, pp. 587–593. DOI: 10.1038/s41586-018-0871-y.

Mikhailov, E. et al. (2009). "Amorphous and crystalline aerosol particles interacting with water vapor: conceptual framework and experimental evidence for restructuring, phase transitions and kinetic limitations." In: *Atmospheric Chemistry and Physics* 9.24, pp. 9491–9522. DOI: 10.5194/acp-9-9491-2009.

Mishchenko, M. I., L. D. Travis, and A. A. Lacis (2002). *Scattering, Absorption, and Emission of Light by Small Particles*. Cambridge: Cambridge University Press.

Möhler, O. et al. (2003). "Experimental investigation of homogeneous freezing of sulphuric acid particles in the aerosol chamber AIDA." In: *Atmospheric Chemistry and Physics* 3.1, pp. 211–223. DOI: 10.5194/acp-3-211-2003.

Möhler, O. et al. (2006). "Efficiency of the deposition mode ice nucleation on mineral dust particles." In: *Atmospheric Chemistry and Physics* 6.10, pp. 3007–3021. DOI: 10.5194/acp-6-3007-2006.

Möhler, O. et al. (2008). "The effect of organic coating on the heterogeneous ice nucleation efficiency of mineral dust aerosols." In: *Environmental Research Letters* 3.2, p. 025007. DOI: 10.1088/1748-9326/3/2/025007.

Murphy, D. M. (1998). "In Situ Measurements of Organics, Meteoritic Material, Mercury, and Other Elements in Aerosols at 5 to 19 Kilometers." In: *Science* 282.5394, pp. 1664–1669. DOI: 10.1126/science.282.5394.1664.

Murphy, D. M. (2005). "Something in the Air." In: *Science* 307.5717, pp. 1888–1890. DOI: 10.1126/science.1108160.

Murphy, D. M. and T. Koop (2005). "Review of the vapour pressures of ice and supercooled water for atmospheric applications." In: *Quarterly Journal of the Royal Meteorological Society* 131.608, pp. 1539–1565. DOI: 10.1256/qj.04.94.

Murphy, D. M. et al. (2006). "Single-particle mass spectrometry of tropospheric aerosol particles." In: *Journal of Geophysical Research: Atmospheres* 111.D23, pp. 23–32. DOI: 10.1029/2006JD007340.

Murphy, D. M. et al. (2019). "The distribution of sea-salt aerosol in the global troposphere." In: *Atmospheric Chemistry and Physics* 19.6, pp. 4093–4104. DOI: 10.5194/acp-19-4093-2019.

Murray, B. J., K. S. Carslaw, and P. R. Field (2021). "Opinion: Cloud-phase climate feedback and the importance of ice-nucleating particles." In: *Atmospheric Chemistry and Physics* 21.2, pp. 665–679. DOI: 10.5194/acp-21-665-2021.

Murray, B. J. et al. (2010). "Heterogeneous nucleation of ice particles on glassy aerosols under cirrus conditions." In: *Nature Geoscience* 3.4, pp. 233–237. DOI: 10.1038/ngeo817.

Nachbar, M., D. Duft, and T. Leisner (2019). "The vapor pressure of liquid and solid water phases at conditions relevant to the atmosphere." In: *The Journal of Chemical Physics* 151.6, p. 064504. DOI: 10.1063/1.5100364.

Niedermeier, D. et al. (2010). "Heterogeneous freezing of droplets with immersed mineral dust particles – measurements and parameterization." In: *Atmospheric Chemistry and Physics* 10.8, pp. 3601–3614. DOI: 10.5194/acp-10-3601-2010.

Niedermeier, D. et al. (2011). "Heterogeneous ice nucleation: exploring the transition from stochastic to singular freezing behavior." In: *Atmospheric Chemistry and Physics* 11.16, pp. 8767–8775. DOI: 10.5194/acp-11-8767-2011.

O'Meara, S., D. O. Topping, and G. McFiggans (2016). "The rate of equilibration of viscous aerosol particles." In: *Atmospheric Chemistry and Physics* 16.8, pp. 5299–5313. DOI: 10.5194/acp-16-5299-2016.

Onasch, T. B. et al. (1999). "Infrared spectroscopic study of the deliquescence and efflorescence of ammonium sulfate aerosol as a function of temperature." In: *Journal of Geophysical Research: Atmospheres* 104.D17, pp. 21317–21326. DOI: 10.1029/1999JD900384.

Pandis, S. N., A. S. Wexler, and J. H. Seinfeld (1995). "Dynamics of Tropospheric Aerosols." In: *The Journal of Physical Chemistry* 99.24, pp. 9646–9659. DOI: 10.1021/j100024a003.

Park, R. J. (2004). "Natural and transboundary pollution influences on sulfate-nitrate-ammonium aerosols in the United States: Implications for policy." In: *Journal of Geophysical Research* 109.D15, p. D15204. DOI: 10.1029/2003JD004473.

Parrish, D. D. et al. (2009). "Comparison of air pollutant emissions among mega-cities." In: *Atmospheric Environment* 43.40, pp. 6435–6441. DOI: 10.1016/j.atmosenv.2009.06.024.

Peckhaus, A. et al. (2016). "A comparative study of K-rich and Na/Ca-rich feldspar ice-nucleating particles in a nanoliter droplet freezing assay." In: *Atmospheric Chemistry and Physics* 16.18, pp. 11477–11496. DOI: 10.5194/acp-16-11477-2016.

Petters, S. S. et al. (2019). "Temperature- and Humidity-Dependent Phase States of Secondary Organic Aerosols." In: *Geophysical Research Letters* 46.2, pp. 1005–1013. DOI: 10.1029/2018GL080563.

Piedehierro, A. A. et al. (2021). "Ice nucleation on surrogates of boreal forest SOA particles: effect of water content and oxidative age." In: *Atmospheric Chemistry and Physics* 21.14, pp. 11069–11078. DOI: 10.5194/ACP-21-11069-2021.

Pöschl, U. (2005). "Atmospheric Aerosols: Composition, Transformation, Climate and Health Effects." In: *Angewandte Chemie International Edition* 44.46, pp. 7520–7540. DOI: 10.1002/anie.200501122.

Pöschl, U. and M. Shiraiwa (2015). "Multiphase Chemistry at the Atmosphere–Biosphere Interface Influencing Climate and Public Health in the Anthropocene." In: *Chemical Reviews* 115.10, pp. 4440–4475. DOI: 10.1021/cr500487s.

Prenni, A. J. et al. (2009). "Heterogeneous ice nucleation measurements of secondary organic aerosol generated from ozonolysis of alkenes." In: *Geophysical Research Letters* 36.6, p. L06808. DOI: 10.1029/2008GL036957.

Price, H. C. et al. (2015). "Water diffusion in atmospherically relevant α-pinene secondary organic material." In: *Chemical Science* 6.8, pp. 4876–4883. DOI: 10.1039/C5SC00685F.

Prospero, J. M. (1999). "Long-range transport of mineral dust in the global atmosphere: Impact of African dust on the environment of the southeastern United States." In: *Proceedings of the National Academy of Sciences* 96.7, pp. 3396–3403. DOI: 10.1073/pnas.96.7.3396.

Pruppacher, H. and R. Jaenicke (1995). "The processing of water vapor and aerosols by atmospheric clouds, a global estimate." In: *Atmospheric Research* 38.1-4, pp. 283–295. DOI: 10.1016/0169-8095(94)00098-X.

Pruppacher, H. and J. Klett (1997). *Microphysics of Clouds and Precipitation*. Springer.

Ramanathan, V. (2001). "Aerosols, Climate, and the Hydrological Cycle." In: *Science* 294.5549, pp. 2119–2124. DOI: 10.1126/science.1064034.

Raoult, F.-M. (1889). "Recherches expérimentales sur les tensions de vapeur des dissolutions." In: *Journal de Physique Théorique et Appliquée* 8.1, pp. 5–20. DOI: 10.1051/jphystap:0188900800500.

Reid, J. P. et al. (2018). *The viscosity of atmospherically relevant organic particles*. DOI: 10.1038/s41467-018-03027-z.

Reimann, S. and A. C. Lewis (2007). "Anthropogenic VOCs." In: *Volatile Organic Compounds in the Atmosphere*. Oxford, UK: Blackwell Publishing Ltd, pp. 33–81. DOI: 10.1002/9780470988657.ch2.

Richardson, M. (2009). "Making Real Time Measurements of Ice Nuclei Concentrations at Upper Tropospheric Temperatures : Extending the Capabilities of the Continuous Flow Diffusion." PhD thesis, p. 274.

Roberts, P. and J. Hallett (1968). "A laboratory study of the ice nucleating properties of some mineral particulates." In: *Quarterly Journal of the Royal Meteorological Society* 94.399, pp. 25–34. DOI: `10.1002/qj.49709439904`.

Robock, A. (2000). "Volcanic eruptions and climate." In: *Reviews of Geophysics* 38.2, pp. 191–219. DOI: `10.1029/1998RG000054`.

Rogers, D. C. (1988). "Development of a continuous flow thermal gradient diffusion chamber for ice nucleation studies." In: *Atmospheric Research* 22.2, pp. 149–181. DOI: `10.1016/0169-8095(88)90005-1`.

Rogers, D. C. et al. (2001). "A Continuous-Flow Diffusion Chamber for Airborne Measurements of Ice Nuclei." In: *Journal of Atmospheric and Oceanic Technology* 18.5, pp. 725–741. DOI: `10.1175/1520-0426(2001)018<0725:ACFDCF>2.0.CO;2`.

Rosenoern, T., J. C. Schlenker, and S. T. Martin (2008). "Hygroscopic Growth of Multicomponent Aerosol Particles Influenced by Several Cycles of Relative Humidity." In: *The Journal of Physical Chemistry A* 112.11, pp. 2378–2385. DOI: `10.1021/jp0771825`.

Rothfuss, N. E. and M. D. Petters (2017). "Influence of Functional Groups on the Viscosity of Organic Aerosol." In: *Environmental Science & Technology* 51.1, pp. 271–279. DOI: `10.1021/acs.est.6b04478`.

Ryder, C. L. et al. (2013). "Impact of atmospheric transport on the evolution of microphysical and optical properties of Saharan dust." In: *Geophysical Research Letters* 40.10, pp. 2433–2438. DOI: `10.1002/grl.50482`.

Saathoff, H. et al. (2009). "Temperature dependence of yields of secondary organic aerosols from the ozonolysis of α-pinene and limonene." In: *Atmospheric Chemistry and Physics* 9.5, pp. 1551–1577. DOI: `10.5194/acp-9-1551-2009`.

Sassen, K., Z. Wang, and D. Liu (2008). "Global distribution of cirrus clouds from CloudSat/Cloud-Aerosol Lidar and Infrared Pathfinder Satellite Observations (CALIPSO) measurements." In: *Journal of Geophysical Research* 113.8, D00A12. DOI: `10.1029/2008JD009972`.

Sassen, K. et al. (2003). "Saharan dust storms and indirect aerosol effects on clouds: CRYSTAL-FACE results." In: *Geophysical Research Letters* 30.12, p. 1633. DOI: `10.1029/2003GL017371`.

Satheesh, S. and K. Krishnamoorthy (2005). "Radiative effects of natural aerosols: A review." In: *Atmospheric Environment* 39.11, pp. 2089–2110. DOI: `10.1016/j.atmosenv.2004.12.029`.

Schepanski, K. (2018). "Transport of Mineral Dust and Its Impact on Climate." In: *Geosciences* 8.5, p. 151. DOI: `10.3390/geosciences8050151`.

Schiebel, T. (2017). "Ice Nucleation Activity of Soil Dust Aerosols." PhD thesis. Karlsruhe Institute of Technology. DOI: `10.5445/IR/1000076327`.

Schill, G. P. and M. A. Tolbert (2013). "Heterogeneous ice nucleation on phase-separated organic-sulfate particles: effect of liquid vs. glassy coatings." In: *Atmospheric Chemistry and Physics* 13.9, pp. 4681–4695. DOI: `10.5194/acp-13-4681-2013`.

Schill, G. P., D. O. De Haan, and M. A. Tolbert (2014). "Heterogeneous Ice Nucleation on Simulated Secondary Organic Aerosol." In: *Environmental Science & Technology* 48.3, pp. 1675–1682. DOI: `10.1021/es4046428`.

Schlenker, J. C. and S. T. Martin (2005). "Crystallization Pathways of SulfateNitrateAmmonium Aerosol Particles." In: *The Journal of Physical Chemistry A* 109.44, pp. 9980–9985. DOI: `10.1021/jp052973x`.

Schlenker, J. C. et al. (2004). "Crystals Formed at 293 K by Aqueous SulfateNitrateAmmoniumProton Aerosol Particles." In: *The Journal of Physical Chemistry A* 108.43, pp. 9375–9383. DOI: `10.1021/jp047836z`.

Schnaiter, M. et al. (2012). "Influence of particle size and shape on the backscattering linear depolarisation ratio of small ice crystals – cloud chamber measurements in the context of contrail and cirrus microphysics." In: *Atmospheric Chemistry and Physics* 12.21, pp. 10465–10484. DOI: `10.5194/acp-12-10465-2012`.

Schneider, J. et al. (2021). "High homogeneous freezing onsets of sulfuric acid aerosol at cirrus temperatures." In: *Atmospheric Chemistry and Physics* 21.18, pp. 14403–14425. DOI: `10.5194/acp-21-14403-2021`.

Schwartz, J., D. W. Dockery, and L. M. Neas (1996). "Is Daily Mortality Associated Specifically with Fine Particles?" In: *Journal of the Air & Waste Management Association* 46.10, pp. 927–939. DOI: 10.1080/10473289.1996.10467528.

Seinfeld, J. H. and S. N. Pandis (2012). *Atmospheric Chemistry and Physics: From Air Pollution to Climate Change*. Wiley.

Shilling, J. E., T. J. Fortin, and M. A. Tolbert (2006). "Depositional ice nucleation on crystalline organic and inorganic solids." In: *Journal of Geophysical Research* 111.D12, p. D12204. DOI: 10.1029/2005JD006664.

Shiraiwa, M. et al. (2011). "Gas uptake and chemical aging of semisolid organic aerosol particles." In: *Proceedings of the National Academy of Sciences* 108.27, pp. 11003–11008. DOI: 10.1073/pnas.1103045108.

Shiraiwa, M. et al. (2017). "Aerosol Health Effects from Molecular to Global Scales." In: *Environmental Science & Technology* 51.23, pp. 13545–13567. DOI: 10.1021/acs.est.7b04417.

Silva, R. A. et al. (2013). "Global premature mortality due to anthropogenic outdoor air pollution and the contribution of past climate change." In: *Environmental Research Letters* 8.3, p. 034005. DOI: 10.1088/1748-9326/8/3/034005.

Slade, L., H. Levine, and D. S. Reid (1991). "Beyond water activity: Recent advances based on an alternative approach to the assessment of food quality and safety." In: *Critical Reviews in Food Science and Nutrition* 30.2-3, pp. 115–360. DOI: 10.1080/10408399109527543.

Smith, E. J. and K. J. Heffernan (1954). "Airborne measurements of the concentration of natural and artificial freezing nuclei." In: *Quarterly Journal of the Royal Meteorological Society* 80.344, pp. 182–197. DOI: 10.1002/qj.49708034405.

Smith, S. J. et al. (2011). "Anthropogenic sulfur dioxide emissions: 1850–2005." In: *Atmospheric Chemistry and Physics* 11.3, pp. 1101–1116. DOI: 10.5194/acp-11-1101-2011.

Sorensen, C. M. et al. (2019). "Grand challenges for aerosol science and technology." In: *Aerosol Science and Technology* 53.7, pp. 731–734. DOI: 10.1080/02786826.2019.1611333.

Sorensen, C. M. et al. (2011). "Optical Measurement Techniques: Fundamentals and Applications." In: *Aerosol Measurement*. Hoboken, NJ, USA: John Wiley & Sons, Inc., pp. 269–312. DOI: 10.1002/9781118001684.ch13.

Spann, J. and C. Richardson (1985). "Measurement of the water cycle in mixed ammonium acid sulfate particles." In: *Atmospheric Environment (1967)* 19.5, pp. 819–825. DOI: 10.1016/0004-6981(85)90072-1.

Steiner, A. H. and A. L. Goldstein (2007). "Biogenic VOCs." In: *Volatile Organic Compounds in the Atmosphere*. Oxford, UK: Blackwell Publishing Ltd, pp. 82–128. DOI: 10.1002/9780470988657.ch3.

Stelson, A. and J. Seinfeld (2007). "Relative humidity and temperature dependence of the ammonium nitrate dissociation constant." In: *Atmospheric Environment* 41.5, pp. 126–135. DOI: 10.1016/j.atmosenv.2007.10.063.

Stetzer, O. et al. (2008). "The Zurich Ice Nucleation Chamber (ZINC)-A New Instrument to Investigate Atmospheric Ice Formation." In: *Aerosol Science and Technology* 42.1, pp. 64–74. DOI: 10.1080/02786820701787944.

Stolzenburg, D. et al. (2018). "Rapid growth of organic aerosol nanoparticles over a wide tropospheric temperature range." In: *Proceedings of the National Academy of Sciences* 115.37, pp. 9122–9127. DOI: 10.1073/pnas.1807604115.

Storelvmo, T. (2017). "Aerosol Effects on Climate via Mixed-Phase and Ice Clouds." In: *Annual Review of Earth and Planetary Sciences* 45.1, pp. 199–222. DOI: 10.1146/annurev-earth-060115-012240.

Stubenrauch, C. J. et al. (2013). "Assessment of Global Cloud Datasets from Satellites: Project and Database Initiated by the GEWEX Radiation Panel." In: *Bulletin of the American Meteorological Society* 94.7, pp. 1031–1049. DOI: 10.1175/BAMS-D-12-00117.1.

Sullivan, R. C. et al. (2010). "Irreversible loss of ice nucleation active sites in mineral dust particles caused by sulphuric acid condensation." In: *Atmospheric Chemistry and Physics* 10.23, pp. 11471–11487. DOI: 10.5194/acp-10-11471-2010.

Tang, I. N. and H. R. Munkelwitz (1994). "Water activities, densities, and refractive indices of aqueous sulfates and sodium nitrate droplets of atmospheric importance." In: *Journal of Geophysical Research* 99.D9, p. 18801. DOI: 10.1029/94JD01345.

– (1977). "Aerosol growth studies—III ammonium bisulfate aerosols in a moist atmosphere." In: *Journal of Aerosol Science* 8.5, pp. 321–330. DOI: 10.1016/0021-8502(77)90019-2.

Tang, I. N. (1980). "On the equilibrium partial pressures of nitric acid and ammonia in the atmosphere." In: *Atmospheric Environment (1967)* 14.7, pp. 819–828. DOI: 10.1016/0004-6981(80)90138-9.

Tang, I. N. and H. R. Munkelwitz (1993). "Composition and temperature dependence of the deliquescence properties of hygroscopic aerosols." In: *Atmospheric Environment. Part A. General Topics* 27.4, pp. 467–473. DOI: 10.1016/0960-1686(93)90204-C.

Thomason, L. W. and J.-P. Vernier (2013). "Improved SAGE II cloud/aerosol categorization and observations of the Asian tropopause aerosol layer: 1989–2005." In: *Atmospheric Chemistry and Physics* 13.9, pp. 4605–4616. DOI: 10.5194/acp-13-4605-2013.

Tillmann, R. et al. (2010). "Influence of relative humidity and temperature on the production of pinonaldehyde and OH radicals from the ozonolysis of α-pinene." In: *Atmospheric Chemistry and Physics* 10.15, pp. 7057–7072. DOI: 10.5194/acp-10-7057-2010.

Tomasi, C. and A. Lupi (2017). "Primary and Secondary Sources of Atmospheric Aerosol." In: *Atmospheric Aerosols: Life Cycles and Effects on Air Quality and Climate*. Wiley. DOI: 10.1117/3.2268619.ch5.

Tong, H.-J. et al. (2011). "Measurements of the timescales for the mass transfer of water in glassy aerosol at low relative humidity and ambient temperature." In: *Atmospheric Chemistry and Physics* 11.10, pp. 4739–4754. DOI: 10.5194/acp-11-4739-2011.

Twohy, C. H. et al. (2002). "Deep convection as a source of new particles in the midlatitude upper troposphere." In: *Journal of Geophysical Research: Atmospheres* 107.D21, pp. 6–1. DOI: 10.1029/2001JD000323.

Ullrich, R. et al. (2017). "A New Ice Nucleation Active Site Parameterization for Desert Dust and Soot." In: *Journal of the Atmospheric Sciences* 74.3, pp. 699–717. DOI: 10.1175/JAS-D-16-0074.1.

Umhauer, H., S. Berbner, and G. Hemmer (2000). "Optical In Situ Size and Concentration Measurement of Particles Dispersed in Gases at Temperatures up to 1000°C." In: *Particle & Particle Systems Characterization* 17.1, pp. 03–15. DOI: 10.1002/(SICI)1521-4117(200003)17:1<03::AID-PPSC3>3.0.CO;2-N.

Usher, C. R., A. E. Michel, and V. H. Grassian (2003). "Reactions on Mineral Dust." In: *Chemical Reviews* 103.12, pp. 4883–4940. DOI: 10.1021/cr020657y.

Vaden, T. D. et al. (2011). "Evaporation kinetics and phase of laboratory and ambient secondary organic aerosol." In: *Proceedings of the National Academy of Sciences* 108.6, pp. 2190–2195. DOI: 10.1073/pnas.1013391108.

Vali, G. et al. (2015). "Technical Note: A proposal for ice nucleation terminology." In: *Atmospheric Chemistry and Physics* 15.18, pp. 10263–10270. DOI: 10.5194/acp-15-10263-2015.

Vali, G. (1994). "Freezing Rate Due to Heterogeneous Nucleation." In: *Journal of the Atmospheric Sciences* 51.13, pp. 1843–1856. DOI: 10.1175/1520-0469(1994)051<1843:FRDTHN>2.0.CO;2.

Varga, G. et al. (2021). "Saharan dust and giant quartz particle transport towards Iceland." In: *Scientific Reports* 11.1, p. 11891. DOI: 10.1038/s41598-021-91481-z.

Varutbangkul, V. et al. (2006). "Hygroscopicity of secondary organic aerosols formed by oxidation of cycloalkenes, monoterpenes, sesquiterpenes, and related compounds." In: *Atmospheric Chemistry and Physics* 6.9, pp. 2367–2388. DOI: 10.5194/acp-6-2367-2006.

Vernier, J. P. et al. (2009). "Tropical stratospheric aerosol layer from CALIPSO lidar observations." In: *Journal of Geophysical Research* 114.24, D00H10. DOI: 10.1029/2009JD011946.

Vernier, J.-P., L. W. Thomason, and J. Kar (2011). "CALIPSO detection of an Asian tropopause aerosol layer." In: *Geophysical Research Letters* 38.7, n/a–n/a. DOI: 10.1029/2010GL046614.

Vernier, J.-P. et al. (2018). "BATAL: The Balloon Measurement Campaigns of the Asian Tropopause Aerosol Layer." In: *Bulletin of the American Meteorological Society* 99.5, pp. 955–973. DOI: 10.1175/BAMS-D-17-0014.1.

Vernier, J.-P. P. et al. (2015). "Increase in upper tropospheric and lower stratospheric aerosol levels and its potential connection with Asian pollution." In: *Journal of Geophysical Research: Atmospheres* 120.4, pp. 1608–1619. DOI: 10.1002/2014JD022372.

Virtanen, A. et al. (2010). "An amorphous solid state of biogenic secondary organic aerosol particles." In: *Nature* 467.7317, pp. 824–827. DOI: 10.1038/nature09455.

Voigtländer, J. et al. (2012). "Numerical simulations of mixing conditions and aerosol dynamics in the CERN CLOUD chamber." In: *Atmospheric Chemistry and Physics* 12.4, pp. 2205–2214. DOI: 10.5194/acp-12-2205-2012.

Wagner, R. et al. (2006). *Probing ice clouds by broadband mid-infrared extinction spectroscopy: Case studies from ice nucleation experiments in the AIDA aerosol and cloud chamber*. DOI: 10.5194/acp-6-4775-2006.

Wagner, R. et al. (2012). "Ice cloud processing of ultra-viscous/glassy aerosol particles leads to enhanced ice nucleation ability." In: *Atmospheric Chemistry and Physics* 12.18, pp. 8589–8610. DOI: 10.5194/acp-12-8589-2012.

Wagner, R. and O. Möhler (2013). "Heterogeneous ice nucleation ability of crystalline sodium chloride dihydrate particles." In: *Journal of Geophysical Research: Atmospheres* 118.10, pp. 4610–4622. DOI: 10.1002/jgrd.50325.

Wagner, R. et al. (2009). "A review of optical measurements at the aerosol and cloud chamber AIDA." In: *Journal of Quantitative Spectroscopy and Radiative Transfer* 110.11, pp. 930–949. DOI: 10.1016/j.jqsrt.2009.01.026.

Wagner, R. et al. (2015). "Crystallization and immersion freezing ability of oxalic and succinic acid in multicomponent aqueous organic aerosol particles." In: *Geophysical Research Letters* 42.7, pp. 2464–2472. DOI: 10.1002/2015GL063075.

Wagner, R. et al. (2016). "Pre-activation of ice-nucleating particles by the pore condensation and freezing mechanism." In: *Atmospheric Chemistry and Physics* 16.4, pp. 2025–2042. DOI: 10.5194/acp-16-2025-2016.

Wagner, R. et al. (2017). "Heterogeneous ice nucleation of α-pinene SOA particles before and after ice cloud processing." In: *Journal of Geophysical Research: Atmospheres* 122.9, pp. 4924–4943. DOI: 10.1002/2016JD026401.

Wagner, R. et al. (2020). "Solid Ammonium Nitrate Aerosols as Efficient Ice Nucleating Particles at Cirrus Temperatures." In: *Journal of Geophysical Research: Atmospheres* 125.8, e2019JD032248. DOI: 10.1029/2019JD032248.

Wang, B. et al. (2012). "The deposition ice nucleation and immersion freezing potential of amorphous secondary organic aerosol: Pathways for ice and mixed-phase cloud formation." In: *Journal of Geophysical Research: Atmospheres* 117.D16, n/a–n/a. DOI: 10.1029/2012JD018063.

Warner, J. X. et al. (2017). "Increased atmospheric ammonia over the world's major agricultural areas detected from space." In: *Geophysical Research Letters* 44.6, pp. 2875–2884. DOI: 10.1002/2016GL072305.

Weigel, R. et al. (2021). "In situ observation of new particle formation (NPF) in the tropical tropopause layer of the 2017 Asian monsoon anticyclone – Part 1: Summary of StratoClim results." In: *Atmospheric Chemistry and Physics* 21.15, pp. 11689–11722. DOI: 10.5194/acp-21-11689-2021.

Welti, A. et al. (2020). "SPIN modification for low-temperature experiments." In: *Atmospheric Measurement Techniques* 13.12, pp. 7059–7067. DOI: 10.5194/amt-13-7059-2020.

Whale, T. F. et al. (2017). "The role of phase separation and related topography in the exceptional ice-nucleating ability of alkali feldspars." In: *Physical Chemistry Chemical Physics* 19.46, pp. 31186–31193. DOI: 10.1039/C7CP04898J.

Williams, J. and R. Koppmann (2007). "Volatile Organic Compounds in the Atmosphere: An Overview." In: *Volatile Organic Compounds in the Atmosphere*. Oxford, UK: Blackwell Publishing Ltd. Chap. 1, pp. 1–32. DOI: 10.1002/9780470988657.ch1.

Williamson, C. J. et al. (2019). "A large source of cloud condensation nuclei from new particle formation in the tropics." In: *Nature* 574.7778, pp. 399–403. DOI: 10.1038/s41586-019-1638-9.

Wilson, T. W. et al. (2012). "Glassy aerosols with a range of compositions nucleate ice heterogeneously at cirrus temperatures." In: *Atmospheric Chemistry and Physics* 12.18, pp. 8611–8632. DOI: 10.5194/acp-12-8611-2012.

Wise, M. E., K. J. Baustian, and M. A. Tolbert (2010). "Internally mixed sulfate and organic particles as potential ice nuclei in the tropical tropopause region." In: *Proceedings of the National Academy of Sciences* 107.15, pp. 6693–6698. DOI: 10.1073/pnas.0913018107.

Wise, M. E. et al. (2012). "Depositional ice nucleation onto crystalline hydrated NaCl particles: a new mechanism for ice formation in the troposphere." In: *Atmospheric Chemistry and Physics* 12.2, pp. 1121–1134. DOI: 10.5194/acp-12-1121-2012.

Wolf, M. J. et al. (2020). "A biogenic secondary organic aerosol source of cirrus ice nucleating particles." In: *Nature Communications* 11.1, p. 4834. DOI: 10.1038/s41467-020-18424-6.

Wurzler, S., T. G. Reisin, and Z. Levin (2000). "Modification of mineral dust particles by cloud processing and subsequent effects on drop size distributions." In: *Journal of Geophysical Research: Atmospheres* 105.D4, pp. 4501–4512. DOI: 10.1029/1999JD900980.

Xiao, M. et al. (2021). "The driving factors of new particle formation and growth in the polluted boundary layer." In: *Atmospheric Chemistry and Physics* 21.18, pp. 14275–14291. DOI: 10.5194/acp-21-14275-2021.

Yakobi-Hancock, J. D., L. A. Ladino, and J. P. D. Abbatt (2013). "Feldspar minerals as efficient deposition ice nuclei." In: *Atmospheric Chemistry and Physics* 13.22, pp. 11175–11185. DOI: 10.5194/acp-13-11175-2013.

Yang, Z., A. K. Bertram, and K. C. Chou (2011). "Why Do Sulfuric Acid Coatings Influence the Ice Nucleation Properties of Mineral Dust Particles in the Atmosphere?" In: *The Journal of Physical Chemistry Letters* 2.11, pp. 1232–1236. DOI: 10.1021/jz2003342.

You, Y. et al. (2014). "Liquid–liquid phase separation in atmospherically relevant particles consisting of organic species and inorganic salts." In: *International Reviews in Physical Chemistry* 33.1, pp. 43–77. DOI: 10.1080/0144235X.2014.890786.

Yu, P. et al. (2015). "Composition and physical properties of the Asian Tropopause Aerosol Layer and the North American Tropospheric Aerosol Layer." In: *Geophysical Research Letters* 42.7, pp. 2540–2546. DOI: 10.1002/2015GL063181.

Zawadowicz, M. A. et al. (2015). "Hygroscopic and phase separation properties of ammonium sulfate/organics/water ternary solutions." In: *Atmospheric Chemistry and Physics* 15.15, pp. 8975–8986. DOI: 10.5194/acp-15-8975-2015.

Zelinka, M. D., C. Zhou, and S. A. Klein (2016). "Insights from a refined decomposition of cloud feedbacks." In: *Geophysical Research Letters* 43.17, pp. 9259–9269. DOI: 10.1002/2016GL069917.

Zelinka, M. D. et al. (2017). "Clearing clouds of uncertainty." In: *Nature Climate Change* 7.10, pp. 674–678. DOI: 10.1038/nclimate3402.

Zhang, Q. et al. (2007). "Ubiquity and dominance of oxygenated species in organic aerosols in anthropogenically-influenced Northern Hemisphere midlatitudes." In: *Geophysical Research Letters* 34.13, n/a–n/a. DOI: 10.1029/2007GL029979.

Zhang, R. et al. (2008). "Variability in morphology, hygroscopicity, and optical properties of soot aerosols during atmospheric processing." In: *Proceedings of the National Academy of Sciences* 105.30, pp. 10291–10296. DOI: 10.1073/pnas.0804860105.

Zhang, Y. et al. (2019). "The Cooling Rate- and Volatility-Dependent Glass-Forming Properties of Organic Aerosols Measured by Broadband Dielectric Spectroscopy." In: *Environmental Science & Technology* 53.21, pp. 12366–12378. DOI: 10.1021/acs.est.9b03317.

Zobrist, B. et al. (2006). "Oxalic acid as a heterogeneous ice nucleus in the upper troposphere and its indirect aerosol effect." In: *Atmospheric Chemistry and Physics* 6.10, pp. 3115–3129. DOI: 10.5194/acp-6-3115-2006.

Zobrist, B. et al. (2008a). "Do atmospheric aerosols form glasses?" In: *Atmospheric Chemistry and Physics* 8.17, pp. 5221–5244. DOI: 10.5194/acp-8-5221-2008.

Zobrist, B. et al. (2008b). "Heterogeneous Ice Nucleation in Aqueous Solutions: the Role of Water Activity." In: *The Journal of Physical Chemistry A* 112.17, pp. 3965–3975. DOI: 10.1021/jp7112208.

Zobrist, B. et al. (2011). "Ultra-slow water diffusion in aqueous sucrose glasses." In: *Physical Chemistry Chemical Physics* 13.8, p. 3514. DOI: 10.1039/c0cp01273d.

Zolles, T. et al. (2015). "Identification of Ice Nucleation Active Sites on Feldspar Dust Particles." In: *The Journal of Physical Chemistry A* 119.11, pp. 2692–2700. DOI: 10.1021/jp509839x.

Zuberi, B. et al. (2001). "Heterogeneous Freezing of Aqueous Particles Induced by Crystallized $(NH_4)_2SO_4$, Ice, and Letovicite." In: *The Journal of Physical Chemistry A* 105.26, pp. 6458–6464. DOI: 10.1021/jp010094e.

ACKNOWLEDGEMENTS

This PhD has been a great journey, on both the scientific and personal sides. I am grateful to have had the opportunity to get to know and work with amazing scientists, technicians, and PhD students.

I would like to start by thanking Prof. Dr. Thomas Leisner and Prof. Dr. Joachim Curtius for being my Referee and Co-Referee and for the useful discussions we had during these years.

I am profoundly grateful to Dr. Ottmar Möhler and Dr. Kristina Höhler who gave me the opportunity to perform my PhD here at IMK-AAF and that supervised my work. Your enthusiasm and encouragement have been fundamental to overcome all the difficulties I encountered in these years.

I sincerely thank Dr. Robert Wagner for all the scientific discussions and his fundamental contribution to all the AIDA campaigns. I have really enjoyed working with you in the Lab!

The work presented in this thesis would have not been possible without the help and the collaboration of numerous technicians from the AAF and the CLOUD experiment. In particular, I would like to thank Susanne Bolz, Rainer Buschbacher, Tomasz Chudy, Olga Dombrowski, Jens Nadolny, Georg Scheurig, Frank Schwarz, and Steffen Vogt for their continuous and patient assistance.

I thank all the people that contributed to this thesis providing key measurements for the interpretation of the experiments: Dr. R. Wagner (FTIR data), Dr. M. Wang (Br$^-$-CIMS data), W. Scholz (PTR-MS data), G. Marie (NO$_3^-$-CIMS data), B. Lopez (AMS data from the CLOUD14 campaign), Dr. A. A. Piedehierro and Dr. A. Welti (SPIN data), Z. Brasseur (PINCii data), and J. Song (AMS data from the INCAS01 campaign).

I am grateful to the organizers and the participants of the FIN-01 campaign for providing the valuable data set of the feldspar coating experiments I analyzed in Chapter 8.

A special thank you goes to all the students and scientists that contributed to the CLOUD14 campaign. It is not always easy to be part of a large collaboration, but the nice and enthusiastic atmosphere during the campaigns and the workshops made this experience unique. I am particularly grateful to all the other CLOUD-MOTION students, your friendship and support have been fundamental in these years.

Thanks to all the colleagues with whom I shared a lunch or coffee break at the institute. I spent a very nice time with all of you.

In the end, my deepest thanks to my family Andrea, Anna, Alberto, Federica, and Matteo. You always believe in me even when I do not. I would have never made it to the end of this journey without your support.